Inferring the evolution pathways and the explosion mechanism of core-collapse supernova through nebular spectroscopy

A thesis presented
by

FANG Qiliang

Supervised
by

Professor MAEDA Keiichi

to

The Department of Astronomy, School of Physics

in partial fulfillment of the requirements
for the degree of
Doctor of Philosophy
in the subject of
Astronomy

Kyoto University, Kyoto, Japan

December 2022

Abstract

Core-collapse supernovae, or CCSNe, are the final explosions triggered by the iron-core infall of the massive stars when they reach the end points of their lives after the nuclear fuels are exhausted. The CCSNe are diverse in observation, and how such diversity is linked to the evolution pathways of the progenitors are not clear. During the explosion, a large amount of energy is released, however, the explosion energy yield, the explosion geometry, and their relations with the properties of the progenitors upon the explosions are still under debate. These are all crucial ingredients for revealing the massive star evolution and the explosion mechanism of CCSNe. The properties of the expelled stellar material (*ejecta*) are very important to study these topics. The composition of the ejecta not only contains rich information of the progenitor star (for example, the amount of the oxygen can be used to indicate the zero-age-main-sequence mass), but also reflects the mass-loss history. The dynamics of the ejecta, including the velocity scale and the geometry, also provides important constraints on the explosion mechanism. Inferring these physics properties from the lights captured by the telescopes is not an easy task, we thus need theoretical modeling and statistics based on the large sample.

Late phase (*nebular*) spectra are powerful tools for studying these topics. Following the expansion, the ejecta becomes gradually transparent, allowing one to directly look into the core region where the explosion takes place. In this work, we present the so-far largest nebular spectroscopy sample of stripped-envelope supernovae (SESNe, explosions produced by massive stars that have loss their hydrogen or helium-rich layers). We first develop a method to measure the amount of the helium layer from the strength of the nitrogen emissions, which is then apply to the sample of SESNe. By comparing the degree of stripping with the progenitor mass measured from the oxygen content, we show that the hybrid mass-loss mechanism is at work to shape the diversity of SESNe: the stripping of the hydrogen envelope is mass-independent, and can be naturally explained by binary interaction without major difficulty; while the further stripping of the helium layer strongly depends on the progenitor mass, and stellar wind can be the possible candidate, although the eruptive activities of the massive stars can not be ruled out. We discuss the general properties of the ejecta dynamics, including the velocity (measured by the emission line widths) and the ejecta geometry (measured by the emission line profiles). We demonstrate that the SNe with large oxygen contents tend to have large expansion velocities, which can be explained by the scheme where more massive progenitors lead to more energetic explosions. By performing the radioactive hydrodynamics simulations, for the first time we establish the quantitative relation between the mass of the progenitor carbon-oxygen (CO) core and the kinetic energy, which is required to produce the observed correlation. Through the comprehensive analysis on the emission line profiles, we find that about half of the SESNe in the sample have detectable level of asymmetry, suggesting the deviation from symmetric explosion is common even for normal SESNe. For those SESNe considered as asphericical explosions, we reveal the explosion-made regions are bi-modal, i.e., characterized by two detached iron-rich bubbles. We then explore the relation between the explosion geometry and the progenitor CO core mass, and the statistics reveals (1) whether the explosion is spherical or aspherical is not determined by the CO core masses: indeed, even the oxygen contents are increased by ~10 times, the occurrence rates of the spherical/aspherical explosions remain roughly equal; (2) the aspherical explosions become more collimated, and their bi-modalities also increase as the CO core masses grow. This is the first observational evidence for the relation between the progenitor mass and the explosion geometry.

The results in this work provide important constraints on the important astrophysical problems from

observational grounds: (1) what are the progenitor systems of the CCSNe? How the different stellar systems shape the observed diversity of the CCSNe? (2) What is the explosion process of CCSNe? (3) How the explosion energy yields, and their distributions, depend on the progenitor properties?

Content

Chapter 1. Introduction

When a massive star (with zero-age main-sequence mass >8 solar mass, or $M_{\odot}$) fails in its struggle with the gravity force after the nuclear fuel in its interior is exhausted, without the support from the thermal pressure, the iron core collapses to form a compact object (a neutron star or a black hole). The central region quickly reaches to the density of the neutron star, then bounce back like a piston, which creates the strong shock wave that rapidly eject the rest of the stellar material (the *ejecta*), leading to the catastrophic event called core-collapse supernova (CCSN).

The duration of the collapsing process is very short, appears to be a sudden flash which is not captured from observation until very recent (see for example Bersten et al. 2018). The physics that governs this process is a fascinating problem that has confused astronomers for decades, but it is very difficult to be observed for its extremely short time scale; what we are indeed observing is the hot, expelled ejecta that shines as bright as billions solar luminosity (a typical value is $\sim 10^{49}$ erg s^{-1}). Powered by the decay chain of the unstable radioactive elements generated during the explosion, the ejecta is bright enough to be observed from distant for months to years after the explosion. The physical properties of the ejecta, including its mass, composition, expansion velocity and configuration etc., are key ingredients toward understanding the properties of the supernova progenitor and the explosion.

To decode the physical properties of the ejecta, it is important to understand how the photons are generated and propagate in the ejecta. This is usually done by radiative transfer calculation, i.e., by assuming the specific structure of the ejecta, and then calculate how the photons look like when they escape after their complicated interaction with the ejecta material. The result of the calculation is further compared with the observation, from which we can extract rich information of the ejecta. A complete understanding of the ejecta structure can not only constrain the explosion mechanism, but can also reveal the progenitor stellar system, which is also an important unsolved problem in astronomy.

This thesis focuses on stripped-envelope supernova (SESN), a subtype of CCSNe produced by massive stars that have loss most of the hydrogen- or helium-rich layer before the explosion. We use the late phase ("*nebular*") spectroscopy, which is taken several months after the explosion, to explore the progenitor system of these objects, and constrain the explosion mechanism by comparing the theoretical models and the recent observations of supernovae.

Section 1. *Diversity of core-collapse supernova*

The classification of supernova stems from the scheme proposed by Minkowski (1941) in the middle of 20th century, and is still a systematic and long-standing problem in modern astronomy. In this scheme, the CCSNe are classified into two major types: type I, which show hydrogen (H) features in the early phase spectra, or type II, which do not. Type II supernovae are further divided into two subtypes: type IIP with light curves characterized by prominent plateaus, and type IIL with light curves decline linearly (Barbon et al. 1979). The classification of type I CCSNe are based on the optical spectra (which are usually obtained near the maximum brightness): type Ib show strong helium (He) lines but show no silicon (Si) lines (which is the characterized

feature of type Ia SNe produced by the thermonuclear explosion of white dwarfs); type Ic with spectra characterized by the absence of H, He and Si lines. The schematic classification scheme is shown in Figure 1.1 (A). Some examples CCSNe spectra near the light curve peaks are shown in Figure 1.1 (B).

Based on the spectroscopic properties, CCSNe can be further divided into more subtypes. Here we introduce two subtypes that fall into the interest of this thesis: (1) type IIb SNe with early-phase spectra dominated by hydrogen features, which gradually fade away as the SNe evolve and are replaced by helium features, making the spectra assemble to those of SNe Ib; (2) broad-line type Ic (Ic-BL), a subtype of SNe Ic with early-phase spectra characterized by broad absorption lines (therefore the ejecta is expanding with very high velocity). SNe Ic-BL are particularly interesting because they are occasionally accompanied by the gamma-ray bursts (GRB), i.e., mysterious phenomena possibly created by the bipolar jets (see for example the review by Woosley & Bloom et al. 2006).

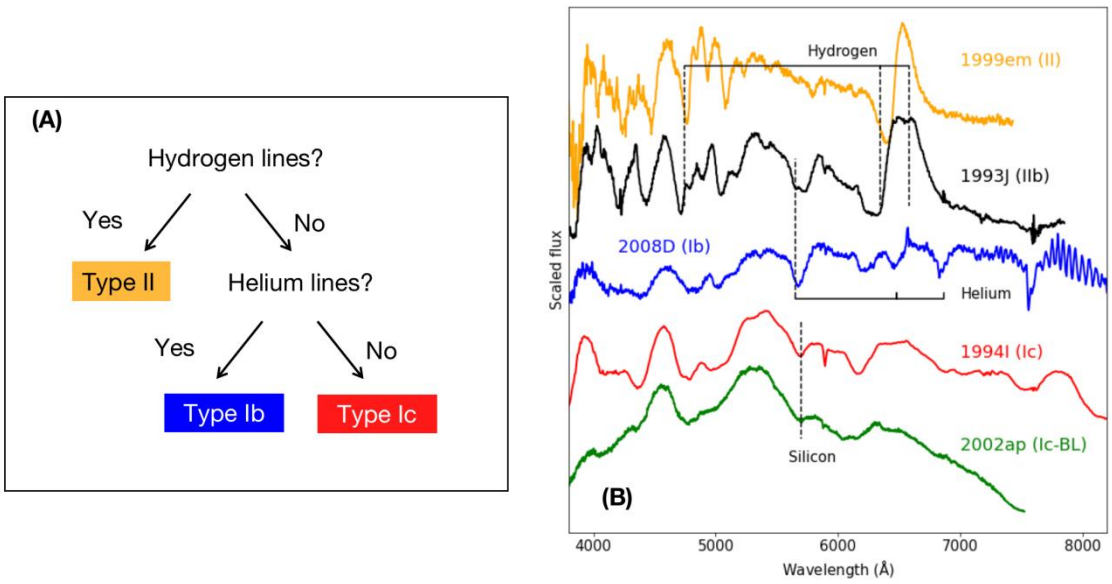

Figure 1.1. **(A) The schematic classification scheme of CCSNe; (B) Some examples of early phase CCSNe spectra.** Sources: Barbon et al. 1995; Clocchiatti et al. 1996; Leonard et al. 2002; Malesani et al. 2009; Modjaz et al. 2014.

A basic open problem is how the different properties of the massive stars upon the explosions map to the different types of CCSNe. Indeed the physics that drives the diversity seen in CCSNe will provide us with deep insights of the explosion mechanism and the stellar evolution pathways that lead to the explosions. It is generally believed that the difference seen in SNe II/IIb/Ib/Ic is the result of different degrees of H-rich and He-rich layers stripping of the progenitor star before the explosion. Without mass-loss during the pre-SN evolution, a massive star would form an onion-like layered structure, with an H-rich envelope, He-rich layer, and C+O core from the surface to the inner part (Heger et al. 2003). A star with a massive H-rich envelope attached will explode as SN II. With substantial mass loss, a massive star explodes as an SN IIb or SN Ib depending on whether a small amount of its hydrogen envelope is left or it is completely removed before the explosion. Further stripping of nearly the entire He-rich layer would result in an SN Ic. Thus SNe IIb/Ib/Ic are unified as stripped-envelope CCSNe (or stripped-envelope SNe (SESNe)).

A question remains unanswered, i.e., the physics mechanism behind the pre-SN mass-loss. It is not clear

whether the stripping of the H- and He-rich layers forms a continuous distribution, or whether different mechanisms are responsible for the removal of the different layers. We will discuss this topic in the next section.

Section 2. *Pre-supernova mass-loss*

Before its explosion, the massive star may experiences substantial mass-loss, as inferred from the lack of the hydrogen or helium features in the spectra of certain SN subtypes. Little is known about the dominant mechanism of the mass-stripping, nor its dependency on the basic properties of the progenitor including the mass and metallicity. From theoretical aspects, two major channels may be responsible for such pre-SN mass-loss:

(1) Stellar wind: The stellar material is emitted from the atmosphere of a star if they are fast enough to escape the gravitational attraction. The winds from massive stars are referred to "line-driven wind" since the main source of opacity is provided by absorption lines of the accelerated materials;

(2) Binary mass transfer: When the stellar surface of a star in a binary system expands following its evolution and fills its Roche lobe, the material will flow to the companion star. As a result, the star gradually loss its outer envelop via this mechanism.

Which mechanism is responsible for the pre-SN mass-loss, or whether the two mechanisms are at work for different stripping processes, are key questions still under debate. Fortunately, the mass-loss rates through these two channels have very different dependencies on the stellar parameters; the efficiency of binary mass transfer is closely related to the separation of the binary orbit and the mass ratio of the donor/accretor, but not sensitive to the stellar mass. In contrast, stellar winds are strong enough to drive significant mass-loss only when the star is massive ($> 30 M_{\odot}$). In this sense, we can simplify the problem to "whether the stripping process is dependent on the stellar mass".

One of the obstruction toward answering this question comes from the difficulty in connecting the progenitor mass and the degree of stripping to the observables. To set a scene, SNe subtypes can be considered as rough indicators of mass stripping (in the sequence of SN IIb/Ib/Ic). Observations of SESNe pose an apparent conundrum: based on analysis of SN emission during the brightest, opaque phase, it has been argued that SNe IIb/Ib/Ic have similar ejecta mass ($M_{\rm ejecta}$), which may indicate similar $M_{\rm ZAMS}$ for all SESN classes (Liu et al. 2016; Lyman et al. 2016; Taddia et al. 2018). On the other hand, the environment in which SNe explode, and in particular the preference of SNe Ic for the most actively star-forming regions (and thus likely larger $M_{\rm ZAMS}$) argues otherwise (Anderson et al. 2012; Kuncarayakti et al. 2018). While there is a recent indirect indication from early-phase SN emission analysis that SN Ic progenitors may have larger $M_{\rm ZAMS}$ than SNe Ib (Fremling et al. 2018), the analysis of early-phase SN emission is complicated by various uncertainties. Additional progress can be made by identifying a set of observables that can directly trace $M_{\rm ZAMS}$ and the the degree of envelope stripping independently, which is a topic to be tackled in this thesis.

Section 3. *Ejecta dynamics*

Knowing how different stellar systems result in different SN explosions is not enough to reveal the explosion mechanism of CCSN. Indeed, within the same SESN subtype (therefore the SNe probably share the same

progenitor system), the explosion is triggered by a wide range of energy with different spatial distributions, leading to diversity in the expansion dynamics of the ejecta.

During the core-collapse process, a large amount of gravitational energy is released (~10^{53} erg), most of which are carried away by neutrino, but still about 10^{51}~10^{52} erg of the released energy is transformed to the kinetic energy of the expanding ejecta through the complicated interaction between the outward moving shock wave and the infalling stellar material. Therefore the dynamics of the ejecta, including its expansion velocity and geometry, can provide important constraint on the explosion mechanism. In particular, from theoretical aspect, asphericity is a crucial ingredient for the successful explosion. Modern numerical simulations show that the outward moving shock is not strong enough to disrupt the star. When the shock travels through the infalling stellar material, its energy dissipates and the propagation stalls. Indeed spherical simulations seldom disrupt the star. Including other aspherical components (for example, multi-dimension turbulence) is the key toward the successful explosion.

A single massive star with spherical structure is expected to explode spherically. However, asphericity can be introduced into the explosion by several factors: (a) random asymmetry develop by the convection or Rayleigh-Taylor instabilities; (b) the non-spherical configuration of the progenitor. For example, when rotation is included, the stellar structure will be distorted; (c) intrinsic spherical breaking of the explosion mechanism. For example, the explosion triggered by the bipolar jet.

Indeed the aspherical explosions are found to be common for CCNSe from observations (a) the non-zero polarization measurements of CCSNe (Wang et al. 2001); (b) the peculiar line profiles emerged in the spectra of SESNe (for example, Mazzali et al. 2005; Modjaz et al. 2008; Maeda et al. 2008; Taubenberger et al. 2009); (c) the connection between SNe Ic-BL and GRB, which requires the presence of the collimated relativistic beam therefore is expected to be highly axisymmetric.

Although evidences of the aspherical explosion have accumulated, the basic problem, i.e., whether the asphericial structure is dependent on the mass of the progenitor, remains unanswered. It is not clear whether the asphericity is a common feature for CCSNe despite their masses, or whether asphericity only favors, for example, high mass stars. The investigation on this topic is crucial to reveal the physics that governs the development of asphericity, which will further be an important constraint on the explosion mechanism.

The topics of interest in this thesis, and their relations, can be summarized into a schematic flowchart, as illustrated in Figure 1.2.

Section 4. *Nebular spectrum of SESN*

In the early phase, the density of the ejecta is so large such that photons generated inside the photosphere (optical depth τ~2/3) cannot escape from the ejecta and be observed by the telescopes. The analysis based on the observation at early phase is therefore restricted to the outermost region of the ejecta. The interpretation regarding the global properties of the ejecta thus relies on extrapolation of the ejecta properties inward.

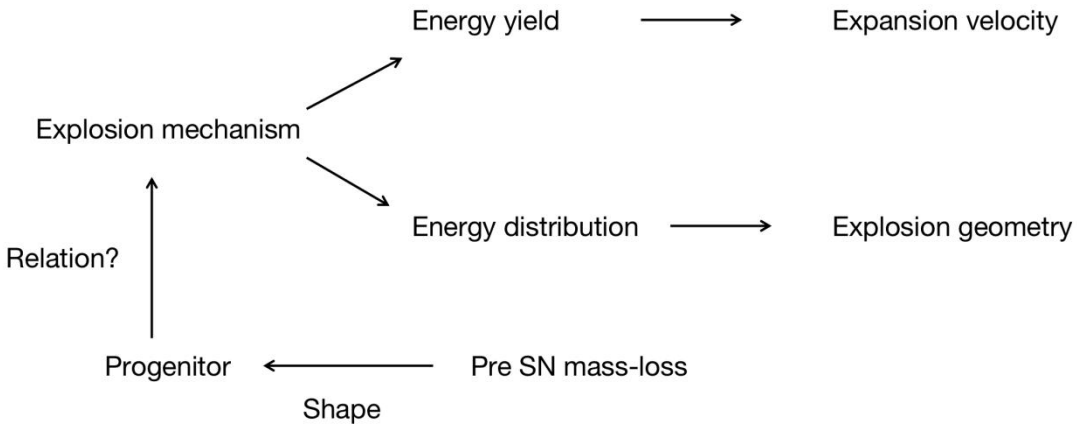

Figure 1.2. **The illustration of the topics of interest in this thesis.**

Following the expansion, the density of the ejecta decreases; further, the free elections are removed by recombination. These two factors effectively reduce the optical depth of the ejecta. Several months after the explosion, the ejecta of the SESN becomes transparent, i.e., the photon generated in any place of the ejecta can escape freely. The structure of the whole ejecta is therefore exposed. The SN enters *nebular* phase, and the spectra are dominated by emission lines from the elements buried deeply in the interior.

During nebular phase, we are looking at the core region where the explosion takes place, the analysis of the nebular observables are therefore very useful to the investigation on the explosion mechanism. The nebular light curve (*"tail"*) can track the amounts and the distributions of the radioactive isotopes. The absolute or relative strengths of the emission lines also contain rich information of the emitting elements. We may pay special attention to the [O I] $\lambda\lambda$6300,6363, which is one of the strongest lines emerged in SESNe nebular spectra. The strength of [O I] is closely related to the amount of the oxygen, which is mainly determined by the ZAMS mass of the progenitor. As a result, the strength of the [O I] line is frequently employed to infer the CO core mass of the progenitor. The [Ca II] $\lambda\lambda$7291,7321 is another line of interest. It is emitted by the newly synthesized calcium in the explosive oxygen burning ash, therefore can be utilized to trace the properties of the explosion-made region (Dessart et al. 2021; Prentice et al. 2022).

The widths and profiles of the emission lines are unique tools to constrain the geometry of the ejecta. During nebular phase, the ejecta expands homologously ($V(r, t) = r/t$, where $V(r, t)$ is the velocity of the point located at radial coordinate r at time t). The velocity of the thermal motion (a few km s^{-1}) is much smaller than the expansion velocity of the ejecta (a few thousands km s^{-1}), the lines are therefore mainly broadened by the Doppler effect, and the widths are determined by the typical velocity scales of the emitting elements. For a photon emitted from r, the Doppler shift of its wavelength is $\Delta\lambda = -\lambda_0(V_r/c)$, where λ_0 is the intrinsic wavelength and V_r is the line-of-sight velocity toward the observer. For the homologously expanding ejecta, $\Delta\lambda \propto d$, where d is the projection of r onto the direction of the line of sight. Therefore the photons emitted from the same plane, which is perpendicular to the line of sight, have the same observed wavelength. As such, the line profile serves as the "scan" of the integrated emissivities on these planes. This process is very similar to the computerized tomography (CT) scan used in the hospitals. Inversely, the observed line profiles can be employed to infer the ejecta geometries.

In summary, the problems regarding the progenitor system and the explosion mechanism, which are shown in Figure 1.2, can be well constraint by the investigation based on late phase observations (Figure 1.3), which is the goal of this thesis.

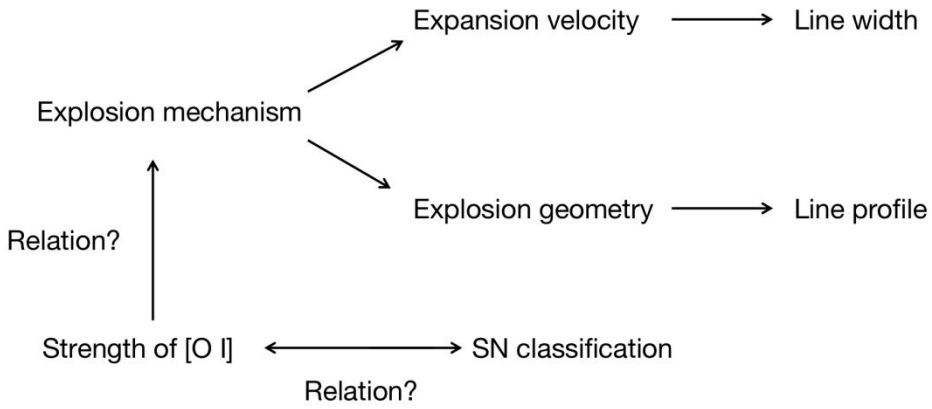

Figure 1.3. **The illustration of how the analysis on nebular spectra solves the topics listed in Figure 1.2.**

Section 5. *Organization of the thesis*

The first chapter is devoted to the introduction to core-collpase supernova including the classification scheme of CCSNe and the general problems of concern in the field, i.e., the mass-loss mechanism that leads to the observed diversity of CCSNe and the ejecta dynamics which is crucial to reveal the explosion mechanism. We also describe the physical properties behind the late phase spectrum, the weapon we use in this thesis to attack the above problems.

The following two chapters investigate the pre-SN mass-loss mechanism. In **Chapter 2**, we reveal the Hα-like structure seen in the late-phase nebular spectra of SNe IIb is [N II] $\lambda\lambda$ 6548,6583 powered by the radioactive elements. Because this line is emitted from the outermost region of the He-rich layer, therefore it is very sensitive to the stripping of this layer. In Chapter 3, with the relative strengths of [N II] $\lambda\lambda$ 6548,6583 and [O I] $\lambda\lambda$6300,6363 being measurements of helium-rich layer stripping and the progenitor mass, we find that the hybrid mechanism is responsible for the pre-SN mass-loss: H-rich layer stripped by binary interaction and He-rich layer further stripped by a mass-sensitive mechanism, with the line-driven wind being the strong candidate.

The following three chapters tackles with the observation and theoretic interpretation of the ejecta dynamics. In **Chapter 4**, based on the large sample consists of the nebular spectra of 103 SESNe, we find at least half of of the SESNe show detectable level of asphericity. Further, a correlation between the [O I] $\lambda\lambda$ 6548,6583 width and the intensity ratio of [O I] $\lambda\lambda$ 6548,6583 and [Ca II] $\lambda\lambda$ 7291,7323 is discerned, which is naturally expected if massive progenitor produces more energetic explosion. The scaling relation between the progenitor carbon-oxygen (CO) core mass and the kinetic energy is derived through the comparison of the observations and the simulation results in **Chapter 5**. In **Chapter 6**, the [Ca II] line, which is emitted from the explosion-made region, and the [O I] line, which is emitted from the unburnt material, are investigated. The

combined analysis of the profiles of these two lines based on the large sample of nebular SESNe spectra again confirms that about half of the SESNe cannot be explained by the spherical explosion. The peculiar double-peaked [Ca II] profiles of some SESNe, along with their broad nature, strongly suggests that the explosive burning ashes of these objects are bimodal, i.e., characterized by two detached iron-rich “bubbles”. This is the first direct look on the geometry of the explosion region. Further, the occurrence rate of the aspherical explosion is found to be independent on the oxygen content (i.e., a rough representation of the progenitor mass). A common mechanism irrelevant to the progenitor mass (for example, magnetic field or rotation) determines whether the explosion is spherical. However, the occurrence rate of the double-peaked [Ca II] smoothly increases with the oxygen content, which suggests once an SESN explodes in a non-spherical configuration (as controlled by the above factor), its asphericity strongly grows with the CO core mass of the progenitor.

Chapter 7 is left to conclusion.

Chapter 2. The Origin of the Hα-like Structure in the Nebular Spectra of Type IIb Supernova

Fang, Q., & Maeda, K. 2018, ApJ, 864, 47

We investigate the origin of the Hα-like structure seen in late-phase nebular spectra of type IIb supernovae (SNe IIb) at ~200 days after the explosion. We compare the luminosities of emission lines in the nebular spectra with the light curve peak magnitudes to reveal their power sources. In this work, we analyze 7 SNe IIb, as well as 2 SNe Ib (SN 2007Y and iPTF 13bvn) that show the Hα-like emission in their nebular spectra. The luminosity of the Hα-like emission shows a tight correlation with the light curve peak magnitude, sharing the same behavior with other nebular lines. This result indicates that the Hα-like emission is powered by the radiative decay of ^{56}Co. The line flux is then expected to roughly follow the mass of the emitting layer. The variation expected from the diversity of the H-rich envelope mass among SNe IIb (reaching nearly to an order of magnitude) is however not seen, suggesting that it is most likely contributed predominantly by [N II], not by Hα. While further analysis is limited by the available sample size, we find a hint that SNe IIb with a double-peak light curve, which is interpreted as an outcome of the more extended and massive hydrogen envelope, tend to show excess in the luminosity of the Hα-like feature than those with a single-peak light curve. This behavior indicates possible additional contribution from Hα. We also find a correlation between the [Ca II]/[O I] ratio and the post-maximum decline rate, indicating that the [Ca II]/[O I] can be used as a diagnostics for the progenitor mass.

Section 1. Introduction

A star with zero-age main-sequence mass larger than $8M_{\odot}$ ends its life with a supernova (SN) explosion triggered by a collapse of its iron or oxygen-neon-magnesium core. Core collapse supernovae (CCSNe) are classified into type II SNe (SNe II, with a hydrogen envelope) and type I (SNe I, without a hydrogen envelope). Type I CCSNe are further divided into SNe Ib and Ic according to whether its helium envelope is retained. Observationally, Balmer lines shape optical spectra of SNe II, while they are (generally) not detected for SNe Ib and Ic.

SNe IIb show spectroscopic properties intermediate between SNe II and Ib. Optical spectra of SNe IIb show strong hydrogen lines around the maximum light. As an SN IIb evolves, the hydrogen lines gradually fade away, eventually resembling to an SN Ib. The small amount of hydrogen retained at the time of the explosion is believed to be responsible for such a transition (Filippenko et al. 1993; Nomoto et al. 1995). The first identification of SN IIb was suggested for SN 1987K (Filippenko et al. 1988). The number of SNe IIb so far discovered is increasing, among which SN 1993J is the best-observed one. However, SN IIb is a relatively rare event, with the volumetric rate of about 12% among SNe II (Li et al. 2011; Smith et al. 2011).

In early phase, the emission from SNe IIb, including the hydrogen lines in their spectra, is powered by the radioactive decay chain ^{56}Ni → ^{56}Co → ^{56}Fe. In nebular phase, they generally show an emission feature centered at ~6500Å. This may be contributed by Hα, but the line identification and the power source have not

been robustly clarified. Indeed, for a fraction of SNe IIb, this feature further develops in later phases (e.g., after ~300 days) and it is considered as a signature of strong interaction with circumstellar material (CSM, see Patat et al. 1995, Mathesson et al. 2000a, Maeda et al. 2015). The behavior is not always seen, and thus questions remain as for what are the line identification and power source for the Hα-like feature in nebular phase but at < 300 days (Maurer et al. 2010a, Jerkstrand et al. 2015a, Maeda et al. 2015). This is related to the still-unresolved question of the mechanism of the envelope stripping toward SNe IIb, and toward SNe Ib and Ic in general (Gräfener & Vink 2016; Stancliffe & Eldridge 2009; Ouchi & Maeda 2017).

Nebular line identification provides us with an opportunity to explore the properties of the entire ejecta structure from the core through the envelope. Although metal lines are unambiguously a result of the radioactive decay chain (Houck & Fransson 1996; Kozma & Fransson 1998), the origin of the Hα-like feature detected generally for SNe IIb already before ~ 300 days has not been clarified. For some SNe IIb, the Hα-like emission is relatively narrow at < 300 days, which is different than a flat and wide line profile predicted by the CSM interaction scenario (Chevalier & Soderberg 2010) as exemplified by SN 2008ax (Taubenberger et al. 2011). Chevalier & Soderberg (2010) also argue that Hα powered by shock-CSM interaction should be undetectable in nebular phase for relative compact objects (e.g., SN 2007Y), but this Hα-like structure still presents in their spectra. Note that while the luminosities of Hα-like structure in relatively early nebular phase are similar for SNe 1993J and 2008ax (Section 4 in this chapter, and Taubenberger et al. 2011), the mass-loss history affecting the interaction power is derived to be very different (Maund et al. 2004; Folatelli et al. 2015), questioning the shock-CSM interaction mechanism as a dominant power source at < 300 days.

Another possibility is that this emission (before ~300 days) is powered by the radioactive decay chain. Patat et al. (1995) argue that the mass of hydrogen envelop of SN IIb is not massive enough to produce such luminous emission through radioactivity, however, Maurer et al. (2010a) suggest that if some amount of hydrogen is mixed into the helium layer, the radioactive decay chain could power the Hα emission with a broad and boxy profile, although some assumptions in their scenario remain to be discussed. Jerkstrand et al. 2015a include [N II] $\lambda\lambda$ 6548, 6583 in their synthetic spectral calculations, and find that the cooling within the He/N zone by [N II] can produce the Hα-like structure seen in SNe IIb in their sample.

Although various scenarios have been proposed, a model-independent (observational and phenomenological) approach, especially based on the statistic behavior of this emission, is missing. As noted before, the early light curve of SNe IIb is powered by the radioactive decay chain, and the peak magnitude is correlated with the mass of ^{56}Ni produced at the explosion (Lyman et al. 2016). However, the power provided by shock-CSM interaction has no direct link to the amount of radioactive decay isotopes, as it is mainly affected by the mass-loss history. Therefore, a combined analysis of early and late phase observations will provide clear diagnostic on the power source leading to this feature. In this work, we compare early and nebular observables to distinguish shock-CSM interaction and radioactive power scenarios. The luminosity scatter level of this feature is also analyzed, in order to further constrain the identity of the feature.

Based on the results of this paper through the model-independent approach, we suggest this emission feature should be powered by the radioactive decay chain. It is more likely [N II] rather than Hα.

This paper is organized as follows. In Section 2, we first introduce the sample of SN IIb used in this paper,

together with our methods of light curve and spectrum analyses. Relations between the observables and physical parameters are also briefly summarized in Section 2, which guides the interpretations in the following Sections. In Section 3, we compare the observables in early phase with those in nebular phase. The discussion part is given in Section 4, and the paper closes in Section 5.

Section 2. Sample description

In this work, we collect SNe IIb for which extensive photometric and spectroscopic data are available from the early to nebular phases (up to ~300 days after the light curve peak in the V-band). However, the SN IIb is a rare event, and the faintness in the nebular phase is an impediment toward observation. These two factors make the sample size of SNe IIb in this study relatively small. In addition to SNe IIb, two SNe Ib, SN 2007Y and iPTF 13bvn, which show the Hα-like feature in their nebular spectra, are also included in our sample for comparison. In summary, our sample includes 7 SNe IIb and 2 SNe Ib, and 58 nebular spectra. The analysis of this work is based on the spectra and photometric data compiled from the literature. Most of the spectral data were downloaded from the Weizmann Interactive Supernova data REPository (WISeREP[1], Yaron & Gal-Yam 2010). The sources of the photometric data, distances, and reddening adopted in this work are listed in Table 2.1. The spectral sequence is listed in Table 2.2. The date when the V-band maximum is reached is derived from low-degree polynomial fitting, and it is employed as the baseline of the photometric or spectral phases throughout this work.

Section 2.1. *Photometric data*

In this section, we describe our light curve analysis method. We also briefly summarize the relation between the observables and physical properties of the CCSNe.

Section 2.1.1. *Light curve in the early phase*

The photometric data of the SNe used in this work were compiled from the literature. After correcting for extinction and distance moduli listed in Table 2.1, Figure 2.1 shows the *V*-band light curves, which highlight the similarity and diversity among the sample. The scatter in the peak magnitude can reach ~1.5 mag, and the decline rates after the maximum brightness also vary. Differences in the peak magnitude and the shape of the light curves imply some diversities in the explosion parameters. The interpretation between the observables to the explosion parameters can be constructed in a simple manner (Valenti et al. 2008; Lyman et al. 2016). As shown in Figure 5 of Lyman et al. (2016), the peak bolometric magnitude is tightly correlated with the mass of ^{56}Ni ($M_{\rm Ni}$) ejected by the explosion. Morales-Garoffolo (2016) also found a correlation between the *R*-band peak magnitude and $M_{\rm Ni}$ for SNe IIb. In principle, we could (roughly) convert the bolometric peak magnitude to the ^{56}Ni mass using an analytical model (Arnett 1982). However, the absolute value of the ^{56}Ni mass is not important in this work. Therefore, we use the relative values of the *V*-band peak magnitudes as a representative observable to be connected to the variation of the mass of ^{56}Ni in the sample of SNe IIb (and SN Ib) to reduce uncertainty from analytical models. The mass of ^{56}Ni is then characterized by the *V*-band peak magnitudes as

[1] https://www.wiserep.org/

$$\log_{10} M_{\rm Ni} \sim -0.4 \times V_{\rm peak} + \text{constant}, \quad (2.1)$$

where $M_{\rm Ni}$ is the mass of ^{56}Ni and $V_{\rm peak}$ is the V-band peak magnitude. Since we are interested only in the relative values of $M_{\rm Ni}$, the constant in Equation (2.1) can be taken as a given arbitrary value.

The light curve parameters also contain information about the ejecta mass. For simplicity, we assume that the luminosity of an SN decreases as

$$L(\mathrm{t}) = L_{\rm peak} \times \exp(\frac{t}{t_0}), \quad (2.2)$$

and t_0 is the characteristic timescale for the luminosity decrease and $L(t)$ is the luminosity at time t, where t = 0 represents V-band peak. In magnitude scale, Equation (2.2) transforms to

$$M(\mathrm{t}) = M_{\rm peak} + 1.08 \times \frac{t}{t_0}, \quad (2.3)$$

where $M(t)$ is the magnitude at time t after peak is reached.

Analogous to SNe Ia, we characterize the light curve width by Δm_{15}, i.e., a change in the magnitude 15 days after the light curve peak. Again, we choose the V-band in our analysis. Therefore, we have

$$\Delta m_{15} = \frac{18.2}{t_0} \propto t_0^{-1}. \quad (2.4)$$

The width of the light curve contains information on the ejecta mass and the kinematic energy. Equation (1) of Valenti et al. (2008) gives

$$w_{\rm lc} \propto \frac{M_{\rm ejecta}^{3/4}}{E_{\rm K}^{1/4}}, \quad (2.5)$$

where $w_{\rm lc}$ is the width of light curve, $M_{\rm ejecta}$ is the ejecta mass, and $E_{\rm K}$ is the kinematic energy (see also Arnett 1982). Since the scatter in the expansion velocities of SN IIb is relatively small (8300 ± 750 km s^{-1} , see Lyman et al. 2016). we have

$$\log_{10} M_{\rm ejecta} \sim -2 \times \log_{10} \Delta m_{15}. \quad (2.6)$$

To derive the characteristic light curve parameters, we fit the light curve data by a low-degree polynomial function. For SNe IIb, the typical maximum date in the V-band is ~20 days after the explosion. As show in Figure 2.1, some SNe IIb show a light curve with two peaks. The power source of the first peak is the thermal energy deposited at the explosion (the so-called "cooling emission," see Arnett 1980), and that of the second peak is the radioactive decay chain of ^{56}Ni and ^{56}Co. To restrict our analysis to the radioactive-powered peak, only data points at 5 ~ 30 days after the explosion are fitted. An additional polynomial fit after the (second) peak is also applied to estimate Δm_{15} whenever necessary. The results are shown in Figure 2.2. A low-degree polynomial fit provides reasonable fitting for most objects, although for some objects (SNe 2007Y and 2008ax), the fitting results slightly deviate from the observations at the very early phase. This inconsistency can be remedied by raising the degree of the polynomial function. However, our analysis on the

early light curve is only restricted to the phase of the maximum and 15 days after. To avoid introducing additional uncertainty by enlarging the parameter space, we restrict our fitting by using a polynomial function with 3 ~ 5 degrees and the inconsistency at the very early phase is neglected. The peak magnitude and that at 15 days after the maximum are labeled by the open circles in Figure 2.2.

For simplicity, we neglect uncertainty in the peak magnitude, since the photometric error around the peak is small. The errors in distance and extinction are not included in Figures 2.1 and 2.2, while they are added in the subsequent analyses (note however that it would not introduce a random scatter in most of the analyses in this paper, as these errors enter into the early-phase and late-phase fluxes in the same manner). Uncertainty in Δm_{15} is negligible in most of the sample as it does not depend on the estimate of the distance and extinction. The main error budget in Δm_{15} comes from uncertainty in the peak date, but this is constrained as ±1 days. The largest uncertainty in Δm_{15} is found for SN 2003bg, which lacks well-sampled photometric data around the maximum, and the error in the peak date is as large as ±2 days (Hamuy et al. 2009). We calculate the magnitudes at 15 ± 1 (or ± 2 for SN 2003bg) days after the maximum brightness, and the deviation is defined to be the uncertainty of Δm_{15}. The light curve parameters and uncertainties adopted in this work are listed in Table 2.3.

Object	$E(B - V)$ (mag)	Distance module (mag)	Source
SN 1993J	0.19	27.81 ± 0.12	(1) (2)
SN 2003bg	0.02	31.68 ± 0.14	(3)
SN 2007Y	0.11	31.36 ± 0.14	(4)
SN 2008ax	0.40	29.92 ± 0.29	(5) (6)
SN 2011dh	0.07	29.46 ± 0.10	(7)
SN 2011fu	0.17	31.85 ± 0.15	(8)
SN 2011hs	0.10	34.36 ± 0.15	(9)
SN 2013df	0.10	31.65 ± 0.30	(10)
iPTF 13bvn	0.12	32.14 ± 0.20	(11) (12)

Table 2.1. **The host data and light curve sources of the SNe in this chapter.** References: (1) Matheson et al. (2000b); (2) Richmond et al. (1996a); (3) Hamuy et al. (2009); (4) Stritzinger et al. (2009); (5) Taubenberger et al. (2011); (6) Tsvetkov et al. (2009); (7) Ergon et al. (2014); (8) Bufano et al. (2014);(9) Morales-Garoffolo et al. (2014); (10) Morales-Garoffolo et al. (2015); (11) Fremling et al. (2016); and (12) Tully et al. (2013).

Section 2.1.2. *Light curve in the nebular phase*

For long-slit spectroscopy, absolute flflux calibration can be difficult, and spectra downloaded from WISeREP may previously be normalized only with spectroscopic standard stars. Therefore, we use photometric data to further calibrate the absolute flux of the nebular spectra in this study. We choose the *R*-band magnitude for the calibration, because it is generally better sampled than *V*-band magnitudes in the nebular phase, and the strong nebular lines of interest in this work fall within the wavelength range of this band pass. However, the R-band light curves of SN 2007Y and iPTF 13bvn are not available. We thus use *r*-band photometric data to calibrate the nebular spectra of these SNe. For spectra that do not cover the wavelength range of the R-band, we alternately use *V*-band photometric data to anchor their fluxes.

The emission in the nebular phase is mainly powered by the radioactive decay chain. The light curve therefore behaves quasi-linearly in the magnitude scale as a function of time (Maeda et al. 2003). Later on, the behavior may be complicated by increasing contribution from the positron deposition (Cappellaro et al. 1997) or shock–CSM interaction. Therefore, a linear or quadratic fit to the light curve is applied at > 60 days, in order to estimate the *R*-band magnitude for each spectrum. Following Bessell & Murphy (2012), we calculate the spectroscopic magnitude for a given spectrum by convolving it with the filter function. The deviation of the the spectroscopic magnitude from the observed photometry is then used to anchor the flux scale.

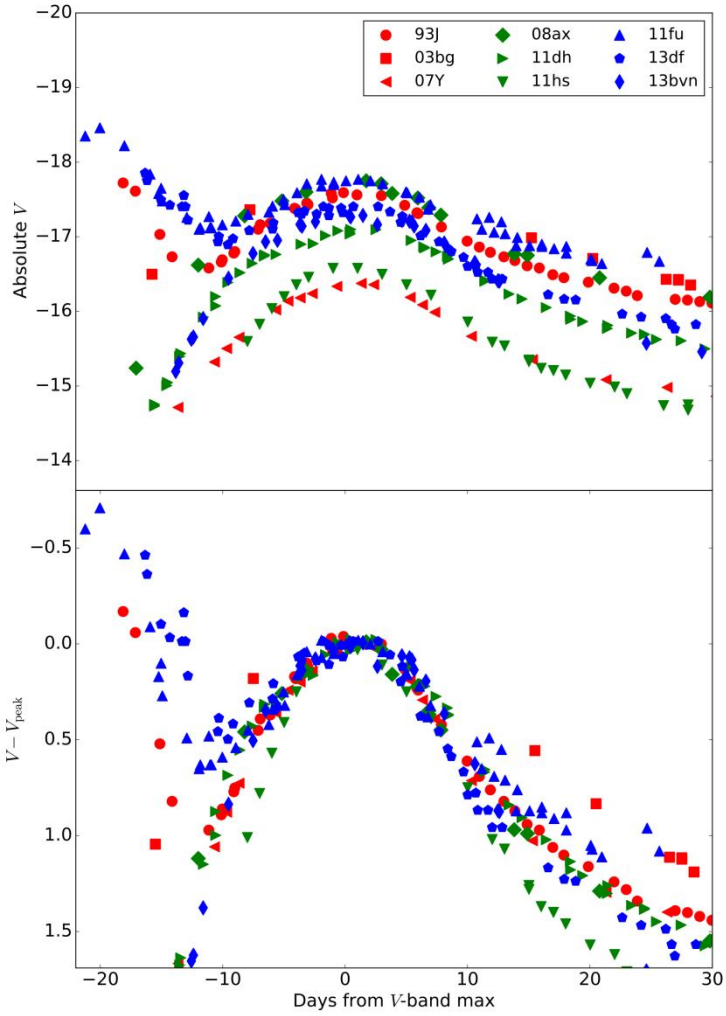

Figure 2. 1.**The *V*-band light curves of 7 SNe IIb and 2 SNe Ib studied in this work**. In the top panel, the absolute magnitude scale is adopted. In the bottom panel, the magnitudes are normalized by the peak magnitudes.

Object	Date (YY/MM/DD)	Phase (days)	Reference
SN 1993J	93/09/14	149	(1) (2) (3)
	93/09/15	150	
	93/09/20	155	
	93/10/19	184	
	93/11/07	203	
	93/11/15	211	
	93/11/19	215	
	93/12/08	234	
	93/12/17	243	
	94/01/05	262	
	94/01/21	278	
	94/02/17	305	
	94/03/09	325	
	94/0310	326	
	94/03/25	341	
	94/03/30	346	
	94/05/14	391	
	94/05/17	394	
	94/06/12	420	
SN 2003bg	03/08/20	153	(4)
	03/09/18	182	
	03/11/16	241	
	03/11/29	254	
	03/12/16	271	
	03/12/23	278	
SN 2007Y	07/09/22	200	(5)
	07/10/21	229	
	07/11/30	269	
SN 2008ax	08/07/24	122	(3) (6) (7)
	08/07/30	128	
	08/08/01	130	
	08/11/24	245	
	08/12/08	259	
	09/01/25	308	
	09/02/25	338	
	09//04/22	394	
SN 2011dh	11/12/18	182	(8) (9)
	11/12/19	183	
	11/12/24	188	
	11/01/25	220	
	11/02/23	249	
	11/03/18	273	

	11/03/24	340	
	11/07/19	396	
SN 2011fu	12/02/22	133	(10)
	12/07/20	281	
SN 2011hs	12/05/01	160	(11)
	12/06/21	211	
	12/06/23	213	
SN 2013df	13/11/08	135	(12) (13)
	13/12/05	162	
	13/12/21	178	
	14/02/04	223	
	14/05/06	314	
	15/02/21	602	
iPTF 13bvn	14/02/21	234	(14)
	14/05/28	329	
	14/06/26	359	

Table 2.2. **The spectrum sequence of this chapter.** References: (1) Barbon et al. 1995; (2) Jerkstrand et al. (2015a); (3) Modjaz et al. (2014); (4) Hamuy et al. (2009); (5) Stritzinger et al. (2009); (6) Milisavljevic et al. (2010); (7) Taubenberger et al. (2011); (8) Shivvers et al. (2013); (9) Ergon et al. (2015); (10) Morales-Garoffolo et al. (2014); (11) Bufano et al. (2014); (12) Morales-Garoffolo et al. (2015); (13) Maeda et al. (2015) and (14) Fremling et al. (2016).

Object	t_{peak} (JD-2400000)	V_{peak} (mag)	Δm_{15}
SN 1993J	49094.8	-17.55	0.97 ± 0.06
SN 2003bg	52718.3	-17.56	0.52 ± 0.11
SN 2007Y	54164.2	-16.36	1.01 ± 0.06
SN 2008ax	54549.6	-17.74	1.04 ± 0.07
SN 2011dh	55732.0	-17.07	0.92 ± 0.08
SN 2011fu	55846.4	-17.75	0.82 ± 0.05
SN 2011hs	55888.5	-16.61	1.25 ± 0.08
SN 2013df	56469.8	−17.40	1.06 ± 0.04
iPTF 13bvn	56475.1	-17.28	1.17 ± 0.08

Table 2.3. **Light Curve Parameters.**

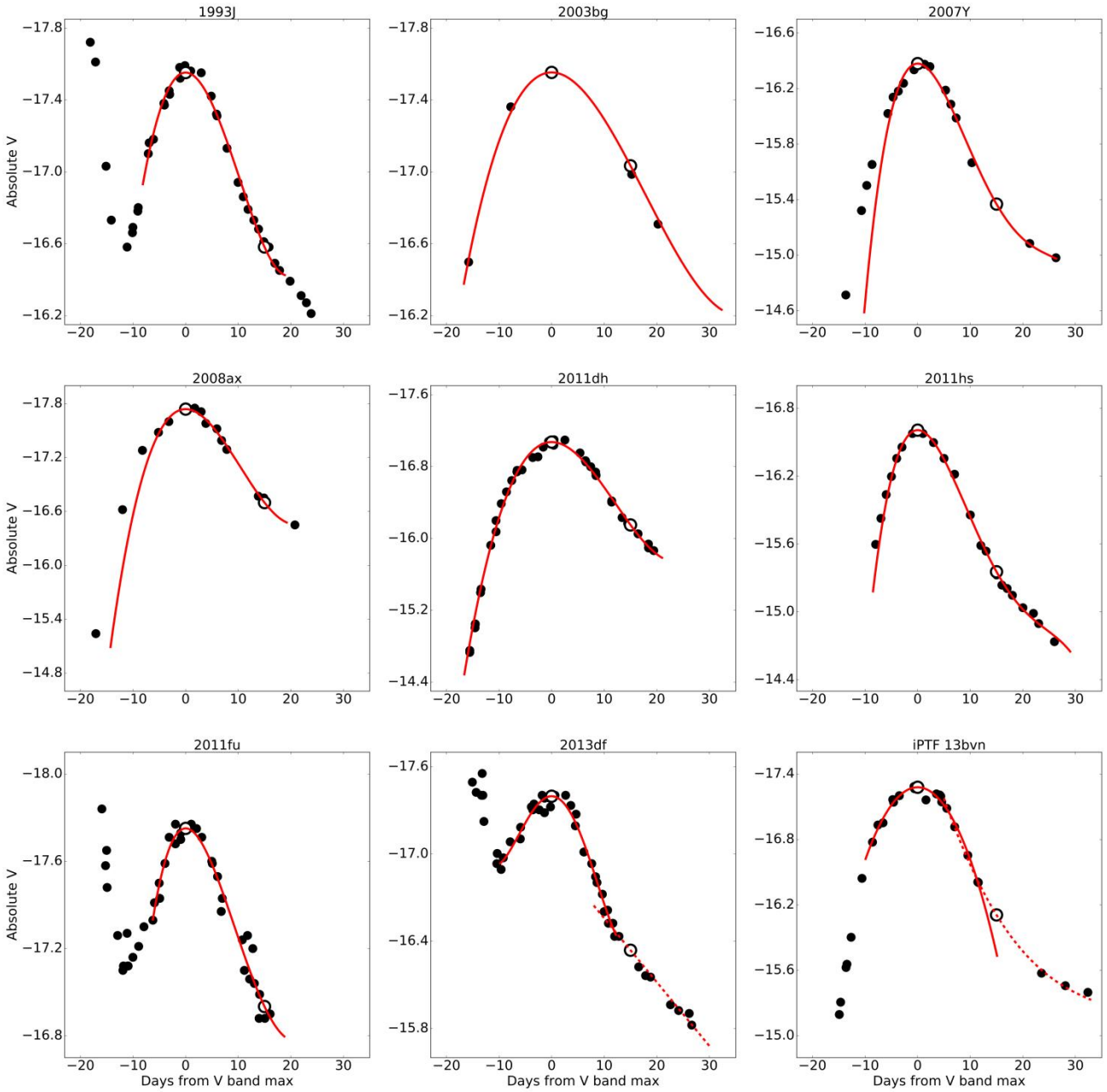

Figure 2.2. **The lighr curve fitting results.** The *V*-band light curves corrected for extinction and distance moduli (filled points). The red solid line in each panel is the fitting result by a low-degree polynomial function. The derived peak magnitude and the magnitude at 15 days after the maximum are marked by the open circles.

Section 2.2. Nebular spectrum

In the early phase, only the outermost layer of SN ejecta is observed. As it evolves, the ejecta becomes more transparent, and a deeper region is exposed. Several months after explosion, an SN enters into the nebular phase, where its spectrum is dominated by forbidden lines superposed on a faint continuum. The luminosities and structures of the nebular emission lines are useful tracers of the properties of the ejecta (Maeda et al. 2008; Modjaz et al. 2008; Taubenberger et al. 2009).

In this work, we compare the early and nebular phase observables to reveal the power source(s) of the Hα-like

structure, which appears in nebular spectra of SN IIb and some SNe Ib. The well-studied nebular lines, including [O I] doublet, [Ca II] doublet, and Na I D are also studied for comparison. To this end, nebular spectra are pre-processed as follows. First, the absolute fluxes are calibrated to match to the photometric data. After that, the spectra are de-reddened with the Cardelli extinction law (Cardelli et al. 1989), assuming R_V = 3.1. For simplicity, the total extinction is applied to the observed wavelength. This is not exact for the host extinction, but the effect is negligible for our low-redshift samples. Finally, the redshifts are corrected.

Figure 2.3 shows the overall spectra of our sample at ~200 days after the light curve peak is reached. The color region illustrates the Hα-like feature.

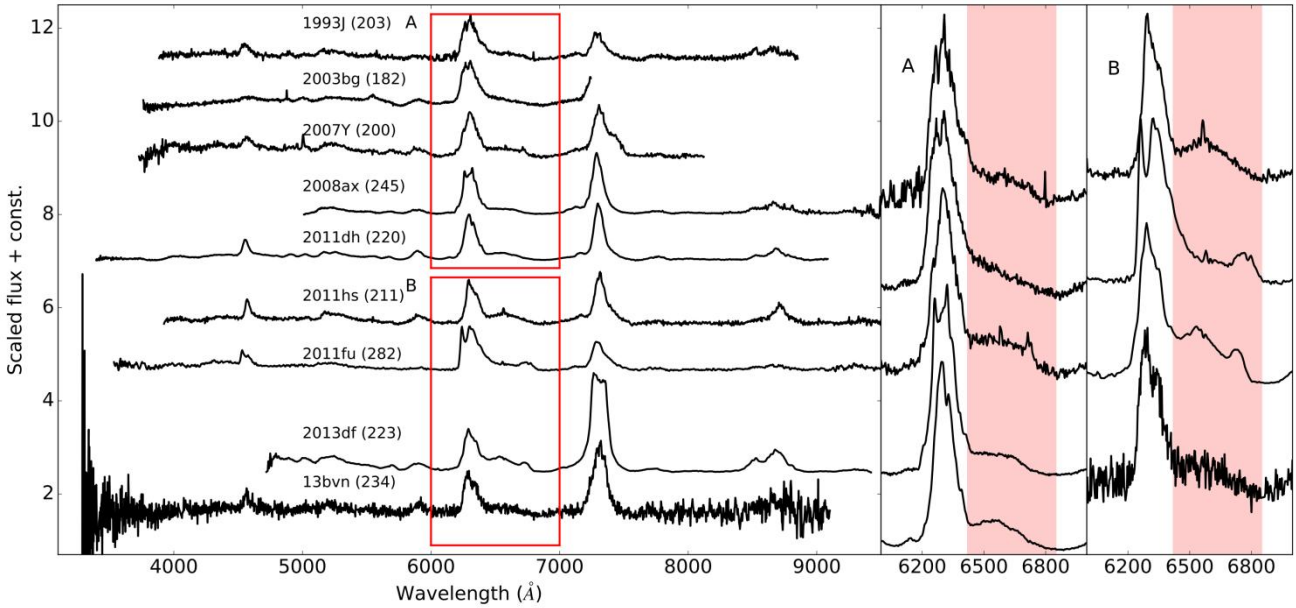

Figure 2.3. **The spectra of SNe IIb/Ib at ~200 days after the peak magnitude is reached**. All spectra are shifted to the rest wavelength and phases relative to the *V*-band maximum are listed in parenthesis. In the right panels, the wavelength region for the emission complex, including the [O I] and Hα-like feature, is shown.

Section 2.2.1. *[O I] λλ 6300,6363 and the Hα-like structure*

The [O I] doublet and the Hα-like structure together form an emission complex. To separate these two components, the first step is to remove local continuum from the spectrum. For an emission-free wavelength regime, determining the local continuum is straightforward. We first (slightly) smooth a spectrum by convolving it with a Gaussian kernel, then we find the local minima within a wavelength range of a few 100 Å on both sides of this emission complex. A straight line connecting these two minima is defined to be the local continuum.

The Hα-like structure is de-blended from [O I] λλ 6300, 6363 after local continuum is removed. The line profifile of the [O I] is assumed to be double-Gaussian. The centers of these two Gaussian functions are fixed at 6300, 6363 Å, and they are assumed to have the same velocity structure (therefore, the same σ in the Gaussian profifile). To avoid contamination from the Hα-like structure, only the blue part of the doublet is fitted. We tested two options for the ratio of the doublet peaks, either leaving it as a free parameter or fixing it

to be 3:1 as expected in the optically thin limit. We find virtually no difference in the fitted flux of the [O I], and further in the subtraction of this feature from the spectra. Therefore, in the subsequent analysis, the line ratio is fixed to be 3:1, which is generally applicable to SNe IIb/Ib/Ic with a few exceptions (Elmhamdi 2011; Jerkstrand et al. 2015a). After removing the local continuum and the fitted [O I] profile, the residual flux represents the Hα-like emission. It is then fitted with a flat-topped profile. An example of this fitting procedure is presented in the top panel of Figure 2.4.

However, the power source of this emission line is a topic to investigate in this paper. Assuming it to be flat-topped, which is the characteristic expected from the shock–CSM interaction scenario, indeed conflicts with the purpose of this work. The flux of this emission line can also be calculated by integrating over the spectrum after the local continuum and the fitted oxygen doublets are subtracted, where the upper and lower limits are the zero-flux points in the fitted flat-topped profile. Figure 2.5 illustrates and compares these two strategies for determining the flux of the Hα-like feature, showing that they give mutually consistent results. In what follows, we will thus adopt the integral flux. This method does not assume the center wavelength and the line profile, so it is indeed a better and more model-free approach to tackle to the origin and power source of this particular emission feature than assuming a flat-topped profile.

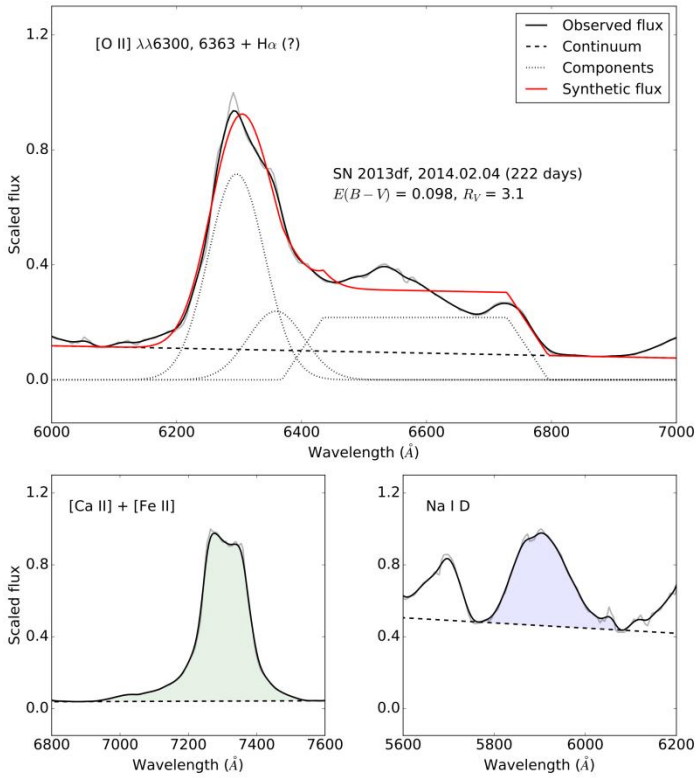

Figure 2.4. **An example of the line decomposition.** Top panel: the black-solid line is the observed spectrum, and the red-solid line is the composed spectrum from the fits to the different components. The local continuum and different components are presented by black-dotted and dashed lines, respectively. Bottom panels: illustrations of the continuum determinations and integral fluxes of Na I and [Ca II].

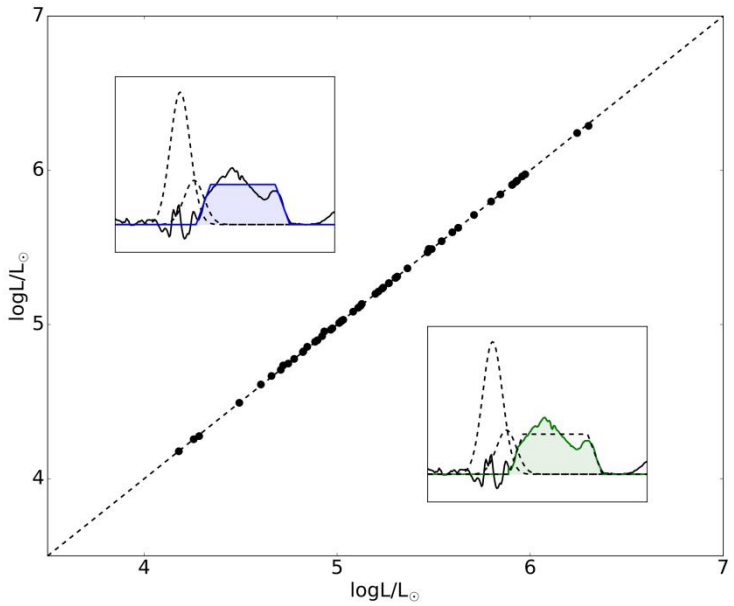

Figure 2.5. **A comparison between the results of the two fitting strategies to the Hα-like fluxes in the nebular spectra.** Illustrations of these two fitting strategies are presented, where the integration of the colored areas are adopted as the flux of the Hα-like feature.

Section 2.2.2. *[Ca II] λλ 7291,7323 and the Na I D*

[Ca II] λλ 7291, 7324 and [Fe II] λ 7155 are difficult to de-blend. This complex, together with Na I D, will be employed as tracers of the nebular lines powered by the radioactive decay.

The first step is to remove the local continuum. As is the same for [O I] and the Hα-like feature, the local continuum is assumed to be the line determined by the minima at both sides of the emission feature. After subtracting it, the flux is integrated, where the upper and lower limits are given by the two minima. Although a line decomposition method for the [Ca II]/[Fe II] complex has been discussed in Terreran et al. (2016), a detailed line profile of each emission is not a topic that will be investigated in this paper. In any case, [Ca II] dominates this feature, and further subtraction of the minor contribution from [Fe II] to the flux of this complex does not affect our conclusions and arguments (see, e.g., Figure 2.4 for the wavelength dependence). To avoid introducing uncertainty from line decomposition, we only discuss the sum of the [Ca II] and [Fe II] emissions. An illustration of the integration of the fluxes of the [Ca II]/[Fe II] complex and Na I D is presented in the bottom panels of Figure 2.4.

Uncertainties of the line luminosities mainly come from uncertainty in the photometric magnitude used for the flux calibration, except for the errors in the distance and extinction. In this work, a typical error of nebular photometric magnitude is estimated to be 0.1 mag, and it is quadratically added with uncertainty from the magnitude estimation (see Section 2.2), which includes the uncertainty in the distance and the extinction. Uncertainty in the magnitude is then converted to the luminosity scale. We also include uncertainty from the continuum determination, which is conservatively estimated to be 10% in this work. Note that the uncertainties in distance and extinction cancel out in comparing the flux scales in the early and late phases.

Section 2.3. Line luminosities evolution

Figure 2.6 shows the luminosity evolution, where the Hα-like structure and other nebular lines decline linearly (in logarithmic scale) at <300 days. The dashed lines give the best linear fits, using luminosities only at <300 days for most objects (except for iPTF 13bvn, which is fitted using all available spectroscopic data). In comparing the early and late-time fluxes, line luminosities are all placed at the same phase (200 days after the *V*-band maximum). The estimated luminosities are labeled by open markers.

To calculate the uncertainty of the estimated line luminosities, we perform 10^3 Monte Carlo simulations. In eachtrial, the line luminosities are perturbed by Gaussian error reported in Section 2.2. Then we perform a linear fit and estimate the luminosity at $t = 200$ days. The standard deviation from these simulations is taken as the uncertainty of the luminosities at 200 days. The luminosities and their uncertainties thus obtained are listed in Table 2.4.

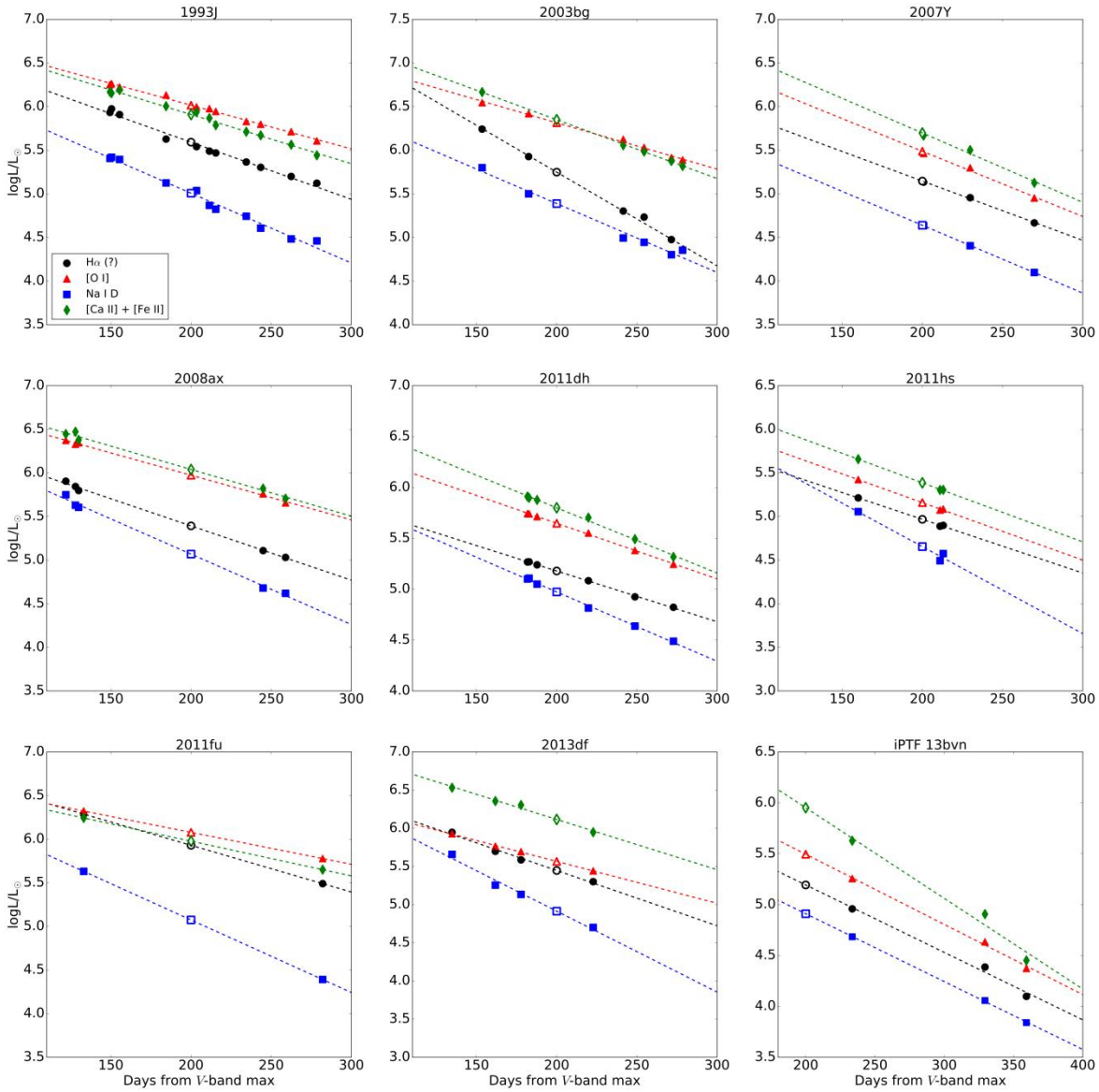

Figure 2.6. **Evolution of the luminosities of the different nebular lines**, which are labeled by different colors and markers. Dashed lines are the best-fitted lines. The open markers are the estimated luminosities at 200 days after the *V*-band maximum.

Line[2]	93J	03bg	07Y	08ax	11dh	11fu	11hs	13df	13bvn	Slope
Hα(?)	5.59	5.75	5.15	5.39	5.18	5.93	4.97	5.46	5.19	1.27
[O I]	6.02	6.31	5.49	5.97	5.65	6.08	5.16	5.58	5.49	1.47
[Ca II]	5.91	6.35	5.70	6.04	5.80	5.98	5.39	6.13	5.95	1.06
Na I D	5.01	5.39	4.64	5.07	4.97	5.07	4.65	4.92	4.91	0.95
Uncertainty[3]	0.06	0.10	0.07	0.07	0.06	0.12	0.07	0.08	0.09	...

Table 2.4. **Nebular luminosities in this work.** Line fluxes are calculated as Section 2.2 and distances are listed in Table 2.1. The reported error includes the error of the photometric data, uncertainty from background determination (which is estimated to be 10%, corresponds to ~0.04 dex in logarithm scale), uncertainty from line fitting procedure, and uncertainty from the estimation of the luminosity described in Section 3. The error in distance listed in Table 1 is quadratically added whenever necessary.

Section 3. Results

In Figure 2.7, the luminosities of the nebular lines (in logarithmic scale) are plotted against $-0.4 \times V_{\rm peak}$, which represents a relative value of $M_{\rm Ni}$ produced in the explosion. A clear correlation is seen for all the emission lines. The Pearson correlation coefficients are $r = 0.79$, 0.78, 0.76, and 0.82 for the Hα-like structure, [O I], [Ca II]/[Fe II] complex, and Na I D, respectively. For [Ca II]/[Fe II], Na I D, and [O I], this correlation is expected, given the robust identity of these lines as radioactive decay powered metal lines (Houck & Fransson 1996; Kozma & Fransson 1998; Jerkstrand et al. 2015a). However, the correlation between the 56Ni mass and the luminosity of the Hα-like structure is not readily foreseen. Indeed, in the shock-CSM interaction scenario, the flux of this feature is expected to be correlated with the mass-loss history before the explosion, leaving no direct link to the ^{56}Ni mass. The correlation between the nebular line luminosities and the peak magnitude thus implies that they share the same power source, i.e., the radioactive decay chain, with other metal lines. The slopes in the fits are listed in Table 2.4.

Section 3.1. The effect of gamma-ray deposition

Although the correlations in Figure 2.7 imply that the nebular lines are powered by the radioactive decay chain, the luminosity scatter is relatively large. We now investigate whether such a scatter would be mainly originated in a different amount of the gamma-ray energy deposition, i.e., the fraction of energy available to excite a given ion.

For the radioactive power model, $L \propto (1 - e^{-\tau}) \times M_{\rm Ni}$ is expected, where τ is the optical depth to the decay gamma-rays. In the nebular phase, $\tau << 1$, which gives $1 - e^{-\tau} \sim \tau$, therefore $L \propto \tau \times M_{\rm Ni}$ (Maeda et al. 2003). At a given phase (in this work, 200 days after V-band maximum is reached), we have

$$\tau \propto {M_{\rm ejecta}^2}/{E_{\rm K}} \sim M_{\rm ejecta}. \quad (2.7)$$

[2] Units:log$L/L_{\odot}$, where $L_{\odot} = 3.842\times10^{33}$ erg s^{-1}.

[3] Uncertainty from photometric adopted for flux calibration is dominated, therefore different emission lines have almost same uncertainty.

Here, we assume that the variation in M_{ejecta}/E_K is negligible given that the photospheric velocities from light curve and early spectra modeling are similar among SNe IIb (Lyman et al. 2016, and reference therein). We therefore have the following expression:

$$L \propto M_{\rm ejecta} \times M_{\rm Ni}. \quad (2.8)$$

Figure 2.7 does not contain information on the possible diversity of the ejecta mass, which would be partly related to the diversity in the light curve decline rates in the bottom panel of Figure 2.1 among different objects. To test the effect of ejecta mass, the line luminosities are plotted against $M_{ejecta} \times M_{Ni}$ in logarithmic scale in Figure 2.8. This value in the x-axis is estimated by the observables as follows:

$$\log_{10} M_{\rm ejecta} \times M_{\rm Ni} \propto -0.4 \times V_{\rm peak} - 2 \times \Delta m_{15}. \quad (2.9)$$

As shown in Figure 2.8, the additional (possible) correction for the ejecta mass does not break the correlations, and indeed the scatters seen in the nebular line luminosities decrease. In general, the nebular line luminosities are found to be consistent scatter, which possibly comes from a diversity in the masses of the emitting regions of various lines (but not correlated with M_{Ni}). Alternatively, the ejecta mass estimated by the early phase light curve may miss the internal structure affecting the gamma-ray deposition (Maeda et al. 2003).

In Figure 2.9, the luminosity scatter is compared among different emission lines. The Hα-like structure gives a level of scatter similar the other nebular lines. The envelope mass varies significantly among SNe IIb, from 0.5 to 1 $M_\odot$ for SN 1993J (Shigeyama et al. 1994) to ~0.1 $M_\odot$ for SN 2011dh (Bersten et al. 2012). If the emission would mainly come from the hydrogen envelope through the γ-ray deposition, we would expect that the line luminosity is roughly proportional to the mass of the emitting region for the following reasons: (1) The ejecta are optically thin to the γ-rays. Therefore, the deposition rate at a given layer is proportional to its optical depth (i.e., column density) to γ-rays, which is scaled as M_H^2/V_H, where M_H is the H-rich envelope mass and V_H is the characteristic velocity of the H-rich envelope (Kozma & Fransson 1992; Maeda et al. 2003; Maeda et al. 2007). The dispersion in V_H can be inferred from the Hα absorption velocity around the maximum light. The scatter in the Hα absorption velocity is at most within a factor of 1.5 for different SNe IIb (Liu et al. 2016), which is negligible as compared to the variation in M_H. The deposited luminosity is therefore roughly proportional to the mass of the hydrogen envelope in this case. (2) The ejecta is optically thin to optical photons. Therefore, the deposited energy is instantaneously converted to optical photons, and the luminosity from a given layer is proportional to its mass. (3) We expect Hα is produced through recombination following the non-thermal ionization. In this case, the line luminosity is insensitive to the thermal condition, and roughly scaled by the deposited luminosity, i.e., the mass of the H envelope. Given the above reasons, we expect that the luminosity scatter level would reach ~0.7–1 dex, much larger than the root mean square (rms) ~0.13 dex we find in our sample, or larger than the maximum level of the difference between the objects (~0.4 dex). Therefore, we conclude that this emission comes from the inner layer, rather than the hydrogen-rich envelope.

Prentice & Mazalli (2017) reached a similar conclusion by a different approach. They compare the velocities of emission and absorption features, and found that the velocity of this Hα- like structure is always lower than the Hα absorption velocity around the maximum but is consistent with the He velocity. They concluded that this Hα-like structure more likely comes from the He layer, which is consistent with our result.

According to the analyses in this section, we conclude that (1) the power source to the Hα-like structure is the radioactive decay input, and (2) this is emission from the inner layer (e.g., He layer), not from the H-rich layer. Robust identification of the nature of the emission (i.e., ion) from the current phenomenological approach is not easy, and thus we rely on insight obtained through theoretical investigation. In spectral synthesis simulations (Jerkstrand et al. 2015a), the only other candidate proposed for this feature so far is [N II]. Our finding is in line with this identification.

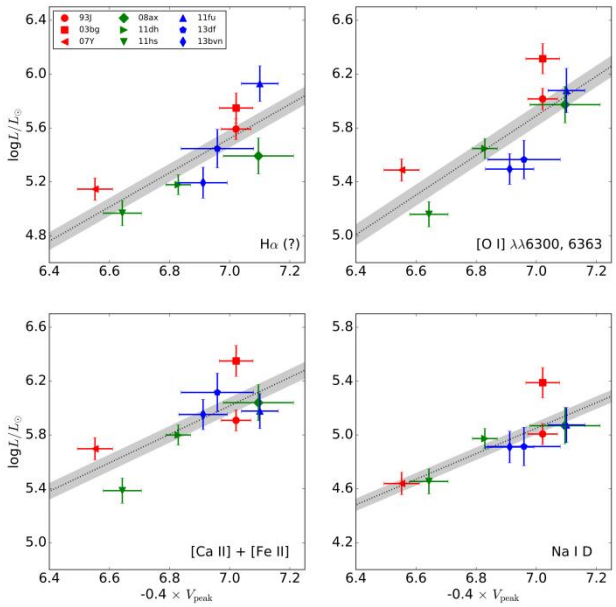

Figure 2.7. ***V*-band peak magnitudes (representing relative logM_{Ni}) vs. the luminosities of the nebular lines in logarithmic scale, at 200 days after the *V*-band maximum**. The error in distance is included. In each plot, the dashed line is the best-fit result and the shaded region is the standard deviation of the fitting. The slopes are listed in Table 2.4.

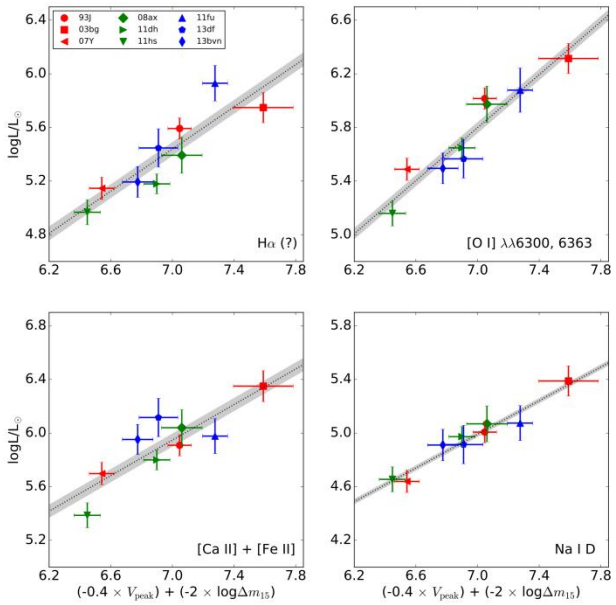

Figure 2.8. **Relative gamma-ray deposition luminosities (see Equation 2.9) vs. the luminosities of the nebular lines in logarithmic scale, at 200 days after the *V*-band maximum.** The error in distance is included. In each plot, the dashed line is the best-fit result and the shaded region is the standard deviation of the fitting.

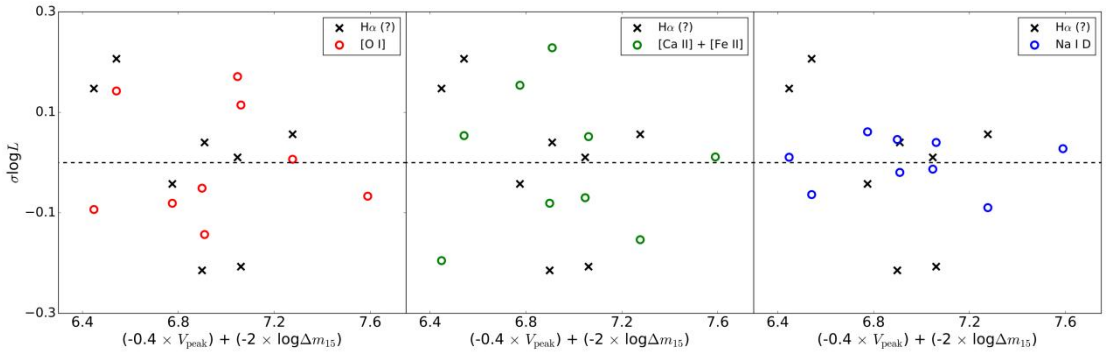

Figure 2.9. **Luminosity scatter level of Hα-like structure compared with other emission lines.** The Hα-like structure is labeled by black crosses, while other emission lines are labeled by open circles. The Hα-like structure has approximately the same luminosity scatter as the [O I] doublet and [Ca II] + [Fe I] complex, but is larger than that of Na I D.

Section 3.2. Further analysis on the physical properties: [Ca II] to [O I] ratio

Our previous discussion is model-free and mainly based on the observations. However, further insight can be obtained by connecting the observables and the physical parameters. For the ^{56}Ni mass, its relation to the peak magnitude has been intensively studied and well established (e.g., Lyman et al. 2016). The ejecta mass (with a combination of the kinetic energy) can be connected to Δm_{15}, following the frequently adopted argument of the diffusion timescale and the shape of the light curve around the maximum phase. However, this relation has not been intensively tested from observational quantities, which are independent of the early-phase light curve.

It has been proposed that the ratio of [O I] to [Ca II] (similarly [O I] per energy deposition) can be a tracer of the progenitor mass (Fransson & Chevalier 1989; Maeda et al. 2007; Elmhamdi 2011; Jerkstrand et al. 2015a; Kuncarayakti et al. 2015). Figure 2.10 compares Δm_{15} and the line ratio (L_O/L_{Ca}). The black-dashed line is the linear fit to all these points. A weak correlation (Pearson coeffificient r = 0.47) can be discerned, and SN 2003bg seems to be an outlier. If we omit SN 2003bg in our fitting, the correlation will become more significant (r = 0.68, as shown by the black-dotted line). Objects with a small value of −2 × logΔm15 (i.e., faster decliners) tend to have a smaller value of L_O/L_{Ca}.

The behavior is in line with the idea that a more massive progenitor (with a larger oxygen core) tends to have more massive ejecta. Indeed, we emphasize that this diagnostic of the [O I]/[Ca II] ratio (or [O I] alone) for the progenitor mass has not been tested for a sample of striped envelope SNe, and Figure 2.10 is the first attempt to clarify that the relation exists in the observational data. The scatter is however still present, which might indicate that the ejecta mass is not a single function determining the efficiency of the gamma-ray deposition in the late phases (Maeda et al. 2003). Still, the present analysis suggests that the ejecta mass is a main parameter to determine the gamma-ray deposition rate, and we can assume that a more massive progenitor produces more massive ejecta. Therefore, we conclude that Δm_{15} can be a tracer of the ejecta mass to some extent.

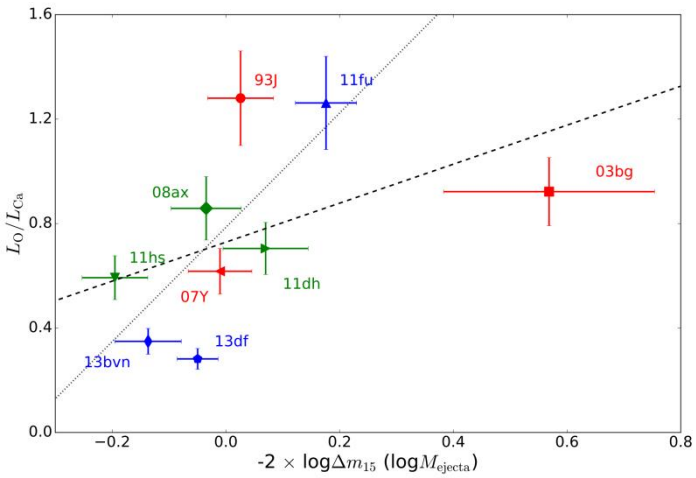

Figure 2.10. **The ejecta mass, estimated from V- band light curve,versus the line ratio of [O I] to [Ca II].** The dashed line is the best fit for all the objects, while the dotted line is the fit where SN2003bg is excluded. Different objects are labeled by the last two digits of the explosion year and letters.

Section 4. Discussion

Chevalier & Soderberg (2010) categorize SNe IIb into two groups[4]: extended SNe IIb (eIIb) and compact SNe IIb (cIIb). SNe eIIb are expected to have a more massive and extended hydrogen envelope than SNe cIIb and their light curves have two peaks at the early phase. Ben-Ami et al. (2015) have also revealed the different properties of these two groups. By comparing ultraviolet spectra of SNe IIb in the early phase, they found that objects with a double-peak light curve (SN 1993J and SN 2013df) have strong UV excess, while for objects with a single-peak light curve (SN 2001ig and SN 2011dh) such excess is absent (or relatively weak). They attribute this feature to different amounts of CSM around the progenitors, and thus different intensities of the shock-CSM interaction. Maeda et al. (2015) also found a possible correlation between the extent of the hydrogen envelope of the progenitors and the amount of CSM for SNe IIb.

These works highlight the difference among the two SN IIb groups. In this section, we will discuss whether these differences (the amount of the hydrogen envelope and different intensities of shock-CSM interaction) contribute to the emergence of the Hα-like structure.

Section 4.1. *Flattening of the Hα-like structure in very late phase*

In previous sections, we conclude that at ~200 days, the Hα-like structure is powered by the radioactive decay of ^{56}Co, and [N II] is a promising candidate (Jerkstrand et al. 2015a). However, some previous works suggest that this emission line becomes increasingly strong at later epochs for some objects, highlighted by the extended SNe IIb (SNe eIIb) 1993J and 2013df. At later epochs (>300 days), this feature is unambiguously dominated by the shock-CSM interaction (Matheson et al. 2000a; Weiler et al. 2007; Maeda et al. 2015). In

[4] Note however that this terminology has been revised by several authors. For example, Maeda et al. (2015) prefer the “more extended” and “less extended” progenitors.

this work, the evolution of line luminosity into the very late phase (400 days after the *V*-band maximum is reached) is also investigated, but only four objects (SN 1993J, SN 2008ax, SN 2011dh, and SN 2013df) have both photometric data and nebular spectra from the early (<200 days) to late (>400 days) phases. The result is shown in Figure 2.11. Note that the logarithm luminosities are shifted by a constant in this figure for illustration purpose, since only the trend in the evolution is important for the discussion in this section.

For all the objects, the luminosities of the emission lines of interest in this work linearly decline in logarithmic scale before ~300 days. However, for the two SNe eIIb, the decline of the luminosities of the Hα-like structure and Na I D is significantly flattened after ~300 days. In the case of SN 1993J, data points at <300 days and >330 days are fitted separately, and the change in the slope is evident for both emission lines. For SN 2013df, the luminosity of the Hα-like structure and Na I D at ~600 days is obtained by simply integrating the spectrum shown in the inner panel (which is subtracted from Maeda et al. 2015). Here we assume that [O I] is too faint to contribute to the Hα-like feature significantly at this epoch (Maeda et al. 2015). A similar flattening takes place at ~300 days for both SNe eIIb, while such a transition is absent in their relatively compact counterparts up to ~400 days.

Such a flattening is absent in the evolution of the [O I] and [Ca II] luminosity for all SNe IIb, irrespective of the nature of the progenitor. This conclusion may not be evident for SN 2013df, as the noise of the spectrum at ~600 days is too large for the luminosity of [Ca II] to be accurately calculated. However, the luminosity of [Ca II] at ~200 days is almost an order of magnitude larger than that of the Hα-like structure (Figure 2.6). Therefore, if such a flflattening would have occurred, [Ca II] should have remained sufficiently bright to be easily detected. To estimate the [Ca II] luminosity for SN 2013df at ~600 days, we smooth the spectrum by convolving it with a Gaussian kernel (red solid line in inner panel of Figure 2.11), and the luminosity of [Ca II] is calculated by integrating flfluxes at a few hundreds angstrom around 7300 Å. Given that the signal-to-noise ratio is too low to distinguish the (possible) emission feature from the background, the estimated [Ca II] luminosity should be regarded as an upper limit. The derived upper limit rejects the possibility of the flattening of the [Ca II] luminosity similar to those of the the Hα-like feature and Na I D.

Given that SNe eIIb tend to have a strong shock-CSM interaction, the behaviors in the luminosities of the Hα-like structure (and Na I D), compared to [O I] and [Ca II], indicate a change in the energy source from the radioactive power at ~200 days to the interaction power at ~400 days. The Hα-like structure at ~200 days, which is identified as [N II] in the prior sections, is possibly contaminated by Hα. Similarly, Na I D may already be contaminated by He I 5876 powered by the shock-CSM interaction. The shock–CSM interaction may thus provide an additional power to these lines, even if this is not a major power source.

To estimate the interaction power at ~200 days, we assume that the logarithmic luminosity from the radioactive power decays linearly, and the input from shock–CSM interaction is constant. The solid lines are the fitted results. By this extrapolation of the shock–CSM interaction power back to ~200 days, we estimate that the fractions of 15% (SN 1993J) and 12% (SN 2013df) in the Hα-like structure come from the shock-CSM interaction at ~200 days, and the fractions of 6% (SN 1993J) and 17% (SN 2013df) in the “Na I D” are contributed by the shock-powered He I 5876.

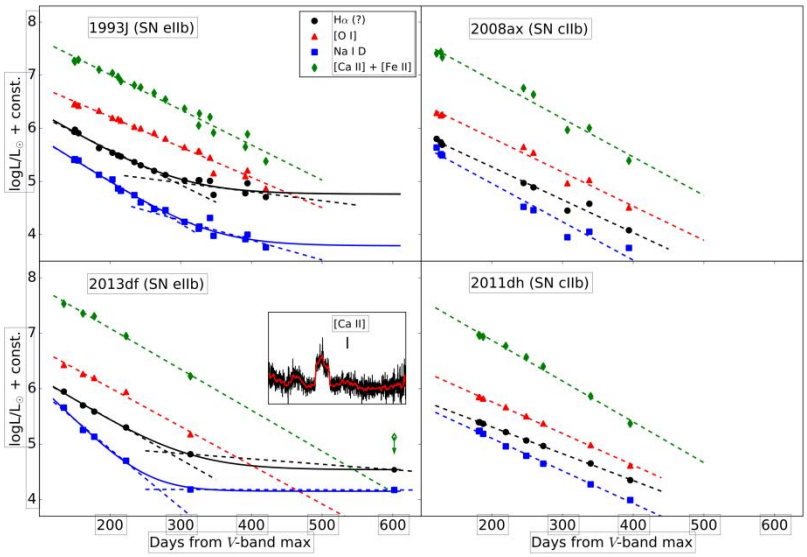

Figure 2.11 **The evolution of the luminosities of nebular lines into the very late phase.** Different emission lines are labeled by different colors and markers. The dashed lines are the best-fit results (see the text for more details). The inner panel shows the spectrum of SN 2013df at ~600 days, where the red solid line is its smoothed version. The Hα-like features and Na I D seen in the hydrogen-rich SNe 1993J and 2013df are flattened at 300 days after the V-band maximum, while [O I] and [Ca II] do not show such a transition. The solid lines are the best-fitted results when constant interaction luminosities are included. For the hydrogen-poor SNe 2008ax and 2011dh, the luminosities of all emission lines linearly decline.

Section 4.2. Possible contribution from other sources to the H*α-like structure*

We now investigate whether the Hα-like structure is additionally contributed by another mechanism (for example, Hα powered by the shock-CSM interaction or by the radioactive decay input).

The luminosity scatter of the nebular lines at different epochs are compared for this purpose. The line luminosities at five epochs are compared: 150, 200, 250, 300, and 350 days after the *V*-band maximum. Most of the line luminosities at a given epoch are estimated from a linear fit (Figure 2.6). The analysis at 150 days omits iPTF 13bvn, since the earliest nebular spectra in our sample for this SN was taken at 234 days and the estimation of luminosity at 150 days from a linear fit can be very uncertain. SN 2011hs is also excluded in the comparison at 300 days for the same reason. At 350 days, only five objects (SNe 1993J, 2008ax, 2011dh, 2013df, and iPTF 13bvn) are compared because of a lack of such late-phase spectra for the other objects. Here we note that at ~300 days, for SNe 1993J and 2013df, the evolution of the luminosity of Hα-like structure and Na I D is flattened (see Figure 2.11), and the linear fit to the line luminosity evolution will underestimate the luminosities. Therefore, for SNe 1993J and 2013df, luminosities of the Hα-like structure and Na I D are estimated from interpolation.

Figure 2.11 (left panels) compares the deposited gamma-ray luminosity equivalent to the line luminosities of the Hα-like structure and [O I] at different epochs. We note that for SN 2003bg, the luminosity of the Hα-like structure evolves unusually fast, and it seems to be an outlier (also see Figure 2.11). However, a detailed discussion on SN 2003bg is beyond the scope of this paper. The dashed lines in the left excluded, while the dotted lines are the results when SN 2003bg is included. The shaded regions show the 1σ deviation of the fitting. The evolution of the rms and the quadratic difference between the rms of the Hα-like and those of

other emission lines are also illustrated in the right panel of Figure 2.12 (for which SN 2003bg is excluded). The Pearson correlation coefficients r are listed in Table 2.5

There are three interesting features seen in Figure 2.11: (1) At epochs t < 300 days, the luminosities of all the emission lines are correlated with the deposited gamma-ray luminosity. At = 350 days, the luminosities of [O I] and [Ca II] still correlate with the deposited gamma-ray luminosity (r = 0.98 and 0.86, respectively), while for the Hα-like structure and Na I D, no clear correlation can be discerned anymore (r = 0.51 and −0.15, respectively). (2) At epochs t < 250 days, the Hα-like structure, [O I], and [Ca II] show a similar level of dispersion. At t = 350 days, the luminosity spread of the Hα-like structure is larger than the other emission lines, and the quadratic difference increases after 250 days. A similar behavior is seen in Na I D. (3) If SNe with similar deposited gamma-ray luminosities are compared (i.e., SN 1993J versus SN 2008ax; SN 2011dh versus SN 2013df), the extended SNe IIb (SNe 1993J and 2013df) show more luminous Hα-like structure than their compact counterparts.

These features can be interpreted by introducing additional contribution at 200 days from another source, which is linked to the properties of the hydrogen envelope. As the contribution from the shock-CSM interaction is evident after t ~ 350 days, this mechanism is a promising candidate. We estimate from the light curve evolution that the fraction of the contribution from the shock–CSM powered Hα is ~15% at 200 days (Section 4.1), which is smaller than the 60%–80% difference seen in the Hα-like structures between SNe eIIb and SNe cIIb (point 3 above). Another indication that opposes this interpretation is that there is no gradual increase of the Hα-like feature up to t = 300 days. These features are against the shock–CSM interaction as an additional source of power at ~200 days, while a caveat is that this argument is dependent on the time evolution of the shock–CSM interaction power, which is not yet well established. Alternatively, the feature may be contaminated by Hα but powered by the radioactive decays. In Section 3.1 we concluded that this is not a main contributor, but the variation in the H envelope mass, through different deposition efficiency, may still explain the difference in the flux of the Hα-like feature between SNe eIIb and cIIb. In any case, our sample is small, and the difference between SNe eIIb and cIIb in the Hα-like structure at ~200 days is not statistically signifificant but only indicative. A larger sample size of SN IIb with high-quality nebular data is required to reach to a firm conclusion.

Pearson r		Hα	[O I]	[Ca II]	Na I D
150 days	03bg included	0.92	0.93	0.81	0.95
	03bg excluded	0.87	0.88	0.65	0.91
200 days	03bg included	0.88	0.95	0.86	0.97
	03bg excluded	0.90	0.93	0.77	0.95
250 days	03bg included	0.78	0.93	0.92	0.94
	03bg excluded	0.92	0.95	0.90	0.89
300 days	03bg included	0.47	0.95	0.90	0.87
	03bg excluded	0.90	0.94	0.91	0.73
350 days	03bg excluded	0.51	0.98	0.86	-0.16

Table 2.5. **Pearson Correlation Coefficients of line luminosity-deposited energy at different phases.**

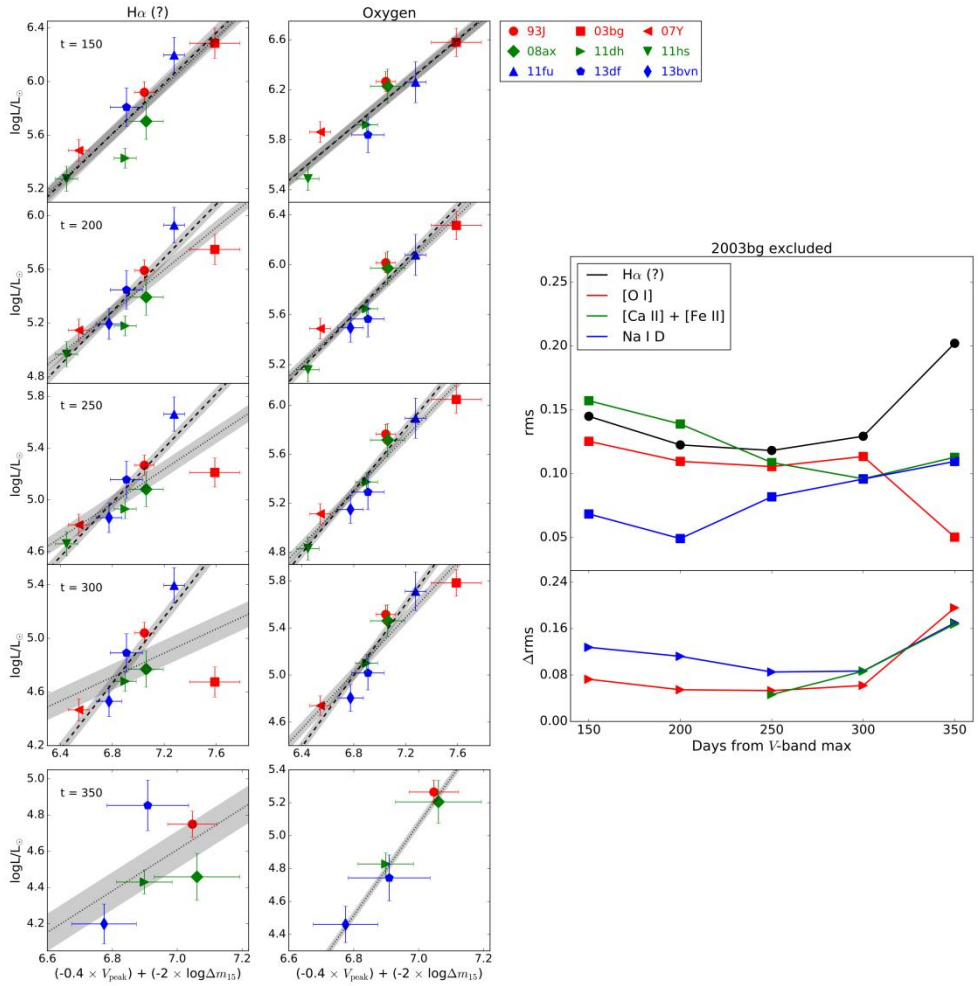

Figure 2.12. Left panels: **deposited energy vs. line luminosity at different epochs**. Only the Hα-like structure and [O I] doublet are illustrated. The dashed lines are fitting results when SN 2003bg is included, while the dotted lines are results when SN 2003bg is excluded. The shaded regions are 1σ deviations of the fitting. Right panel: **evolution of the rms of different emission lines and the quadratic differences of the rms of the Hα-like structure and other nebular lines.**

Section 5. Conclusion

In this work, we have analyzed the photometric data and nebular spectra compiled for 7 SNe IIb and 2 SNe Ib. We have investigated the power source of the nebular lines, including the origin of the late-time Hα-like structure seen in these objects. We have further investigated a possible origin of the diversity among these events from a statistical and model-independent approach.

In previous works, several scenarios have been proposed as the origin of the Hα-like structure seen in nebular spectra of SN IIb, at ~200 days after the maximum brightness. We find a correlation between the luminosity of this emission feature and the mass of ^{56}Ni produced in the explosion, which is not expected for the shock-CSM interaction scenario. This points to the radioactive decay of ^{56}Co as a predominant power source of this feature. Further, our analysis clarifies that the level of the scatter in the luminosities of this feature is similar to that of the other metal lines. This is not consistent with the idea that the feature is Hα powered by

the radioactive decay, as in this case the diversity in the mass of the hydrogen envelope among SNe IIb would create a larger scatter in the luminosities of this Hα-like feature than other lines. This is further supported by the mass of the hydrogen envelope itself generally inferred for SNe IIb, which is not enough to produce such a luminous emission line (Patat et al. 1995). We therefore conclude that this line is mainly emitted from the inner layer and powered by radioactive decay chain. Since [N II] in the He layer is the only candidate from simulations so far, we attribute the origin of this emission as [N II]. While we are not able to robustly exclude other possibilities from our phenomenological and observational approach, this identification provides a picture consistent with the observational constraints we have investigated in this paper.

Our conclusion on the origin of this Hα-like emission, as dominated by [N II] powered by the radioactive decay of ^{56}Co, is in line with the nebular spectral synthesis models by Jerkstrand et al. (2015a). In addition to our main analyses presented in this paper, we have further investigated if the variation expected for the masses of the N/He layer would be seen as a scatter in the sample of SNe IIb (plus 2 SNe Ib). We do not see such a variation, suggesting either that the progenitor mass range is relatively small for SNe IIb or that the expected variation is absorbed in the dependence on the progenitor mass, or both. Identifying the origin of this feature as [N II] thus is an interesting avenue for further investigation, i.e., a possible difference in the progenitor mass range for SNe IIb, Ib, and Ic, which is presented in Fang et al. 2019. The Hα-like structure is also presented in nebular spectra of some SNe Ib (e.g., SN 2007Y and iPTF 13bvn analyzed in this work, and SN 2007C, see Taubenberger et al. 2009). If it is [N II] powered by the radioactive decay, whether such an emission is present can be used as an indicator of the level of the He layer stripping.

We also find a possible systematic difference in the strengths of the Hα structure between the extended SNe IIb (SNe 1993J and 2013df) and the compact ones (SNe 2008ax and 2011dh), already at ~200 days before the clear shock–CSM signature is observed for the former (t > 300 days). The luminosity evolution in the very late stage is also compared among different objects. The logarithmic luminosities of the Hα-like structure and [Ca II] linearly decline before ~250 days. However, for SNe IIb with an extended envelope, i.e., SNe 1993J and 2013df, a transition takes place at ~300 days where the evolution of luminosity of the Hα-like structure is significantly flattened. In contrast, such a flflattening is absent for SNe IIb with a less extended envelope up to ~400 days. The luminosities of [O I] and [Ca II] continue to drop for all SNe IIb for which the analysis is possible. The flattening of the evolution of Hα-like structure luminosity is interpreted as a result of a transition of energy source from radioactivity to shock-CSM interaction. However, the expected level of the shock-CSM contribution is not consistent with the difference between SNe eIIb and cIIb at 200 days, if we assume luminosity from the shock–CSM interaction is constant. Alternatively, the difference may simply reflect the variation of the masses in the H envelope. In any case, this work extends the intrinsic difference among SN IIb, and concludes that the two types of SNe IIb behave differently in the nebular phase, which is a topic investigate in Fang et al. (2019).

As an additional analysis, we further investigate a relation between the line ratio of [O I]/[Ca II] and the post-maximum light curve decline rate. The correlation exists, and this finding suggests that the line ratio [O I]/[Ca II] can be an indicator of the progenitor mass and ejecta mass. A systematic study of this line ratio to a sample of SNe IIb/Ib/Ic is presented in Fang et al. (2019).

We note that our result is limited by the relatively small sample size. Our future work aims at enlarging the sample of both nebular spectra and photometric data of SNe IIb, and further extending to SNe Ib and Ic. The analyses we present in this paper can form a solid basis to apply to a larger sample of SNe IIb/Ib/Ic.

Q.F. acknowledges the support of a MEXT scholarship awarded by the Ministry of Education, Culture, Sports, Science and Technology, Japan. K.M. acknowledges the support of the Japan Society for the Promotion of Science (JSPS) KAKENHI Grant Nos. 17H02864 and 18H04585. We thank Zhuo Li, Jinyi Shangguan, and Herczeg Gregory for stimulating discussions and helpful comments. We thank Antonio Morales-Garoffolo for kindly providing us with the spectra of SN 2013df. We thank the anonymous referee for many constructive comments to improve the analysis. We thank the WISeREP for access to the supernova data.

Chapter 3. The Mass loss mechanism of stripped-envelope core-collapse supernova

Fang, Q., Maeda, K., Kuncarayakti, H., et al. 2019, NatAs, 3, 434

The final evolution of massive stars leading to supernova (SN) explosion, especially the mass loss mechanism, is an important open problem in astrophysics. Stripped-envelope SNe (SESNe) are explosions of massive stars with a large amount of the outer envelope stripped away before the explosion; type IIb, Ib, and Ic in order of increasing degree of envelope stripping (Nomoto et al. 1995; Filippenko 1997; Gal-yam 2017). In this work, a new analysis of late-time nebular spectra of SESNe is presented. The results show that the progenitors of SNe IIb and Ib are indistinguishable except for the residual amount of H-rich envelope. The progenitors of SNe Ic are distinctly different in the nature of the carbon-oxygen (C+O) core, which is interpreted to be more massive than SNe IIb and Ib. These findings strongly suggest that different mechanisms are responsible for the removal of the outer H-rich envelope and the deeper He-rich layer.

Section 1. *Main text*

When nuclear fuel in the core of a massive star with a zero-age main-sequence mass $M_{\rm ZAMS} > 8M_{\odot}$ is exhausted, the central part (the iron or oxygen-neon-magnesium core) collapses and forms a neutron star or a black hole (Heger et al. 2003). The material above the collapsing core is rapidly ejected, leading to an SN explosion. Without mass-loss in the pre-SN evolution, a massive star would form an onion-like layered structure, with a H-rich envelope, He-rich layer, and C+O core from the surface to the inner part (Heger et al. 2003). With substantial mass loss, a massive star explodes as an SN IIb or SN Ib depending on whether a small amount of its hydrogen envelope is left or it is completely removed before its explosion. Further stripping of nearly entire He-rich layer would result in an SN Ic. SNe IIb can be further divided into extended (eIIb) and compact (cIIb) classes, where the latter has a lower amount of residual hydrogen (Chevalier & Soderberg 2010; Ouchi & Maeda 2017; Yoon 2017). A special class of SNe Ic (SNe Ic-BL) show broad absorption lines in early spectra, indicating fast expansion velocities, and are sometimes accompanied by a gamma-ray burst (Iwamoto et al. 1998). In the massive stars leading to SESNe, the envelope is presumably stripped either via strong stellar winds (Heger et al. 2003; Groh et al. 2013; Smith 2014; Yoon 2015) or due to mass transfer to a companion star in a close binary orbit (Eldridge et al. 2013; Yoon 2015;Ouchi & Maeda 2017). It is not clear which process is dominant, and whether different mechanisms are at work for different classes of SESNe.

Observations of SESNe pose an apparent conundrum: based on analysis of SN emission during the brightest, opaque phase, it has been argued that SNe IIb/Ib/Ic have similar ejecta mass ($M_{\rm ej}$), which may indicate similar $M_{\rm ZAMS}$ for all SESN classes (Liu et al. 2016; Lyman et al. 2016; Taddia et al. 2018). On the other hand, the environment in which SNe explode, and in particular the preference of SNe Ic for the most actively star-forming regions (and thus likely larger $M_{\rm ZAMS}$) argues otherwise (Anderson et al. 2012; Kuncarayakti et al. 2018). While there is a recent indirect indication from early-phase SN emission analysis that SN Ic progenitors may have larger $M_{\rm ZAMS}$ than SNe Ib (Fremling et al. 2018), the analysis of early-phase SN

emission is complicated by various uncertainties. Additional progress can be made by identifying a set of observables that can directly trace M_{ZAMS} and the the degree of envelope stripping independently.
In this work, late-time nebular spectra of SESNe are collected and analyzed (see caption of Figure 3.1 and Methods). The average spectrum of each SN subtype is show in Figure 3.1. It is shown that SNe Ic and Ic-BL have much larger ratios of [O I] to [Ca II]. The average spectrum of SNe Ib lies in between those of SNe IIb and SNe Ic. SNe Ib are manifestly different from SNe Ic (and SNe Ic-BL), while the difference with respect to SNe IIb may be statistically insignificant. The [O I]/[Ca II] ratio has been theoretically proposed to be an indicator of the final C+O core mass (M_{CO}), which is higher for larger initial progenitor mass (M_{ZAMS}). The idea has been applied to a number of individual SNe (Jerkstrand et al. 2012; Kuncarayakti et al. 2015; Maeda et al. 2007a), but has not been tested observationally for a sample of SESNe.

Figure 3.2 shows how the [OI]/[Ca II] ratio (indicating M_{CO} and thus M_{ZAMS}) depends on the early phase SN observables (indicating M_{ejecra}). The horizontal axis traces M_{ejecta} via a measure of the diffusion time scale (see Methods); for a given SN type, M_{ejecta} is expected to be larger for higher M_{CO} and M_{ZAMS}. A relatively weak but clear correlation is discerned, which is statistically valid. While this investigation is limited by the relatively narrow SESN ejecta mass range, it supports the idea that the [O I]/[Ca II] ratio can be used as a measure of M_{ZAMS}. It should however be emphasized that M_{ejecta} is not a direct measure of M_{ZAMS} and a significant scatter is naturally expected (see Methods), which motivates the use of nebular spectra as a more direct diagnostic than early-phase data.

A second prominent difference is the structure around ~ 6600Å. An emission feature can be discerned for both SNe Ib and SNe IIb, but it is absent for SNe Ic/Ic-BL. This line has been argued to be dominated by [N II] for SNe Ib and cIIb theoretically (Jerkstrand et al. 2015a) and observationally (Fang & Maeda 2018), while SNe eIIb, which likely contain additional Hα contribution, show stronger emission and drive the total IIb spectrum up when included. Since [N II] is mostly emitted from the outermost region (He/N layer) of the He-rich envelope (Jerkstrand et al. 2015a), this line can be employed as a sensitive tracer of the CNO-cycle processed region and provides a measure of the He-rich layer stripping, as it can be strong only if the He-rich layer is almost entirely intact.

Figure 3.3 shows the distribution of individual SESNe in the [O I]/[Ca II] vs. [N II]/[O I] ratio diagram. The cumulative distribution in the [O I]/[Ca II] ratio shows statistically significant difference between SNe Ic/Ic-BL and SNe IIb/Ib, with only 0.2% chance probability that SNe Ib and SNe Ic originate from the same population using a Kolmogorov-Smirnov (KS) test. The hypothesis that SNe IIb and Ib originate from the same population cannot be rejected (86.3% from the KS test) and is consistent with no difference as visually indicated by the cumulative distribution. As the [O I]/[Ca II] ratio is expected to trace the nature of the C+O core, this finding provides a strong and direct evidence that the progenitors of SNe Ic/Ic-BL are intrinsically different from those of SNe IIb/Ib. Assuming the connection between this ratio and M_{ZAMS} (see Methods), the progenitors of SNe Ic should be more massive than SNe IIb/Ib. On the other hand, the progenitors of SNe eIIb/cIIb/Ib are mutually indistinguishable and can originate from essentially the same progenitors except for the amount of residual H-rich envelope. The same behavior is also evident in the [N II]/[O I] ratio, except for SNe eIIb which likely have a contribution from Hα. The ratio levels off for SNe Ic and Ic-BL, which may indicate that the He/N layer is completely stripped away for these progenitors. Note that this finding alone already has significant implication for SN Ic progenitors; it has been suggested that difference between SNe Ib and Ic may originate from different degree of mixing at the explosion rather than from a different amount

of the He-rich envelope (Dessart et al. 2012), but the finding in this work rejects such a possibility (Yoon et al. 2019). For SNe cIIb and Ib this line ratio is statistically not distinguishable, similarly to the case for the [O I]/[Ca II] ratio. SNe cIIb retain a small amount of hydrogen, and thus the mass stripping probably does not penetrate down to the He-rich layer. The similarity between SNe cIIb and Ib thus suggests that SNe Ib suffer from little or no He-rich envelope stripping. The continuous decrease of [N II]/[O I] toward larger [O I]/[Ca II] can then be interpreted as increased pre-SN He burning for larger $M_{\rm ZAMS}$ stars, which decreases the mass of the He/N layer, rather than due to He-rich layer stripping. Given that a large fraction of the He-rich layer must be stripped away for SNe Ic, and yet there is no distinguishable [N II]/[OI] ratio between SNe cIIb and Ib, the He-rich layer stripping apparently does not form a continuous sequence with the H-rich envelope stripping, suggesting there is an intrinsic difference in the stripping mechanism for the H-rich envelope and the He-rich layer.

The model-independent finding can be further strengthened by comparing the observed distribution in Figure 3.3 with model predictions for SNe IIb without He-rich layer stripping (Jerkstrand et al. 2015a). The model shows an increasing ratio of [O I]/[Ca II] for increasing $M_{\rm ZAMS}$ as expected. Taking the model at face value, it is interesting that the [O I]/[Ca II] ratio of SNe IIb/Ib reaches an upper limit of $M_{\rm ZAMS} \sim 17 M_{\odot}$. This distribution overlaps with the measured progenitor mass distribution of SNe II (Smartt 2009), which do not experience substantial H-rich envelope stripping. This may be further evidence that the H-rich envelope stripping process leading to SESNe may be independent from $M_{\rm ZAMS}$; if it would be determined mainly by $M_{\rm ZAMS}$, one should expect different $M_{\rm ZAMS}$ between SNe IIb/Ib and SNe II. SNe Ic arise from more massive progenitors according to the model, with $M_{\rm ZAMS} > 13 M_{\odot}$ and extending to $M_{\rm ZAMS} > 17 M_{\odot}$. Note however that the comparison between the SN IIb models and SNe Ic data should not be over-interpreted, especially on the quantitative mapping between the observed ratio and $M_{\rm ZAMS}$ (see Methods); it is possible that there would be clear dividing mass between SNe IIb/Ib and SNe Ic rather than having the overlap in $M_{\rm ZAMS} \sim 13-17 M_{\odot}$. The models also roughly reproduce the decreasing sequence in the [N II]/[O I] ratio by more significant He burning for larger $M_{\rm ZAMS}$.

The following picture now emerges for the formation of SESN progenitors. First, the H-rich envelope is stripped by a mass-insensitive process. The candidates for this process would include rotation, metallicity, and the binary interaction. However, the former two would still create strong mass dependence, and even the combination of rapid rotation and high metallicity would require at least $M_{\rm ZAMS} > 25 M_{\odot}$ to strip the entire H-rich envelope away (the critical mass depends on the assumption of stellar mass loss rates during the RSG phase, see Vanbeveren et al. 1998; Yoon 2015). Binary interaction provides a straightforward interpretation without major difficulty; its effect is most sensitive to the initial binary separation, which is dependent on $M_{\rm ZAMS}$ but not strongly sensitive (Ouchi & Maeda, 2017; Yoon et al. 2017). The finding in this work also suggests that binary interaction must be inefficient to further strip the He layer. A less massive star, whose He-rich layer is therefore intact, explodes as an SN Ib or IIb, depending on how much hydrogen is retained. Here, a metallicity-driven wind may be an important driver to remove a thin H-rich envelope left after the binary interaction (Yoon 2017). The He-rich layers of more massive SESN progenitors are further stripped by a mass-dependent process, leading to an SN Ic/Ic-BL explosion. This process could be the stellar wind from the H-poor SESN progenitors in the post binary interaction phase; it has recently been suggested that a strong wind could set in once the He mass fraction decreases in the outermost layer, creating a sharp decrease in the amount of the He-rich envelope for SESN progenitors beyond $M_{\rm ZAMS} \sim 25 M_{\odot}$ (Yoon 2017) . While this mass limit seems to be still high to be compatible to the inferred mass range for SNe Ic progenitors ($M_{\rm ZAMS}$ at least

down to $\sim 17 M_{\odot}$), this scenario is qualitatively in line with the findings in this work. Another interesting possibility is eruptive mass loss toward the end of the life of a massive star, if that occurs selectively for the more massive stars (Pastorello et al. 2007; Smith et al. 2014). The hybrid picture suggested here may not require a large difference in $M_{\rm ZAMS}$ between SNe IIb/Ib and Ic as required for the completely single stellar evolution without binary interaction. Further investigation of the mass-dependent process of the He-rich layer stripping is now warranted, connecting the outcome of binary interaction models to the final $\sim 0.5-1$ million years. Such investigations will fill in the gap between the observed diverse population of massive SN progenitors and theoretical understanding, leading toward a complete understanding of the final stages of massive star evolution.

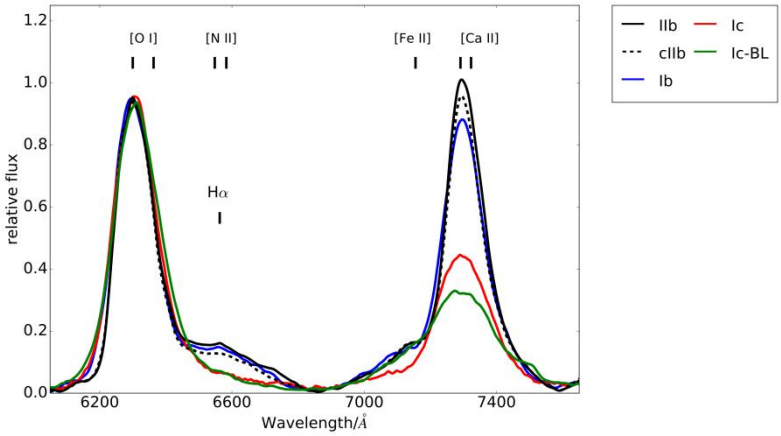

Figure 3.1.**The average spectra of different SESN subtypes obtained around 200 days after maximum light**. The sample includes 13 SNe IIb, 16 SNe Ib, 16 SNe Ic and 8 SNe Ic-BL . For each object, background emission is subtracted (see Method for details) and the spectra are normalized to the peak of the [O I] doublet.

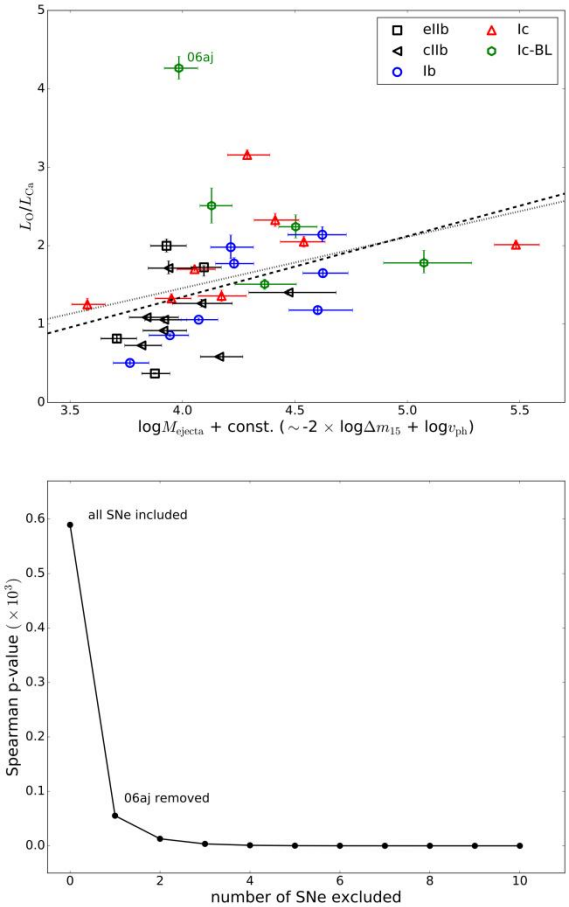

Figure 3.2. **The correlation between early light curve width and the [O I]/[Ca II] ratio.** In the upper panel, the [O I]/[Ca II] ratio is plotted against the measure of the early-phase diffusion time scale. This combination of the early-phase observables characterizes the ejecta mass ($M_{\rm ejecta}$, see Methods). Supernovae of different subtypes are labeled by different colors and symbols. Error bars are given for 1σ uncertainties. The dotted line is the fit to all points, while the dashed line is the fit when the possible outlier SN 2006aj is excluded. To check the possible correlation between the early and late phase quantities further, possible outliers are picked up as follows; One object is removed and the Spearman p value of the residual sample is calculated, and this procedure is repeated until the p value falls below a certain value (2×10^{-4}). The lower panel shows how the p value changes as SNe are removed. It is found that SN Ic-BL 2006aj can be regarded as an outlier, and the correlation is significantly strengthened once this is omitted.

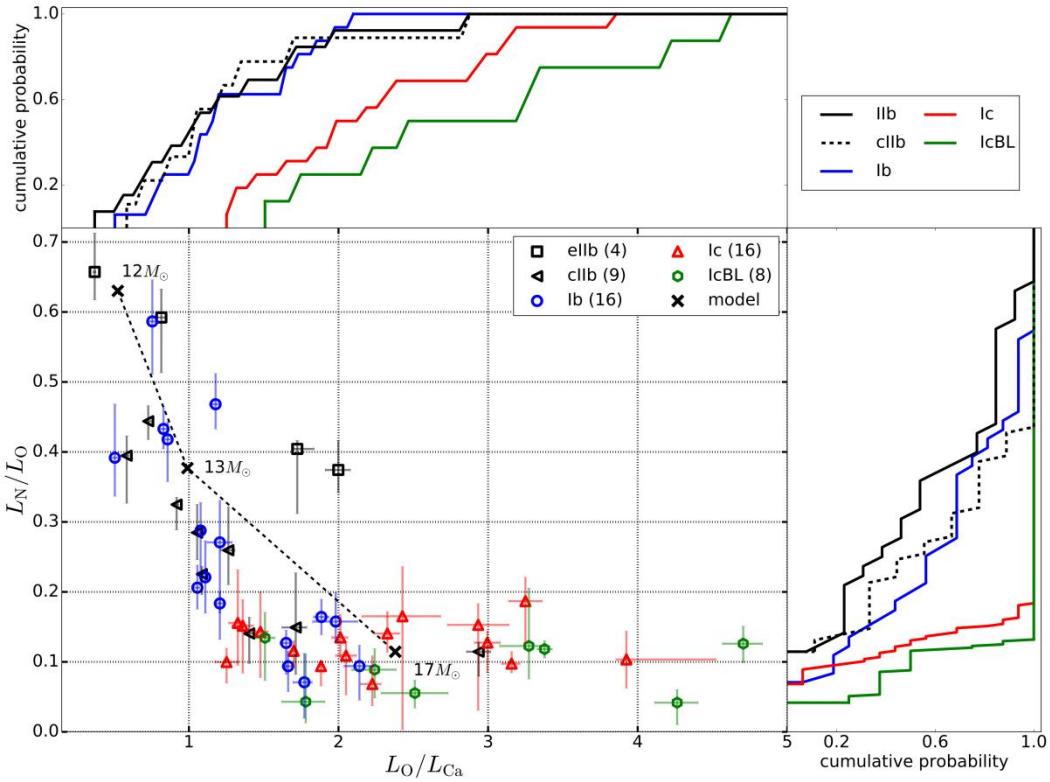

Figure 3.3. **The distribution of L_N/L_O ([N II]/[O I]) and L_O/L_{Ca} ([O I]/[Ca II]) among different SN subtypes**. Central panel: L_N/L_O is plotted against L_O/L_{Ca}. The cumulative probabilities of these ratios are shown in the right and upper panels. Objects with different subtypes are labeled by different colors and symbols. Error bars are given for 1σ uncertainties. Note that the '[N II]' emission for SNe eIIb deviates from a single relation, which is likely due to contamination by Hα. The model predictions for SNe IIb (i.e., no He stripping) from Jerkstrand et al. 2015a are also shown by black crosses, for M_{ZAMS} = 12, 13, and 17 $M_\odot$ respectively .

Section 2. *Methods*

Section 2.1. Sample selection

To construct the supernova sample in this work, SESNe whose nebular spectra (from 150 to 300 days after light curve peak) are available in the literature are included. A large fraction of the data have been collected at Weizmann Interactive Supernova data REPository (WISeREP, Yaron & Gal-Yam 2012), the Open Supernova Catalog (Guillochon et al. 2017) and the Berkeley Supernova Database (SNDB, Shivvers et al. 2019). The discovery date is restricted to be later than 1990. The sample of this work includes nebular spectra of 53 SESNe, including 13 SNe IIb, 16 SNe Ib, 16 SNe Ic and 8 SNe Ic-BL. The spectra and their sources, as well as the classifications and phases, are listed in Table S3-1 in Supplementary material. Some examples are illustrated in Figure S3-1.

A key question in the present investigation is whether there is difference among common and canonical SESNe. Progenitors of SNe Ic-BL have been suggested to be distinctly more massive than other SESNe, while it is not a main focus of this work. No late-time spectra are available for the so-called ultra-stripped SN candidates, for which binary interaction is suggested to play a major role for removing the entire H-rich and

He-rich envelopes (Tauris et al. 2015). Also, the so-called super-luminous SNe are not included in this sample (Jerkstrand et al. 2017).

Section 2.2. Early light curve parameters

The explosion parameters are calculated from V −band light curves, which are derived from different sources (Table S3-2). The ejecta mass can be estimated from the combination of light curve width ($w_{\rm lc}$) and photospheric velocity ($v_{\rm ph}$), using a frequently-adopted scaling Relation (Arnett 1982; Valenti et al. 2008; Lyman et al. 2016):

$$w_{\rm lc} \propto \frac{M_{\rm ejecta}^{3/4}}{E_{\rm K}^{1/4}}, \quad (3.1)$$

where $M_{\rm ejecta}$ and $E_{\rm K}$ are the ejecta mass and kinetic energy. The width of the light curve is estimated from a low-degree polynomial fit to the photometric data around the peak, and is characterized by $w_{\rm lc} \propto \Delta m_{15}{}^{-1}$, where Δm_{15} is the change of the V-band magnitude in 15 days since the peak. Photospheric velocities of SNe are taken from the literatures. If the photospheric velocity is not available in the literature, the average value of each subtype is employed (SN IIb: 8300 ± 750; SN Ib: 9900 ± 1400; SN Ic: 10400 ± 1200; SN Ic-BL: 19100 ± 5000; units: km s^{-1}, see Lyman et al. 2016). The ejecta mass can be estimated as:

$$\log_{10} M_{\rm ejecta} \sim -2 \times \log_{10} \Delta m_{15} + \log_{10} v_{\rm ph}. \quad (3.2)$$

Error in the ejecta mass estimation in this formalism consists of two parts: error of the light curve width and error of the photospheric velocity. The fifirst part is estimated by shifting peak date within the uncertainty (a typical value is 1 day). The difference is employed as the 1σ error of the light curve width. The error of the photospheric velocity is taken from the literature. It should be noted that this is a very simplified method, and likely suffers from various uncertainties which are not taken into account here (Dessart et al. 2012). For example, there is one apparent outlier in the SN Ic sample in terms of the early-phase observables, SN 2011bm showing not only a broader light curve but also a lower velocity than other SNe Ic. Such an outlier may introduce a large error in the conversion from the early-phase observables to $M_{\rm ejecta}$. Furthermore, $M_{\rm ejecta}$ is not a direct measure of $M_{\rm CO}$ or $M_{\rm ZAMS}$. Subtracting the mass of the newly formed neutron star ($\sim 1.5 M_{\odot}$), one roughly expects that a He-free star with $M_{\rm CO} \sim 4.5 M_{\odot}$ would result in an SN Ic with $M_{\rm ejecta} \sim 3 M_{\odot}$. On the other hand, a star with $M_{\rm CO} \sim 3 M_{\odot}$ attached with the He-rich envelope ($\sim 1.5 M_{\odot}$) would result in an SN Ib with the same ejecta mass. Namely, the progenitors with different $M_{\rm CO}$ can lead to similar $M_{\rm ejecta}$.

Section 2.3. Nebular spectrum

A nebular spectrum is smoothed, de-reddened and corrected for redshift of the host galaxy taken from HyperLeda (Makarov et al. 2014) before the line decomposition. The extinction values $E(B-V)$ are derived from the literature (Table S3-1 in Supplementary material), most of which are estimated from their color evolution. For objects whose multi-band light curves are not available, the extinction is calculated from the equivalent width (EW) of Na I D near the light curve peak (Turatto et al. 2003). For objects without these information, $E(B-V)$ is set to be 0.36 mag, which is the average value of SN Ib/Ic (Drout et al. 2011). While the estimation of $E(B-V)$ is quite uncertain, the quantities of interest in this work are not sensitive to $E(B-$

V). The background emission is estimated by a line connecting the two minima at both wings of the emission complex. After the background is subtracted, the emission complex is decomposed.

(1) [O I]/[N II] complex: The oxygen line in this complex is fitted by a double Gaussian profile. The Gaussian profiles have the centers located at 6300 and 6363 Å with the same standard deviation, and the flux ratio is fixed to be 3:1. The excess flux of this complex relative to the fitted oxygen profile is estimated to be the flux of [N II]. This method will give a none-zero value for the [N II]/[O I] ratio for SNe Ic/Ic-BL. However, this does not necessarily mean that the He/N layer is still present for these objects. Other factors may contribute, including contamination from the star-forming region or continuum scattering from electrons and dust (Jerkstrand 2017), and therefore the flux may well be leveled off when the [N II]/[O I] ratio is practically zero.

(2) [Ca II]/[Fe II] complex: First, the flux of this complex is calculated as the total integrated flux in the wavelength range of interest, which is dominated by [Ca II] with a smaller contribution from [Fe II]. To estimate the contribution by [Fe II], the integrated flux of the smoothed spectrum is calculated between the blue wing of the complex and 7155 Å (i.e., the central wavelength of [Fe II]). Assuming that [Fe II] has a roughly symmetric profile with respect to its central wavelength, the flux of [Fe II] is then estimated by multiplying this integrated flux by a factor of two. This method is based on the reasonable assumption that the flux at < 7155 Å is not strongly contaminated by [Ca II]. With the flux of [Fe II] thus determined, this is then subtracted from the total integrated flux of the complex to give the flux of [Ca II].

Examples of the line decomposition of different SN subtypes are illustrated in Figure S3-2.

Errors in the line ratios consist of several parts. The quadratic sum of these errors is assigned as the total error of the line ratio under consideration.

(1) Poisson noise: To estimate the error related to the Poisson noise, the degree of smooth is increased (overly smoothed) or decreased, and the deviation of line ratio estimated in this way is associated to the error contributed by the Poisson noise.

(2) Background determination: Although the edge of the [O I]/[N II] complex is well determined for SNe IIb and some SNe Ib, it can be easily contaminated by background for SNe Ib/Ic/Ic-BL with weak or absent [N II] emissions. The uncertainty from the background determination is estimated by shifting the minima, which determine the edges of the complex, within 50 ~ 100 Å, then re-measure the line ratios. The deviation from the original line ratio is estimated to be the uncertainty contributed by background determination.

(3) **Line fitting:** The line profile of [O I] can affect the edge of the [N II] feature, and therefore its flux. The main budget of this uncertainty comes from the uncertainty of the width of [O I]. By changing the width of [O I] (by 1σ estimated from line fitting), one can have different estimation on the line ratios. The difference is then employed to be the uncertainty from the line fitting.

Section 2.4. Discussion

Section 2.4.1. Possible time dependence

Spectra of different SNe were obtained at different phases. The mean phase and the standard deviation of the spectra used for different SNe subtypes are as follows: 227 ± 37 days (SN IIb), 208 ± 38 days (SN Ib), 212 ± 37 days (SN Ic) and 217 ± 29 days (SN Ic-BL). No statistical difference between spectral phases among different SNe subtypes can be discerned from a KS test. Since the span in the spectral phase is small, the possible effect of spectral evolution should not affect the conclusion, which will be tested in this section.

A direct way to investigate the effect of time evolution is to measure line ratios at different phases for a single object. The SN luminosities evolve quasi-exponentially as a function of time, therefore the evolution of line ratios is expected to be approximated by $r(t) \sim e^{-\alpha t}$, where $r(t)$ is the line ratio at phase t and α characterizes the speed of its evolution. In Figure S3-3, the line ratio is plotted against the spectral phase. It is clear that the [O I]/[Ca II] ratio hardly evolves as compared with the overall scatter, which is consistent with the slowly evolving nature of this ratio reported in the literature (Elmhamdi et al. 2004; Kuncarayakti et al. 2015). The mean values and standard deviations of the slopes in logarithm scale are 0.039 ± 0.185 /(100 days) for [O I]/[Ca II] (right panel in Figure S3-3). On the other hand, the [N II]/[O I] line evolves relatively quickly for a few objects; The mean values and standard deviations of the slopes in logarithm scale are -0.128 ± 0.688 /(100 days) for [N II]/[O I]. These slopes correspond to a change in the line ratio by ~25% (for [O I]/[Ca II]) and ~60% (for [N II]/[O I]) in the time span of 100 days.

The above discussion suggests that the evolution of the line ratio may require further consideration. To test how the evolution of the line ratio could affect the conclusion in the main text, 10^4 Monte-Carlo simulations are carried out. In each simulation, a randomly-generated slope (which is assumed to be normally distributed, with the mean value and standard deviation identical to the observationally derived values) is attached to each object and the line ratio is corrected to 220 days by $r(220) = r(t) \times e^{\alpha(220-t)}$ where t is spectral phase in the unit of days. The distribution of the line ratios is then obtained for each Monte-Carlo simulation, and the KS test is performed for each simulated distribution.

The results of the simulations are shown in Figure S3-4. The solid lines are the mean values of 10^4 simulations and the dashed lines are the 1σ deviations. It is seen that even when the effect of time evolution is taken into consideration, the main conclusion is not affected. SNe IIb and SNe Ib have similar line ratios, with average and standard deviation of the KS test coefficients are $0.863^{+0.087}_{-0.214}$ for the [O I]/[Ca II] ratio and $0.541^{+0.338}_{-0.228}$ for the [N II]/[O I] ratio. SNe Ic have a systematically larger [O I]/[Ca II] ratio than SNe Ib, with the average and standard deviation of the KS test coefficient being $0.014^{+0.008}_{-0.007}$. The KS coefficient for various combinations of different subtypes are listed in Table S3-3. The effect of spectral evolution is proven to be insignificant.

Section 2.4.2. Possible factors that would affect [O I]/[Ca II]

To set a scene, general ideas which underline the use of the [O I]/[Ca II] ratio as an indicator of M_{CO} are firstly summarized (Fransson & Chevalier 1989; Maeda et al. 2007a; Jerkstrand et al. 2014; Anderson et al. 2018; Fang & Maeda 2018). First, the sum of the line luminosities emitted from a given layer should be roughly

equal to the radioactive energy deposition rate in the layer through the balance of cooling and heating rates. Therefore the ratio of the total luminosities of two different layers is roughly determined by their mass ratio. Next, [O I] is the main coolant in the C+O core (excluding the innermost O/Si/S zone which is created by the explosive nucleosynthesis at the explosion), and [Ca II] is so in the explosive incomplete Si burning region (including both Si/S and O/Si/S layers, see Fransson & Chevalier 1989; Jerkstrand et al. 2015a). As such, thermal conditions in these layers are largely set by these lines; it is not that these line strengths are determined by independently determined thermal condition. This property in these lines makes their strengths a tracer of the mass in each layer, which is controlled by M_{CO}. Further discussion for some additional possibilities which might affect the [O I]/[Ca II] ratio will be provided below.

First, the most important question is whether the different [O I]/[Ca II] ratio for SNe IIb/Ib and SNe Ic could be explained by considering same M_{CO} but attaching He-rich layer to SNe Ib/IIb. This will result in higher characteristic velocity and lower density for SNe Ic than the SN IIb/Ib counterparts. A few simulations exist in the literature which test different velocity scales for $8M_{\odot}$ and $4M_{\odot}$ He star models, corresponding to M_{ZAMS} = 25 and $15M_{\odot}$, respectively (Fransson & Chevalier 1989). These models show that the [O I]/[Ca II] ratio is decreased by a factor of few once the velocity is increased by a factor of two. Namely, if SNe Ic and SNe IIb/Ib share same M_{CO}, the [O I]/[Ca II] ratio is predicted to be lower for SNe Ic, which is opposite to the finding in this work.

The result stems from a general feature in the thermal condition under typical SESN late-time conditions. The assumption that [O I] and [Ca II] dominate the cooling is more valid under lower density condition, while for high density condition, contributions from Mg I] 4571 and [O I] 5577 in the C+O core become strong. In the incomplete Si burning region, at high density, Ca II H&K, NIR triplet and Si I 1.099 μm become strong. Among these additional contributions, those in the incomplete Si burning region are more sensitive to density. Therefore, by decreasing density (SN Ic model), the [O I]/[Ca II] ratio decreases in the spectrum synthesis model.

Another effect would be the macroscopic mixing during the explosion, which is expected to take place for SNe IIb/Ib at the interface between the C+O core and the He-rich envelope. Qualitatively, it will bring up the C+O core material and thus increase the volume and average velocity. This is then expected to only reduce the difference in the thermal conditions between the hypothesized SNe IIb models and Ic models based on the same M_{CO}.

The possible effect of variation in the thermal condition can also be inferred obesrvationally. Indeed, the simulation of Fransson & Chevalier (1989) adapt a larger velocity difference than observed (Lyman et al. 2016), which overestimate the effect. Observationally, one should expect that the time evolution of [O I]/[Ca II] ratio for individual SESNe can be used as a measure of the importance of the variation in thermal condition; between 150 and 250 days, the density should decrease by a factor of ~ 5. However, the evolution in the [O I]/[Ca II] ratio (Figure S3-3) is negligible, which phenomenologically suggests that the variation in the [O I]/[Ca II] ratio is not driven by thermal condition externally set by other lines.

The above arguments are based on the assumption that the masses of the [Ca II] emitting region are the same for SNe IIb/Ib and SNe Ic. If pre-SN CO core would be identical between them, one would not expect difference in the explosion mechanism (O'Connor & Ott 2011; Suwa et al. 2019). Observationally, there is a

hint that SNe Ic on average may eject a larger amount of newly synthesized elements (Lyman et al. 2016; Taddia et al. 2018), and this will work to reduce the [O I]/[Ca II] ratio for SNe Ic, as opposed to the observational relation.

Another concern would be raised as for what would happen if microscopic mixing, i.e., diffusive mixing of different elements into the same fluid element, would take place; [Ca II] is an efficient coolant, so it would dominate [O I] if the mass fraction of Ca would exceed $\sim 10^{-3}$ (Fransson & Chevalier 1989). Since calcium is mostly the product of the explosive burning at the explosion, such microscopic mixing is very unlikely expected, e.g., as inferred for Cas A(Fransson & Chevalier 1989; Ennis et al. 2006; Maeda et al. 2007a). The microscopic mixing should therefore be limited to the pre-SN hydrostatic evolution phase; even if such hypothesis would explain the difference in the [O I]/[Ca II], this already means that there is difference between the progenitors of SNe IIb/Ib and Ic. Furthermore, to the authors' knowledge, no progenitor models for SNe Ic (or SESNe in general) exists in the literature which leads to the substantial mixing of Ca into the C+O core.

In sum, the observed difference in the [O I]/[Ca II] ratio between SNe IIb/Ib and SNe Ic is difficult to reconcile if they have identical pre-SN C+O cores. The straightforward interpretation, without introducing any unknown mechanism, is that the SN Ic progenitors have larger $M_{\rm CO}$ and thus larger $M_{\rm ZAMS}$. Detailed spectral synthesis modeling is beyond the scope of this work, in order to provide a model-independent discussion. Still, it should be emphasized that late-time spectrum synthesis simulations specifically tuned to different SESNe subtypes is highly encouraged. Such a model will especially be important to quantitatively investigate the mass range for SNe Ic, as has been done for SNe II (Jerkstrand et al. 2014, 2015a). In this aspect, it should also be emphasized that comparison between the [O I]/[Ca II] ratios observed for SNe Ic and those simulated for SN IIb models (Figure 3.3) must not be over-interpreted. For example, the overlap in the ratio for SNe IIb/Ib and Ic at [O I]/[Ca II] $\sim 1-2$ may not mean any physical similarity between the two classes; one of the above arguments qualitatively suggests that the [O I]/[Ca II] may indeed be decreased for given $M_{\rm CO}$ once the He-rich envelope is stripped, and such an effect may contribute to create the overlapped region without introducing the overlap in $M_{\rm ZAMS}$ for SNe IIb/Ib and Ic.

Section 3. Supplementary material

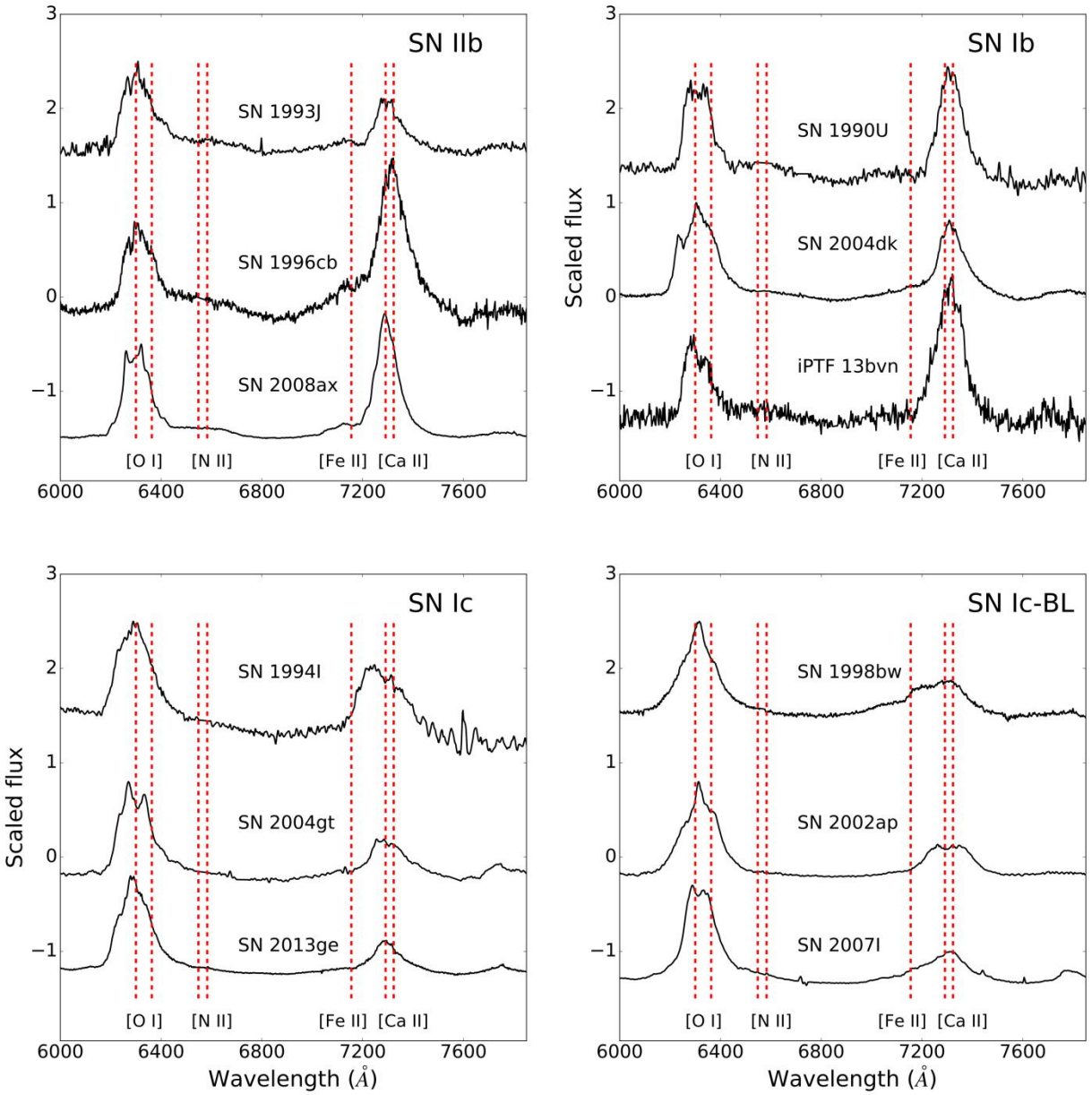

Figure 3S-1. **An illustration of SNe of different subtypes in this work.** The spectra are corrected for host redshifts and the flflux is scaled for demonstration purpose. The red vertical lines are emission lines of interest. From left to right: [O I] $\lambda\lambda$6300, 6363; [N II] $\lambda\lambda$6548, 6583; [Fe II] λ7155; [Ca II] $\lambda\lambda$7291, 7323.

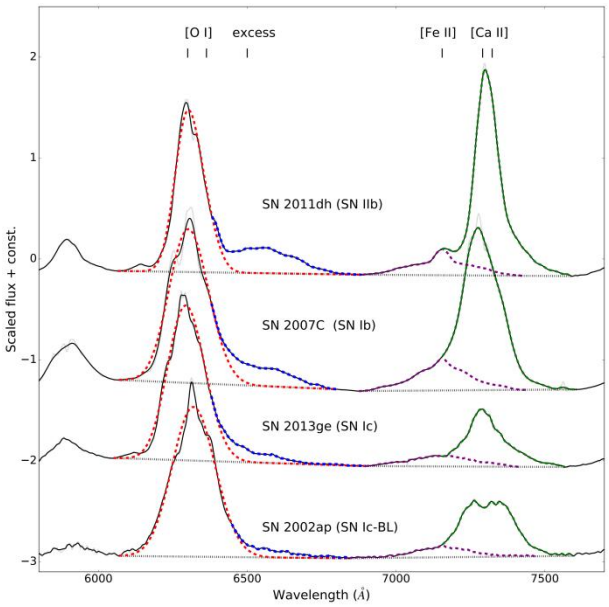

Figure 3S-2. **Examples of the line decomposition for SNe of different subtypes.** All spectra are corrected for redshift and extinction. The black dotted line is background emission and the red dashed line is the best-fitted double Gaussian profile of the [O I] doublet.The excess flux ([N II]) is illustrated by blue dashed line. Purple dashed line defines the blue wing of [Fe II], together with its mirror image relative to 7155 Å . The green dashed line is the [Ca II] doublet.

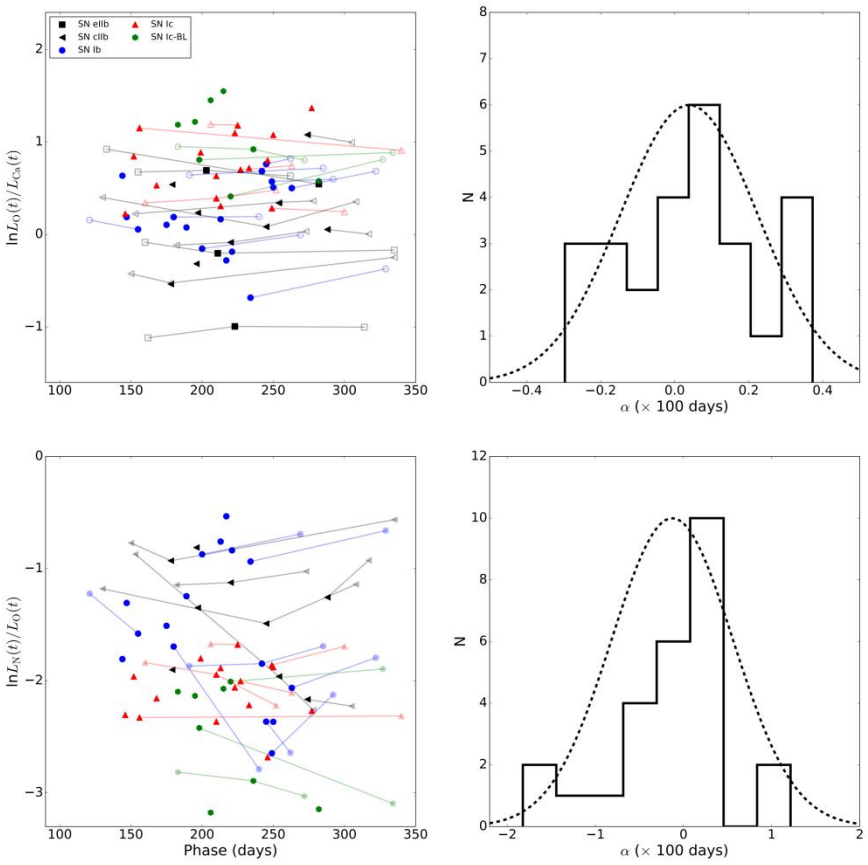

Figure 3S-3.**Effects of line evolutions.** The left panels show evolution of the line ratios in a logarithmic scale. The upper left panel is for [O I]/[Ca II] and the lower left panel is for [N II]/[O I]. SNe of different subtypes are labeled by different colors and symbols. The solid points are the line ratios adopted in the main text and the transparent points are line ratios at other spectral phases. Points for the same object at different phases are connected by a line. Since SNe eIIb contain additional contribution from Hα in the '[N II] feature', they are omitted in the lower panels. The right panels show distributions in the speed of the evolution for these two line ratios, characterized by α (see text for details). The dashed lines are Gaussian functions (which are adopted in the Monte-Carlo simulations), with the same mean values and standard distributions as the observed distribution.

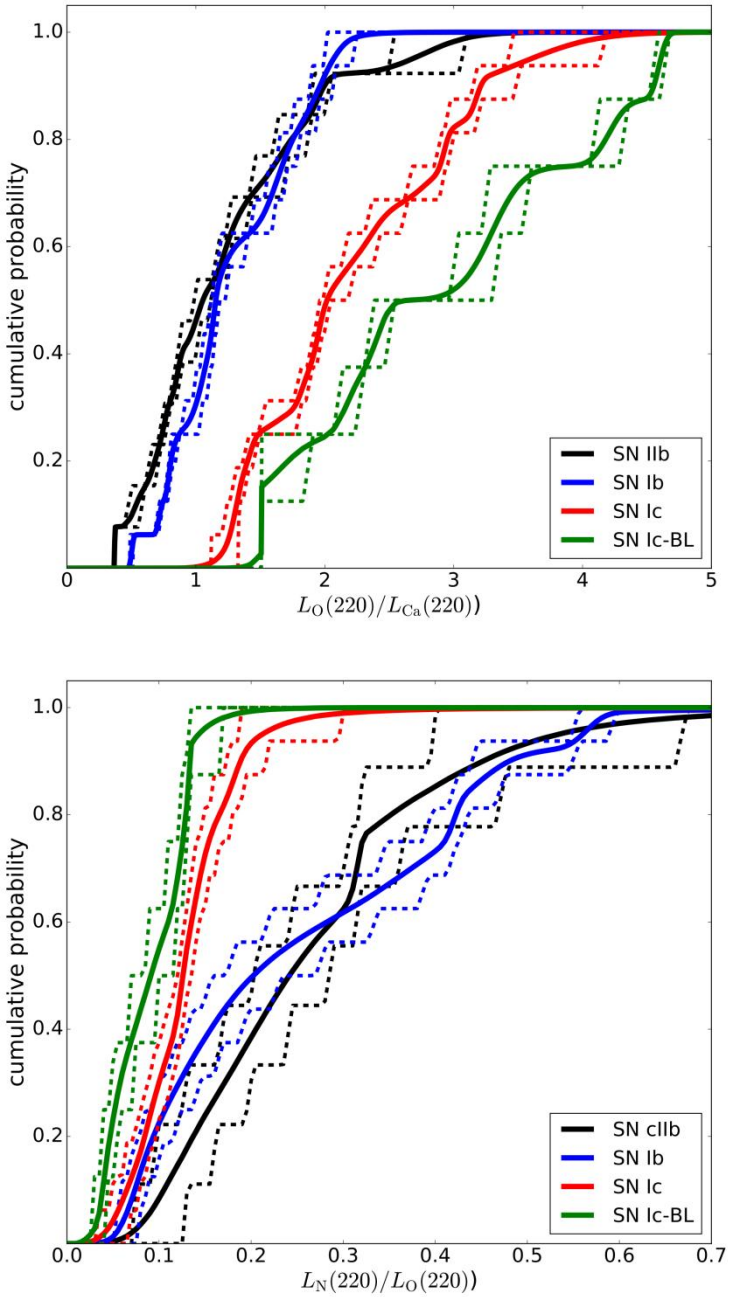

Figure 3S-4.**The distribution of the line ratios of different SNe subtypes from 10^4 Monte-Carlo simulations.** Solid lines are average values and dashed lines are 1σ deviations. SNe of different subtypes are labeled by different colors.

Name	Date	Phase	*E(B-V)*	References
		IIb		
1993J	1993/09/20	155	0.19	Jerkstrand et al. 2015a;
	1993/11/07	203		Matheson et al. 2000b
	1994/01/05	262		
1996cb	1997/06/03	150	0.03	Qiu et al. 1999
	1997/07/01	178		
	1997/12/25	335		
2001ig	**2002/10/08**	274	0.10	Maund et al. 2007
	2002/11/08	305		
2003bg	2003/08/20	153	0.02	Hamuy et al. 2009
	2003/11/29	254		
	2003/12/23	278		
2006T	**2006/11/26**	288	0.08	Modjaz 2007; Maeda et al. 2008;
	2006/12/25	317		Modjaz et al. 2014
2008ax	2008/08/01	130	0.40	Taubenberger et al. 2011;
	2008/11/25	245		Modjaz et al. 2014
	2009/01/25	345		
2008bo	**2008/10/27**	197	0.08	Shivvers et al. 2019
2011dh	2011/12/18	182	0.07	Shivvers et al. 2013;
	2012/01/25	220		Ergon et al. 2014;
	2012/03/18	273		Ergon et al. 2015
2011fu	2012/02/22	133	0.10	Morales-Garoffolo et al. 2015
	2012/07/20	282		
2011hs	2012/03/18	160	0.17	Bufano et al. 2014
	2012/06/21	211		
	2013/01/22	334		
2012P	**2012/08/08**	197	0.29	Fremling et al. 2016
2013ak	**2013/09/12**	179	0.39	Yaron & Gal-Yam 2012
2013df	2013/12/05	162	0.10	Morales-Garoffolo et al. 2014;
	2014/02/04	223		Maeda et al. 2015
	2014/05/06	314		
		Ib		
1990U	**1991/01/06**	189	0.52	Gómez&Lopez 1994;
				Matheson et al. 2001;
				Taubenberger et al. 2009
1990W	**1991/02/21**	180	0.36	Wheeler et al. 1994;
	1991/04/21	239		Taubenberger et al. 2009
2004ao	**2004/11/14**	250	0.12	Elmhamdi et al. 2011;
				Shivvers et al. 2019
2004dk	**2005/05/11**	263	0.34	Drout et al. 2011
	2005/07/09	322		Modjaz et al. 2008, 2014;
				Shivvers et al. 2017
2004gn	**2005/07/06**	217	0.36	Maeda et al. 2008;

				Shivvers et al. 2019
2004gq	**2005/08/26**	249	0.25	Modjaz et al. 2008, 2014; Maeda et al. 2011; Drout et al. 2011
	2005/10/06	292		
2004gv	2005/07/06	191	0.25	Modjaz et al. 2008, 2014; Maeda et al. 2011
	2005/08/26	242		
	2005/10/08	285		
2005bf	**2005/12/11**	213	0.14	Follatelli et al. 2006; Modjaz et al. 2014
2006F	**2006/06/30**	175	0.54	Maeda et al. 2008; Drout et al. 2011
2006gi	**2007/02/10**	144	0.38	Taubebberger et al. 2009; Elmhamdi et al. 2011
2007C	2007/05/17	121	0.64	Taubenberger et al. 2009; Drout et al. 2011; Modjaz et al. 2014
	2007/06/20	155		
2007Y	**2007/09/22**	200	0.11	Stritzinger et al. 2011
	2007/11/30	269		
2009jf	**2010/06/19**	245	0.12	Sahu et al. 2011; Valenti et al. 2011; Modjaz et al. 2014
	2010/07/08	264		
iPTF 13bvn	**2014/02/21**	234	0.07	Fremling et al. 2016
	2014/05/28	330		
2014 C	**2014/08/25**	221	0.75	Milisavljevic et al. 2015a; Shivvers et al. 2019
PS 15bgt	**2015/12/17**	147	0.23	Shivvers et al. 2019
			Ic	
1991N	1992/01/09	277	0.12	Matheson et al. 2001; Maeda et al. 2008
1994I	1994/09/02	146	0.45	Filippenko et al. 1995; Richmond et al. 1996b; Modjaz et al. 2014
1996D	1996/09/10	199	0.36	Taubenberger et al. 2009
1996aq	1996/02/11	160	0.36	Taubenberger et al. 2009
	1996/04/02	210		
	1996/05/14	252		
1997dq	**1998/05/30**	206	0.11	Matheson et al. 2001; Taubenberger et al. 2009; Modjaz et al. 2014
	1998/06/18	226		
2004aw	**2004/11/14**	233	0.37	Taubenberger et al. 2009; Modjaz et al. 2014
2004fe	**2005/07/06**	249	0.32	Maeda et al. 2008; Drout et al. 2011; Modjaz et al. 2014
	2005/08/26	300		
2004gk	**2005/07/10**	223	0.47	Maeda et al. 2008; Elmhamdi et al. 2011; Modjaz et al. 2014
2004gt	**2005/05/24**	152	0.10	Gal-Yam et al. 2005; Taubenberger et al. 2009; Modjaz et al. 2014

2005kl	**2006/06/30**	213	0.29	Maeda et al. 2008; Drout et al. 2011; Modjaz et al. 2014
2006ck	**2007/01/24**	246	0.36	Maeda et al. 2008; Modjaz et al. 2014
2007gr	**2008/02/12**	170	0.09	Drout et al. 2011; Shivvers et al. 2019
2011bm	**2011/12/17**	227	0.06	Valenti et al. 2012
	2012/01/22	263		
2013ge	**2014/04/28**	156	0.07	Drout et al. 2016
	2014.10/23	334		
2014eh	**2015/06/16**	210	0.36	Shivvers et al. 2019
		Ic-BL		
1997ef	**1998/09/21**	282	0.00	Iwamoto et al. 2000; Mazzali et al. 2000; Matheson et al. 2001; Modjaz et al. 2014
1998bw	**1998/11/26**	198	0.06	Patat et al. 2001; Clocchiatti et al. 2011; Modjaz et al. 2016
	1999/04/12	335		
2002ap	**2002/08/09**	183	0.08	Mazzali et al. 2002; Foley et al. 2003; Yoshii et al. 2003; Modjaz et al. 2016
	2002/10/01	236		
	2002/11/06	272		
2005kz	**2006/06/30**	215	0.46	Maeda et al. 2008; Drout et al. 2011
2005nb	**2006/06/30**	183	0.36	Maeda et al. 2008; Modjaz et al. 2014
2006aj	**2006/09/21**	206	0.15	Modjaz et al. 2006;2014;2016
2007I	**2007/07/15**	195	0.36	Taubenberger et al. 2009; Modjaz et al. 2014
2012ap	**2012/09/21**	272	0.45	Milisavljevic et al. 2015b
	2012/11/16	328		

Table 3S-1. **Spectra list of SNe used in this Chapter.** Spectra marked by bold face are used for analyses in the main text.

Object	Type	Δm_{15}	v_{ph}	References[5]
1993J	IIb	$0.971^{+0.052}_{-0.078}$	8000^{+1000}_{-1000}	L16
1994I	Ic	$1.745^{+0.091}_{-0.140}$	15000^{+1000}_{-1400}	Richmond et al. 1996b; L16
1996cb	IIb	$0.764^{+0.059}_{-0.072}$	8500^{+1300}_{-1000}	Qiu et al. 1999; L16
1997ef	Ic-BL	$0.331^{+0.025}_{-0.050}$	13000^{+5000}_{-5000}	Iwamoto et al. 2000
1998bw	Ic-BL	$0.782^{+0.065}_{-0.079}$	19000^{+1700}_{-1000}	Clocchiatti et al. 2011; L16
2002ap	Ic-BL	$0.983^{+0.045}_{-0.071}$	13000^{+2000}_{-1000}	Patat et al. 2001; L16
2003bg	IIb	$0.520^{+0.100}_{-0.122}$	8000^{+1000}_{-1000}	Hamuy et al. 2009;L16
2004aw	Ic	$0.564^{+0.047}_{-0.056}$	13000^{+1000}_{-1900}	Taubenberger et al. 2006; L16
2004dk	Ib	$0.468^{+0.041}_{-0.049}$	9200^{+1400}_{-1000}	D11; L16
2004fe	Ic	$1.100^{+0.078}_{-0.100}$	11000^{+1000}_{-1000}	Stritzinger et al. 2018; L16

[5] D11: Drout et al. (2011); L16; Lyman et al. (2016)

2004gq	Ib	$0.876^{+0.066}_{-0.082}$	13000^{+1000}_{-1500}	D11; L16
2004gt	Ic	$0.634^{+0.058}_{-0.068}$	10400^{+1200}_{-1200}	Stritzinger et al. 2018
2004gv	Ib	$0.777^{+0.058}_{-0.072}$	9900^{+1400}_{-1400}	Stritzinger et al. 2018
2005bf	Ib	$0.433^{+0.057}_{-0.058}$	7500^{+1800}_{-1000}	Folatelli et al. 2006; L16
2005kl	Ic	$0.835^{+0.087}_{-0.095}$	10400^{+1200}_{-1200}	Bianco et al. 2014
2006aj	Ic-BL	$1.367^{+0.095}_{-0.127}$	18000^{+1000}_{-1000}	Bianco et al. 2014; L16
2006T	IIb	$0.951^{+0.071}_{-0.090}$	7500^{+1000}_{-1000}	Stritzinger et al. 2018; L16
2007C	Ib	$0.966^{+0.062}_{-0.084}$	11000^{+1000}_{-1400}	D11; L16
2007Y	Ib	$1.012^{+0.052}_{-0.080}$	9000^{+1000}_{-1700}	Stritzinger et al. 2009; L16
2007gr	Ic	$0.940^{+0.072}_{-0.089}$	10000^{+1000}_{-1000}	Hunter et al. 2009; L16
2008ax	IIb	$1.041^{+0.061}_{-0.087}$	7500^{+2100}_{-1000}	Taubenberger et al. 2011; L16
2008bo	IIb	$1.228^{+0.061}_{-0.093}$	9900^{+1400}_{-1400}	Bianco et al. 2014; L16
2009jf	Ib	$0.476^{+0.080}_{-0.026}$	9500^{+2100}_{-1000}	Sahu et al. 2011; L16
2011bm	Ic	$0.172^{+0.016}_{-0.018}$	9000^{+1000}_{-1000}	Valenti et al. 2012; L16
2011dh	IIb	$0.923^{+0.071}_{-0.088}$	7000^{+1000}_{-1000}	Ergon et al. 2014, 2015; L16
2011fu	IIb	$0.816^{+0.039}_{-0.063}$	8300^{+750}_{-750}	Morales-Garoffolo et al. 2015
2011hs	IIb	$1.252^{+0.067}_{-0.101}$	8000^{+1000}_{-1000}	Bufano et al. 2014; L16
2012P	IIb	$0.786^{+0.073}_{-0.084}$	7500^{+1750}_{-1750}	Fremling et al. 2016
2012ap	Ic-BL	$0.908^{+0.070}_{-0.087}$	19100^{+5000}_{-5000}	Milisavljevic et al. 2015b
2013ak	IIb	$0.961^{+0.081}_{-0.099}$	8000^{+1000}_{-1000}	Brown et al. 2014
2013df	IIb	$1.059^{+0.031}_{-0.052}$	8500^{+1000}_{-1000}	Morales-Garoffolo et al. 2014; Szalai et al. 2016
2013ge	Ic	$0.732^{+0.061}_{-0.074}$	10400^{+1200}_{-1200}	Drout et al. 2016
iPTF 13bvn	Ib	$1.170^{+0.069}_{-0.088}$	8000^{+1000}_{-1000}	Fremling et al. 2016

Table 3S-2. **Early phase parameters of SNe in this work.**

	IIb/Ib	IIb/Ic	IIb/Ic-BL	Ib/Ic	Ib/Ic-BL	Ic/Ic-BL
[O I]/[Ca II]	$0.863^{+0.027}_{-0.214}$	$0.004^{+0.010}_{-0.001}$	$0.008^{+0.000}_{-0.006}$	$0.007^{+0.000}_{-0.005}$	$0.002^{+0.004}_{-0.000}$	$0.354^{+0.233}_{-0.153}$
[N II]/[O I]	$0.541^{+0.338}_{-0.228}$	$0.006^{+0.035}_{-0.008}$	$0.005^{+0.019}_{-0.004}$	$0.023^{+0.042}_{-0.021}$	$0.006^{+0.030}_{-0.004}$	$0.191^{+0.163}_{-0.150}$

Table 3S-3. **KS correlation coefficients after phases are corrected.**

Chapter 4. Constraint on the ejecta dynamics I: Observation

Fang, Q., Maeda, K., Kuncarayakti, H., et al. 2022, ApJ, 928, 151

We present an analysis of the nebular spectra of 103 stripped-envelope (SE) supernovae (SNe) collected from the literature and observed with the Subaru Telescope from 2002 to 2012, focusing on [O I] λλ6300, 6363. The line profile and width of [O I] are employed to infer the ejecta geometry and the expansion velocity of the inner core; these two measurements are then compared with the SN subtypes, and further with the [O I]/[Ca II] ratio, which is used as an indicator of the progenitor CO core mass. Based on the best-fit results of the [O I] profile, the objects are classified into different morphological groups, and we conclude that the deviation from spherical symmetry is a common feature for all types of SESNe. There is a hint (at the ~1σ level) that the distributions of the line profile fractions are different between canonical SESNe and broad-line SNe Ic. A correlation between [O I] width and [O I]/[Ca II] is discerned, indicating that the oxygen-rich material tends to expand faster for objects with a more massive CO core. Such a correlation can be utilized to constrain the relation between the progenitor mass and the kinetic energy of the explosion. Further, when [O I]/[Ca II] increases, the fraction of objects with Gaussian [O I] profile increases, while those with double-peaked profile decreases. This phenomenon connects ejecta geometry and the progenitor CO core mass.

Section 1. Introduction

When the central nuclear fuel is exhausted, a massive star (>8 $M_{\odot}$) will suffer from core collapse, resulting in a core-collapse supernova (CCSN), expelling the material above the core. The explosion energy and the geometry of the ejecta of this catastrophic event, together with their relations with the properties of the progenitor, are important factors for understanding the final evolution of massive stars.

Before an SN explodes, the massive star progenitor may suffer from a certain degree of envelope stripping either by binary evolution or stellar wind, or the combination of both (Heger et al. 2003; Groh et al. 2013; Smith 2014; Yoon 2015; Fang et al. 2019). If the hydrogen envelope is mostly retained before the explosion, the star will explode as a type II supernova (SN II), with strong hydrogen features in its spectra. Otherwise it will explode as a stripped-envelope supernova (SESN). SESNe can be further classified into type IIb SNe (SNe IIb; with strong hydrogen lines in early-phase spectra, which are later replaced by helium lines), type Ib SNe (SNe Ib; with spectra dominated by helium lines, showing no or weak hydrogen signatures), and type Ic SNe (SNe Ic; with spectra lacking both hydrogen and helium lines). Type Ic SNe can be further divided into normal SNe Ic and broad-line type Ic (SNe Ic-BL). The early-phase spectra of the latter type show broad absorption features, indicating fast-expanding ejecta (by a factor of ~2 faster than normal SNe Ic at maximum brightness) and large kinetic energy (1052 erg, compared with ~10^{51} erg for typical SNe). SNe Ic-BL are sometimes associated with gamma-ray bursts (GRBs; see Galama et al. 1998; Hjorth et al. 2003; Woosley & Bloom 2006 for a review).

The explosion mechanism of CCSNe is an important open problem in modern astronomy. It is not yet clear how the gravitational energy is transformed to the kinetic energy of the outward-moving material. Placing observational constraints on the explosion geometry is one of the keys to answering this problem. The explosion energy may also depend on the progenitor masses (Ugliano et al. 2012; Müller et al. 2016; Sukhbold et al. 2016). Therefore, it is important to explore possible relations between these quantities from observational data; we thus need to have indicators of the kinetic energy, the ejecta geometry, and the progenitor mass independently from observables. For the mass of the progenitor star, the most robust method is to use a high-resolution image of the progenitor, although it still depends on the theoretical calculation of stellar evolution and therefore introduces some uncertainties (Smartt 2009;2015). The direct detection of the progenitors is only feasible in a relatively small volume, where CCSNe are rare events. The direct images of CCSNe are only available for a few number of cases, especially those lacking hydrogen-poor SNe (Maund et al. 2004, 2011; Van Dyk et al. 2014; Folatelli et al. 2015; Kilpatrick et al. 2017; Tartaglia et al. 2017). For reviews, see Smartt (2009, 2015). So far only two SNe Ib, iPTF 13bvn and SN 2019yvr, have been identified (Cao et al. 2013; Kilpatrick et al. 2021).

SNe in their early phases are luminous enough so that they can be observed in distant galaxies. The luminosity scale and the shape of the light curve are dependent on the amount of radioactive elements, and the mass and the kinetic energy of the ejecta. The shape of the light curve is also affected by how the radioactive power source is mixed in the envelope. Many works have been conducted that allow investigation of a possible relation between the ejecta mass and the explosion energy based on large samples (Drout et al. 2011; Dessart et al. 2016; Lyman et al. 2016; Prentice et al. 2016; Taddia et al. 2018). However, the early-phase emission mainly originates from the outermost region of the optical thick ejecta, and is not directly related to the inner core; thus, converting the ejecta mass estimated in this way to the progenitor mass may involve a large uncertainty. Further, the early-phase observables are generally not sensitive to the ejecta geometry except for the polarization signal (Wang et al. 2001; Wang & Wheeler 2008; Nagao et al. 2021). Indeed, most of the codes employed to model the early-phase SN light curve assume that the ejecta are spherically symmetric, which is not necessary valid (Maeda et al. 2008; Taubenberger et al. 2009).

Observation during the nebular phase naturally meets all of the requirements. After the massive star explodes, the density of the ejecta decreases with time following the expansion. At the same time, recombination also reduces the electron density. These effects together reduce the optical depth of the ejecta. When the ejecta becomes transparent to expose the inner region, the SN enters its nebular phase, and the spectrum is dominated by emission lines, most of which are forbidden lines. An SN usually enters its nebular phase several months to about one year after the explosion, depending on the physical conditions of the ejecta. For SNe II that retain most of their hydrogen envelope before the explosion, the nebular phase usually starts later than their envelope-stripped counterparts (SN IIb/Ib/Ic).

The optically thin nature of the late-time ejecta allows for a non-biased view on the entire ejecta, especially sensitive to the innermost region. One can therefore obtain indications of the geometry, the mass, and the expansion velocity of the innermost core, using the same late-phase data. The width of an emission line, together with its profile, allows one to explore the velocity scale and the geometry of the emitting region. The absolute or relative strength of emission lines is also related to the mass, volume, and physical conditions of the emitting regions (Fransson & Chevalier 1989;Jerkstrand et al. 2015a; Jerkstrand 2017; Dessart et al. 2021).

The information thus obtained can be utilized to infer the properties of the progenitor and constrain the explosion mechanism.

In this work, we conduct a study on the properties of the emission lines, including the width, profile, and strength based on the so-far largest sample of SESN nebular spectra. In the sample, 88 spectra are collected from the literature, and 15 spectra are newly presented from the observations carried out with the Subaru Telescope from 2002 to 2012. In the present work, we focus on the forbidden line [O I] $\lambda\lambda$6300,6364, as it is one of the most luminous emission lines in the optical window of SESN nebular spectra. Further, oxygen is one of the most abundant elements in the ejecta of SESNe, and the [O I] dominates the emission from the CO core; the [O I] $\lambda\lambda$6300,6364 doublet is thus an ideal tool to trace the geometry of the ejecta and the properties of the progenitor.

This Chapter is organized as follows. In Section 2, the full sample, the data reduction methods, and the measurement of the observables are introduced. The latter includes the width and line profile of the [O I] $\lambda\lambda$6300,6364, and the line ratio [O I] $\lambda\lambda$6300,6364/[Ca II] $\lambda\lambda$7291,7323. In Section 3, we perform statistical analysis on the line profile. The statistics of the [O I]/ [Ca II] ratio as well as its correlations with other observables, including the [O I] width and the line profile, are presented in Section 4. Section 5 is devoted to the physical implications of the statistical results of Sections 3 and 4. The validity and the possible affecting factors of the measurements are discussed in Section 6. Finally, the conclusions are given in Section 7.

Section 2. Data set

Section 2.1. *Sample description*

The sample in this work includes the late-time spectra of 103 SESNe (26 SNe IIb, 31 SNe Ib, 32 SNe Ic, 9 SNe Ic-BL, and 5 SNe Ib/c), among which 15 objects are not published in the previous literature. The spectra are selected if the signal-to-noise level is acceptable, and the wavelength covers 6000–8000 Å so that the measurements in this work ([O I] and [Ca II]) are possible. The phases of the spectra are restricted to later than 100 days after the explosion or the peak luminosity (if the light curve is available). The objects that are decidedly nebular are also included, even if early-phase observations do not exist and the exact phase is unknown. If multiple nebular spectra are available for a specific object, we pick the one closest to 200 days. However, the quantities of interest in this work ([O I]/[Ca II] and the [O I] width) are not sensitive to the spectral phase within the range used here, so the effect of temporal evolution is generally negligible (see Maurer et al. 2010b and Fang et al. 2019 for the time evolutions of [O I] width and [O I]/[Ca II], respectively; see also the discussion in Section 6). The previously published spectra are collected from The Open Supernova Catalogue (Guillochon et al. 2017) and WiseRep (Yaron & Gal-Yam 2012). The full sample of this work is listed in Tables 4A.1 in Appendix A in this Chapter.

Section 2.2. *Data reduction*

For the new data set presented in this paper, the spectroscopic observations for the 15 SESNe were performed from MJD 52432 (2002 June 7) to MJD 56222 (2012 October 22) with the 8.2 m Subaru Telescope equipped with the Faint Object Camera and Spectrograph (FOCAS; Yoshida et al. 2000; Kashikawa et al. 2002). The typical instrumental setup is as follows: we used the 0.8" slit and the B300 (with no filter) and R300 (equipped with the O58 filter) grisms, or the 0.8" offset slit and the B300 grism equipped with the Y47 filter. The spectral resolution is ~500, or ~13 Å at 6300 Å. The log of the observations is listed in Table 4.1. The spectra are reduced following the standard procedures using IRAF[6] (Tody 1986, 1993), including bias subtraction, flat-fielding, sky subtraction, 1D spectral extraction wavelength calibration using ThAr or HeNeAr lamps and skylines, and cosmic-ray rejection using LAcosmic (van Dokkum 2001). Flux calibration is performed by using standard stars observed in the same night. The spectra are shown in Figure 4.1.

Object	Date (YY/MM/DD)	Instrument (grism/filter)	Exposure time (s)
2005bj	05/08/25	B300off/Y47	3 × 1200
2005aj	05/10/26	B300off/Y47	2 × 1200
2006G	06/06/30	B300off/Y47	1 × 1200
2006ep	06/12/24	B300off/Y47	1 × 1200
2007D	07/09/18	B300off/Y47	2 × 1500
2007ay	07/11/05	B300off/Y47	1 × 1200
2008fo	09/04/05	B300cen, R300cen/O58	1 × 1200
2008fd	09/07/23	B300cen, R300cen/O58	1 × 1200
2008hh	09/08/18	B300cen, R300cen/O58	2 × 1000
2008im	09/08/18	B300cen, R300cen/O58	2 × 720
2009C	09/10/26	B300cen, R300cen/O58	2 × 900
2009K	09/10/26	B300cen, R300cen/O58	2 × 900
2008ie	09/10/27	B300cen, R300cen/O58	4 × 1200
2009jy	10/05/06	B300cen, R300cen/O58	2 × 1200
2009ka	10/05/06	B300cen, R300cen/O58	1 × 900

Table 4.1. **Log of Spectroscopic Observations with FOCAS.**

[6] IRAF is distributed by the National Optical Astronomy Observatory, which is operated by the Association of Universities for Research in Astronomy, Inc., under cooperative agreement with the National Science Foundation. PyRAF is a product of the Space Telescope Science Institute, which is operated by AURA for NASA.

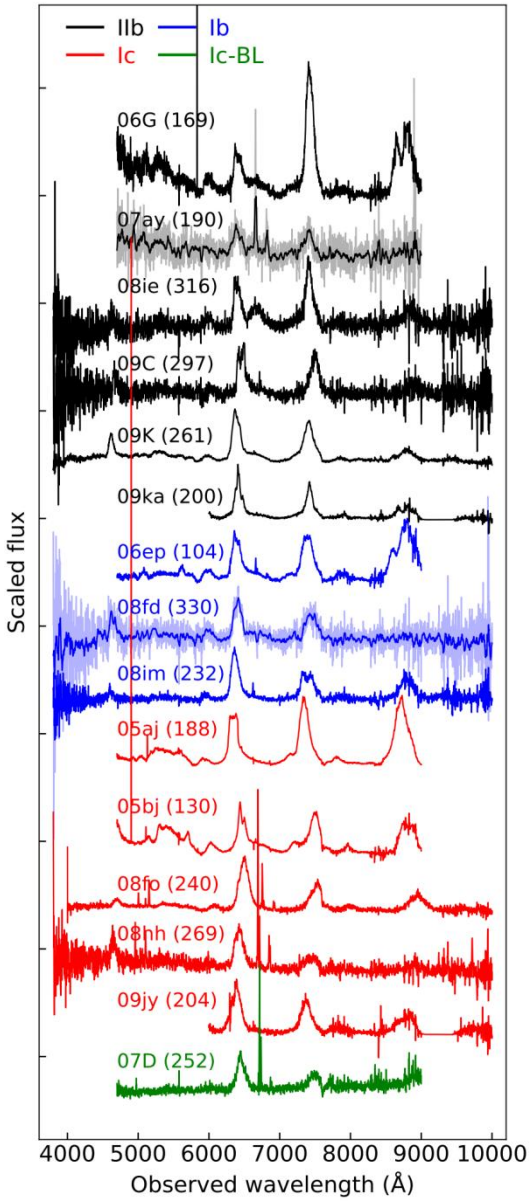

Figure 4.1. **The nebular spectra of the Subaru/FOCAS objects**. The fluxes of the spectra are first normalized, and then added by different constants for illustration. The objects are labeled by the last two digits of the discovery year and letter(s). The phase relative to the discovery date or light-curve maximum (if available) of each spectrum is listed in the parentheses (unit: days). SNe of different subtypes are plotted with different colors. SN2007ay and SN2008fd are smoothed for illustrative purposes.

Section 2.3. *Measurement of observables*

The goal of this work is to investigate the physical properties of the ejecta and the progenitors, by using a large data set of nebular spectra of SESNe. In this work, we are not attempting to fit the nebular spectra with full spectral modeling; instead, several observables are employed as the indicators of the physical properties of the ejecta or the progenitor, including the line ratio of [O I] λλ6300,6364 to [Ca II] λλ7291,7323, which is suggested to be related to the CO core mass, and thus the zero-age-main-sequence (ZAMS) mass of the

progenitor (see later discussion). Following Taubenberger et al. (2009), the line profile and the width of [O I] are utilized to probe the geometry and velocity scale of the ejecta.

The nebular spectra of SESNe are dominated by [O I] and [Ca II] emissions. Before measuring the observables, a nebular spectrum is de-reddened and corrected for redshift at the first step. The color excess $E(B-V)$ of the host galaxy and the Milky Way absorption are derived from previous literature (see the references in Tables 4A.1). For SNe without reported $E(B-V)$, the extinction is estimated from the equivalent width of Na ID absorption, using the relation derived from Turatto et al. (2003), if spectra around the light-curve peak are available. Otherwise $E(B-V)$ is set to be 0.36 mag, which is the average value for SN Ib/c by Drout et al. (2011). The spectra are then corrected for extinction by applying the Cardelli law (Cardelli et al. 1989), assuming $R_V = 3.1$.

The redshifts for most objects are inferred from the central wavelength of the narrow emissions from their explosion sites (Hα, [N II], etc.). If such narrow lines are absent in the spectrum, the redshift of the host galaxy from HyperLeda is adopted (Makarov et al. 2014).

The next step is to remove the underlying continuum emission. Following Fang et al. (2019), we first slightly smooth the spectra and find the local minimum at both sides of the [O I]/Hα-like structure (also [Ca II]/[Fe II]) complex. A line connecting the two minima is defined to be the local continuum emission and is then subtracted. Indeed, the continuum of nebular-phase SNe is not real continuum emission, but made of thousands of weak overlapping lines (Li & McCray 1996; Dessart et al. 2021). Subtracting the straight line defined above may result in some residual, which therefore affects the measurement. However, as long as all objects are treated with the same method, the effect of the residual on statistics will be negligible. After these two steps, we can start to measure the line ratios and [O I] profiles.

(1) [O I] and [Ca II]: The relative flux of [Ca II] is measured following the same procedure as in Fang et al. (2019). As for [O I], instead of fitting the [O I] with a double Gaussian function as illustrated in Fang et al. (2019), we assume the Hα-like structure located at the red side of [O I] is symmetric with respect to 6563 Å. Its profile is constructed by reflecting the red wing to the blue side with respect to 6363 Å, and the relative flux is then computed. The Hα-like structure is commonly seen in the nebular spectra of SNe IIb and some SNe Ib, and is identified as Hα or [N II] (Patat et al. 1995; Jerkstrand et al. 2015a; Fang & Maeda 2018). As will be discussed in Section 6, the measured line width is not sensitive to the assumed symmetric center; therefore, the exact identification of this line is not important for the purpose of this work. Given that the symmetric center of the [N II] doublets is close to 6563 Å, to avoid further complication, we assume the excess emission is symmetric with respect to 6563 Å. After the Hα-like complex is subtracted, the profile and the relative flux of [O I] can be determined.

(2) Line width of [O I]: The line width of [O I] is measured after the Hα-like structure is subtracted from the complex. We first define λ_c, such that the integrated fluxes at both sides are equal. We then find λ_{blue} and λ_{red}, where the integrated fluxes between $\lambda_{blue}...\lambda_c$ and $\lambda_c...\lambda_{red}$ take 34% of the total emission. The line width measured in this way defines 1σ if the [O I] profile is Gaussian. A detailed example of line width measurement is presented in Figure 4.2. Throughout this work, the blue width $\Delta\lambda_{blue}$ ($=\lambda_c - \lambda_{blue}$) is employed as the measurement of the line width, instead of using the half width $\Delta\lambda_{half}$ ($=0.5\times(\lambda_c - \lambda_{blue})$) or the red width

$\Delta\lambda_{red}$ ($\equiv\lambda_{red} - \lambda_c$). This is because $\Delta\lambda_{blue}$ is less affected by the subtraction process or the profile of the Hα-like structure. A detailed discussion is left to Section 6.

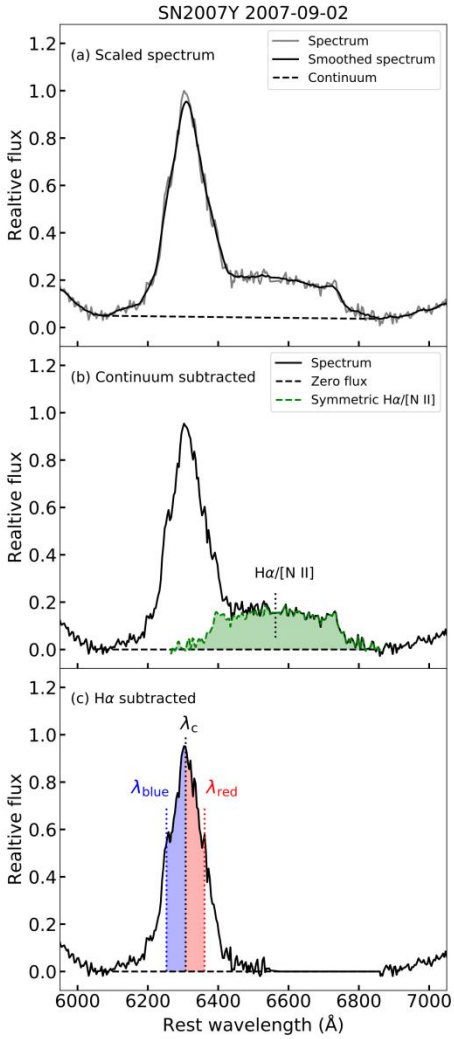

Figure 4.2. **A detailed example of observable measurement in Section 2.3.** The spectrum of SN2007Y is corrected for extinction and redshift, then multiplied by a constant for illustrative purposes. Upper panel: the spectrum is smoothed and the continuum level is determined as illustrated by the dashed line. Middle panel: the continuum is subtracted and the symmetric Hα-like structure is constructed. Lower panel: the Hα-like structure is subtracted. The line width is determined by $\lambda_c - \lambda_{blue}$.

The emission lines are broadened by the instrument. The measured line width can be corrected to account for the resolution of the instrument as

$$\Delta\lambda_{\text{intrinsic}} = \sqrt{\Delta\lambda^2_{\text{observed}} - \Delta\lambda^2_{\text{narrow}}}, \qquad (4.1)$$

where $\Delta\lambda_{intrinsic}$, $\Delta\lambda_{observed}$, and $\Delta_{\lambda narrow}$ are the intrinsic line width, observed line width, and the width of the narrow emission from the explosion site (Hα, [N II], etc.). Here, the width of the narrow emission reflects the instrumental broadening. According to the definition of $\Delta\lambda_{blue}$, the emission within this range takes 34% of the total flux, which is the same as 1σ if the line is Gaussian. Therefore the narrow Hα (from the explosion site) is fitted by a Gaussian function, and the derived variance σ is set to be $\Delta\lambda_{narrow}$. The narrow lines from the explosion site are absent for some objects in the sample. For these objects, the instrumental resolution is

derived from the source paper, which is usually measured from the FWHM of the sky line, and transformed to the Gaussian σ as

$$\sigma = \frac{\mathrm{FWHM}}{2\sqrt{2\ln 2}}. \qquad (4.2)$$

The average $\Delta\lambda_{narrow}$ is 4.02 Å, and the variation is 1.87 Å.

The uncertainties of the measurements are estimated using a Monte Carlo method. A nebular spectrum is slightly smoothed at the first step by convolving with a boxcar filter. The smoothed version of the spectrum is then subtracted from the original one. The standard deviation at the range of 6000–7800 Å of the residual flux is employed as the noise level of the spectrum. Ten-thousand simulated spectra are generated by adding noise on the smoothed spectrum. We further change the endpoints of the (continuum) background by the −25...25 Å range, which is assumed to be distributed uniformly with $\Delta\lambda = 1$ Å increments. The symmetry center of the Hα-like structure, initialized as 6563 Å, is also allowed to be shifted by −45...45 Å following the uniform distribution. The above measurements of the observables are then performed on the simulated spectra. Finally the measured line width is corrected for the effect of instrumental broadening. The 84% and 16% of the results of the 104 measurements are taken as the upper and lower limits of the observables, respectively.

In Figure 4.3, the measured line widths are compared with those of the previous works with overlapping objects. For the comparison work, we take the result of the one-component fit of Taubenberger et al. (2009), and the FWHM from the full spectral modeling of Maurer et al. (2010). The measurement of the line width in this work agrees well with Taubenberger et al. (2009), while it is systematically smaller than that in Maurer et al. (2010a); however, a correlation can still be discerned, and the systematic offset may simply be due to different definitions of the line velocity/width. The line width measurement in this work does not assume the geometry or the detailed physical conditions of the [O I] emitting region, and thus allows for more general discussion on the velocity scale and structure of the ejecta than previous works.

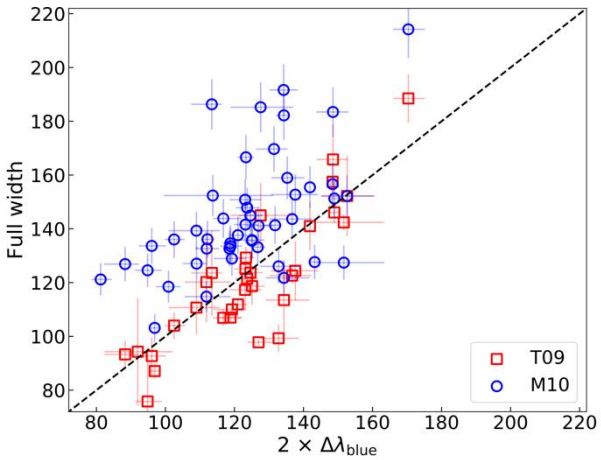

Figure 4.3. **A comparison between the line width measure in this work and previous works.** The red squares are for the FWHM from the one-component fit of Taubenberger et al. 2009 (hereafter T09). The blue circles represent the line widths transformed from the v_{50} in Maurer et al. 2010 (hereafter M10). The uncertainty is set to be 10%. The black dashed line is for one-to-one correspondence.

Section 2.4. *Fitting the [O I] λλ6300,6364*

After the background and the Hα-like structure are subtracted, the [O I] is fitted with multiple Gaussian profiles using the method described in Taubenberger et al. (2009). We define a single "doublet" component as two Gaussian functions with the same standard deviation, central wavelengths separated by 3000 km s^{-1} , and intensity ratio of 3:1, which is expected if the ejecta are optically thin. A single component has three parameters: the center wavelength λ_{peak}, the width σ, and the (scaled) intensity. The fitting procedure involves up to two components, and then we have five free parameters in total (note that one parameter is reduced since only the relative intensity matters).

The fitting starts from one component. If the residual exceeds the noise level, an additional component is introduced as follows. We first set four types of initial guesses: (1) two components red- and blue-shifted by 2000 km s^{-1} , with σ = 1000 km s^{-1} and the same intensity; (2) A broad component centered at zero velocity and σ = 2500 km s^{-1}, with a narrow component (σ = 500 km s^{-1}) centered at v = 0 km s^{-1} . The intensity of the narrow component is initialized to be 30% of the broad base; (3) Same as above, but with the narrow component centered at v = 2000 km s^{-1}; (4) Same as above, but with the narrow component centered at v = −2000 km s^{-1} . We then start the fitting with these initials guesses. For case (1), the two components are forced to be blue- and red-shifted by more than 1000 km s^{-1} (resolution R ~ 300), and the relative contribution of each component to the flux is forced to be >0.3; otherwise, it is considered unacceptable. For cases (2), (3), and (4), the center of the broad base is allowed to vary within −1600...600 km s^{-1} . Here the broad base is allowed to suffer from bulk blueshift up to 1000 km s^{-1} to account for the effect of residual opacity in the core of the ejecta (see Figure 3 of Taubenberger et al. 2009). The additional ± 600 km s^{-1} corresponds to a spectroscopic resolution of ~500. The result with the smallest residual is taken to be the final result.

According to the results, the line profifiles are classifified into four classes: Gaussian, narrow core, double-peaked, and asymmetric (hereafter GS, NC, DP, and AS, respectively). In the following, the definitions and the physical implications of the line profiles are briefly summarized. The readers may refer to Taubenberger et al. (2009) for more details. In Section 5.1, we will further discuss the expected profiles from a specific bipolar-type explosion, given as an example in the list below. Some examples of the line profiles are shown in Figure 4.4.

(1) Gaussian (GS): The line can be well fitted by one component. The emitter is expected to originate from the Gaussian distribution in the radial direction of a spherically symmetric ejecta. While there is no need to introduce deviation from spherical symmetry to explain the GS profile, it does not reject a possible asphericity; for example, a bipolar-type explosion (with the torus-like distribution of oxygen) viewed from the intermediate angle also results in a similar profile.

(2) Narrow core (NC): The line can be fitted by two components: a broad base and a narrow additional one with very close center wavelengths (in this work, it is defined to be offset <1000 km s−1)[7]. A

[7] In Taubenberger et al. (2009), the narrow core is defined to have the narrow component with offset <1000 km s^{-1} with respect to the rest wavelength. Such offset can also be the result of residual opacity, which will affect both broad and narrow components, rather than pure geometrical effect. We therefore employ offset relative to the center of the broad base as the criterion for the narrow core.

straightforward interpretation is the emission from spherically symmetric ejecta with an enhanced core density. The axisymemtric configuration as described above but viewed from the polar direction (perpendicular to the O-rich torus) can also produce a similar profile. Indeed, the profile simply requires that there is a massive O-rich component with a negligible velocity along the line of sight, and thus even a single massive blob moving perpendicular to the line of sight is not rejected.

(3) Double-peaked (DP): The line can be well fitted by two components with similar intensities, one blue-shifted and the other red-shifted by similar amounts (case (1) in the above text). If interpreted simply as a geometrical effect, this profile is not reproduced under the assumption of spherical symmetry, and requires two components having the symmetry in the line-of-sight velocity distribution. A simple configuration leading to this profile is the axisymmetric explosion mentioned above but viewed from the edge of the torus.

(4) Asymmetry (AS): The line can be fitted by a broad component accompanied by an additional component with arbitrary width and shift of the center wavelength. This again requires a deviation from a pure sphericallysymmetric ejecta, pointing to the existence of a single dominating blob corresponding to the narrow component, in addition to the bulk distribution representing the broad component. It should be noted that the only difference between NC and AS is the relative shift of the narrow component. Whether NC/AS are distinct populations is not clear. See the statistic results in Sections 3.1 and 6.3.

Most of the objects in the sample can be well fitted by the method applied in this work (see Figures 4B.1 to 4B.4 in Appendix B), although some objects, e.g., SN 2006ld and SN 2008aq, possibly require more complicated ejecta geometry.

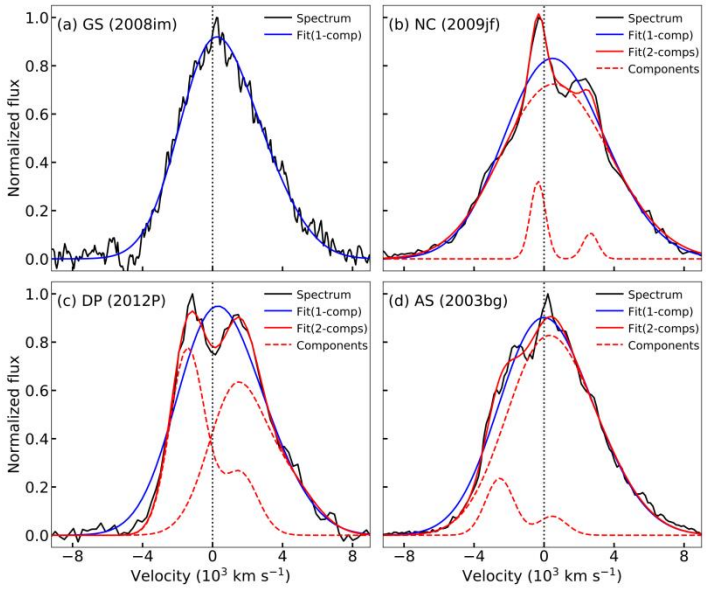

Figure 4.4. **Examples of the four line profiles.** Before the fitting procedure, the spectra are subtracted by the background and the symmetric Hα-like profile as described in the text. The red solid line is the result of the two components fit, and the red dashed lines are the corresponding components. The blue solid line represents the one component fit, and is also plotted in panels (b), (c), and (d) for comparison. In this work, we use the same classification scheme as Taubenberger et al. (2009).

Section 3. Statistics of the [O I] profile

The profile of the emission line is a useful tracer of the geometry of the ejecta (e.g., Taubenberger et al. 2009). Although it is not possible to recover the full 3D distribution of the emitter, the measurement in this work can still provide some information on any possible deviation from spherical symmetry. The classifications of [O I] line profiles are listed in Tables 4A.1.

Section 3.1. *Quantitative classification*

To quantify the difference between the classifications, for objects fitted by two components ($N = 82$), in Figure 4.5, the fractional flux of the secondary component α_w, which is defined to be the component with the smaller flux, is plotted against the absolute central wavelengths offset between the two components. Similarly to Figure 6 of Taubenberger et al. (2009), objects of different line profile classes, by definition, occupy different regions in the plot and are well separated. NC objects are characterized by a narrow strip located in the lower-left region ($\alpha w < 0.4$, $|\lambda_1 - \lambda_2| < 1000$ km s^{-1}). The DP and AS objects have wider central wavelength separation, and are separated at $\alpha_w \sim 0.3$. It should be emphasized that the boundary between NC and AS is changeable. In this work, we choose the same criterion as Taubenberger et al. (2009), i.e., offset = 1000 km s^{-1} (~22 Å). Moreover, the uncertainty of the fitting allows some objects, especially those near the boundary, to be reclassified to the other category. Objects with non-negligible probability (>0.05) of shifting to the other category are labeled by filled markers in Figure 4.5. According to the classification of Taubenberger et al. (2009), objects with narrow component shifts smaller (or larger) than 1000 km s^{-1} are classified as NC (or AS). However, as shown in Figure 4.5, the narrow component shift has a continuous distribution, and it is questionable whether NC and AS are two distinct populations. A more detailed discussion on the classification of NC/AS is left to Section 6.3.

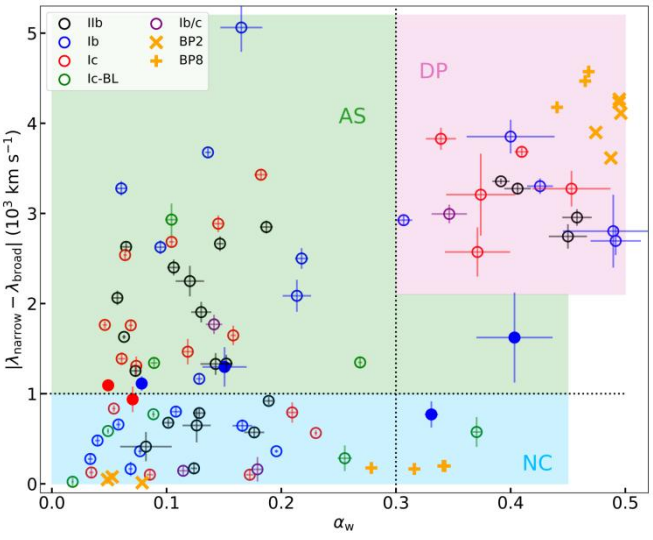

Figure 4.5. **The fractional flux of the secondary component is plotted against the central wavelength's separation.** Different [O I] profile classes are well separated by $\alpha_w = 0.3$ and $|\lambda 1 - \lambda 2| = 1000$ km s−1 (the dotted lines). Objects of different profile classes are labeled by different colors and markers. BP2 and BP8 are the bipolar explosion models in Maeda et al. (2008) with different degrees of axisymmetry. We apply the same fitting procedure as described in Section 2.4 to the theoretical spectra. See Section 5.1 for detailed descriptions on the BP models.

Section 3.2. *Statistical evaluation*

The fractions of the line profiles are shown in Table 4.2. In the sample of this work, the fractions of GS, NC, DP, and AS objects are: 0.20 ($N = 21$), 0.29 ($N = 30$), 0.16 ($N = 16$), and 0.35 ($N = 36$), respectively. The large fraction of AS/DP objects suggests that the deviation from spherical symmetry is common for the ejecta of SESNe. These two categories require the deviation from spherical symmetry, and thus place a lower limit of ~50% on SESNe having non-spherical ejecta (note that the other two categories, GS/NC, can be explained by, but do not require, spherically symmetric ejecta; Section 2.4). This finding is consistent with previous studies (Maeda et al. 2008; Modjaz et al. 2008; Taubenberger et al. 2009; Milisavljevic et al. 2010). The line profile fractions are generally in good agreement with the results of Taubenberger et al. (2009). Given that the fractions show no significant variation after the sample is enlarged by a factor of 2.5 (39 objects in Taubenberger et al. 2009 and 103 objects in this work), we conclude that the distribution of [O I] profiles, which is directly linked to the ejecta geometry, is already statistically well determined, and can be a potential constraint on the explosion mechanism.

The distributions of the line profiles of different SN subtypes, along with the full sample for comparison, are shown in Figure 2.6. In general, the line profile distributions of the canonical SESNe (IIb/Ib/Ic) are quite similar to each other. The uncertainties of the fractions of different line profiles in different SN subtypes are estimated by a bootstrap-based Monte Carlo method. We run 10^4 simulations. In each trial, the SNe sample is resampled with replacement. For NC and AS objects, the probability of reclassification into the other category is also included (see Section 3.1). The fractions of different line profiles of the new sample and the different SN subtypes are then calculated. The 16% and 84% levels of the 10^4 trials are employed as the lower and upper limits of the line profile fractions, respectively.

Taubenberger et al. (2009) suggested the objects with an extended envelope tend to be more aspherical, as the SNe Ib in their sample mainly belong to the AS category. The results in this work do not support their finding. Although the fraction of AS objects in the SNe IIb sample is slightly larger than the average, we find no significant difference in the line profile distributions among SNe IIb/Ib/Ic. The similarity likely indicates a limited effect of the presence of the helium layer or the residual hydrogen envelope on the ejecta geometry. For each subtype, at least 50% (and likely more) of the objects can not be interpreted by the spherical symmetric ejecta, and such deviation is commonly seen for all types of canonical SESNe.

Types	Full	IIb	Ib	Ic	Ic-BL	Ib/c
GS	0.20	0.12	0.23	0.28	0.11	0.20
NC	0.29	0.27	0.29	0.22	0.56	0.40
DP	0.16	0.15	0.16	0.16	0.00	0.20
AS	0.35	0.46	0.32	0.34	0.34	0.20

Table 4.2. **The fractions of different line profiles among different SN subtypes.**

Some differences of SNe Ic-BL when compared with the average behavior can be discerned: (1) large fraction of NC objects, and (2) lack of DP objects. However, in this work, the number of SNe Ic-BL is small ($N = 9$). The lack of DP objects can be the result of small-sample statistics. We therefore need to estimate the upper

limit of the intrinsic DP fraction above which the non-detection is statistically significant. For this purpose, we run 10^4 simulations. In each trial, the GS, NC, and AS fractions (f_{GS}, f_{NC}, and f_{AS}) are randomly drawn from the full sample with the bootstrap-based Monte Carlo method introduced above. The intrinsic DP fraction f_{DP} is varied from 0 to 0.2, with the ratio of f_{GS}, f_{NC}, and f_{AS} kept fixed. For the fixed f_{DP}, 10^3 samples (size $N = 9$) are generated according to the current line profile distribution. The rate of the samples with DP detected is then calculated. The relation between the intrinsic DP fraction and the detection probability are shown by the green dashed line in Figure 4.6(e). The shaded region is the 95% confidence interval (CI) of the 10^4 simulations. When $f_{DP} = 0$, no DP object can be detected in all trials by definition. As f_{DP} increases, the probability of detection increases as expected. The upper limit of f_{DP} is defined to be the value such that detection probability $p_{detect} = 0.68$ (or non-detection probability = 0.32). This 1σ upper limit ranges from 0.112 to 0.126 (mean value = 0.119), as indicated by the vertical dotted lines in Figure 4.6(e). The conservative value 0.126 is employed as the upper limit of the DP fraction of SNe Ic-BL, which is still smaller then the DP fraction (0.155) of the full sample, but slightly larger than its lower limit (0.120). Therefore, there is an indication, at a confidence level of about 1σ, that the lack of double-peaked SNe Ic-BL is an intrinsic feature rather than statistical effect. A hint that the distribution of the line profiles of SNe Ic-BL is different from those of the canonical SESNe can thus be discerned, which suggests a difference in ejecta geometry. From early-phase observation, SNe Ic-BL are already found to be distinct from other SESNe with their extreme nature. The finding in this work further extends such distinction in the nebular phase.

The full sample is large enough for statistical evaluation. However, the size of each SNe subtype is still limited, especially lacking SNe Ic-BL. Inferences made based on the fractions of small samples are uncertain (Park et al. 2006). To reliably investigate the dependence of the line profiles on SNe subtypes, an even larger sample is required.

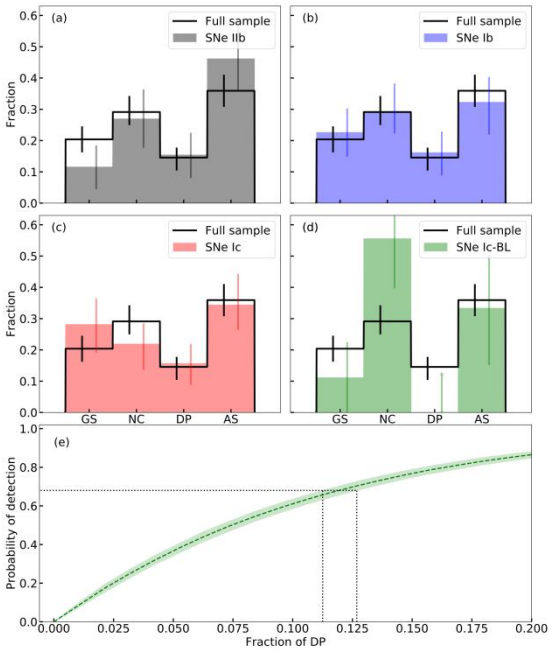

Figure 4.6. **(a)–(d) The distributions of the [O I] profile of different SN subtypes,** which are shown in different colors and panels. The histogram plotted by the black solid line is the distribution of the full sample. The error bars are estimated by the bootstrap Monte Carlo method described in the main text. The 1σ upper limit of the DP fraction of SNe Ic-BL is marked by the arrow in panel (d). **In panel (e), the probability for DP detection as a function of intrinsic DP fraction for SNe Ic-BL is shown.** The shaded region represents the 95% CI. The vertical dotted lines mark the range of f_{DP} such that the probability of detection is equal to 0.68.

Section 4. [O I]/[Ca II] ratio and [O I] width

The individual measurements of the [O I]/[Ca II] ratio and the [O I] width $\Delta\lambda_{blue}$ for each object in the sample is plotted in Figure 4.7(a). The cumulative distributions of these two quantities are plotted in panels (b) and (c), respectively, where the objects of different SN subtypes are labeled by different colors, and the cumulative fraction of the full sample is labeled by the black dashed line. Objects of different line profile classes (i.e., GS, NC, DP, and AS; see the previous section for details) are discernible by different markers.

Section 4.1. *Statistical evaluation*

Similarly to the result in Fang et al. (2019), for [O I]/[Ca II], an increasing sequence is discerned: SNe IIb/Ib → SNe Ic → SNe Ic-BL. Although compared with the results in Fang et al. (2019), SNe Ib seem to have slightly larger average [O I]/ [Ca II] ratios than SNe IIb, still the hypotheses that the SNe IIb/Ib have the same [O I]/[Ca II] distribution can not be rejected at the significance level $p > 0.25$, based on the two-sample Anderson–Darling (AD) test. For SNe Ic, the difference is significant when compared with He-rich objects (SNe IIb + Ib), with $p < 0.001$. Similarly, the [O I]/[Ca II] of SNe Ic-BL is significantly larger than SNe IIb/Ib ($p < 0.001$ when compared with both IIb and Ib), but the distribution is indistinguishable from SNe Ic ($p \approx 0.23$). These findings are consistent with Fang et al. (2019).

From Figure 4.7(c), a possible [O I] width sequence is also discerned: SNe IIb → SNe Ib → SNe Ic → SNe Ic-BL. Unlike the case of [O I]/[Ca II], the differences between SNe IIb/Ib/Ic are significant, showing an increasing trend ($p \approx 0.09$ for SNe IIb versus SNe Ib and $p \approx 0.04$ for SNe Ib versus SNe Ic). While SNe IIb and SNe Ic are limited to a narrow range, occupying the low and high ends of $\Delta\lambda_{blue}$, respectively, the range of the [O I] width of SNe Ib is rather large.

In the early-phase spectra, the SNe Ic-BL show evidence of fast-expanding ejecta. The average photospheric velocity of SNe Ic-BL, measured near light-curve peak, is about 20,000 km s^{-1} , much larger than that of the canonical SNe (<10,000 km s^{-1} ; see Lyman et al. 2016). Surprisingly, the [O I] width distribution of SNe Ic-BL is not statistically different from normal SNe Ic. The null hypothesis can be rejected only at the significance level $p \approx 0.21$ from the AD test when compared with SNe Ic. The AD significance level p reduces to 0.012 when the [O I] width distribution of SNe Ic-BL is compared with the canonical SNe (IIb + Ib + Ic). If the [O I] width is transformed to velocity as

$$\frac{\Delta\lambda_{\rm blue}}{6300\ \text{Å}} = \frac{v}{c}, \qquad (4.3)$$

the average velocity of SNe Ic-BL is about 3300 km s^{-1}, slightly larger than that of the canonical SNe (about 2900 km s^{-1}) and SNe Ic (about 3100 km s^{-1}). The difference of the velocity scales of the innermost ejecta between SNe Ic-BL and the canonical objects is not as striking as the photospheric velocities around the light-curve peak, which measure the expansion velocities of the outermost ejecta.

For both [O I]/[Ca II] and [O I] width, it is clear from Figures 4.7(b) and (c) that SNe IIb/Ib are lower than the average (black dashed line), while SNe Ic and Ic-BL are higher. The above discussions are summarized in Figure 4.8.

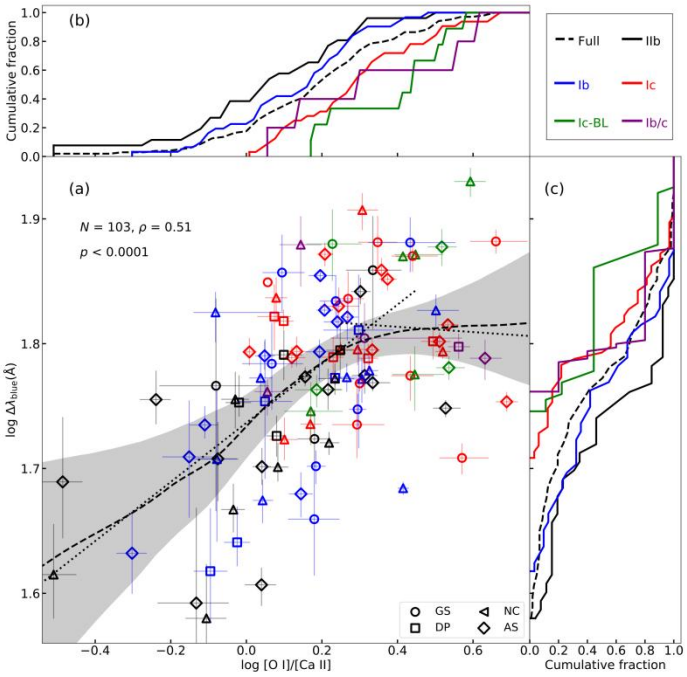

Figure 4.7. (a) **The relation between the [O I]/[Ca II] ratio and the [O I] width $\Delta\lambda_{blue}$.** SESNe of different SN subtypes and line profile classes are labeled by different colors and markers. The black dashed line is the result of the local non-parametric regression for the full sample, and the shaded region represents the 95% CI. The black dotted lines are the results of the linear regression performed for the objects with log [O I]/[Ca II] < 0.4 and log [O I]/[Ca II] > 0.4, respectively. (b) **Cumulative fraction of the [O I]/[Ca II] ratio**. (c) **Cumulative fraction of the [O I] width $\Delta\lambda_{blue}$.**

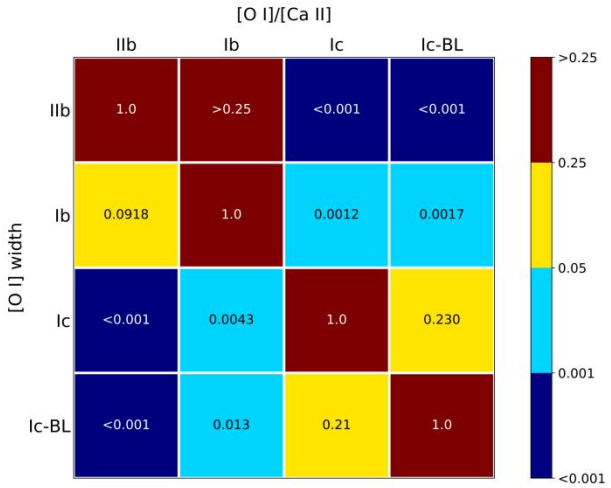

Figure 4.8. **Matrix of AD test significance level when the [O I]/[Ca II] and [O I] width distributions of different SN subtypes are compared.** The upper-right region is for the [O I]/[Ca II] ratio, and the lower-left region is for the [O I] width $\Delta\lambda_{blue}$. The color bar indicates the probability that the samples are drawn from the same distribution, and the blue end indicates significant differences.

Section 4.2. *[O I]/[Ca II]-[O I] width correlation*

In Figure 4.7(a), the [O I]/[Ca II] ratio is plotted against the [O I] width for comparison. The objects with small [O I]/[Ca II] tend to have narrow [O I]. The two quantities are moderately correlated (Spearman correlation coefficient $\rho = 0.51$), and the correlation is significant, with $p < 0.0001$ for the sample size of

103 objects.

To further investigate the dependence of the [O I] width on the [O I]/[Ca II] ratio, in Figure 4.7, the local non-parametric regression is performed to the full sample (black dashed line). To estimate the uncertainties, we run 10^4 simulations. In each trial, the sample is resampled with replacement, and for each object in the new sample, its [O I]/[Ca II] ratio and the [O I] width are added by the errors, which are assumed to follow Gaussian distribution. Then local non-parametric regression is applied to the new sample. The 97.5% and 2.5% percentages of the results from 10^4 simulations are defined to be the boundaries of the 95% CI of the regression, as labeled by the gray shaded region in Figure 4.7.

The linear regression is performed to the full sample, because analytical form could be useful for further study. The best-fit result gives

$$\log_{10}\frac{\Delta\lambda_{\rm blue}}{\text{Å}} = (0.16 \pm 0.03) \times \log_{10}\frac{\text{[O I]}}{\text{[Ca II]}} + (1.74 \pm 0.01). \qquad (4.4)$$

From the result of local non-parametric regression, the increasing tendency stops at roughly log[O I]/[Ca II] = 0.4 (or [O I]/[Ca II] = 2.5). If the line regression analysis is restricted to the objects with log[O I]/[Ca II] < 0.4 (N = 82), the correlation becomes significant with ρ = 0.56 and p < 0.0001. For objects with log[O I]/[Ca II] < 0.4, the best linear regression gives

$$\log_{10}\frac{\Delta\lambda_{\rm blue}}{\text{Å}} = (0.22 \pm 0.04) \times \log_{10}\frac{\text{[O I]}}{\text{[Ca II]}} + (1.74 \pm 0.01), \qquad (4.5)$$

while for the rest (log[O I]/[Ca II] > 0.4, N = 21), ρ reduces to −0.07 and p < 0.77, indicating no correlation exists. For this range,

$$\log_{10}\frac{\Delta\lambda_{\rm blue}}{\text{Å}} = (-0.02 \pm 0.14) \times \log_{10}\frac{\text{[O I]}}{\text{[Ca II]}} + (1.82 \pm 0.09). \qquad (4.6)$$

The significance of the correlation between [O I]/[Ca II] and [O I] width may be affected by SN subtypes and line profile classes as follows:

(1) SN sub type: Objects of different SN subtypes (labeled by different colors) behave differently in Figure 4.9. It is clear that the helium-rich objects (SNe IIb + Ib) show an increasing tendency (ρ = 0.53, p < 0.0001). The local non-parametric regression technique is applied to the helium-rich SNe, with the same bootstrap-based uncertainties introduced above. The result and the 95% CI are shown by the blue dashed line and the blue shaded region in Figure 4.9. However, the [O I] width of the helium-deficient SNe (SNe Ic + Ic-BL) remains (almost) constant as [O I]/[Ca II] increases, showing large scatter, and no correlation can be discerned (ρ = 0.10, p < 0.54). This is consistent with the result of the local non-parametric regression, as shown by the red dashed line and the red shaded region (95% CI) in Figure 4.9.

(2) Line profile: The [O I]/[Ca II]-[O I] width correlation separately shown for different line-profile classes is plotted in Figure 4.10. The NC objects have the tightest correlation (ρ = 0.60 with p < 0.0006), followed by DP and AS (ρ = 0.58 and 0.54, with p < 0.0238 and 0.0005, respectively). For GS objects, the correlation is weak and not significant (ρ = 0.34 with p < 0.1297).

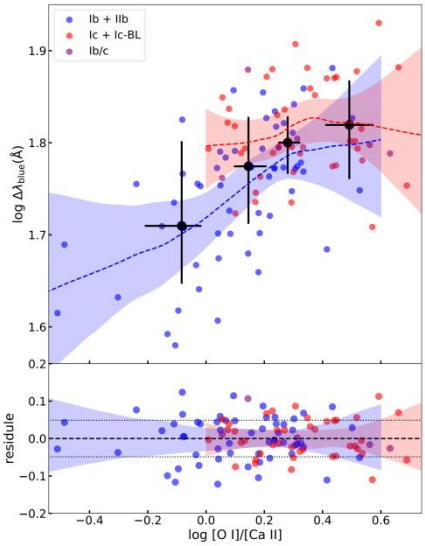

Figure 4.9. **Upper panel: the relation between the [O I]/[Ca II] ratio and the [O I] width $\Delta\lambda_{blue}$**, with SNe of different origins (He star and CO core) labeled by different colors. The 103 objects are divided into five groups (~20 objects in each group) according to the range of the [O I]/[Ca II] ratio, and the black dots represent the mean value of each group. The blue dashed line is the result of the local non-parametric regression to helium-rich SNe (IIb + Ib), and the red dashed line is for helium-deficient SNe (Ic + Ic-BL). The shaded regions are the 95% CI (see the main text for details). A clear increasing trend can be discerned. **Lower panel: the residual of the fitting**. The dotted lines represent the standard deviation of the residual, which is about 0.06 dex (~15% in linear scale).

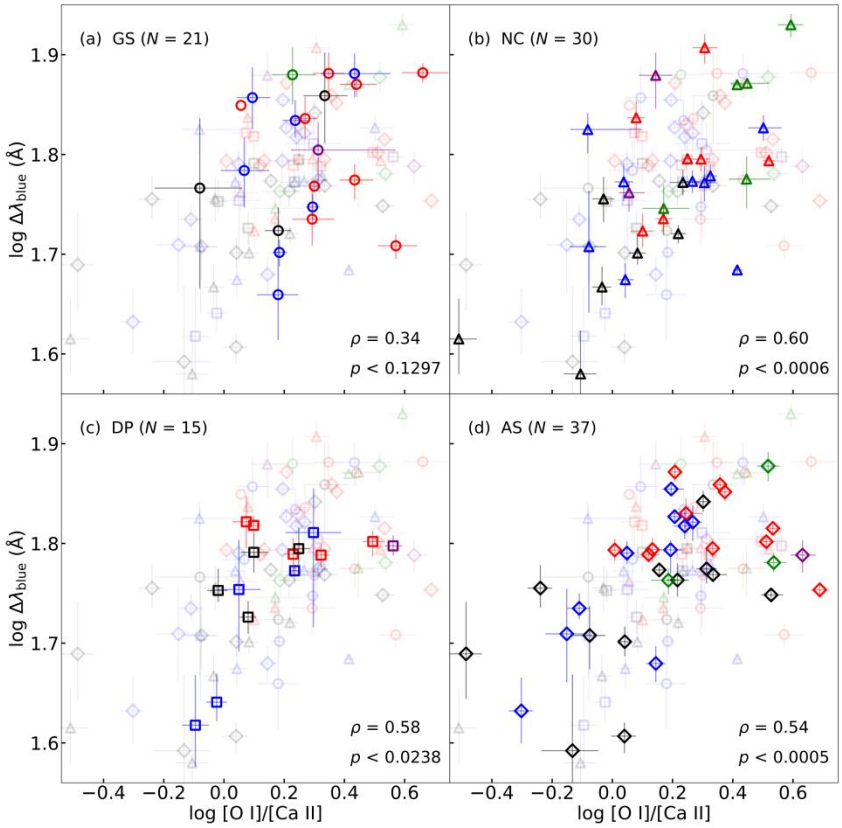

Figure 4.10. **The correlations between the [O I]/[Ca II] ratio and [O I] width of different line-profile classes**, and the comparison with other line profiles, are plotted in different panels. The meanings of the different colors and markers are the same as in Figure 4.7.

	Spearman ρ	*p*
log [O I/[Ca II]		
> 0.4	0.56	<0.0001
< 0.4	-0.07	0.7706
Line profiles		
GS	0.34	0.1297
NC	0.60	0.0006
DP	0.58	0.0238
AS	0.54	0.0005
GS + NC	0.56	< 0.0001
DP + AS	0.50	0.0003
SN subtype		
IIb	0.67	0.0002
Ib	0.48	0.0064
IIb + Ib	0.58	< 0.0001
Ic	0.02	0.8948
Ic-BL	0.56	0.1108
Ic + Ic-BL	0.14	0.3862

Table 4.3. **Factors that would affect the [O I]/[Ca II]-[O I] width correlation.**

Section 4.3. *[O I]/[Ca II] and line profiles*

The cumulative fractions of [O I]/[Ca II] in terms of the line profiles are shown in the upper panel of Figure 4.11. The GS objects tend to have the largest [O I]/[Ca II] on average, followed by NC/AS, then DP. However, such difference is not significant, possibly except for the difference between DP and GS, where the null hypothesis can be rejected at a significance level $p \approx 0.08$ from the AD test. The distributions of the AS and NC objects are remarkably similar, and the [O I]/[Ca II] distributions of all line profiles are indistinguishable from the average ($p > 0.25$ from the AD test).

To investigate how the distributions of the line profiles change as the [O I]/[Ca II] ratio increases, the full sample is binned into five groups with equal numbers of members ($N = 20$ or 21) according to the [O I]/[Ca II]. In each group, the fraction of each line profile is calculated. The results are plotted by the colored solid lines in the lower panel of Figure 4.11.

It is clear that there is a systematic trend where the fraction of GS objects increases as the [O I]/[Ca II] ratio increases, and then becomes saturated at log [O I]/[Ca II] ~ 0.3 ($\rho = 0.82$, $p < 0.09$). For DP objects, the trend goes to the opposite direction ($\rho = -0.82$, $p < 0.06$). Another interesting feature is he fractions of NC and AS objects are fluctuating around 0.3, and no significant dependence on [O I]/[Ca II] can be discerned ($\rho = -0.41$, $p < 0.49$ for NC and $\rho = -0.40$, $p < 0.51$ for AS).

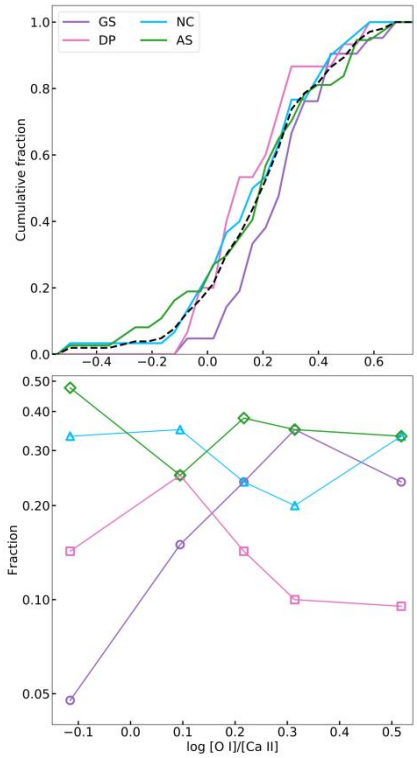

Figure 4.11. **Upper panel: the cumulative fractions of log [O I]/[Ca II] of the objects with different line profiles**. The black dashed line is the distribution of the full sample. **Lower panel: the fractions of line profile as functions of log [O I]/[Ca II] are plotted by different colored solid lines and different markers**.

Section 5. Physical implications

In Sections 3 and 4, the statistical properties of the [O I] profile, the [O I]/[Ca II] ratio, and the [O I] width $\Delta\lambda_{blue}$, along with their mutual relations, were investigated. In this section, the possible physical implications behind the statistics are discussed.

Section 5.1. Constraint on the ejecta geometry

As introduced in Section 2.4, different ejecta geometry will lead to different line profiles. To further constrain the configuration of the ejecta, it is useful to compare the observational data with some models. For this purpose, a specific bipolar explosion model(s) from Maeda et al. (2006) is employed, as this model has been frequently referred to in previous works to study the ejecta kinematics through the [O I] profile. Note that the model prediction should not be over-interpreted, given various assumptions under which the model is constructed. For example, the models are assumed to be perfectly axisymmetric, and the two hemispheres are symmetric, which are probably too simplified. Indeed, both the consistency and the inconsistency between the data and the model are important; the latter will be useful to clarify which components are still missing in the model, by investigating which assumption is a potential cause of the inconsistency.

To compare the observational data to the theoretical predictions, the multi-Gaussian fit procedure is applied to the synthetic spectra of the bipolar explosion models (Maeda et al. 2006) in the same way as it was applied to the observational data. In this model sequence, oxygen-rich materials are distributed in a torus-like structure surrounding the bipolar jets that convert the stellar material (e.g., oxygen) into the Fe-peak elements (Maeda et al. 2002, 2006, 2008; Maeda & Nomoto 2003). The [O I] profiles of the models depend on the degree of asphericity and the viewing angle. In this work, two representative models in Maeda et al. (2006), the mildly aspherical model (BP2) and the extremely aspherical one (BP8), are employed.

A basic assumption of the SN ejecta kinematic is homologous expansion, i.e., $V(r, t) = r/t$, where $V(r, t)$ is the velocity of the point located at radial coordinate r at time t. For a photon emitted from r, the Doppler shift of its wavelength is $\Delta\lambda = -\lambda_0(v_r/c)$, where λ_0 is the intrinsic wavelength and v_r is the line-of-sight velocity toward the observer. For the homologously expanding ejecta, $\Delta\lambda \propto d$, where d is the projection of r onto the direction of the line of sight. At late phases, the photons emitted from the same plane, which is perpendicular to the line of sight, have the same observed wavelength. The line profile therefore provides the "scan" of the integrated emissions on these planes. The readers may refer to Maeda et al. (2008) and Jerkstrand (2017) for more detailed discussions on the formation of the nebular line profile.

For the BP models, the O-rich material is distributed in a torus. When the ejecta is viewed from the edge-on direction, the integrated emission on the scan plane increases as it moves from the outer edge toward the inner edge of the hole, then decreases as it moves further to the center, where the integrated emission reaches its minimum. The [O I] is therefore expected to have a horn-like profile. If the ejecta is viewed from the axial direction, i.e., along the jet, the integrated emission monotonically increases as the scan plane moves toward the center. Most of the O-rich materials are distributed on the equatorial plane, and therefore contribute to the flux at $v \approx 0$ km s^{-1}, giving rise to the narrow-core [O I] profile.

Applying the same multi-Gaussian fit procedure, the [O I] of the extremely aspherical model (BP8) is classified into the NC and DP profiles if the viewing angles from the jet axis are 0°– 30° and 70°–90°, respectively. For the mildly aspherical model (BP2), the corresponding viewing angles change to 0°–20° and 50°–90°. Some examples of the fitting results are shown in Figure 4.12. If the viewing angles are just randomly distributed without any preference, the fractions of different line profiles can be estimated by

$$f = \frac{1}{2\pi}\int_{\theta_0}^{\theta_1} \sin\theta \mathrm{d}\theta, \qquad (4.7)$$

where θ_0 and θ_1 are the lower and upper limits of the viewing angle described above. The occurrence rates of the DP objects for the bipolar explosion are 34% (BP8) and 68% (BP2). Using the same method, the corresponding NC fractions are 13% and 6%. The results are summarized in Table 4.4.

It should be noted that the assumption of randomly distributed viewing angle may not be valid for SNe Ic-BL, as these events are frequently accompanied by the occurrence of GRBs and may favor the axial direction. However, the number of these events is small in this sample ($N = 9$ out of 103). The following analysis will be restricted to the canonical SESNe (SNe Ic-BL excluded), and SNe Ic-BL will be discussed separately.
The line profile fractions of canonical SESNe are: 21% (GS), 27% (NC), 16% (DP), and 36% (AS). Based on the bipolar explosion models, the observed fraction of DP objects suggests that the fraction of the bipolar supernovae is ~25% (BP2) to 48% (BP8), if the sample is assumed to be unbiased in orientation and all of the DP objects are originated from the oxygen-rich torus viewed from the edge-on direction. The relatively low fraction of bipolar supernovae also implies that most of the NC objects can not be interpreted by the same configuration but viewed axially. Using the estimated occurrence rates of the NC objects (6% and 13% for BP2 and BP8), the expected NC fraction arising from this configuration is only about 1.5% (BP2) to 6.2% (BP8) of the full canonical SESNe sample, much less than the observed NC fraction (27%). Therefore more than ~80% of the NC objects can not be interpreted by the bipolar explosion. This may leave a massive oxygen blob moving perpendicular to the line of sight or the enhanced core density as more plausible scenarios.

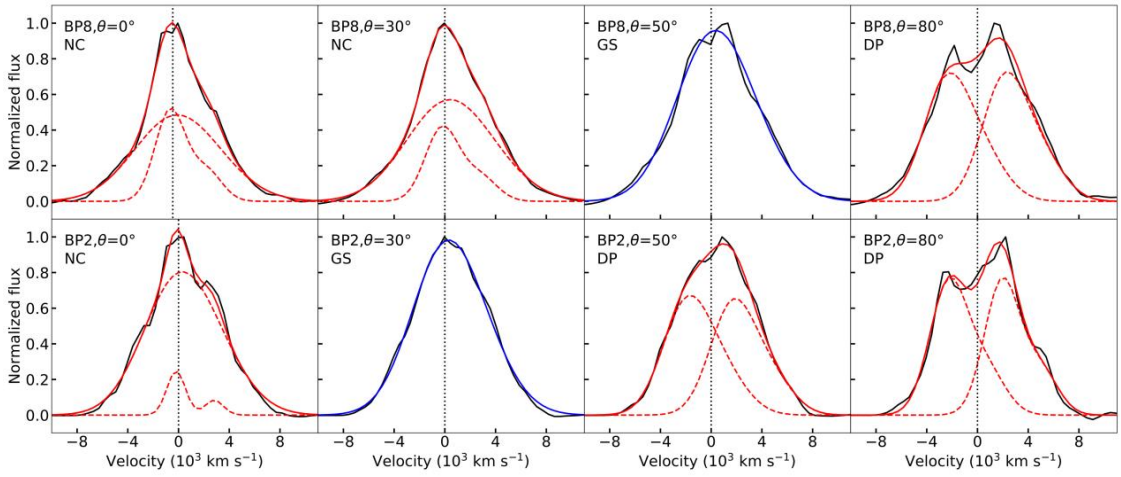

Figure 4.12. **The fitting results of the bipolar explosion models with different degrees of axisymmetry and different viewing angles from the direction of the poles.** The black solid lines are the model spectra. The blue and red solid lines are the results of one-component and two-component fits. The red dashed lines are the corresponding components. The spectra are plotted in velocity space. The dotted vertical lines represent zero velocity (6300 Å).

		BP2	BP8
NC	Angle[8]	≦20°	≦30°
	Fraction	0.06	0.13
	[O I] width scatter	0.003	0.004
GS	Angle	30°...40°	40°...60°
	Fraction	0.30	0.53
	[O I] width scatter	0.050	0.014
DP	Angle	50°≦	70°≦
	Fraction	0.64	0.34
	[O I] width scatter	0.012	0.004

Table 4.4. **Properties of the BP2 and BP8 models.**

However, as stated above, the model should not be over-interpreted. The classification of the model [O I] profiles into the NC and GS categories is one issue; this is very sensitive to the detailed density distribution, which might be affected by the details of the model construction (e.g., the treatment of the boundary condition in the explosion model). Conservatively, we may thus consider a combination of the NC and GS profiles as the "single-peak" category. If we allow this combined classification, then the single-peak fraction expected in the model is 36% (BP2) to 66% (BP8). Taking into account the fraction of the bipolar model as constrained by the BP fraction (i.e., 26% in BP2 or 50% in BP8), the expected fraction of the single-peak objects is ~9.4% (BP2) or 33% (BP8). The fraction of the single-peak objects in the canonical SESNe sample is 48%, and thus the bipolar configuration can explain up to 70% of the NC/GS objects in this case.

Another issue is the classification of the AS and DP profiles as individual classes, for the following two reasons: (1) the classification of the AS and DP objects in the fitting procedure is not very strict, and for some objects, the classification is found to be interchangeable (see Section 6.3 for further discussion); (2) There is indeed no "AS" profile predicted in the model, and this stems from the two strong assumptions in the model; perfect axisymmetry plus symmetry in the two hemispheres, from which only the line profile symmetric with respect to the line rest wavelength is predicted. In reality, these two assumptions are probably too strong; for example, the observed neutron star kick naturally indicates there must be some overall shift in the momentum distribution within the ejecta (Holland-Ashford et al. 2017; Katsuda et al. 2018). Therefore, we may consider the AS and DP collectively as the "non-single profile" category and compare it to the model DP fraction. As combined with the above caveat on the classification between the NC and GS categories, we may then compare the fractions of the "single-peaked category" (NC and GS) and the "non-single profile" category (AS and DP). Then, the observed fraction of the non-single profile category is 52%, while this is 64% (BP2) or 34% (BP8). The single-peak category accounts for 48% of the canonical SESNe sample, and its fraction is 34% (BP2) or 66% (BP8). Therefore, the bipolar-like model could account for the full canonical SESNe sample, once one allows the deviation from either the axisymmetry or the symmetry between the two hemispheres to some extent. In other words, the above analysis suggests that (1) the deviation from spherical symmetry could be a common feature in the SN explosion; (2) most of the SN explosion would also have a

[8] The dividing angles for DP objects of BP2 and BP8 models are different from those in Maeda et al. (2008). This is because we employ a different definition of DP in this work, which is based on the fitting procedure described in Section 2. To avoid confusion, throughout the paper, we will adhere to this criterion.

specific direction, and (3) the configuration having negligible deviation from the axisymmetry and the two-hemisphere symmetry could account for only up to one-third of the canonical SESNe.

The leading scenario for GRBs includes two components: a narrow and relativistic jet for a high-energy GRB emission and a quasi-spherical (but perhaps with a substantial asphericity) component for an optical SN emission. For those associated with GRBs, there could indeed be a preferential viewing direction (Maeda et al. 2006). In the sample of nine SNe Ic-BL, two are definitely associated with GRBs (SNe 1998bw and 2006aj). SN 1997ef might also have been associated with a GRB, and there could also be a bias in the viewing direction for SN 2012ap given its strong radio emission. Therefore, up to ~45% of the SNe Ic-BL in this sample may indeed suffer from an observational bias in the viewing direction. If we would take this fraction in the model prediction (Table 4.4), then the NC, GS, and DP fractions expected in the model would change to (as the most extreme case) 48%:17%:35% (BP2) or 52%:29%:19% (BP8). This is indeed compatible with the observed fractions of the NC (56%) and GS (11%) objects, or the sum of the NC and GS fractions (67%; see above for the uncertainty associated with the NC/GS classifications) among the SN Ic-BL sample.

While the specific model used here would not allow for quantitative discussion on the difference between the NC and GS categories (see above), qualitative comparison between different SN subtypes may still be possible; a larger degree of asphericity leads to a larger ratio of the NC objects to the GS object. This may partly explain a larger fraction of the NC objects in SNe Ic-BL than the other subtypes, together with the effect of a possible bias in the viewing direction as stated above. A lack of the DP objects in SNe Ic-BL is puzzling[9]. As one possibility, this may indicate that SNe Ic-BL may tend to have a specific direction in the explosion, and the deviation from the axisymmetry and/or two-hemisphere symmetry is more important than in the other SESN subtypes. This might be further related to the larger asphericity indicated by a large fraction of the NC objects in SNe Ic-BL. Further investigation focusing on the difference of nebular behaviors between SNe Ic-BL with and without GRB association, based on a larger sample, is required.

Section 5.2. *[O I]/[Ca II]-[O I] width correlation*

In Section 4.2, using the thus far largest spectral sample of nebular SESNe, a correlation between the [O I]/[Ca II] ratio and the [O I] width is discerned. In the computed nebular spectra of SESNe, the [O I]/[Ca II] ratio is found to be positively correlated with the progenitor CO core mass (Fransson & Chevalier 1989; Jerkstrand et al. 2015a; Dessart et al. 2021), and is therefore routinely employed as the indicator of this very important quantity (Kuncarayakti et al. 2015; Maeda et al. 2015; Fang et al. 2019). Based on this assumption (its validity will be discussed in Section 5.4), the correlation implies that the ejecta of SN with a larger CO core tend to expand faster. The typical velocity of the ejecta can be estimated as

$$v^2 \sim \frac{E_{\rm K}}{M_{\rm ejecta}} = \frac{E_{\rm K}}{M_{\rm pre-SN} - M_{\rm NS}}. \quad (4.8)$$

Within each subtype, a more massive progenitor will thus tend to have a larger ejecta mass. If the kinetic energy of the ejecta is a constant, for example, 10^{51} erg, the velocity of the ejecta would be expected to be

[9] SN 2003jd is a prototype of the DP object (Mazzali et al. 2005; Taubenberger et al. 2009). However, its publicly available spectra do not meet the wavelength range required in this work, so it is not included in our sample.

anti-correlated with the progenitor ZAMS mass or the CO core mass, which contradicts the result in this work. The positive correlation of the [O I] width and [O I]/[Ca II] ratio implies that the SN with a progenitor possessing a more massive CO core will tend to have a larger kinetic energy. Assuming that the kinetic energy is a function of the CO core mass, i.e., $E_K = E_K(M_{CO})$, the observational tendency in this work can be qualitatively reproduced.

For SNe Ic/Ic-BL, the typical velocity can be estimated as

$$v^2 \sim \frac{E_K}{M_{ejecta}} = \frac{E_K(M_{CO})}{M_{ejecta}} \approx \frac{E_K(M_O)}{M_O}, \quad (4.9)$$

where M_{CO} is the CO core mass and M_O is the mass of the oxygen in the ejecta. Since M_O is tightly correlated with M_{CO}, $E_K(M_{CO})$ can also be written as $E_K(M_O)$. We assume $M_{ejecta} \approx M_O$, as the oxygen-rich material makes up a significant part of the ejecta of SNe Ic/Ic-BL. If the dependence of E_K on M_O is in the form of a power law, i.e., $E_K \propto M_O^{\alpha}$, and the power index α is close to unity, the typical velocity of SNe Ic/Ic-BL will be a constant.

For SNe IIb/Ib, if the residual hydrogen envelope of SNe IIb is neglected (~ 0.1 $M_\odot$), Equation (4.9) becomes

$$v^2 \sim \frac{E_K}{M_O + M_{He}} = \frac{E_K(M_{CO})}{M_{ejecta}} \approx \frac{E_K(M_O)}{M_O} \frac{1}{1 + M_{He}/M_O}, \quad (4.10)$$

where M_{He} is the mass of the helium in the ejecta. The quantity M_{He}/M_O is a decreasing function of CO core mass, as the He burning is efficient for large M_{ZAMS} (Dessart et al. 2020). Therefore, the typical velocity of SNe IIb/Ib is an increasing function of M_{CO} if α ~ 1, which explains the behaviors of SNe IIb/Ib in Figure 4.9.

The gravitational binding energy of a pre-SN progenitor is $E_g \sim M^2/R$, where M is its mass and R is the radius. The above qualitative analysis gives $E_K \propto M_O$. Based on the helium star models in Dessart et al. 2020 (the parameters are listed in their Table 1), we derive the scaling relation $E_K \propto E_g^{0.60}$ to explain the observed correlation. However, the above discussion is greatly simplified, and highly dependent on the stellar evolution and the mass-loss scheme. A more detailed treatment of the quantitative relation between the kinetic energy and the progenitor CO core mass will be presented in Chapter 5.

Another interesting feature is the dependence of the correlation on the line profile. In Figure 4.10, if only NC objects are included, the [O I]/[Ca II] ratio and the [O I] width have the tightest correlation, followed by AS and DP objects. If the NC objects originate from the oxygen-rich torus viewed from the axial direction, then the difference in the velocity projection can be neglected, because the viewing angle is restricted to a small range. The effect of the viewing angle can thus be a potential origin of the relatively large scatter seen in GS objects.

To test how the viewing angle affects the scatter level, the same [O I] width measurement is applied to the BP2 and BP8 model spectra. As shown in Section 5.1, the range of the viewing angle relative to the jet-on direction will affect the emission line profile. We measure the [O I] width of the models, and calculate the standard deviation in each line profile group. The results are summarized in Table 4.4. In general, the scatter levels of the models are much smaller than observation (about 0.06 dex; see the lower panel of Figure 4.9), but both the BP2 and BP8 models give the correct tendency. The scatter levels of the NC and DP types are

relatively small compared with the GS type, as the viewing angles of the NC and DP models are restricted to a narrow range where the effect of velocity projection can be neglected.

Section 5.3. *[O I]/[Ca II]-[O I] profile correlation*

The relation between the [O I]/[Ca II] ratio and the line profiles (Section 4.3) can be summarized as follows: (1) the GS objects have the largest average [O I]/[Ca II], followed by AS/ NC, then DP; (2) the fraction of GS objects increases with [O I]/[Ca II]; (3) the fraction of DP objects decreases with [O I]/[Ca II]; and (4) the fractions of NC and AS objects are not monotonic functions of [O I]/[Ca II].

The relation between the [O I] profile distribution and the [O I]/[Ca II] ratio suggests the geometry of the O-rich ejecta probed by the [O I] profile is a function of the progenitor CO core mass, which is assumed to be measured by the [O I]/ [Ca II] ratio. The interpretation of this relation is uncertain. In the classification scheme of Taubenberger et al. (2009), the geometry origins of GS/NC/AS objects are degenerated. Meanwhile, the DP objects are unambiguously related to the O-rich torus, and therefore can be a useful indicator of bipolar explosion. However, the fraction of DP objects is affected by two factors, i.e., the occurrence rate and the (average) degree of asymmetry of the bipolar explosion. Two extreme cases will be discussed in the following, which account for the effects of (A) the bipolar explosion rate and (B) the degree of asymmetry on the interpretation of the [O I]/[Ca II]-[O I] profile relation.

(1) **Case A**. The global geometry of the ejecta is assumed to be either spherically symmetric (a broad GS base, possibly plus a moving blob to account for the AS and NC objects) or have an axisymmetric bipolar configuration with the fixed degree of asymmetry. In this case, the fraction of the DP objects can be an indicator of the occurrence rate of the bipolar explosion. The decreasing trend of the DP fraction in Figure 4.11 implies the rate of this configuration is anti-correlated with the progenitor CO core mass. Therefore, the ejecta of SESN with a more massive progenitor will tend to be spherically symmetric. This is also consistent with the increasing trend of the GS fraction. By assuming no spatial preference in the viewing angle, only a small fraction of NC objects originate from the bipolar explosion model viewed from the jet-on direction. The NC/AS objects are characterized by globally spherical symmetry plus a narrow component, which can be interpreted as the massive moving blob or enhanced core density. The insensitivity of the fractions of the AS/NC objects on the [O I]/[Ca II] suggests that the CO core mass is not responsible for the occurrence of these local clumpy structures.

(2) **Case B**. The SESNe in this sample are all assumed to be originated from bipolar explosions (i.e., the occurrence rate is fixed to be 100%) with different degrees of asymmetry, which are reflected by the fractions of the DP objects (Table 4.4). The bipolar explosions are allowed to be non-axisymmetric to account for the AS objects (see the discussion in Section 5.1). As already discussed in Section 5.1, if the GS and NC profiles are combined as a “single-peak profile,” and the AS and DP profiles are combined as a “non-single profile” (the assumption of perfect axisymmetry is discarded), the bipolar explosion models could account for the line profile distribution of the full sample. If this is the case, the dependence of the single-peak/non-single profiles on the [O I]/[Ca II] may provide a important constraint on the development of the bipolar configuration of SNe.

The cumulative fractions of log [O I]/[Ca II] of the objects with single-peak and non-single profiles are plotted in the upper panel of Figure 4.13. Although the average log [O I]/[Ca II] of single-peak objects is slightly larger than that of objects with non-single profiles, the difference is not significant, and the [O I]/[Ca II] distributions are indistinguishable ($p > 0.25$ based on the two-sample AD test). The relation between the [O I]/ [Ca II] ratio and the distribution of line profile is derived using the same method as Section 4.3. As shown in the lower panel of Figure 4.13, the trends where the fraction of the single-peak objects increases as log [O I]/[Ca II] increases, while the fraction of their non-single counterparts decreases, can be discerned ($p = \pm 0.90$, respectively, and $\rho < 0.03$).

The discussion in Section 5.1 shows that the BP2 model has a smaller fraction of single-peak objects than the BP8 model (see Table 4.4). With [O I]/[Ca II] being a measurement of the CO core mass, the statistics evaluation is qualitatively consistent with the scenario where the ejecta geometry develops as the progenitor CO core mass increases, gradually converting from the mildly aspherical BP2 cases to the extremely aspherical BP8 cases, i.e., the deviation of the explosion from spherical symmetry develops as the CO core mass (or ZAMS mass of the progenitor) increases.

Comparison of the data using the specific bipolar model is just for demonstrative purposes. In reality, the ejecta structure can be more complicated, and the full SESNe samples may not be represented by a single model sequence, we thus limit ourselves to discuss the general tendency using these specific models.

The investigation on the physics that governs the dependence of the ejecta geometry on the progenitor CO core mass is related to the development of the asphericial explosion, which may put an important constraint on the explosion mechanism of SESNe. However, the interpretation of this dependence can be different (or even opposite) when different assumptions are made, as exemplified by the two extreme cases discussed above. In reality, the situation may be the mixture of the two cases, or even more complicated. To firmly interpret the relation between the [O I]/[Ca II] ratio and the distribution of line profile, we thus need another tool, which should be independent from the [O I] profile, to probe the geometry of the ejecta. The investigation on this topic will be presented in Chapter 6.

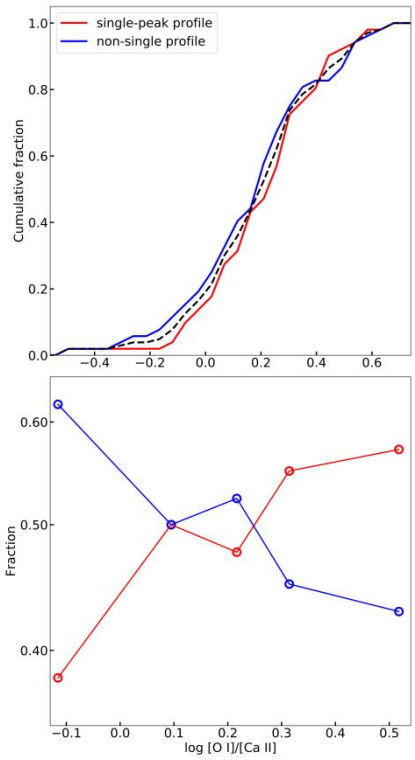

Figure 4.13. **Upper panel: the cumulative fractions of log [O I]/[Ca II] of the objects with single-peak (NC + GS) and non-single (DP + AS) profiles.** The black dashed line is the distribution of the full sample. **Lower panel: the same as the lower panel of Figure 4.11 but based on the classification scheme of single-peak and non-single profiles.**

Section 5.4. *[O I]/[Ca II] as measurement of progenitor M_{ZAMS}*

The discussion in Sections 5.2 and 5.3 is largely based on the assumption that the [O I]/[Ca II] ratio is positively correlated with the progenitor CO core mass, and thus its ZAMS mass. This is the case for the currently available models (Fransson & Chevalier 1989; Jerkstrand et al. 2015a; Jerkstrand 2017; Dessart et al. 2021). However, whether this diagnostics is robust remains uncertain (Jerkstrand 2017); the [O I]/[Ca II] ratio is affected by the phase of observation, the expansion velocity of the ejecta (or more specifically, kinetic energy), and the distribution of the calcium. In Section 6.1, we will show that the spectral phase will not affect the above correlation. In this subsection, the latter two points, i.e., the effect of kinetic energy, and the pollution of calcium into the O-rich material, are discussed.

(1) **Kinetic energy.** The [Ca II] is emitted from the ash of the explosive burning, the physical properties of which are affected by the explosion energy. The density structure of the ejecta is also related to its expansion velocity, which again affects the [O I]/[Ca II] ratio (Fransson & Chevalier 1989). We will now investigate whether the effect of the explosion energy alone can account for the wide range of the [O I]/[Ca II] ratio.

To simplify the discussion, the amount of the newly synthesized elements, including calcium, is assumed to be positively correlated with the kinetic energy of the ejecta (Woosley et al. 2002; Limongi & Chieffifi 2003). With this assumption, for a fixed CO core mass, the kinetic energy will affect the [O I]/[Ca II] in two aspects: (a) SNe with larger kinetic energy will synthesize a larger amount of calcium,

which increases the intensity of the [Ca II] and decreases the [O I]/[Ca II] ratio, and (b) with larger kinetic energy, the ejecta will expand faster, which decreases its density and, again, decreases the [O I]/[Ca II] ratio (Fransson & Chevalier 1989). For the same CO core with different kinetic energy injected, the [O I]/[Ca II] will be expected to be anti-correlated with the expansion velocity of the ejecta, which contradicts the observed correlation in Figure 4.7. The correlation of the [O I]/[Ca II] ratio and the [O I] width suggests that the effect of the kinetic energy is limited and can not be a main driver of the large range of [O I]/[Ca II] (~1 dex).

(2) **Calcium pollution.** The [Ca II] is mainly emitted by the newly synthesized calcium from the explosive oxygen burning ash (Jerkstrand et al. 2015a). However, in several CCSN nebular models, if the calcium produced by the pre-SN nucleosynthesis is microscopically mixed into the O-rich layer through a shell merger (which may happen during the Si burning stage), its contribution to the [Ca II] becomes significant (Dessart et al. 2021). The [O I]/ [Ca II] will be dramatically reduced because [Ca II] is a very effective coolant (Dessart & Hillier 2020; Dessart et al. 2021). In this case, [O I]/[Ca II] is no longer a monotonic function of progenitor CO core mass.

Several works (Collins et al. 2018; Dessart & Hillier 2020) reported that the occurrence rate of calcium pollution is high for a more massive star. If the progenitor mass is increased, the [O I]/[Ca II] will be affected by two competing factors along different directions, increased by the CO core mass, but decreased by the higher degree of microscopically mixed calcium. We may consider the most extreme case, in which the effect of the calcium pollution on the progenitor mass is so strong that the correlation between the [O I]/[Ca II] and CO core mass is inverted, i.e., a small [O I]/[Ca II] implies large CO core mass. With this assumption, a constant kinetic energy can produce the correlation between [O I]/[Ca II] and [O I] in Figure 4.7.

From the current observation, the degree of calcium pollution is difficult to constrain. However, its effect on [O I]/[Ca II] is probably not very strong from several observational lines of evidence. (a) The measured progenitor masses of SNe 2011dh, 2013df, and iPTF 13bvn are relatively small from pre- or post-SN images (Maund et al. 2011; Cao et al. 2013; Van Dyk et al. 2014), and their [O I]/[Ca II] are among the lowest of the full sample. SNe 1998bw and 2002ap are also believed to have massive progenitors; meanwhile, their [O I]/[Ca II] are at the highest end (Nakamura et al. 2001; Mazzali et al. 2002). (b) A correlation between the light-curve width and the [O I]/[Ca II] ratio is reported by Fang et al. (2019). The light-curve width can be an independent measurement of the ejecta mass. If the [O I]/[Ca II] is mainly determined by the degree of microscopic mixing, an anticorrelation between the [O I]/[Ca II] and light-curve width would be expected, which contradicts the observation.

We have discussed the possible factors that would affect the [O I]/[Ca II] ratio. However, it should be emphasized that the current understanding on the [O I]/[Ca II] ratio itself, as well as its relations with the physical properties (CO core mass, kinetic energy, microscopic mixing, etc.) is still limited. To firmly establish the relations between the observables and the ejecta properties, which is crucial to explain the correlation in Figure 4.7, a sophisticated nebular SESN model with all of the above factors involved is needed.

Section 6. Discussion

Section 6.1. *Temporal Evolution*

The nebular spectra in this work cover quite a large range of phases (mean value <phase> = 213 days,standard deviation σ = 61 days). Therefore it is important to investigate whether the phases of the spectra will affect the correlation in Figure 4.7.

The most straightforward method is to calculate the rate of change of the [O I]/[Ca II] ratio or [O I] width by following the evolution of each object. However, the number of objects with multiple nebular spectra covering a wide range of phases is too small for such investigation. Fortunately, the main focus of this work is on the statistical properties of these two quantities. Unless there is a strong bias in the sample (for example, objects with large [O I]/[Ca II] tend to be observed in late phases), the average difference of the quantities at different phases can be employed to estimate the effect of the spectral phase on bulk statistics.In this work, two methods are employed to estimate the rates of change of [O I]/[Ca II] ratio or [O I] width; one based on the statistics of the full sample, and the other based on the evolution of individual objects.

The left panels of Figure 4.14 show the time dependence of the [O I]/[Ca II] ratio and the [O I] width $\Delta\lambda_{blue}$ of the full sample. In these panels, each data point represents an individual object. The $\Delta\lambda_{blue}$ is weakly correlated with the spectral phase ($\rho = -0.29$, $p < 0.02$). The slope from the linear regression is -0.023 ± 0.012 (unit: dex per 100 days. In the following text of this Chapter, unless explicitly mentioned, the units of rates of change of both [O I]/[Ca II] and [O I] width are dex per 100 days). The uncertainty is estimated from 104 bootstrap resamples, and the 95% CIs are indicated by the shaded regions. If we attribute this phase dependence to the temporal evolution of $\Delta\lambda_{blue}$, on average, $\Delta\lambda_{blue}$ changes by about −7.7% to −2.5% per 100 days, which is in good agreement with the decrease rate reported by Maurer et al. (2010a). The same analysis is performed with the [O I]/[Ca II] ratio, which in turn shows no evidence of temporal evolution ($\rho = -0.03$, $p < 0.79$). Linear regression suggests [O I]/[Ca II] changes by only -0.012 ± 0.029 dex (or about −9.7%–4.0% in linear scale) per 100 days.

To examine the evolution of the [O I]/[Ca II] ratio and the [O I] width of individual objects, we turn to those SNe in the sample with multiple nebular spectra available from the literature, and the maximum phase span is required to be larger than 100 days. The corresponding measurements of these objects are plotted in the middle panels of Figure 4.14. The evolution rates are estimated by linear regression. In the SESNe models of Jerkstrand et al. (2015a), the oxygen element spreads across a wide range of zones. Initially the [O I] is dominated by the emission from the outermost region. As the ejecta expands, the contribution from the innermost region becomes larger, which decreases the average velocity of the emitting elements and therefore the width of the emission line. For most objects ($N = 12$ out of 16), the [O I] width decreases with time, which is consistent with the above picture. The average and standard deviation of the slopes are -0.026 ± 0.033. The distribution of the slopes is also shown in the lower-right panel of Figure 4.14, with a peak around −0.029. This is consistent with the slope estimated from the full sample (−0.023), and can fully explain the overall time dependence of [O I] width in the lower-left panel of Figure 4.14.

However, the temporal evolution of [O I]/[Ca II] depends on the physical conditions of the ejecta. The complexity is also discerned in the observational data; the observed slopes of the [O I]/[Ca II] ratio spread over a wide range. The average and standard deviation of the slopes are 0.027 ± 0.094. Unlike the [O I] width, the distribution of the evolution rates of [O I]/[Ca II] lacks a clear peak, which may possibly explain the lack of correlation between the spectral phase and [O I]/[Ca II]; the different directions of evolution cancel each other out.

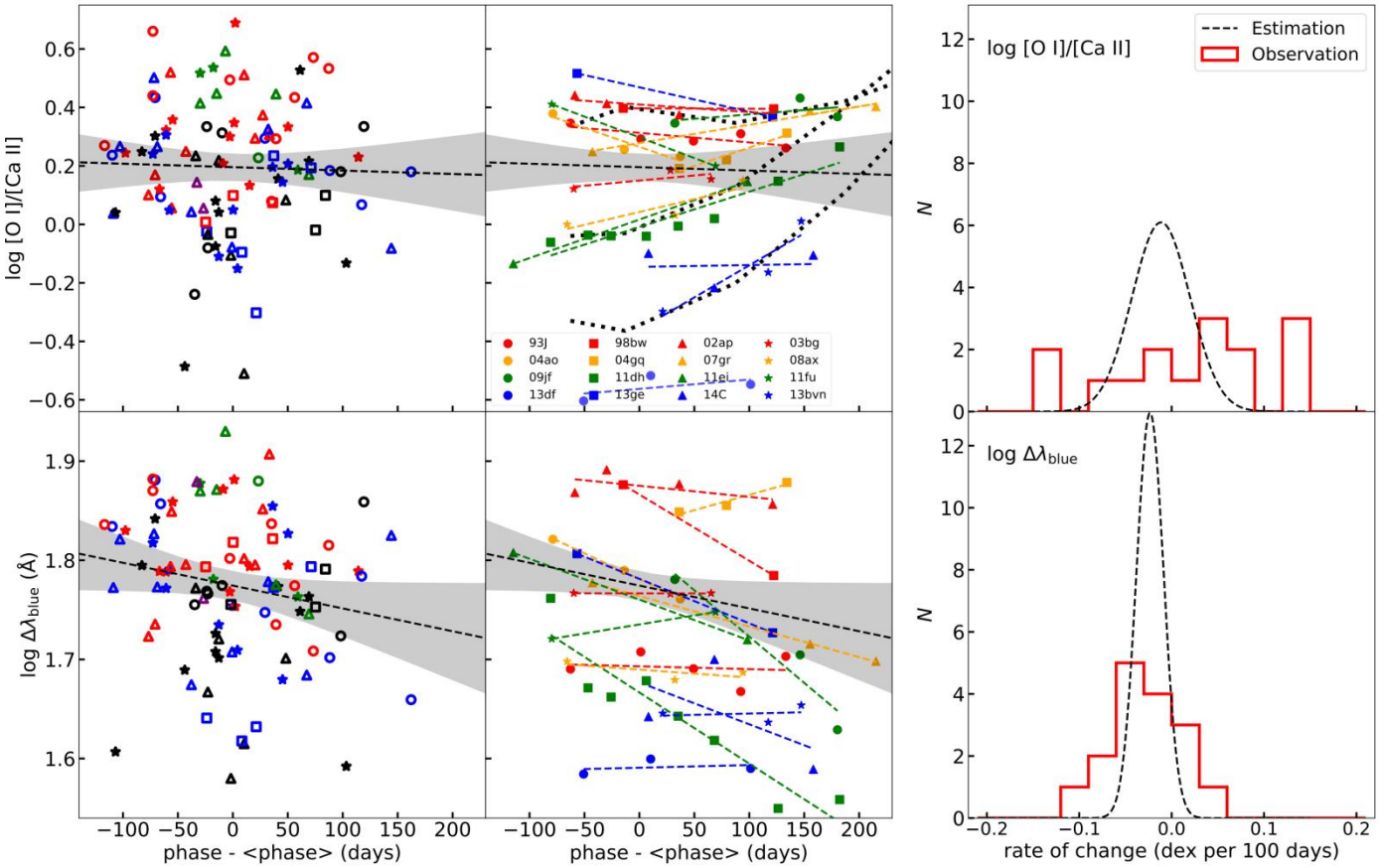

Figure 4.14.**Left panels: the [O I]/[Ca II] ratio and the [O I] width Δλblue vs. the spectral phase relative to the mean value of the sample** (<phase> = 213 days). The black dashed lines are the results of the linear regression for the full sample, and the shaded regions are the 95% CIs estimated from the bootstrap-based Monte Carlo method. The meanings of the different colors and markers are the same as in Figure 4.7. **Middle panels: the time evolution of [O I]/[Ca II] and $\Delta\lambda_{blue}$ of individual objects**. Different objects are labeled by different colors and markers. The color dashed lines are the results of linear regression for each object. The fitting results of the full sample are also plotted for comparison. The black dotted lines in the upper-middle panel are the measurements of the model spectra from Jerkstrand et al. (2015a). **Right panels: the distributions of the rates of change of log [O I]/[Ca II] and log $\Delta\lambda_{blue}$**. The red histograms are the observed rates of change of individual objects. The black dashed lines are the expected distributions of the rates of change estimated from the linear regression of the full sample, scaled to $N = 16$. The sources of the spectra are: SN 1993J (Barbon et al. 1995; Matheson et al. 2000a; Jerkstrand et al. 2015a); SN 1998bw (Patat et al. 2001); SN 2002ap (Foley et al. 2003); SN 2003bg (Hamuy et al. 2009); SN 2004ao (Modjaz et al. 2008; Shivvers et al. 2019); SN 2004gq (Maeda et al. 2008; Modjaz et al. 2014); SN 2007gr (Shivvers et al. 2019); SN 2008ax (Chornock et al. 2011; Taubenberger et al. 2011; Modjaz et al. 2014); SN 2009jf (Valenti et al. 2011; Modjaz et al. 2014); SN 2011dh (Shivvers et al. 2013; Ergon et al. 2015); SN 2011ei (Milisavljevic et al. 2013a); SN 2011fu (Morales-Garoffolo et al. 2015); SN 2013df (Morales-Garoffolo et al. 2014; Maeda et al. 2015); SN 2013ge (Drout et al. 2016); SN 2014C (Milisavljevic et al. 2015a; Shivvers et al. 2019); and iPTF 13bvn (Fremling et al. 2016).

It is useful to compare the evolution of [O I]/[Ca II] with theoretical models. For the SNe IIb model spectra of Jerkstrand et al. (2015a), the [O I]/[Ca II] increases with time (see also Figure 13 in Jerkstrand 2017). Using the same measurement method in this work, the evolution of the [O I]/[Ca II] of these models is plotted by the black dotted lines in the upper-middle panel of Figure 4.14 for comparison. The [O I]/[Ca II] and the evolution of the He star model with $M_{ZAMS} = 12\ M_{\odot}$ (M12 hereafter) is consistent with iPTF 13bvn. When compared with SN 2011dh and SN 2008ax, the M13 model evolves faster, but the behaviors are qualitatively similar; the change of [O I]/[Ca II] is mild before ~300 days, while at later phases, the slope increases. For M17 model and the objects with large [O I]/[Ca II], the rates of change are approximately negligible before ~300 days.

The above discussion motivates the investigation on the possible dependence of the rate of change of [O I]/[Ca II] on [O I]/[Ca II] itself. The He star models of Jerkstrand et al. (2015a) and the observational data suggest objects with large [O I]/[Ca II] tend to have slowly evolving [O I]/[Ca II]. For the 16 SNe with wide spectral phase spans and the He star models in Jerkstrand et al. (2015a), their [O I]/[Ca II] ratios are corrected to the mean phase (213 days), which are then compared with the slopes estimated from linear regression, as shown in Figure 4.15. The uncertainties of the corrected [O I]/[Ca II] and the slopes are estimated from the bootstrap-based Monte Carlo method, which includes the uncertainties of the measurement of [O I]/[Ca II] at different phases. An anti-correlation between the slopes and the [O I]/[Ca II] ratios can be discerned ($\rho = -0.64$, $p < 0.007$), especially for objects with log[O I]/[Ca II] > 0. The relation between the [O I]/[Ca II] and the slope at the low [O I]/[Ca II] end is hard to constrain because only three objects are available (SNe 2013df, 2014C, and iPTF 13bvn) and the scatter is large. The 16 observational data points are then fitted by local non-parametric regression, the result of which is plotted by the black dashed line in Figure 4.15, and the 95% CI estimated from the bootstrap-based Monte Carlo method is shown by the shaded region.

Limited by the sample size ($N = 16$), the result in this work provides the starting point for the investigation on the dependence of the evolution rate of [O I]/[Ca II] on [O I]/ [Ca II]. To firmly establish this relation, we need a larger sample of SESNe with nebular spectra covering large ranges of phases, especially later than 300 days.A direct comparison of the nebular spectra at different phases is presented in Figure 4C.1 for some well observed examples.

To eliminate the effect of spectral evolution, we run 10^4 simulations, and in each trial, the rates of change of [O I]/[Ca II] and [O I] width are assigned to each object, which are randomly drawn from (1) the slope estimated from the full sample (the black dashed lines in the right panels of Figure 4.14), or (2) the distributions of slopes derived from following the evolution of individual objects (the red histograms in the right panels of Figure 4.14), or (3) the [O I]/[Ca II]-dependent evolution rate (the shaded region in Figure 4.15). The [O I]/[Ca II] and [O I] width are then corrected to the mean phase. We find that no matter which distributions and combinations are chosen, the two quantities are significantly correlated, with ρ ranging from 0.50 to 0.54 and $p < 0.0001$ for all cases. We therefore conclude that the spectral evolution will not significantly affect the correlation in Figure 4.7.

In Figure 4.9, the helium-rich SNe behave differently from their helium-deficient counterparts. However, the average phases of the SN subtypes in this work are similar and no statistical difference can be discerned; 220 ± 58 days for SNe IIb, 203 ± 80 days for SNe Ib, 202 ± 56 days for SNe Ic and 223 ± 36 days for SNe Ic-BL. Therefore temporal evolution can not be the main reason for the different behaviors of the different SN

subtypes in both Figures 4.7 and 4.9, which can be another evidence of the limited effect of the spectral phase on the correlation.

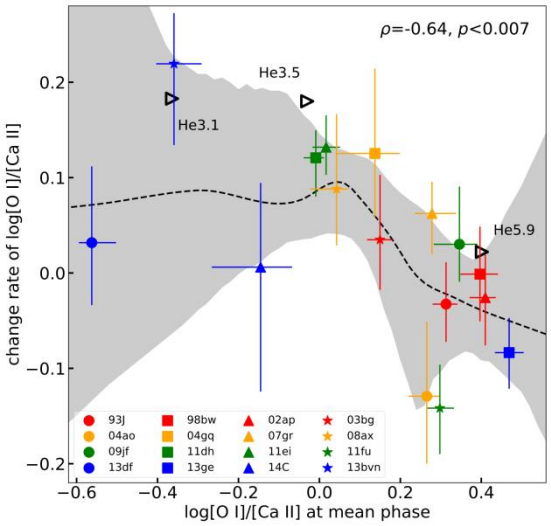

Figure 4.15. **The relation between log [O I]/[Ca II] and its time evolution rate** (unit: dex per 100 days). Different objects are labeled by different colors and markers. The SNe IIb model spectra of Jerkstrand et al. (2015a) are also plotted for comparison, and the evolution rates of the models are calculated from the measurements at 150–400 days. The dashed line is the result of local non-parametric fit,and the shaded region is the 95% CI estimated from the bootstrap-based Monte Carlo method (see the main text).

Section 6.2. *Asymmetric Hα/[N II]*

In Section 2, to derive the "clean" [O I] profile, the excess flux at the red wing of [O I] is subtracted by assuming it is not necessarily valid and will affect the line width measurement. For example, if the real center of the excess flux is redshifted, assuming a symmetry with respect to 6563 Å will result in over-subtraction of the [O I] and under-estimation of the line width. It is not always easy to tell whether such asymmetry exists from the nebular spectra, as the [O I] and the excess flux are always blended. In this subsection, we will quantitatively estimate how the asymmetry of the Hα-like structure affect the measurements.

First, an [O I] component, which is composed of two Gaussian functions with the same standard deviation (σ = 50 Å), is simulated. The central wavelengths are fixed at 6300 and 6364 Å, and the intensity ratio is set to be 3:1 (see Section 2). We then generate a set of excess emissions with detailed profiles listed in Table 4.5 to account for different distributions of the emitters. The half-width at zero intensity of these profiles is fixed to be 220 Å, based on the ~10,000 km s^{-1} outer edge velocity of the excess profile estimated by Maeda et al. (2015). The fluxes of these profiles are set to be 40% of the [O I] emission (about 84% of the full sample). At the same time, we allow the symmetric center λ_{sym} to move from 6453 to 6673 Å, corresponding to $|v_{shift}| \sim$ 5000 km s^{-1}.

After adding the [O I] profile by the simulated excess emissions, we repeat the measurement in Section 2, assuming the excess flux is symmetric with respect to 6563 Å. The deviation of the measured line widths ($\Delta\lambda_{blue}$, $\Delta\lambda_{red}$, and $\Delta\lambda_{normal}$, see Figure 4.2) from $\Delta\lambda_{6563}$, which is defined to be the corresponding measured line

widths when the excess emission is symmetric with respect to 6563 Å, is plotted against the symmetric center λ_{sym} in Figure 4.16.

Geometry	Profile[10]	Notes
Thin shell	Flat-top	$dR_{sh}=0.2R_{sh}$
Thick shell	Flat-top	$dR_{sh}=0.6R_{sh}$
Uniform dist	$\sqrt{1-x^2}$	$\Delta\lambda$ = 220 Å
Uniform sphere	$1-x^2$	$\Delta\lambda$ = 220 Å

Table 4.5. **The profiles of the excess emission (Hα/[N II]).**

It is clear that the asymmetry of the excess flux indeed affects the measured line width. The red width $\Delta\lambda_{red}$ is sensitive to the distribution of the emitters and the shift of the symmetric center. If the symmetric center is heavily shifted, or the profile is sharply peaked (i.e., thick shell versus thin shell, or disk versus sphere), the deviation will be large and reach to about 15%–23%. However, the blue width $\Delta\lambda_{blue}$ does not show significant deviation in all cases. The deviation of $\Delta\lambda_{blue}$ changed by about 5%–8%. Even in the most extreme cases, the deviation will not exceed ~12% or 0.05 dex, and can not account for the 0.3 dex line width difference reported in this work. Given that $\Delta\lambda_{blue}$ is not sensitive to the λ_{sym} and the spatial distribution of the emitters, in this work, $\Delta\lambda_{blue}$ is employed as the measurement of line width.

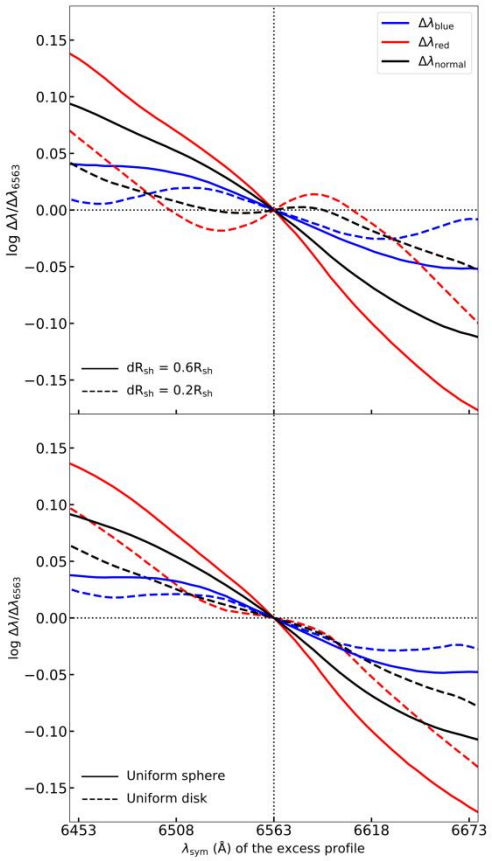

Figure 4.16.**The symmetric center of the excess emission and the deviation of the measured line widths from $\Delta\lambda_{6563}$ (see the main text for definitions)**. $\Delta\lambda_{blue}$, $\Delta\lambda_{red}$, and $\Delta\lambda_{normal}$ are labeled by different colors, and different distributions of the emitters are labeled by different line styles.

[10] $x = (\lambda - \lambda_{sym})^2/\Delta\lambda^2$

The excess emission can be attributed to shock-CSM induced Hα, radiative powered [N II], or the combination of both (Patat et al. 1995; Jerkstrand et al. 2015a; Fang & Maeda 2018). The insensitivity of the $\Delta\lambda_{blue}$ to the λ_{sym} suggests that the identification of the excess emission will make no difference on the measurement. We note that the conditions tested here are quite extreme, as most objects do not have excess emission as large as (Hα or [N II])/[O I] = 0.4 (Fang et al. 2019), and the assumption that $|v_{shift}| \sim 5000$ km s^{-1} does not seem realistic. From the very late-phase observation of SN 1993J and SN 2013df, no evidence supports that the boxy profile is significantly asymmetric with respect to Hα or [N II] (Maeda et al. 2015), so allowing the central wavelength to move at a velocity as large as 5000 km s^{-1} (~110 Å) is indeed very conservative.

Observationally, no significant correlation can be discerned between the central wavelength (λ_c in Figure 4.2) and the [O I] width ($\rho = 0.12$, $p < 0.21$), as would be expected if the difference of the [O I] width was significantly affected by the Hα-like structure subtraction, which again supports the argument here.

Section 6.3. *Narrow core (NS) and Asymmetry (AS): Doppler-shifted moving blobs?*

As introduced in Section 2.4, the narrow component of the NC profile can be interpreted as a massive oxygen-rich blob moving nearly perpendicular to the line of sight, or enhanced core density. Similarly, the AS profile would require a blob moving with non-negligible motion in the direction of the line of sight to account for the narrow component. The geometrical origins of NC and AS objects can be unified as ejecta of globally spherical symmetry plus (1) Doppler-shifted moving blobs, or (2) enhanced core density. In the enhanced core density scenario, the narrow component is expected to be centered at its rest wavelength. Further, if the direction of the moving massive blob is isotropic, the amount of the red- and blue-shifted narrow components would be similar. In conclusion, the distribution of the narrow component offsets of the AS/NC objects is expected to be symmetric with respect to zero velocity. Any deviation from such distribution would require an additional effect beyond geometrical effect.

For the combined sample of NC and AS objects, the shift of the broad base is −5.9 Å. The standard deviation is 9.9 Å, which is comparable to the resolution 12.6 Å ($R \sim 500$). The low velocity of the broad base is in good agreement with the Gaussian distributed emitter and global spherical symmetry. The histogram of the central wavelength offsets of the narrow component with respect to the broad base are shown in the upper panel of Figure 4.17. On average, the narrow component is blueshifted (−14 Å), which is comparable to its typical width (~16 Å), too large for the enhanced core density scenario. The amount of the redshifted objects is only about half of the blueshifted ones ($N_{red}/N_{blue} \sim 0.46$). This is also not expected if the narrow core originates from the massive moving blob.

Milisavljevic et al. (2010) already noticed the [O I] with double horns can be classified into two classes: the two horns are symmetric with respect to zero velocity, or one of the horns is located close to 6300 Å and the other one is blueshifted. These two types can both be fitted by a broad base plus a blueshifted narrow component. The result in this work suggests the lack of the redshifted narrow component is a statistically significant phenomenon.

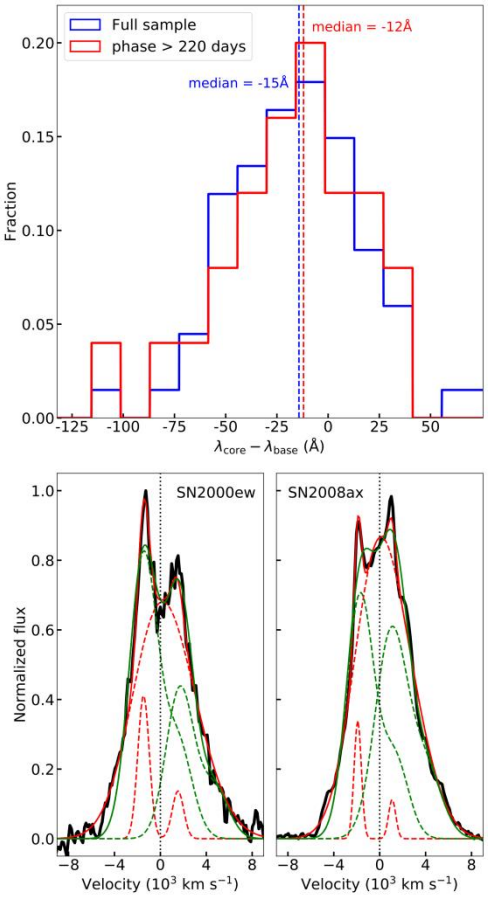

Figure 4.17.**Upper panel: the histogram of the central wavelength offset of the narrow core with respect to the broad base**. The blue histogram refers to the full NC + AS sample, while the red one is restricted to the objects observed later than 220 days. The dashed lines indicate the median values. **Lower panels: alternative fits to the SNe 2000ew and 2008ax**. The red solid lines are the results of the two-component fit with an initial guess of case (4), as described in Section 2.4, and the green solid lines are the results where the two components have similar intensity and are forced to blue- and redshifted. The dashed lines are the corresponding components.

The imbalance of N_{blue} and N_{red} is mainly driven by the objects with large narrow component offsets. If the analysis is restricted to NC objects, we find N_{red} = 14 and N_{blue} = 16, while for AS objects, N_{red} = 7 and N_{blue} = 30. The above statement is not affected by the boundary of AS/NC. To be specific, the boundary velocity between AS/NC vboundary, which is by default 1000 km s^{-1} , is allowed to vary from 500 to 3000 km s^{-1} . The N_{red}/N_{blue} ratio of the NC objects (narrow component offset within $-v_{boundary}$ to $v_{boundary}$) is then calculated. The result is shown as a function of $v_{boundary}$ by the blue solid line in Figure 4.18. When $v_{boundary}$ varies from 500 to 1500 km s^{-1}, N_{red}/N_{blue} fluctuates between 0.7 and 1.0, consistent with the moving blob or enhanced core density scenarios. The ratio of the red- and blueshifted narrow components continues to drop if $v_{boundary}$ is larger than about 1500 km s^{-1} . This phenomenon suggests the sample especially lacks objects with the narrow component being redshifted by >−1500 km s^{-1} , or has an unusually enhanced number of objects with narrow components blueshifted by >1500 km s^{-1} .In the following, the possible reasons are discussed.

One possibility is the effect of the residual opacity of the inner ejecta. The imbalance of the red- and blueshifted narrow component can be possibly explained by the radiative transfer effect. Jerkstrand et al. (2015a) found the opacity of their He star models is not negligible at around 200 days. For an He star with *M*

= 4 $M_{\odot}$, the escape probability of a photon (λ = 6300 Å) passing through 3500 km s^{-1} material is ~0.85. If the photon is emitted from the rear side, it experiences twice the effective opacity. If the inner ejecta is optically thick, the emission from the rear side will be effectively scattered or absorbed, which possibly explains the lack of the redshifted narrow components. However, this interpretation does not seem realistic for the reasons below: (1) The effect of radiative transfer decreases with the column density, which scales as t^{-2} , we therefore expect to see more redshifted narrow component at later phases. However, no correlation can be discerned between the narrow component offset and the spectral phase (ρ = 0.05, p < 0.64). Further, if the analysis is restricted to the objects observed later than 220 days, the imbalance is not eased ($N_{\rm red}/N_{\rm blue}$ ~ 0.47), and the overall blueshift, which is about −12 Å, is still too large for the enhanced core density or the moving blob scenarios. In Figure 4.18, we already find that the $N_{\rm red}/N_{\rm blue}$ of NC objects is a decreasing function of $v_{\rm boundary}$, while no statistical difference can be discerned from the mean phases when $v_{\rm boundary}$ varies from 500 to 3000 km s^{-1} (red solid line in Figure 4.18). (2) If the opaque ejecta is scattering-dominated, the peak of the emission will be blueshifted. This effect is usually not very large (see Taubenberger et al. 2009 for some simple models), and can possibly contribute to the small blueshift of the broad base. However, the effect of scattering is not enough to explain the large overall blueshift of the narrow component. (3) The fractional flux of the narrow component, α_w, can be a rough estimation of the fractional mass of the moving blob. The average value of α_w is about 0.15. If the effect of self-absorption is included, to absorb the light emitted from such a massive blob, the ejecta will be unrealistically optical thick, resulting in a flux defificit at the redshifted part of the broad base. The line profile will accordingly be heavily distorted, which contradicts the observation.

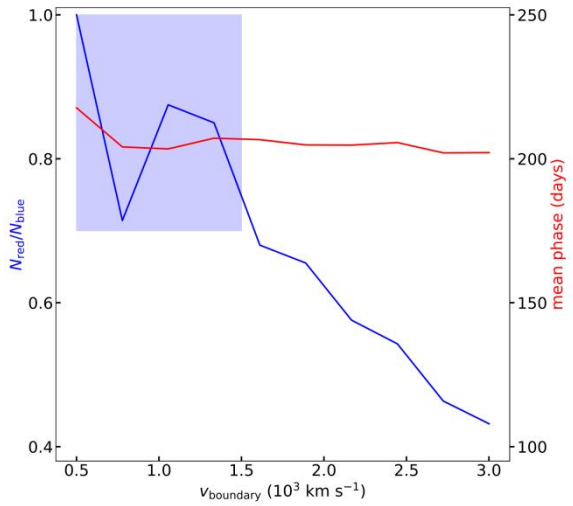

Figure 4.18.**The blue solid line shows the relation between the $N_{\rm red}/N_{\rm blue}$ ratio of the NC objects and the $v_{\rm boundary}$,** which is defined to be the boundary velocity shift between NC/AS (by default 1000 km s^{-1}). The shaded region indicates the ratio from 0.7 to 1.0. **The red solid line shows the relation between the mean phase of the NC objects and $v_{\rm boundary}$,** labeled by the right y-axis.

The relation between $N_{\rm red}/N_{\rm blue}$ of NC objects and $v_{\rm boundary}$ in Figure 4.18 can place an important constraint on the asphericity development of SESNe ejecta. The limited range of $v_{\rm boundary}$, within which $N_{\rm red}/N_{\rm blue}$ is balanced, suggests that the objects with narrow components shifted by −1500 to 1500 km s^{-1} can be explained by the moving blob or enhanced core density scenarios. However, the velocity of the blob can not be too large, otherwise more redshifted narrow components with large velocities would be expected.

Another possibility is the mis-classification of the DP/AS profiles. In the lower panels of Figure 4.17, we take

two AS objects, SNe 2000ew and 2008ax, which have narrow component offsets <−2000 km s^{-1}, as examples. The line profile classification in this work is dependent on the initial guess of the fitting, as described in Section 2.4. For these two objects, the initial guess of case (4), i.e., broad base plus a blueshifted narrow component, indeed gives a lower residual than the other cases, and therefore is the *numerical* best fit. However, the initial guess of case (1), i.e., blue- and redshifted components with equal width and intensity, also gives a reasonably good fit, as plotted by the green solid lines in the lower panels of Figure 4.17.

Taking SNe 2000ew and 2008ax as examples, we are inclined to believe at least some of the AS objects are Mis-classified, especially those with a trough located at ~6300 Å. The mis-classification explains the unusual enhancement of N_{blue}. It turns out that, if a fraction of the AS objects are reclassified to DP, the imbalance of the red- and blueshifted narrow components can be eased. However, for a specific object, it is difficult to decide which profile is more appropriate, as both the DP and AS profiles give similarly good fits, while the geometry origins are totally different. The fitting procedure also has an internal shortcoming; each component is assumed to be emitted by the Gaussian distributed emitter, while the intrinsic profile can be much more complicated. This also introduces uncertainty to the geometrical interpretation of the line profile.

Section 7. Conclusion

We have conducted a systematic study on the statistical properties of the SESNe nebular spectra. The sample includes 26 SNe IIb, 31 SNe Ib, 32 SNe Ic, 9 SNe Ic-BL, and 5 SNe Ib/ c. The investigation involves the morphology of the doublet [O I] λλ6300,6364, [O I] width, and the [O I]/[Ca II] ratio. The [O I] λλ6300,6364 is emitted from the oxygen-rich region, the amount of which is closely related to the properties of the core of the progenitor, especially its mass.Moreover, the [O I] line is also one of the strongest emissions in the nebular spectrum of SESN, and is usually unblended, making it an ideal tracer of the geometry of the O-rich ejecta.

The measurement of the line width is based on the fractional flux of the line, and the result is in good agreement with those estimated in previous works. Although we have discussed the line profile of the [O I], the measurement method of its width applied in this work does not assume any specific profile of the emission, allowing a more general discussion on the velocity scale of the ejecta.

To investigate the geometry of the oxygen-rich ejecta, a multi-Gaussian fitting is applied to the [O I] λλ6300,6363 of all of the nebular spectra in the sample. The same classification scheme of Taubenberger et al. (2009) is applied, and according to the best-fit parameter, the line profiles are classified as: Gaussian (GS), narrow core (NC; characterized by a Gaussian broad base plus a narrow component with center wavelength $|v_{shift}| < 1000$ km s^{-1}), double-peaked (DP; characterized by a horn-like profile, i.e., blue- and redshifted components with similar widths and intensities), and asymmetry (AS; characterized by a Gaussian broad base plus a narrow component with center wavelength $|v_{shift}| > 1000$ km s^{-1}).

We then conduct a statistical analysis on the [O I] profile, [O I] width, and the [O I]/[Ca II] ratio, along with the mutual relations between these quantities. For convenience, the observational fifindings are concluded as follows:

1. Although the sample size in this work is about 2.5 times as large as that of Taubenberger et al. (2009), the distributions of the line profile fractions are similar. The similarity between the results of the two samples suggests the sample size is sufficiently large to allow for statistical study.

2. For SNe IIb/Ib/Ic, the distributions of the line profiles are consistent with each other, which indicates the effects of the helium-rich layer and the small amount of the residual hydrogen envelope of SNe IIb are limited. On the other hand, there is a hint (at the 1σ level) that the distribution of the line profiles of SNe Ic-BL is different from canonical SESNe (SNe IIb/Ib/Ic).

3. The distributions of the [O I]/[Ca II] ratio of SNe IIb and Ib are similar, but the average ratio for SNe IIb/Ib is significantly smaller than SNe Ic/Ic-BL. This result is consistent with the finding in Fang et al. (2019).

4. The [O I] width shows a similar sequence: it is larger for SNe Ic/Ic-BL than SNe IIb/Ib. The average velocity of SNe Ic-BL, inferred from the line width, is only slightly larger than the canonical SNe. It seems that the velocity of the innermost region is not strongly correlated with the velocity of the outermost ejecta. We leave the systematic investigation on the relation between the velocities measured from the early- and nebular-phase spectra to future works.

5. A significant correlation between the [O I]/[Ca II] ratio and the [O I] width is discerned, where objects with large [O I]/[Ca II] tend to have fast-expanding ejecta. The correlation is dependent on the SN subtypes. For SNe IIb/Ib, the correlation is significant, but can not be discerned for SNe Ic/Ic-BL.

6. The above correlation between the [O I]/[Ca II] ratio and the [O I] width is found to be strong for objects showing a specific line profile. Among the line profile classes, NC objects have the tightest correlation, followed by DP/AS, then GS.

7. The dependence of the line profile on the [O I]/[Ca II] ratio is also observed. The average [O I]/[Ca II] of GS is the largest, followed by AS/NC, then DP objects. By dividing the sample into five groups with an equal number of members and calculating the fractions of the line profiles in each group, we find a steadily increasing tendency for the fraction of GS objects when [O I]/[Ca II] increases, while the fraction of DP objects goes to the opposite direction. Meanwhile, the fractions of NC/AS objects are not monotonic functions of [O I]/[Ca II].

To interpret the observational results, it is crucial to connect the observables to the theoretical models. In this work, we use the [O I]/[Ca II] ratio as the measurement of progenitor CO core mass, as predicted by several nebular SESN models (Fransson & Chevalier 1989; Jerkstrand et al. 2015a). The line fitting procedure is applied to the bipolar explosion models of Maeda et al. (2008) to qualitatively constrain the ejecta geometry. The observational results can be interpreted as follows:

1. For the canonical SNe, the material above the CO core (helium-rich layer and the residual hydrogen envelope) has a limited effect on the ejecta geometry.

2. More than 50% of the objects can not be interpreted by the spherically symmetric ejecta. The deviation from spherical symmetry is commonly seen for all types of SESNe.

3. The fraction of the DP objects is too low for the "strictly" bipolar explosion to be a majority. However, if we discard the condition of perfect axisymmetry and symmetry between the two hemispheres, and further combine the GS and NC profiles as "single-peak" profile and the DP and AS profiles as "non-single" profile, the bipolar explosion can account for the observed line profile fractions of the full sample. If this is the case, the deviation of the observed line profiles from the specific bipolar model sequence can be used to further constrain the nature of the explosion. We conclude that a large fraction of SESNe should have a non-axisymmetry configuration or imbalance in the two hemispheres to explain the distribution of the line profiles.

4. The progenitors of SNe Ic/Ic-BL have, on average, a more massive CO core than SNe IIb/Ib. The helium-rich layer is most likely stripped by the mass-dependent stellar wind.

5. The correlation between the CO core mass and expansion velocity of the ejecta, inferred from the line width, can not be explained by the constant kinetic energy for different progenitors. In Chapter 5, we will show that the correlation can be explained by assuming the kinetic energy is tightly correlated with the progenitor CO core mass.

6. Taking the DP profile as an indicator of the non-spherical ejecta, especially those with bipolar configurations, the relation between the [O I]/[Ca II] and DP fraction suggests the ejecta geometry is dependent on the progenitor CO core mass. However, the profifile of [O I] itself is not enough to reveal the geometry of the full ejecta. To firmly establish the relation between the progenitor CO core mass and the ejecta geometry, we thus need another probe of the ejecta with bipolar configuration, which should be independent from [O I]. The investigation on this topic will be presented in Chapter 6.

There remain uncertainties of the theoretical interpretation to the observational relations. (1) Our understanding on the important observable, [O I]/[Ca II], along with its relation with the physical properties (CO core mass, kinetic energy, calcium pollution, etc.), is highly dependent on the current He star model spectra. (2) The line fitting procedure and the classification scheme proposed by Taubenberger et al. (2009) are empirical. The geometrical interpretation of the line profile is complicated by the degeneracy of the fitting, as exemplified by SNe 2000ew and 2008ax; they are originally classified as AS, but the DP profile also provides a reasonably good fit. The inference from the line profile to the ejecta geometry is not straightforward. To better connect the observation to the properties of the SESNe progenitor, a sophisticated radiative transfer modeling of the ejecta involving different geometrical configurations, viewing angles, and randomly distributed moving blobs, is required.

The authors would like to thank Takashi Nagao, Luc Dessart, and Tomoya Takiwaki for the very helpful and enlightening discussions. The authors would like to thank the anonymous reviewer for comments that helped to improve the article. Q.F. acknowledges support by Japan Society for the Promotion of Science (JSPS) KAKENHI grant (20J23342). K.M. acknowledges support by JSPS KAKENHI grant (20H00174, 20H04737, 18H05223). M.T. acknowledges support by MEXT/JSPS KAKENHI grant (17H06363, 19H00694, 20H00158, 20H00179). H.K. is funded by the Academy of Finland projects 324504 and 328898.

This research is based (in part) on data collected at Subaru Telescope, which is operated by the National Astronomical Observatory of Japan. We are honored and grateful for the opportunity of observing the universe from Maunakea, which has cultural, historical, and natural significance in Hawaii.

Software: IRAF (Tody 1986, 1993); LAcosmic (van Dokkum 2001); SciPy (Virtanen et al. 2020); NumPy (Harris et al. 2020); Astropy (Astropy Collaboration et al. 2013, 2018); Matplotlib (Hunter 2007), R (R Core Team 2021), *locfit* (Loader 1999, 2018).

Appendix A: SNe in This Chapter

Table 4A-1. **The list of SNe in this Chapter.**

Object	Type	Date (YY/MM/DD)	Phase	Redshift	$E(B-V)$	Profile	Reference
1987K	IIb	88/02/24	211	0.0027	0.36(+)	NC	F88
1993J	IIb	93/11/07	203	-0.0001	0.19	AS	M00,J15
1996cb	IIb	97/07/01	176	0.0030	0.03	AS	Q99
2001ig	IIb	02/10/08	274	0.0066	0.10	AS	M07a,S09a
2003bg	IIb	03/11/29	254	0.0049	0.02	AS	H09
2006G	IIb	06/06/30	169	0.0171	0.36(+)	NC	This work
2006T	IIb	06/11/26	284	0.0086	0.08	DP	M07b,M08a,M14
2007ay	IIb	07/11/05	>190	0.0147	0.36(+)	GS	This work
2008aq	IIb	08/06/26	108	0.0075	0.36(+)	AS	M14
2008ax	IIb	08/11/24	245	0.0019	0.40	AS	T11,M14
2008bo	IIb	08/10/27	195	0.0053	0.08	AS	S19
2008ie	IIb	09/10/27	316	0.0136	0.36(+)	AS	This work
2009C	IIb	09/10/26	297	0.0226	0.36(+)	DP	This work
2009K	IIb	09/10/26	261	0.0113	0.36(+)	NC	This work
2009ka	IIb	10/05/06	200	0.0175	0.36(+)	NC	This work
2010as	IIb	10/08/05	130	0.0078	0.44	DP	F14
2011dh	IIb	11/12/24	187	0.002	0.07	NC	S13,E14,E15
2011ei	IIb	12/06/18	311	0.0089	0.24	GS	M13a
2011fu	IIb	12/07/20	282	0.0185	0.10	AS	MG15
2011hs	IIb	12/06/21	211	0.0057	0.17	NC	B14
2012P	IIb	12/08/08	197	0.0045	0.29	DP	F16
2012dy	IIb	12/12/23	nebular	0.0103	0.36(+)	AS	Y12
2013ak	IIb	13/09/13	179	0.0035	0.30	NC	Y12
2013bb	IIb	14/03/02	332	0.0190	0.30	GS	Y12,S19
2013df	IIb	14/02/04	223	0.0024	0.10	NC	MG14,M15a
ASASSN-14az	IIb	14/11/25	189	0.0067	0.36(+)	AS	S19
1985F	Ib	85/04/01	280	0.0002	0.23	NC	F86
1990I	Ib	91/04/21	357	0.0097	0.12	NC	E04
1990U	Ib	91/01/06	189	0.0081	0.52	DP	G94, M01,T09,M14
1997X	Ib	97/05/13	103	0.0035	0.18	GS	G02,T09
1999dn	Ib	00/09/01	379	0.0090	0.10	GS	B11

2000ew	Ib	01/03/17	110	0.0033	0.36(+)	AS	T09
2002dz	Ib	02/08/10	nebular	0.0184	0.36(+)	DP	S19
2004ao	Ib	04/11/14	250	0.0059	0.12	DP	E11,S19
2004dk	Ib	05/05/11	263	0.0052	0.34	AS	M08b, D11, M14,S17
2004gn	Ib	05/07/06	217	0.0061	0.36(+)	AS	M08a
2004gq	Ib	05/08/26	249	0.0059	0.25	AS	M08a,M08b,D11,M14
2004gv	Ib	05/08/26	242	0.0200	0.25	GS	M08a, M08b,M14
2005bf	Ib	05/12/11	213	0.0186	0.14	DP	F06,M14
2006F	Ib	06/06/30	175	0.0139	0.54	NC	G06, M08a,D11
2006ep	Ib	06/12/24	104	0.0152	0.36(+)	NC	This work
2006gi	Ib	07/02/10	145	0.0094	0.38	NC	T09,E11
2006ld	Ib	07/07/17	258	0.0140	0.36(+)	AS	T09
2007C	Ib	07/06/20	155	0.0056	0.64	AS	T09, D11,M14
2007Y	Ib	07/09/22	200	0.0040	0.11	AS(NC)	S09b
2007uy	Ib	08/06/06	141	0.0063	0.79	NC(AS)	R13,M14
2008D	Ib	08/06/07	140	0.0072	0.65	AS	M09
2008fd	Ib	09/07/23	330	0.0181	0.36(+)	GS	This work
2008im	Ib	09/08/18	232	0.0090	0.36(+)	GS	This work
2009jf	Ib	10/06/19	245	0.0068	0.12	NC	S11,V11,M14
2012au	Ib	12/12/19	284	0.0045	0.06	AS(NC)	M13b
iPTF13bvn	Ib	14/02/21	234	0.0045	0.07	AS(NC)	F16
2014C	Ib	14/08/25	221	0.0029	0.75	DP	S19
2014ei	Ib	15/03/27	142	0.0148	0.36(+)	GS	S19
2015Q	Ib	16/01/07	212	0.0078	0.36(+)	NC	S19
2015ah	Ib	16/01/07	152	0.0160	0.10	NC	S19
PS15bgt	Ib	15/12/17	147	0.0090	0.23	GS	S19
1987M	Ic	88/02/25	157	0.0043	0.45	GS	F90,J91
1990aa	Ic	91/01/23	140	0.0170	0.36(+)	GS	M01
1991A	Ic	91/04/07	96	0.0105	0.42	GS	M01
1991N	Ic	92/01/09	>286	0.0035	0.12	GS	F91, M01,M08
1994I	Ic	94/09/02	146	0.0015	0.45	AS	W94, F95, R96,M14
1996aq	Ic	97/04/02	228	0.0055	0.36(+)	AS	N96,T09
1996D	Ic	96/09/10	214	0.0149	0.36(+)	GS	D96,T09
1997B	Ic	97/09/23	252	0.0095	0.36(+)	GS	T09
1997dq	Ic	98/05/30	210	0.0011	0.33	DP	N97, M01, T09,M14
2003gf	Ic	03/11/29	158	0.0087	0.36	AS	S19
2004aw	Ic	04/11/14	232	0.0159	0.37	NC	T06,M14
2004fe	Ic	05/07/06	240	0.0180	0.32	DP	M08a,D11,M14
2004gk	Ic	05/07/10	223	-0.0005	0.47	AS	M08a,D11,M14
2004gt	Ic	05/05/24	152	0.0046	0.10	DP	GY05, T09,M14
2005aj	Ic	05/08/25	188	0.0085	0.36(+)	AS	This work
2005bj	Ic	05/08/25	136	0.0222	0.36(+)	NC	This work
2005kl	Ic	06/06/30	213	0.0034	0.29	DP	M08a, M14,D11
2005kz	Ic	06/06/30	215	0.0278	0.46	AS	F05, M08a,D11

2006ck	Ic	07/01/24	246	0.0245	0.39	NC(AS)	C06, M08a,M14
2007gr	Ic	08/02/12	170	0.0020	0.09	NC	S19
2007rz	Ic	08/04/01	115	0.0135	0.36(+)	AS	M14
2008fo	Ic	09/04/05	240	0.0289	0.36(+)	AS(NC)	This work
2007hb	Ic	08/01/11	140	0.0222	0.36(+)	GS	M14
2008hh	Ic	09/08/18	269	0.0196	0.26	GS	This work
2009jy	Ic	10/05/06	204	0.0103	0.36(+)	AS	This work
2010mb	Ic	11/03/04	248	0.1325	0.01	NC	B14
2011bm	Ic	12/01/22	263	0.0212	0.06	AS	V12
PTF12gzk	Ic	13/06/10	299	0.0139	0.14	AS	S19
2013ge	Ic	14/04/28	156	0.0045	0.07	NC	D16
2014L	Ic	14/06/29	142	0.0078	0.67	NC	Z18,S19
2014eh	Ic	15/06/16	210	0.0106	0.36(+)	GS	S19
iPTF15dtg	Ic	16/10/31	327	0.0544	0.06	DP	T16,T19
1997ef	Ic-BL	98/09/21	282	0.0117	0.00	NC	I00, M00, M01,M14
1998bw	Ic-BL	98/11/26	198	0.0096	0.06	NC	P01, C11,M16
2002ap	Ic-BL	02/08/09	183	0.0021	0.08	NC	F03, Y03,M16
2005nb	Ic-BL	06/06/30	183	0.0235	0.36(+)	AS	M08a, M14,Q06
2006aj	Ic-BL	06/09/21	206	0.0330	0.15	NC	M06, M14,M16
2007D	Ic-BL	07/09/18	252	0.0232	0.91	NC	This work,D16
2007I	Ic-BL	07/07/15	182	0.0215	0.36(+)	AS	B07, T09,M14
PTF10qts	Ic-BL	10/04/27	231	0.0912	0.02	GS	W14
2012ap	Ic-BL	12/09/23	272	0.0212	0.45	AS	M15b
1990W	Ib/c	91/02/21	186	0.0042	0.36(+)	NC	T09
1990aj	Ib/c	91/03/10	180	0.0053	0.36(+)	NC	M01
1995bb	Ib/c	96/01/21	nebular	0.0055	0.36(+)	GS	M14
2005N	Ib/c	05/01/22	nebular	0.0163	0.36(+)	AS	H08
2012fh	Ib/c	12/11/14	nebular	0.0017	0.36(+)	DP	S19

References: F90: Filippenko et al. (1990);F86: Filippenko & Sargent (1986); F88: Filippenko (1988); E90: Evans et al. (1990); F91: Filippenko & Korth (1991); J91: Jeffery et al. (1991); G94: Gómez & López (1994); W94: Wheeler et al. (1994); F95: Filippenko et al. (1995); D96: Drissen et al. (1996); N96: Nakano et al. (1996); R96: Richmond et al. (1996b); N97: Nakano et al. (1997); Q99: Qiu et al. (1999); I00: Iwamoto et al. (2000); M00: Matheson et al. (2000b); M01: Matheson et al. (2001); P01: Patat et al. (2001); G02: Gómez & López (2002); ; F03: Foley et al. (2003); Y03: Yoshii et al. (2003); E04: Elmhamdi et al. (2004);F05: Filippenko et al. (2005); GY05: Gal-Yam et al. (2005); C06: Colesanti et al. (2006) ;F06: Folatelli et al. (2006); G06: Green (2006); M06: Modjaz et al. (2006);Q06: Quimby et al. (2006);T06: Taubenberger et al. (2006); B07: Blondin et al. (2007);M07a: Maund et al. (2007); M07b: Modjaz (2007); H08: Harutyunyan et al. (2008); M08a: Maeda et al. (2008); M08b: Modjaz et al. (2008); H09: Hamuy et al. (2009); M09: Modjaz et al. (2009); S09a: Silverman et al. (2009); S09b: Stritzinger et al. (2009); T09: Taubenberger et al. (2009); B11: Benetti et al. (2011); C11: Clocchiatti et al. (2011);D11: Drout et al. (2011); E11: Elmhamdi et al. (2011); T11: Taubenberger et al. (2011); S11: Sahu et al. (2011); V11: Valenti et al. (2011); V12: Valenti et al. (2012); Y12: Yaron & Gal-Yam (2012); M13a: Milisavljevic et al. (2013a); M13b: Milisavljevic et al. (2013b); R13: Roy et al. (2013); S13:Shivvers et al. (2013); B14: Bufano et al. (2014); BA14: Ben-Ami et al. (2014);E14: Ergon et al. (2014); F14: Folatelli et al. (2014); M14: Modjaz et al. (2014); MG14: Morales-Garoffolo et al. (2014); W14: Walker et al. (2014); E15: Ergon et al. (2015); J15: Jerkstrand et al. (2015a); M15a: Maeda et al. (2015); M15b: Milisavljevic et al. (2015b); MG15: Morales-Garoffolo et al. (2015); D16: Drout et al. (2016); F16: Fremling et al. (2016); M16: Modjaz et al. (2016);T16: Taddia et al. (2016); S17: Shivvers et al. (2017); Z18: Zhang et al. (2018); S19: Shivvers et al. (2019); T19: Taddia et al. (2019).

Appendix B: Line Fitting Results

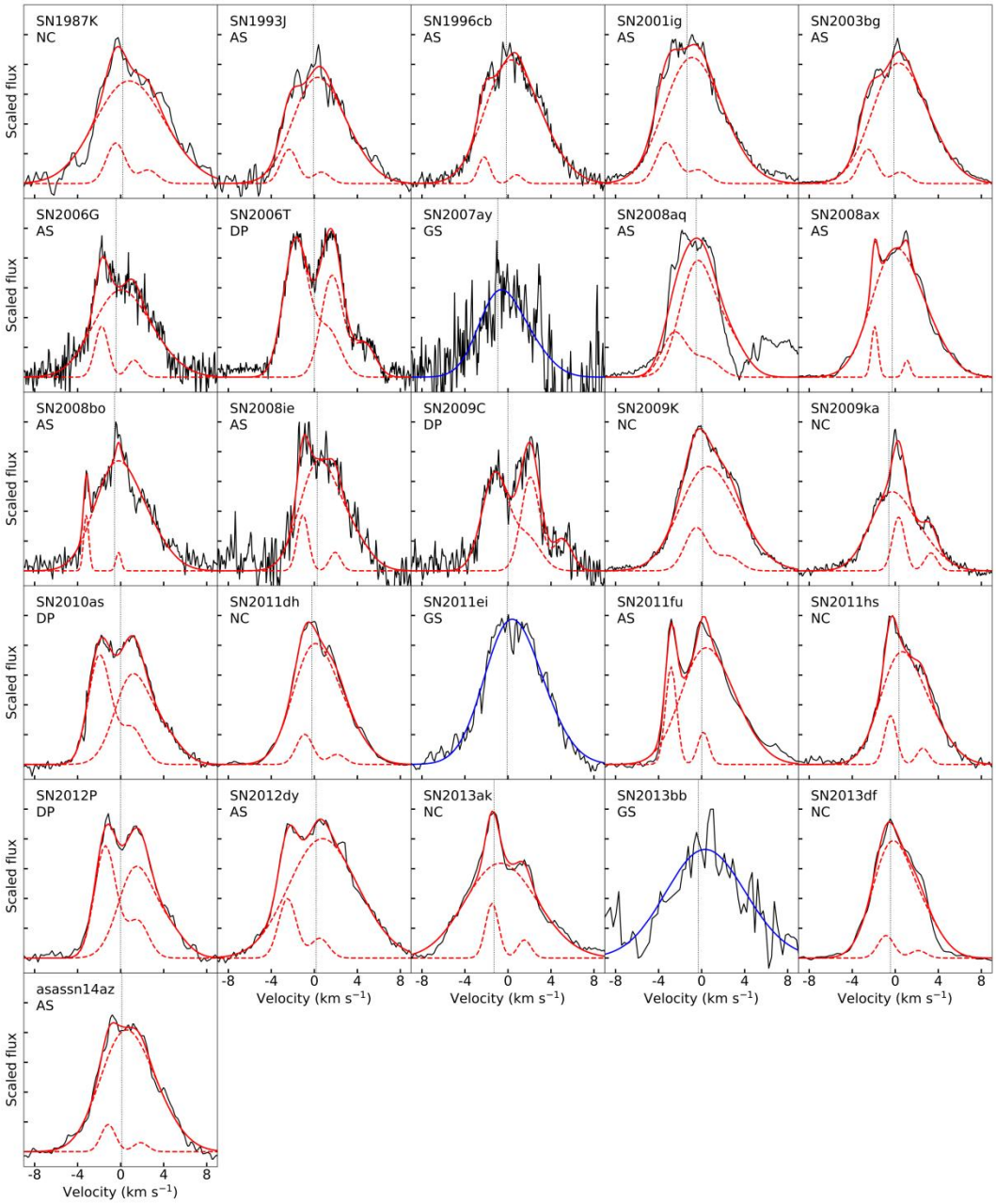

Figure 4B-1. **Observed [O I] of the SNe IIb in the sample fitted by multi-Gaussians.** The spectra (black solid lines) are already subtracted by the background and the symmetric Hα/[N II]. The blue solid lines are the results of a one-component fit. The red solid lines are the results of a two-component fit, and the red dashed lines are the components. The vertical dotted lines are zero velocity (6300 Å) for DP objects or the center wavelength of the Gaussian broad base for GS, NC, or AS objects for reference.

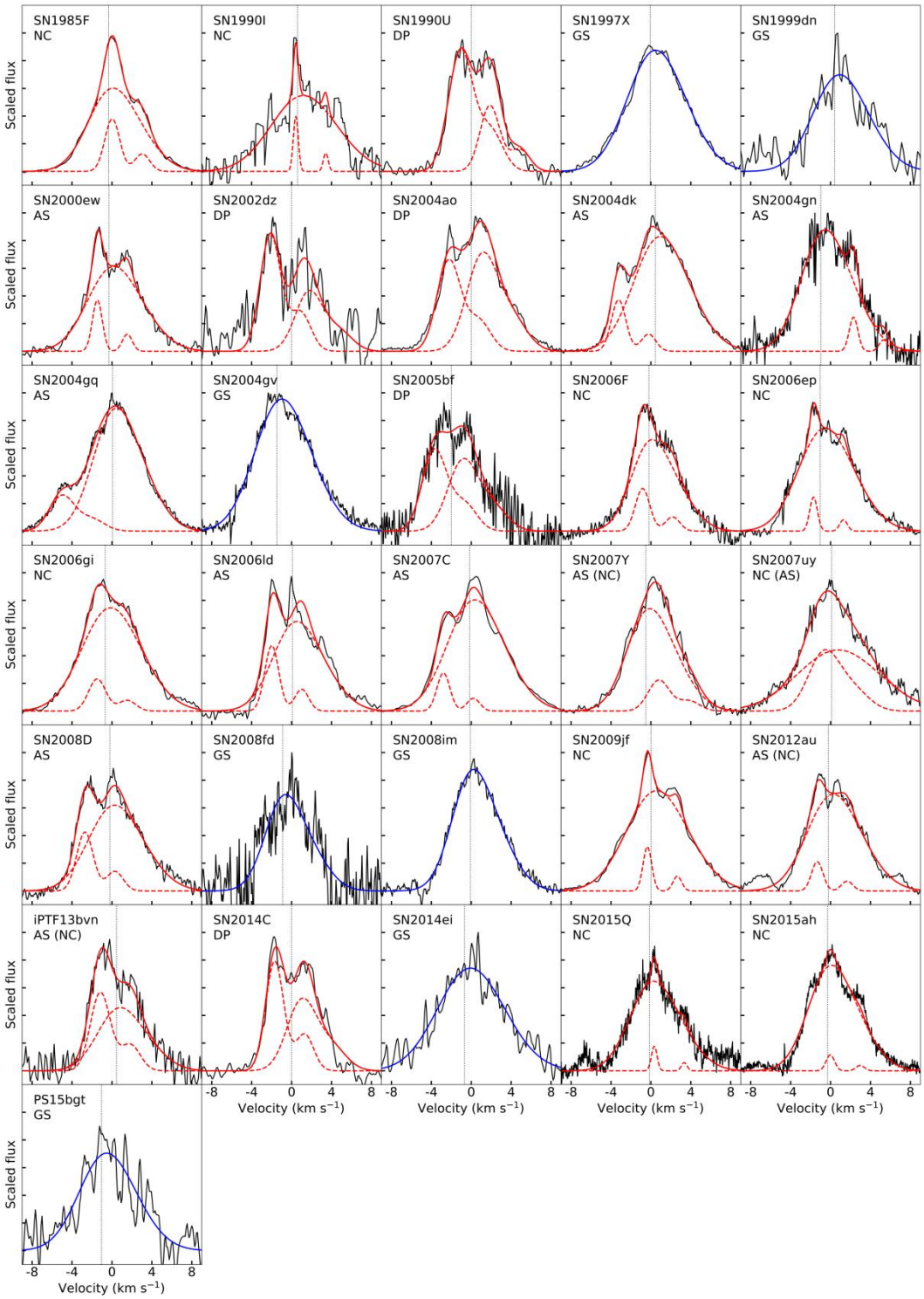

Figure 4B-2. **Same as Figure 4B-1, but for the SNe Ib sample.** The [Ca II] of SN 2005bf is blueshifted by ~2000 km s^{-1} , which is taken as the "center" of SN 2005bf.

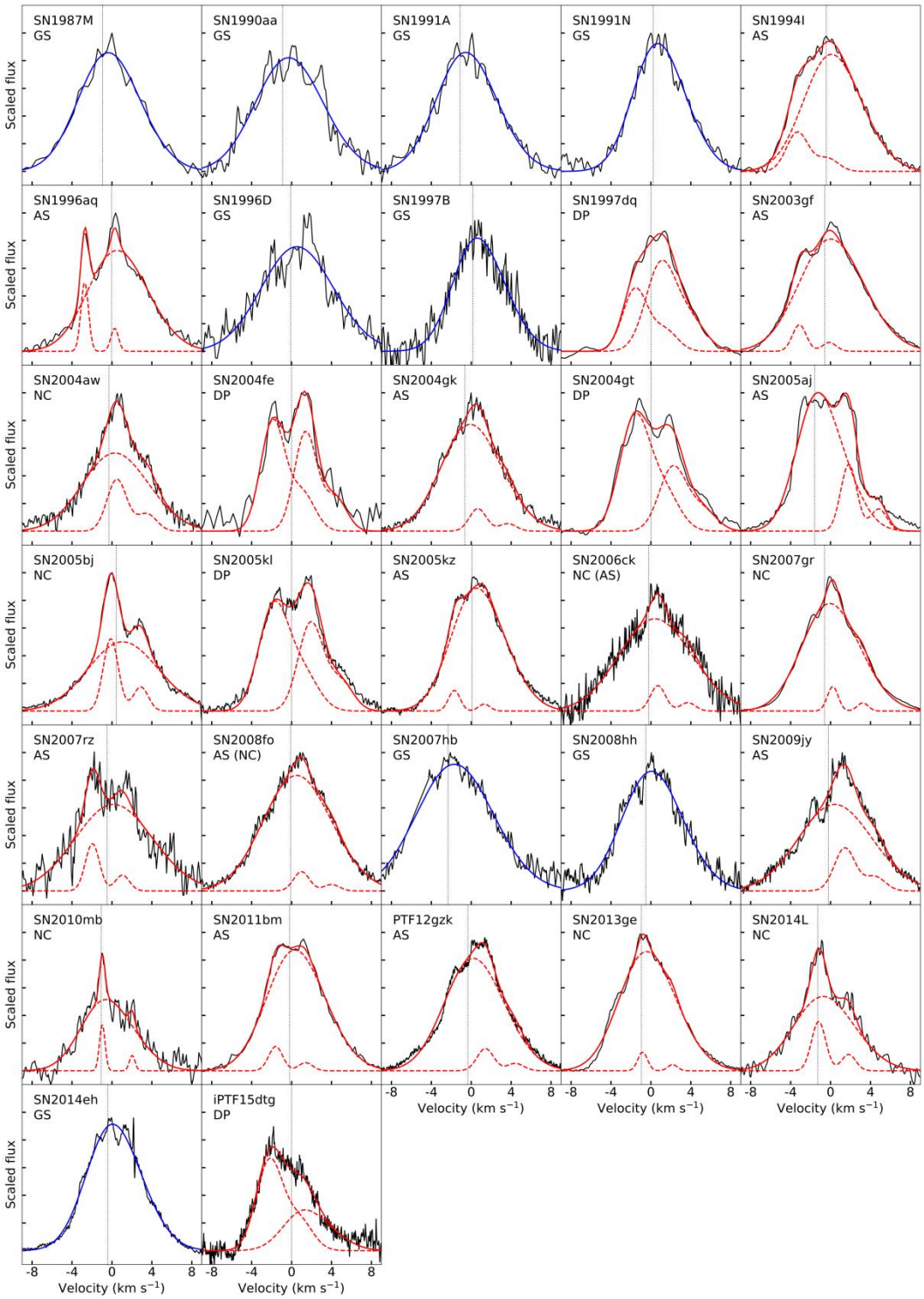

Figure 4B-3. **Same as Figure 4B-1, but for the SNe Ic sample.**

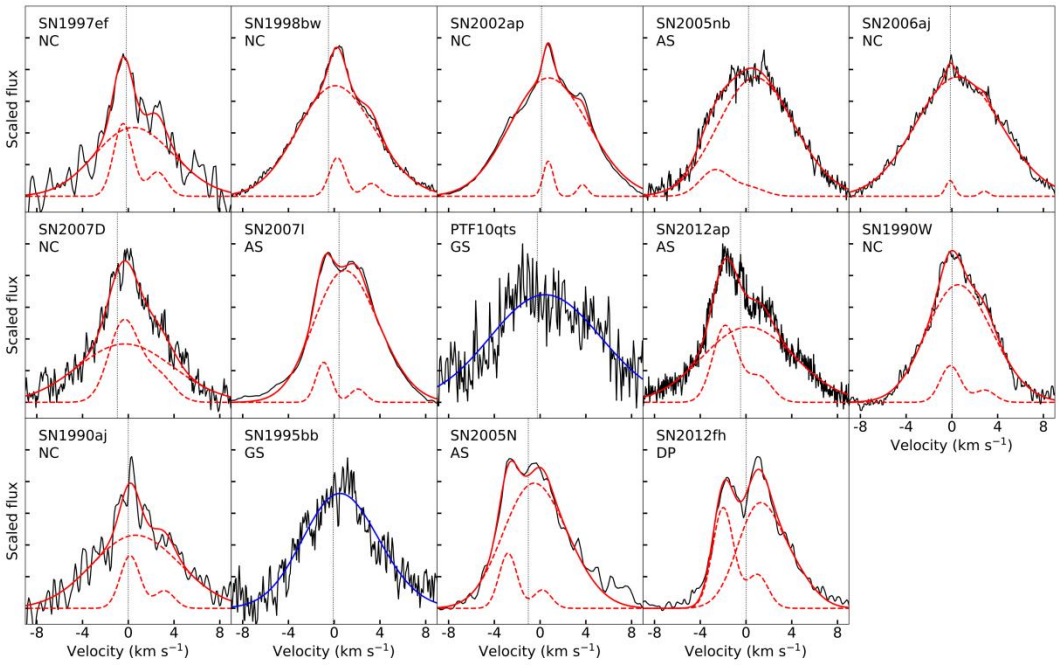

Figure 4B-4. **Same as Figure 4B-1, but for the SNe Ic-BL and SNe Ib/c sample.**

Appendix C: Examples of Multiphase Nebular Spectra

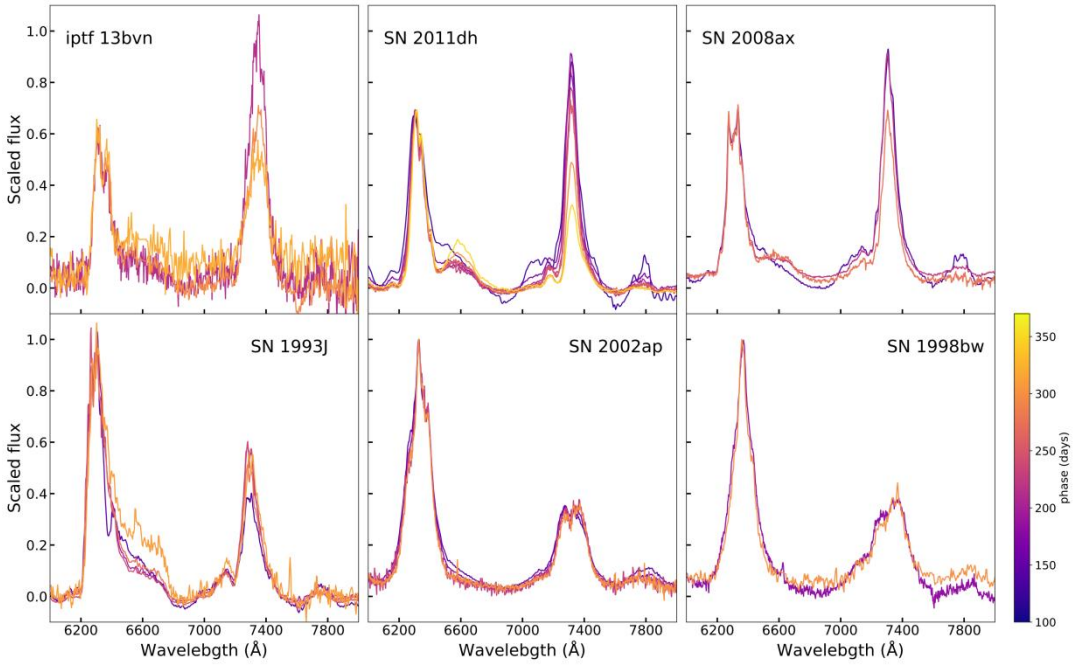

Figure 4C-1.**The evolution of [O I]/[Ca II] of well-observed SNe.** The spectra are scaled to the peak of the [O I]. The colors of the lines indicate the phase of the spectra, with the late-phase spectra plotted with the colors at the red end. The SNe with spectra plotted in the upper panels have fast evolving [O I]/[Ca II] and relatively low [O I]/[Ca II] (<1) at ~200 days. The SNe with spectra plotted in the lower panels are examples with relatively large [O I]/[Ca II] (>1.5), and their [O I]/[Ca II] hardly evolve.

Chapter 5. Constraint on the ejecta dynamics II: Theory

Fang, Q., & Maeda, K., submitted to ApJ

The relation between the progenitor mass and the kinetic energy of the explosion is a key toward revealing the explosion mechanism of stripped-envelope (SE) core-collapse (CC) supernovae (SNe). Here, we present a method to derive this relation using the nebular spectra of SESNe, based on the correlation between the [O I]/[Ca II], which is an indicator of the progenitor mass, and the width of [O I], which measures the expansion velocity of the oxygen-rich material. To explain the correlation, the kinetic energy ($E_{\rm K}$) is required to positively correlated with the progenitor mass as represented by the CO core mass ($M_{\rm CO}$). We demonstrate that the SNe IIb/Ib and SNe Ic/Ic-BL follow the same $M_{\rm CO}$-$E_{\rm K}$ scaling relation, which suggests the helium-rich and helium-deficient SNe share the same explosion mechanism. The $M_{\rm CO}$-$E_{\rm K}$ relation derived in this work is compared with the ones from early phase observations. The results are largely in good agreement. Combined with early phase observation, the method presented in this work provides a chance to scan through the ejecta from the outermost region to the dense inner core, which is important to reveal the global properties of the ejecta and constrain the explosion mechanism of core-collapse supernovae.

Section 1. Introduction

Core-collapse supernovae (CCSNe) mark the final stage of the evolution of a massive star (zero-age main-sequence mass larger than $8M_{\odot}$). The explosion mechanism of this catastrophic event is yet to be clarified. How the properties of the explosion process depends on those of the progenitor is an important open problem in astronomy.

CCSNe are diverse in observable signatures, leading to classification into different subtypes. Type II supernovae (SNe II) show strong hydrogen features in their optical spectra. CCSNe lacking permanent hydrogen signatures are classified as stripped-envelope supernovae (SESNe). Among them, type Ib SNe (SNe Ib) do not exhibit hydrogen features, but their spectra are dominated by helium features. The spectra of type Ic SNe (SNe Ic) lack both hydrogen and helium features. Type IIb SNe (SNE IIb) are transitional events between SNe II and Ib. These objects initially show strong hydrogen signatures, but their spectra eventually resemble to those of SNe Ib as the ejecta continue to evolve. SNe Ic can be further classified as normal SNe Ic and broad line SNe Ic (SNe Ic-BL). The latter type is characterized by the broad absorption features and its (occasion) association with a gamma-ray burst (Galama et al. 1998; Hjorth et al. 2003; Woosley & Bloom 2006). The readers are referred to Filippenko (1997) and Gal-Yam (2017) for the classification of SNe. The lack of hydrogen (or helium) in the spectra of SESNe indicates the hydrogen-rich envelope (or the helium-rich layer) has been stripped away before the explosion. Several channels may be responsible for the pre-SN mass-loss, including binary interaction, stellar wind, or the combination of both (Heger et al. 2003; Groh et al. 2013; Smith 2014; Yoon 2015; Fang et al. 2019).

Understanding how the explosion process is dependent on the state of the progenitor is a key toward revealing the explosion mechanism of CCSNe. We thus need independent measurements of the progenitor properties and the explosion parameters. The relation between the two basic parameters, i.e., the progenitor mass and the amount of the kinetic energy, is particularly important but not established. The pre-explosion image, which allows one to directly identify the progenitor, is only feasible to a very limited sample, especially lacking those of SESNe. So-far the pre-explosion image is only available for two SNe Ib (iPTF 13bvn, Bersten et al. 2014 and SN 2019yvr, Kilpatrick et al. 2021). Currently, modeling of the bolometric light curve is the main tool to infer the properties of the progenitor and the explosion, and most of them are based on the model by Arnett (1982). For the hydrogen-poor SNe, the ejecta is mainly powered by the decay of the radioactive 56Ni, and the diffusion time scale determines the width of the light curve. With the photospheric velocity compiled from the spectra at maximum light, the ejecta mass, the kinetic energy, and their mutual relation can be determined. However, previous research based on this method is mainly conducted at the photospheric phase, i.e., the period during which the ejecta is still optically thick, and the analyses constrain the nature of the outermost region of the ejecta. The interpretation regarding the global properties of the ejecta thus relies on extrapolation of the ejecta properties inward.

In this work, we propose a method to constrain the relation between the progenitor mass and the kinetic energy of SESNe based on the observation at nebular phase, i.e., several months after the explosion when the ejecta becomes transparent. Fang et al. (2022) report a correlation between the [O I]/[Ca II] ratio, which serves as an indicator of the progenitor mass (Fransson & Chevalier 1989; Jerkstrand et al. 2015a; Kuncarayakti et al. 2015; Jerkstrand 2017; Fang et al. 2019; Dessart et al. 2021; Fang et al. 2022), and the [O I] width, which measures the characteristic expansion velocity of the oxygen-rich material (Taubenberger et al. 2009; Maurer et al. 2010a), using a large sample of nebular spectra of 103 SESNe. In contrast to the observation, at photospheric phase, the nebular phase observation is sensitive to the properties in the dense innermost region where the explosion is initialized, and thus the explosion mechanism.

To build up the connection between the progenitor CO core mass $M_{\rm CO}$ and the kinetic energy $E_{\rm K}$, we explode the helium star and CO star models generated by the one-dimensional stellar evolution code, Modules for Experiments in Stellar Astrophysics (MESA, Paxton et al. 2011, 2013, 2015, 2018, 2019), with a wide range of kinetic energy injected, using the SuperNova Explosion Code (SNEC, Morozova et al. 2015). Omitting detailed spectrum synthesis calculations which would require massive computations, including a detailed treatment of the non-local thermal equilibrium (non LTE), we focus on the scaling relations between the model and the observed quantities. We especially apply the relation between the [O I]/[Ca II] ratio and the oxygen mass $M_{\rm O}$ based on the specific models by Jerkstrand et al. (2015a). The properly-weighted velocity is linked to the observed line width. The $M_{\rm CO}$-$E_{\rm K}$ relation is then established by linking the models to the [O I]/[Ca II]-[O I] width correlation.

Finally, the $M_{\rm CO}$-$E_{\rm K}$ relation established from the nebular phase observation is compared to those derived from early-phase observation. The early phase and late phase observation are indeed probing different regions of the ejecta. The combined analysis of the observations from these two periods provides us a unique chance to scan through the ejecta from the outermost layer to the innermost region, which will be useful to reconstruct the full ejecta structure. Further, any possible inconsistency between the observations of early phase and nebular phase will help to clarify what is still missing in the current assumptions on the ejecta structure, and improve our understanding of the ejecta dynamics.

This Chapter is organized as follows. In Section 2, we describe the numerical approach, including the generation of the progenitor models, the mixing scheme, and the set up of the explosion. In Section 3, we introduce how the model quantities are connected to the observables, and derive the quantitative M_{CO}-E_K relation based on the [O I]/[Ca II]-[O I] width correlation. The possible affecting factors, including the dependence of [O I]/[Ca II] on EK and the degree of microscopic mixing, and the effect of macroscopic mixing on line width, are discussed in Section 4. The M_{CO}-E_K relation established in this work is compared with the ones derived from early phase observation in Section 5. The summary is left to Section 6.

Section 2. Numerical Approach

Section 2.1. *MESA: from pre-explosion to core-collapse*

The SN progenitor models are calculated using the one-dimensional stellar evolution code, Modules for Experiments in Stellar Astrophysics (MESA, Paxton et al. 2011, 2013, 2015, 2018, 2019). We start with MESA version 11701 test suites, example_make_pre_ccsn, to calculate the massive star evolution from the pre-main-sequence (pre-MS) to the Fe core infall. The zero-age-main-sequence masses (M_{ZAMS}) are 13, 15, 18, 20, 23, 25, and 28 $M_\odot$. For all the models, the metallicity is assumed to be Z = 0.02. No rotation is introduced.

This work mainly focuses on the pre-SN structure of the helium star (the progenitor of SNe IIb/Ib, if the hydrogen skin of SNe IIb is neglected) and the bare CO core (the progenitor of SNe Ic/Ic-BL), therefore the hydrogen envelope or the helium-rich layer should be removed before the explosion. There are several channels that may be responsible for the envelope-stripping process, i.e., binary mass transfer, stellar wind, or the combination of both (Heger et al. 2003; Groh et al. 2013; Smith 2014; Yoon 2015; Fang et al. 2019). However, after the helium burning is finished, the core structure will not be significantly affected by the presence or the absence of the helium/hydrogen envelope, therefore the detailed mass-loss mechanism is not important for the purpose of this work. The hydrogen envelope or the helium-rich layer is thus removed by hand. After the helium in the center is exhausted, the mass loss rate is manually changed to 10^{-3} (or 10^{-4}) $M_\odot$ yr^{-1} for removal of the H-rich envelope (or the He-rich layer),until the hydrogen (or helium) mass drops below 0.01 $M_\odot$ (or 0.12 $M_\odot$). Observationally, SNe Ic/Ic-BL have a larger progenitor CO core mass than SNe IIb/Ib (Fang et al. 2019), therefore the helium-rich layer is stripped only for models with MZAMS not less than 18 $M_\odot$. After the outer layers are removed, we calculate the evolution of the massive star without mass loss until the Fe-core collapse. The readers may refer to the inlists of example_make_pre_ccsn for more details.

In the upper panel of Figure 5.1, we show the pre-SN density structures of the helium stars with M_{ZAMS} = 13, 18, 23$M_\odot$, and the bare CO core with M_{ZAMS} = 18, 23$M_\odot$. The mass fractions of ^{4}He, ^{12}C, ^{16}O and ^{24}Mg for the helium star with M_{ZAMS} = 20$M_\odot$ is also plotted in the lower panel of Figure 5.1 for illustration. Some properties of the progenitor models are summarized in Table 5.1. In this work, the outer boundary of the CO core is defined to be the mass coordinate with helium mass fraction X_{He} = 0.5 (as marked by the black star in the lower panel of Figure 5.1); the CO core mass (M_{CO}) refers to the mass coordinate at the CO core outer boundary. The mass of the oxygen is

$$M_O = \sum X_O(m_i)\Delta m_i, \quad (5.1)$$

where $X_O(m_i)$ is the oxygen mass fraction of the grid centered at m_i. The CO core mass (MCO) is strongly correlated with M_{ZAMS}. The linear regression (in logrithium) gives

$$M_{\rm CO} \propto M_{\rm ZAMS}^{1.53\pm0.05}. \qquad (5.2)$$

The oxygen mass $M_{\rm O}$ is also correlated with $M_{\rm CO}$, and scales as

$$M_{\rm O} \propto M_{\rm CO}^{1.74\pm0.10}. \qquad (5.3)$$

The above correlations are plotted in Figure 5.2. The effect of the attached helium-rich layer on the CO core properties is negligible.

In the following, we use the term HeXX (or COXX) to represent helium star (or bare CO star) model with $M_{\rm ZAMS}$ = XX $M_{\odot}$. For example, He15 and CO20 represent a helium star with $M_{\rm ZAMS} = 15M_{\odot}$ and a bare CO star with $M_{\rm ZAMS} = 20M_{\odot}$ respectively.

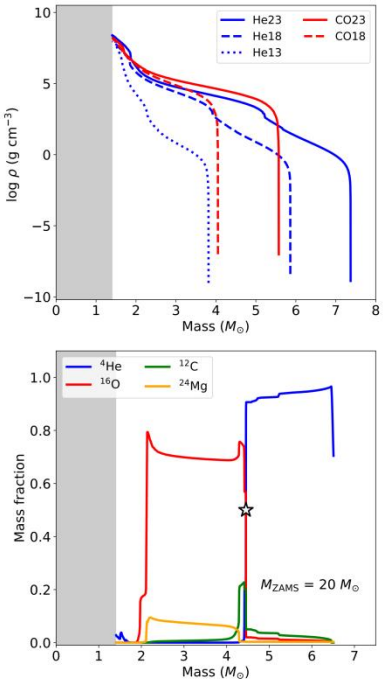

Figure 5.1. **Upper panel: the density structures of the He stars with $M_{\rm ZAMS}$ = 13, 18, 23 $M_{\odot}$, and the bare CO core with $M_{\rm ZAMS}$ = 18, 23 $M_{\odot}$; Lower panel: the mass fractions of ^{4}He, ^{12}C, ^{16}O and ^{24}Mg for the helium star with $M_{\rm ZAMS}$ = 20 $M_{\odot}$.** The star marks the mass coordinate of the CO core boundary. The shaded regions in the two panels represent the region collapsing into the compact remnant.

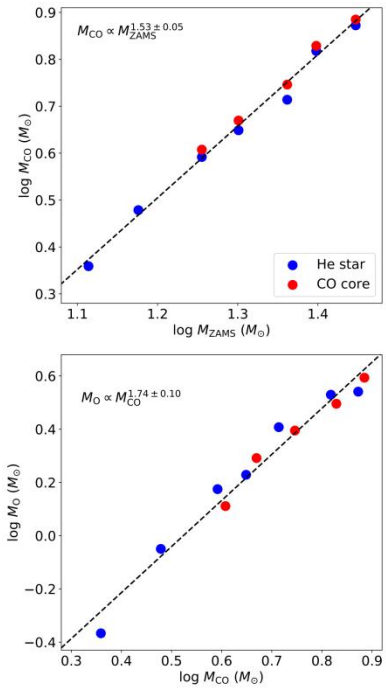

Figure 5.2. **Upper panel: the relation between the CO core mass and the M_{ZAMS} of the progenitor models; Lower panel: the relation between the oxygen mass and the CO core mass.**

Model	M_{ZAMS} ($M_\odot$)	$M_{pre\text{-}SN}$ ($M_\odot$)	M_{CO} ($M_\odot$)	M_O ($M_\odot$)
He13	13	3.82	2.27	0.43
He15	15	4.74	2.99	0.89
He18	18	5.86	3.90	1.50
He20	20	6.51	4.45	1.70
He23	23	7.37	5.18	2.56
He25	25	8.88	6.57	3.37
He28	28	9.96	7.45	3.47
CO18	18	4.05	3.94	1.29
CO20	20	4.67	4.58	1.96
CO23	23	5.57	5.49	2.48
CO25	25	6.74	6.62	3.13
CO28	28	7.67	7.54	3.92

Table 5.1. **Properties of the progenitor models.**

Section 2.2. *^{56}Ni mixing*

During the explosion shock wave propagation, Rayleigh-Taylor and Richtmyer-Meshkov instabilities will develop, resulting in effective mixing of the ejecta (Kifonidis et al. 2003, 2006; Wongwathanarat et al. 2015). Such instabilities are important to the dynamics of the ejecta, but cannot be accurately modeled by 1D simulations. The effect of large scale material mixing, with a focus on the radioactive energy source ^{56}Ni, have long been studied. However, the degree of mixing in the CCSNe ejecta, and its possible dependence on the SNe progenitor is difficult to constrain from observation. By studying the color curve evolution of SESNe,

Yoon et al. 2019) find evidence that the ^{56}Ni is only mildly mixed into the helium-rich layer of SNe IIb/Ib, while the ejecta of SNe Ic is fully mixed. This is also supported by the study on the evolution of photospheric velocity at very early phase. Moriya et al. (2020) calculate the photospheric velocity evolution of SESNe with different degrees of ^{56}Ni mixing, and the models are further applied to the individual object SN 2007Y. For this SN Ib, its photospheric velocity evolution matches well with the model where ^{56}Ni is only mixed into about half of the ejecta in the mass coordinate.

^{56}Ni is the explosive-burning product, and its distribution is not strongly constrained from the current models. In this work, ^{56}Ni is phenomenologically mixed with the method introduced as follow. First, 0.1 $M_{\odot}$ of ^{56}Ni is uniformly put in the innermost 10% (in mass coordinate) of the ejecta by hand. The ejecta is then artificially mixed by the ”boxcar” averaging introduced by Morozova et al. (2015)[11]. We define

$$f = \frac{X_{\rm Ni}(M_{\rm r} = 0.5 M_{\rm ejecta})}{X_{\rm Ni}(M_{\rm r} = 0)}, \quad (5.4)$$

i.e., the ratio of the ^{56}Ni fraction $X_{\rm Ni}$ at the mid-point of the ejecta and $X_{\rm Ni}$ at the center of the ejecta. In this work, this ratio is employed to characterize the mixing degree of the ejecta. For each progenitor model, the degree of mixing f is varied from 0.1 to 1.0 (”fully mixed”) with 0.1 increment by adjusting the width of the boxcar, as shown in the upper panel of Figure 5.3. The other elements in the ejecta are accordingly mixed by the boxcar averaging scheme. The ^{16}O distributions of the mixed ejecta with different f are shown in the middle (He20 model) and lower panels (CO20 model) in Figure 5.3. Yoon et al. (2019) characterized the ^{56}Ni distribution by

$$X_{\rm Ni}(M_{\rm r}) \propto \exp([\frac{M_{\rm r} - M_{\rm Fe}}{f_{\rm Y19} M_{\rm ejecta}}]^2), \quad (5.5)$$

Here, $M_{\rm Fe}$ is the mass of the remnant, which is 1.4 M in this work. By studying the early-phase color curve evolution of a sample of helium-rich SNe, Yoon et al. (2019) conclude that for these objects, the ^{56}Ni is only mixed up to the mid-point of the helium-rich envelope, or $f_{\rm Y19}$= 0.3 to 0.5, which corresponds to f = 0.368 in the present work. Therefore, in the following analysis, we employ f=0.368 as the default case, unlessexplicitly mentioned. The effect of large scale mixing is discussed in Section 4.

[11] The readers may refer to the notes of SNEC for the details of this procedure.

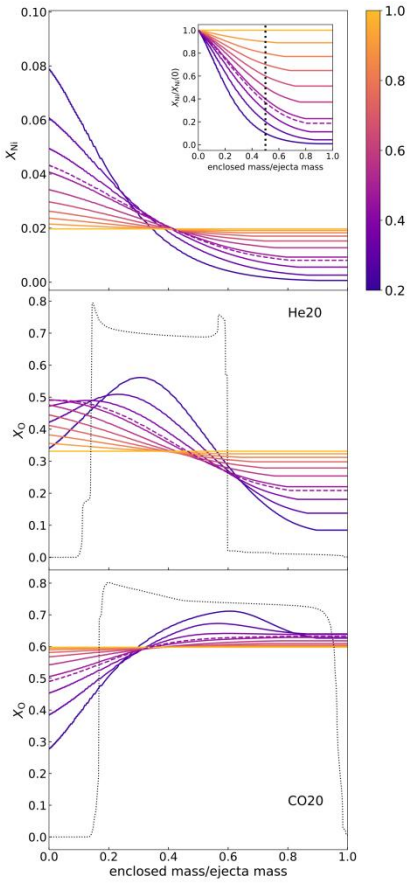

Figure 5.3. **Upper panel: the ^{56}Ni mass fraction of He20 model with different degrees of mixing**, which is defined by Equation (5.4) and are marked by different colors. The insert panel is the ^{56}Ni fraction divided by its maximum. The black dashed line marks the mid-point of the ejecta; **Middle panel: the ^{16}O mass fraction of He20 model with different degrees of mixing.** The ^{16}O mass fraction of the pre-SN model (unmixed) is shown by the black dotted line for comparison; **Lower panel: the ^{16}O mass fraction of CO20 model with different degrees of mixing.** The ^{16}O mass fraction of the pre-SN model is shown by the black dotted line for comparison.

Section 2.3. *SNEC: explosion hydrodynamics*

Once the progenitor models have evolved to the time of core collapse, they are used as the input models of the hydrodynamics simulation of a supernova explosion. In this work, we use the SuperNova Explosion Code (SNEC, Morozova et al. 2015) to solve the hydrodynamic evolution of the SN ejecta. Before the SNEC simulation, the materials are manually mixed as introduced above.

The explosion is initiated as the ”thermal bomb” mode, i.e., the explosion energy is initially injected into a small mass range (ΔM=0.1$M_\odot$) and the injection lasts for 0.2 seconds. We vary the final energies (thermal energies plus kinetic energies) of the explosions ($E_{\rm K}$) from $\sim 10^{51}$ erg to 10^{52} erg with 0.5×10^{51} erg increments. The inner 1.4$M_\odot$ is excised to account for the compact remnant formation.

The γ-ray deposition rates, density profiles and velocity profiles of the ejecta (t=220 days after the explosion) of He18 and CO18 models with different kinetic energies are plotted in Figure 5.4.

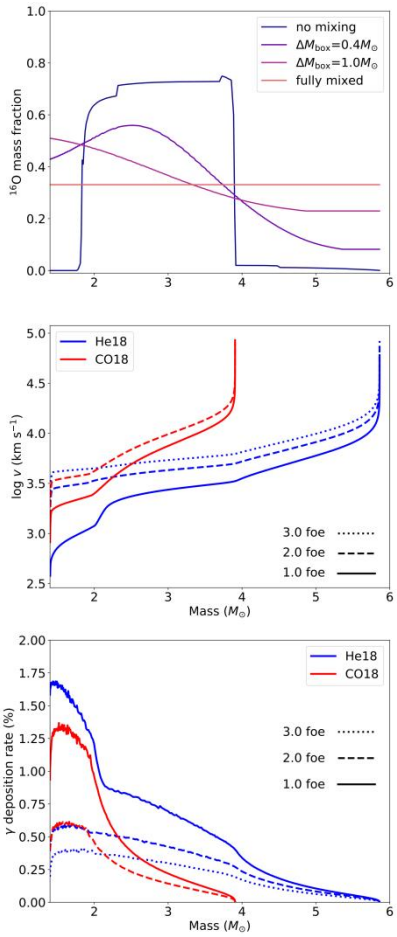

Figure 5.4. **The physical properties of the ejecta of He18 and CO18 models (labeled by different colors) with different kinetic energies (labeled by different line styles).** Upper panel: the γ-ray deposition rate; Middle panel: the density profile; Lower panel: the velocity profile. These properties are shown for 220 days after the explosion.

Section 3. Connecting models to observations

Section 3.1. *Oxygen mass and [O I]/[Ca II]*

The [O I]/[Ca II] ratio is frequently employed as the indicator for estimating the CO core mass of the progenitor. The oxygen mass is mainly determined by the progenitor CO core mass, to which the Ca mass is insensitive. However, the dependence of the [O I]/[Ca II] ratio on the O mass of the progenitor has not been quantitatively clarified from observation.

The SNe IIb spectral models of Jerkstrand et al. (2015a) provide a possible constrain on the connection between the [O I]/[Ca II] ratio and the O mass of the ejecta. We apply the same method as Fang et al. (2022) to the model spectra to measure the [O I]/[Ca II] ratios, which are then compared with the O mass of the progenitor models in Jerkstrand et al. (2015a), as shown in Figure 5.5. The average phase of the nebular SESNe in the sample of Fang et al. (2022) is 220 ± 80 days, therefore the measurement is limited to the model spectra at 150, 200 and 300 days. If we assume [O I]/[Ca II]$\propto M_O^{\alpha}$ the linear regression in logarithmic scale gives α = 0.82 (300 days) and 1.01 (200 days). On average, we have

$$[\mathrm{O\ I}]/[\mathrm{Ca\ II}] \propto M_{\mathrm{O}}^{0.90\pm0.09}. \quad (5.6)$$

This relation will be applied to connect the [O I]/[Ca II] and the M_{O} of the helium star models in this work.

Lacking consistent nebular model spectra of SNe Ic, whether this relation can be applied to the bare CO core models remains uncertain. While keeping this caveat in mind, it is illustrative to extend this relation to the helium-deficient models to compare with the observed SNe Ic/Ic-BL.

It should be noted that [O I]/[Ca II] is not only determined by the oxygen mass M_{O}, but also affected by the physical properties of the ejecta, including temperature, density, and so on. Here we have assumed that these quantities are ultimately determined only by the progenitor mass, therefore their effects on [O I]/[Ca II] are absorbed in the scaling index of M_{O}. A discussion on the variation form of Equation (5.6) is left to Section 4.1. We further note that we have fixed the metallicity in this investigation (assuming the solar metallicity); the metallicity will introduce a totally mass-independent factor to a problem, but the observed variation of the metallicity at the SN site is not exceedingly large (see for example Modjaz et al. 2008).

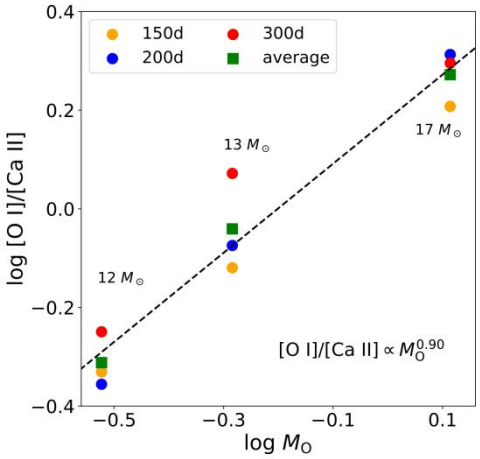

Figure 5.5. **The relation between the [O I]/[Ca II] of SNe IIb model spectra (Jerkstrand et al. 2015a) and the O mass of the ejecta.** Measurements at different phases are labeled by different colors.

Section 3.2. *Ejecta velocity and [O I] width*

The SN ejecta is powered by the deposited γ-rays originally emitted from the decays of ^{56}Ni and ^{56}Co, and the heating process is balanced by the line emissions of the elements in each shell. In the expanding ejecta, each mass shell has different expansion velocity, therefore the centers of the emission lines are Doppler shifted. In the nebular phase, the Doppler effect is the dominating broadening factor of the lines. Inversely, the widths of the emission lines can therefore be utilized to determine the velocity scales of the corresponding emitting elements.

Following the explosion of the massive star, the ejecta expands homologously with $V(r, t) = r/t$, where $V(r, t)$ is the expansion velocity of the mass shell located at radius r at time t. In the spherically symmetric case, the specific flux at frequency ν is

$$F_\nu \propto \int_{V(\nu)}^{V_{\max}} j(V) V \mathrm{d}V\,, \qquad (5.7)$$

Here, V_{max} is the outermost velocity of the ejecta and $V(v)$ is the Doppler velocity of frequency v relative to the rest frame frequency v_0. The emission coefficient of the mass shell with expansion velocity V is $j(V)$. The readers may refer to Jerkstrand (2017) for the detailed discussion on the formation of the nebular line profile.

The rate of radioactive energy deposited in a mass shell is $\varepsilon_{rad}d$ according to definition, where d is the local γ-ray deposition function per mass. Here, ε_{rad} is the rate of energy release per gram of radioactive nickel. We assume that the deposited energy is re-emitted by [O I] at a rate of $X_{[O\ I]}\varepsilon_{rad}d$ (see below). Therefore

$$j_{[O\ I]} \propto \rho X_{[O\ I]} \varepsilon_{rad} d. \quad (5.8)$$

By assuming $X_{[O\ I]} \sim X_O$ and $L(6300)/L(6363)=3$, the [O I] profile can be constructed by Equation (5.7). Some examples are illustrated in Figure 5.6.

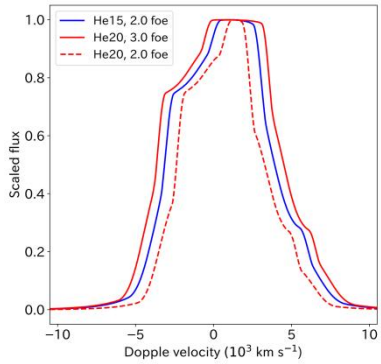

Figure 5.6. **The line profile constructed by Equations (5. 7) and (5. 8) for He15 and He20 models (labeled by different colors) with different kinetic energies (labeled by different line styles).**

Indeed, when the oxygen dominates the cooling, its mass fraction would not sensitively affect the line strength (i.e., the temperature is anyway determined to balance the heating and cooling rates). However, we introduce a factor X_O here, to account for the mixing effect as introduced above, since X_O traces the fraction of the O-rich material in a given volume once it is macroscopically mixed with other characteristic nuclear-burning layers. We note that we are not concerned with the absolute flux scale, and therefore this procedure is justified as long as X_O in the original (unmixed) ejecta is roughly constant within the O-rich region (which is indeed the case; Figure 5.1).

We apply the same line width measurement method as Fang et al. (2022) to the model spectra, i.e., half of the wavelength range (or velocity range) that contains 68% of the total emission flux to the model [O I] profile. The measured line width is dependent on both M_O and E_K. As shown in Figure 5.7, for a fixed He star model (therefore fixed M_O), the measured width V_O scales as $V_O \propto E_K^{0.5}$.

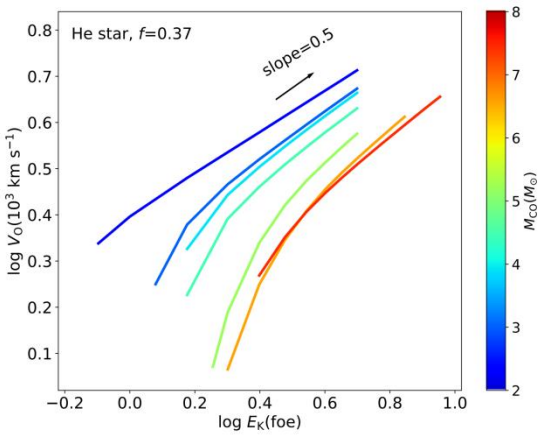

Figure 5.7.**The relation between V_O and the E_K of the ejecta.** The colorbar indicates M_{CO} of the progenitor. For a fixed M_{CO} (or progenitor model), the slope is very close to 0.5 in logarithmic scale at the relatively high E_K end.

Section 3.3. *[O I]/[Ca II]-[O I] width correlation*

In Fang et al. (2022), a correlation between the [O I]/[Ca II] and [O I] width is discerned, based on a large sample of SESN nebular spectra (N=103). For the helium-rich SNe IIb/Ib, the correlation is significant, while it can not be discerned for the helium-deficient SNe Ic/Ic-BL. The correlation itself, along with its different dependence on the SNe sub types, can be qualitatively explained if the kinetic energy of the explosion is correlated with the progenitor CO core mass. In this work, we will derive the quantitative relation between the CO core mass and the kinetic energy E_K that is required to reproduce the correlation.

The observed line width $\Delta\lambda$ is transformed to the typical velocity scale V_{Obs} by

$$V_{\rm obs} = \frac{\Delta\lambda}{6300\ \text{Å}} \times c, \qquad (5.9)$$

where c is the speed of light.

To connect the progenitor models to the observables, we assume [O I]/[Ca II]$\propto M_O^{0.90}$, (see Section 3.1). The oxygen mass M_O and the measured [O I] width V_O of the models are multiplied by constants to match the He13 model (with E_K=0.94 foe, see Fremling et al. 2016) with the [O I]/[Ca II] and V_{Obs} values of iPTF 13bvn. These calibrations give

$$\log\frac{\text{[O I]}}{\text{[Ca II]}} = 0.9 \times \log\frac{M_{\rm O}}{M_\odot} + 0.03, \qquad (5.10)$$

and

$$\log\frac{V_{\rm Obs}}{10^3\ \text{km s}^{-1}} = \log\frac{V_{\rm O}}{10^3\ \text{km s}^{-1}} - 0.07. \qquad (5.11)$$

The upper panel of Figure 5.8 is the observational result of Fang et al. (2022). The local non-parametric regression is performed to the SNe IIb/Ib and SNe Ic/Ic-BL respectively, as marked by the dashed lines. The shaded regions are the 95% confidence intervals (CI). For a specific model, its M_O is transformed to the observed [O I]/[Ca II] using Equation (5.10). With the results from the local non-parametric regression, we derive V_{Obs} required for this progenitor model to reproduce the observed correlation, as marked in the upper panel of Figure 5.8, which is then further transformed to the model velocity (V_O) using Equation (5.11). The

velocity, V_O, is transformed to the kinetic energy of the specific model using the relations in Figure 5.7. The result is summarized in Table 5.3.

It is clear that the kinetic energy of the explosion is required to be larger for He star model with a larger amount of oxygen (therefore larger M_{ZAMS}) to produce the observed [O I]/[Ca II]-[O I] width correlation. This is already pointed out by the qualitative analysis of Fang et al. (2022). The relation between the CO mass (M_{CO}) and kinetic energy (E_K) is shown in the lower panel of Figure 5.8. If only the He star models are included, we have the scaling relation

$$E_K \propto M_{CO}^{1.41\pm0.10}. \quad (5.12)$$

If Equation (5.10) is also applied to the CO core models, with the similar practice, we derive the relation between the M_{CO} and E_K for these models, which is also plotted in the lower panel of Figure 5.8. For the CO core models, the scaling relation is

$$E_K \propto M_{CO}^{1.34\pm0.28}. \quad (5.13)$$

If the He star and the CO core models are combined, the relation between M_{CO} and E_K then becomes

$$E_K \propto M_{CO}^{1.39\pm0.09}, \quad (5.14)$$

which is similar to Equation (5.12) where only helium stars are included. The correlation is significant with ρ=0.98 and p<0.0001. This implies the kinetic energy of SNe Ic has the same dependence on M_{CO} (or M_{ZAMS}) as their helium-rich counterparts, and possibly SNe IIb/Ib and SNe Ic share the same explosion mechanism despite the different degrees of the envelope stripping.

It should be noted that the scaling relation between the [O I]/[Ca II] ratio and *M*O (Eq. 6) is empirically derived from the nebular helium-rich SNe models of Jerkstrand et al. (2015a), therefore it is not necessarily valid for the helium-deficient SNe. The application of this relation to the CO core models and SNe Ic/Ic-BL is only for illustrative purpose. A discussion on this topic is left to Section 4.1.

E_K (foe)	He13	He15	He18	He20	He23	He25	He28	CO18	CO20	CO23	CO25	CO28
Lower	0.88	1.75	2.38	2.92	3.81	4.36	4.49	2.18	3.60	3.66	5.36	5.02
Middle	1.10	1.96	2.58	3.17	4.39	5.42	5.75	2.34	3.88	4.03	5.82	5.83
Upper	1.49	2.20	2.84	3.43	5.03	6.95	7.57	2.51	4.19	4.31	6.36	6.84

Table 5.2.**The kinetic energy required to reproduce the observed correlation for the progenitor models.** The upper and lower limits are transformed from the 95% CI.

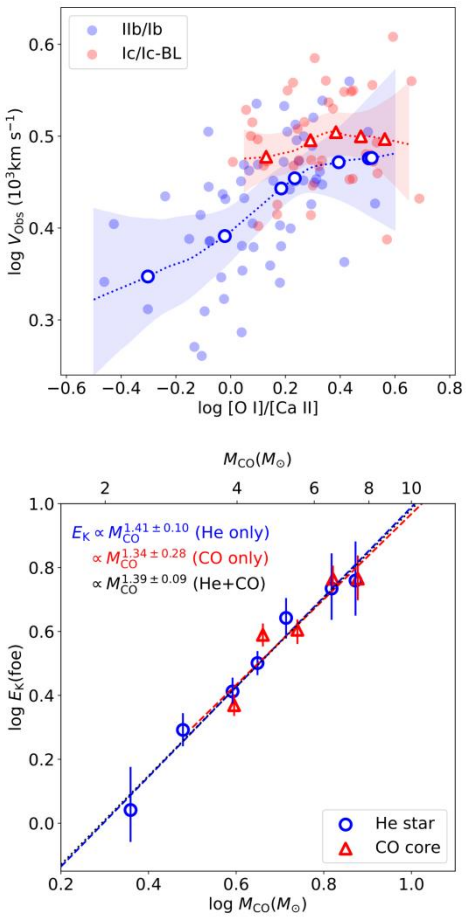

Figure 5.8. **Upper panel: The observed [O I]/[Ca II]-line width correlation.** The helium-rich SNe (type IIb + Ib) and the helium-deficient SNe (type Ic + Ic-BL) are labeled by different colors. The dashed lines are the linear regressions to the observation. The open-squares and open-triangles mark the helium star and CO core models; **Lower panel: The relation between the CO core mass M_{CO} of the models and the kinetic energy required to produce the observed [O I]/[Ca II]-line width correlation.** The helium stars and CO core models are labeled by different colors and markers.

Section 4. Discussion

Section 4.1. *Scaling relations*

Section 4.1.1. *Factors that affect [O I]/[Ca II]*

In the previous sections, we have assumed that [O I]/[Ca II] is determined only by the oxygen mass M_O, which is based on the assumption that other affecting factors (density, temperature, etc.) are also dependent on the progenitor mass so that their effects on [O I]/[Ca II] are all absorbed into the dependence on M_O. However, this assumption is not necessarily valid. The calcium emission [Ca II] comes from the explosive nucleosynthesis region, therefore its strength may well be affected by the kinetic energy of the explosion. Further, the calcium is an efficient cooler. If a certain amount of calcium (mass fraction larger than 10^{-3}) is microscopically mixed into the oxygen-rich shell through diffusion, the strength of the [Ca II] will dominate the [O I] and the [O I]/[Ca II] ratio will be reduced (Fransson & Chevalier 1989; Maeda et al. 2007a; Dessart

& Hillier 2020). These two factors, i.e., (1) the kinetic energy and (2) the microscopic mixing, will affect the [O I]/[Ca II] ratio as follows:

(1) Kinetic energy: the kinetic energy will affect the [O I]/[Ca II] in two aspects: (a) The density of the ejecta. For the same pre-SN structure, the increase of the kinetic energy will increase the expansion velocity of the expelled material, resulting in low density ejecta. The assumption that the [O I] and [Ca II] dominate the emission from the O-rich shell and the explosive nucleosynthesis region, respectively, is more valid when the density is low. If the density of the O-rich shell increases, the contribution from Mg I] 4571 and [O I] 5577 becomes non-negligible. For the explosive nucleosynthesis region, the Ca II H&K, NIR triplet and Si I 1.099 μm become strong when the density of this region increases. However, the emissions from the explosive nucleosynthesis region is more sensitive to the density, therefore the decrease of the density (or increase of the explosion energy) will decrease the [O I]/[Ca II] ratio (Fransson & Chevalier 1989); (b) nucleosynthesis: the amount of the newly synthesized elements, including calcium, generally increases with the explosion energy (Woosley et al. 2002; Limongi & Chieffi 2003). The strength of the [Ca II] thus traces the amount of the explosive nucleosynthesis region. The increase of the explosion energy will therefore decrease the [O I]/[Ca II] ratio.

(2) Microscopic mixing: The [Ca II] is mostly emitted by the newly synthesized calcium in the explosive burning ash (Jerkstrand et al. 2015a). The microscopic mixing is not expected to occur during the explosion because the diffusion time scale is long, as inferred from the chemical inhomogeneity of Cas A (Ennis et al. 2006). However, if the pre-existing calcium, which is synthesized during the advanced stage of massive star evolution, is microscopically mixed into the O-rich shell before the explosion, its contribution to the [Ca II] can become significant, and the [O I]/[Ca II] ratio will decrease because [Ca II] is a more effective coolant than [O I] (Dessart et al. 2021). The microscopic mixing may happen during the Si burning stage through the merger of the Si-rich and O-rich shell, and the occurrence rate is higher for a more massive progenitor between 16 to 26$M_\odot$ (Collins et al. 2018; Dessart & Hillier 2020).

In conclusion, both the increase of the kinetic energy E_K and the diffusion of the calcium into the O-rich shell will tend to reduce the [O I]/[Ca II] ratio. In Section 3, the derivation of the M_{CO}-E_K relation (Equation 5.14) is based on the assumption that the [O I]/[Ca II] ratio is determined *only* by the oxygen content of the progenitor (Equation 5.10). As stated above, this assumption is not necessarily valid. The relations between the [O I]/[Ca ii] ratio and E_K, as well as the microscopic mixing, are complicated, and would possibly affect the M_{CO}-E_K relation. It is therefore important to examine how the M_{CO}-E_K relation is altered if the above two factors are taken into consideration. However, a detailed treatment on this topic would require a large grid of stellar evolution models and radioactive transfer simulations, which is beyond the scope of this paper. In this section, we attempt to quantify the effects of these two factors on the M_{CO}-E_K relation by including them into the scaling relation of [O I]/[Ca II] ratio and M_O in the power-law form. Equation 5.10 then becomes

$$\log\frac{[\mathrm{O\ I}]}{[\mathrm{Ca\ II}]} = (0.9-\alpha)\times\log\frac{M_O}{M_\odot} - \beta\times\log E_K, \qquad (5.15)$$

where α and β (both greater than 0) characterize the effects of microscopic mixing and the kinetic energy respectively. Here, the effect of microscopic mixing is absorbed by the dependence on M_O because the stellar evolution models show that the occurrence rate of shell-merger during the Si burning stage is dependent on

the progenitor mass, and more massive stars would have a higher chance of calcium pollution (Collins et al. 2018; Dessart & Hillier 2020).

Section 4.1.2. M_{CO}-E_K relation of SNe IIb/Ib

To examine the effects of EK and microscopic mixing on the M_{CO}-E_K relation, we first need to derive the scaling relations between the observables and the models. For the He star models with f = 0.368, the measured line width is determined by M_{CO} and E_K, and the linear regression gives

$$\log\frac{V_O}{10^3\ \mathrm{km\ s^{-1}}} = -0.22\times\log\frac{M_O}{M_\odot} + 0.46\times\log\frac{E_K}{\mathrm{foe}} + 0.33, \qquad (5.16)$$

as shown in Figure 5.9

The relation between the observed line width V_{obs} and the [O I]/[Ca II] can also be expressed in the form of power-law derived from the linear regression in logarithm scale:

$$\log\frac{V_{Obs}}{10^3\ \mathrm{km\ s^{-1}}} = 0.18\times\log\frac{[\mathrm{O\ I}]}{[\mathrm{Ca\ II}]} + 0.41. \qquad (5.17)$$

By combining Equations (5.3), (5.15), (5.16) and (5.17), we have $E_K \propto M_{CO}^{\delta}$ (including α and β as unknown parameters), where

$$\delta = \frac{0.63 - 0.31\alpha}{0.46 + 0.18\beta}. \qquad (5.18)$$

If α, β=0 (in this case, Equation 5.15 recovers Equation 5.10, where [O I]/[Ca II] $\propto M_O^{0.90}$), then δ=1.37, which is similar to Equation (5.12) as expected. With Equation (5.18), we can investigate how the scaling index δ of M_{CO}-E_K relation is affected by the effect of E_K and the microscopic mixing (characterized by the parameters β and α respectively).

We first consider the effect of E_K on the [O I]/[Ca II] ratio. In the nebular models of Fransson & Chevalier (1989), [O I]/[Ca II] scales as $E_K^{-0.5}$. In this case (β=0.5 and α=0), we have δ=1.14. Still, this would require E_K tightly correlated with M_{CO}, although the dependence is slightly weaker than Equation (5.12).

Lacking a large grid of nebular spectra models with different degrees of microscopic mixing, it is difficult to derive the exact value of α. However, its range can be roughly constrained from observation. If α is larger than 0.9, then according to Equation 5.15, the [O I]/[Ca II] ratio will be anti-correlated with the progenitor oxygen mass M_O. Observationally, we have several lines of evidence that objects with a massive progenitor tend to have larger [O I]/[Ca II];

(1) A correlation between the light curve width and the [O I]/[Ca II] ratio is reported by Fang et al. (2019). The light curve width can be an independent measurement of the ejecta mass. If the [O I]/[Ca II] is mainly determined by the degree of microscopic mixing, an anti-correlation between the [O I]/[Ca II] and light curve width would be expected, which contradicts the observation. Especially, a group of SESNe with broad light curves have distinctly larger [O I]/[Ca II] ratio (Karamehmetoglu et al. 2022).

(2) The measured progenitor masses of SNe 2011dh, 2013df and iPTF 13bvn are relatively small from pre- or post-SN image (Maund et al. 2011; Van Dyk et al. 2014; Cao et al. 2013), and their [O

I]/[Ca II] are among the lowest of the full sample. SNe 1998bw and 2002ap are also believed to have massive progenitors, meanwhile their [O I]/[Ca II] are at the highest end (Nakamura et al. 2001; Mazzali et al. 2002).

Although the degree of the pre-SN calcium pollution is difficult to be constrained from the current observation, its effect on [O I]/[Ca II] is probably not very strong. The above observational lines of evidence suggest α can not be too large, or at least can not be larger than 0.90, therefore δ>0.76 if β=0, according to Equation (5.18). In the most extreme case where α=0.9 and β=0.5, we have δ=0.64. In conclusion, even the effects of kinetic energy and calcium pollution are taken into account, we would still expect a positive correlation between E_K and M_{CO} to explain the observed correlation in Figure 5.8. However, to derive the exact relation between E_K and M_{CO} based on the correlation between [O I]/[Ca II] and [O I] width, sophisticated models that can constrain both α and β are needed.

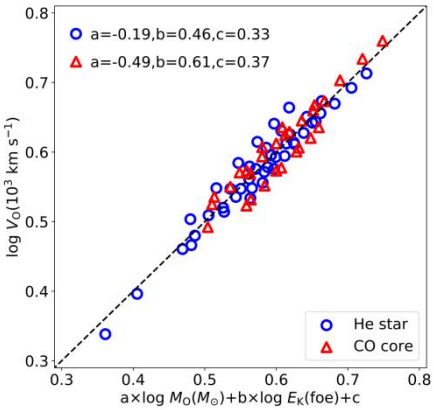

Figure 5.9. **The linear regression to the model line width V_O(M_O, E_K) as function of oxygen mass M_O and kinetic energy E_K.** The helium star and the CO core models are labeled by different colors and markers. The black dashed line is one-to-one correspondence.

Section 4.1.3. *M_{CO}-E_K relation of SNe Ic/Ic-BL*

Similar to the practice of the previous section, for the CO core models, the relation between the model line width V_O, kinetic energy E_K and model oxygen mass M_O is given by:

$$\log\frac{V_O}{10^3\ \mathrm{km\ s^{-1}}} = -0.49\times\log\frac{M_O}{M_\odot} + 0.61\times\log\frac{E_K}{\mathrm{foe}} + 0.37, \qquad (5.19)$$

as shown in Figure 5.9. Also, the relation between the observed line width V_{Obs} and the [O I]/[Ca II] ratio is given by

$$\log\frac{V_{Obs}}{10^3\ \mathrm{km\ s^{-1}}} = 0.04\times\log\frac{[\mathrm{O\ I}]}{[\mathrm{Ca\ II}]} + 0.48. \qquad (5.20)$$

For SNe Ic + Ic-BL, the combination of Equation (5.3), (5.15), (5.19) and (5.20) gives

$$\delta = \frac{0.89 - 0.07\alpha}{0.61 + 0.04\beta}. \qquad (5.21)$$

If α, β=0, δ=1.46, which is consistent with Equation (5.13) as expected. Unlike the helium-rich SNe, the effects of kinetic energy (β) and the level of microscopic mixing (α) on δ is very weak. In the most extreme case where α=0.9 and β=0.5, δ=1.31. The derivation of Equation (5.21) is based on the assumption that the helium-deficient models follow the same scaling relation as the helium star models (Equation 5.10 or 5.15). However, as noted above, these relations are not necessarily valid for CO core models. Observationally, for

SNe Ic/Ic-BL, the dependence of the [O I] width on [O I]/[Ca II] is weak. By applying Equation 5.3 and 5.19 with V_O fixed to be a constant (Figure 5.8) and α,β=0, we have

$$E_K \propto M_{CO}^{1.40}. \quad (5.22)$$

For the helium-deficient SNe, although currently we lack consistent SNe Ic nebular spectra models to constrain the relation between M_O and [O I]/[Ca II], still the power index δ derived from the simple scaling analysis (Equation 5.22) is consistent with that of the helium-rich models, which suggests the SESNe share the same explosion mechanism.

Section 4.2. *Effect of mixing*

Large-scale material mixing in core-collapse SN ejecta would occur due to the instability which likely arises during the explosion. It is expected to take place at the interface between the CO core and the He-rich layer. This process will bring up the material in the CO core to the outer region and thus increases the average velocity. If 56Ni and oxygen are mixed into the outer region (therefore with faster expansion velocity), the line width will increase according to Equation (5.7). In particular, the mixing of the radioactive ^{56}Ni strongly affects the electromagnetic properties and the thermal conditions. The line width is therefore affected by the interplay of these factors even the pre-explosion structure and the kinetic energy E_K is fixed. In this section we will investigate whether the degree of mixing can account for the observed large scatter in [O I] width and affect the M_{CO}-E_K relation.

Using the mixing scheme introduced in Section 2.2, we artificially vary the degree of mixing *f* from 0.1 to 1.0 (being fully mixed), and calculate the velocity with the M_{CO}-E_K relation fixed (Table 5.3). The expected [O I]/[Ca II]-[O I] width relations are shown in Figure 5.10. Given the same explosion of the same He-rich progenitor, the different degrees of large scale material mixing indeed create the scatter in line width, and can fully account for the observed scatter (the blue shaded region in Figure 5.10). However, for the CO core models, the effect of large scale mixing on the line width is negligible. Unlike the He star models, where the material in the CO core are dredged-up to the outer region, for the CO core models, the mixing process will bring the O-rich material down to the inner region and the average velocity is reduced (lower panel in Figure 5.3). This effect is canceled out with the dredge-up of the radioactive ^{56}Ni.

By studying the color evolution of early phase light curves, Yoon et al. (2019) find evidence that the ejecta of SNe Ic is fully mixed, while for SNe IIb/Ib, the radiative ^{56}Ni is only mildly mixed into the helium-rich envelope. This is also supported by the study of early photospheric velocity evolution; Moriya et al. (2020) find the helium star model with about half of the ejecta mixed can explain the photospheric velocity evolution of the type Ib SN 2007Y. These investigations suggest the degree of mixing is possibly related to the properties of the progenitor. In this work, we have assumed the models have the same degree of mixing (*f*=0.368). If *f* is mass-dependent, for example, in the case where more massive progenitors would lead to a larger value of *f*, the required kinetic energy will decrease to reproduce the fixed observed velocity; this reduces the slope in Equation (5.14). We further investigate whether the change of the degree of mixing *f* will affect the M_{CO}-E_K relation. Similarly to the process in Section 3.3, we derived E_K for each progenitor model with different degrees of macroscopic mixing based on the observed line width. We consider two cases (1) *f* is positively correlated with progenitor mass, i.e., the ejecta of a more massive star is more thoroughly mixed, with *f* = 0.1 for He13 model and *f* = 1 for He28 model; (2) *f* is anti-correlated with progenitor mass, with *f* = 1 for He13 model and *f* = 0.1 for He28 model. The results are shown in Figure 5.11, with models with different *f*

labeled by different colors. For case (1), we have $E_K \propto M_{CO}^{1.26}$. For case (2), the dependency increases to $E_K \propto M_{CO}^{1.58}$, as illustrated by the dotted line and dashed line in Figure 5.11 respectively. In conclusion, even the relation between the mixing degree and the progenitor is unknown to the current knowledge, the M_{CO}-E_K relation will not be significantly affected.

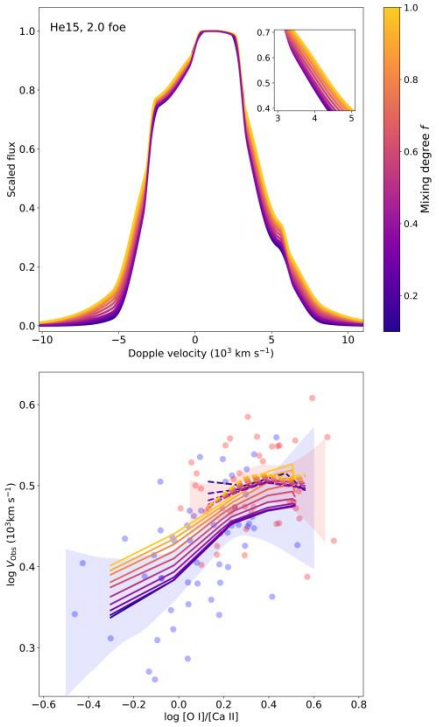

Figure 5.10.**Upper panel: The model [O I] width with different degrees of macroscopic mixing**, labeled by the colorbar; **Lower panel: The [O I]/[Ca II]-line width track of models with different degrees of macroscopic mixing while the M_{CO}-E_K relation is fixed** (Table 5.3). The tracks of the He star models are labeled by the solid line, and the tracks of the CO core models are labeled by the dashed lines. The observed [O I]/[Ca II]-[O I] width relations of SNe IIb/Ib and SNe Ic/Ic-BL are illustrated as the shaded regions for comparison.

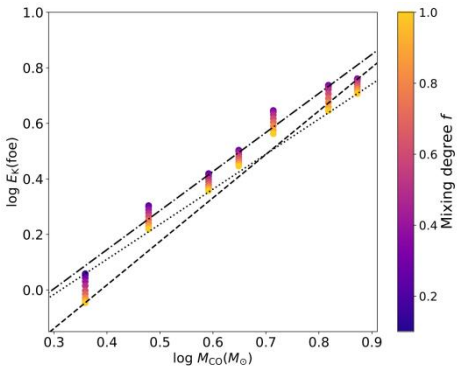

Figure 5.11.**The M_{CO}-E_K relation required to produce the observed [O I][Ca II]-line width relation for the helium star models with different degrees of macroscopic mixing**, labeled by the colorbar. The dashed line is the M_O -E_K relation if the mixing degree f is anti-correlated with the progenitor mass; The dotted line is the M_{CO}-E_K relation if the mixing degree f is correlated with the progenitor mass. The dotdash line is the M_{CO}-E_K relation with f fixed to 0.368 (lower panel of Figure 5.8) for comparison.

Section 5. Comparison with early-phase observation

The relation between the properties of the progenitor and the kinetic energy has long been studied. However, most of the previous investigations focus on the early phase (or photospheric phase) observation (Lyman et al. 2016; Taddia et al. 2018). The width of the light curve and the photospheric velocity estimated from early phase spectra are used to derive the mass of the ejecta and the kinetic energy of the explosion, based on the model of Arnett (1982), where the ejecta is predominantly powered by the decay of the radioactive ^{56}Ni and ^{56}Co.

During the photospheric phase, the ejecta is optically thick. Instead of scanning through the ejecta, the information brought by analyzing the early phase observation is limited to the properties of the outer region. The bulk properties of the ejecta are then estimated from the extrapolation inward based on several simplified assumptions (Arnett 1982; Valenti et al. 2008; Cano 2013; Lyman et al. 2016; Taddia et al. 2018). The observations at the photospheric phase and nebular phase are indeed tracing different regions of the ejecta, therefore it is important to compare the results derived from the two observations to clarify the validity of the assumptions.

The first step in the investigation on this topic is to connect the early phase/nebular phase observables with the models. In this section, we employ the results of the early phase observation from Lyman et al. (2016) and Taddia et al. (2018), which derive the ejecta mass $M_{\rm eje}$ and the kinetic energy $E_{\rm K}$ from the multi-band light curve of large samples of SESNe, based on the Arnett model and the radiation hydrodynamic model respectively. The ejecta mass from the early phase observation are transformed to the pre-SN mass by

$$M_{\rm pre-SN} = M_{\rm ejecta} + 1.4 M_{\odot}, \quad (5.23)$$

assuming that the remnant of the explosion is fixed to 1.4 $M_{\odot}$. For the He star models, the pre-SN mass is further transformed to the CO core mass $M_{\rm CO}$ by

$$\log \frac{M_{\rm CO}}{M_{\odot}} = 0.94 \times \log \frac{M_{\rm pre-SN}}{M_{\odot}} + 0.01. \quad (5.24)$$

Similarly, for the CO core models, we have

$$\log \frac{M_{\rm CO}}{M_{\odot}} = 0.75 \times \log \frac{M_{\rm pre-SN}}{M_{\odot}} - 0.27. \quad (5.25)$$

We First anchor the absolute scale of the ejecta mass from the early phase observation of Lyman et al. (2016). The ejecta mass of iPTF 13bvn derived from the Arnett model is multiplied by a constant to match with the He13 model, which gives

$$\log \frac{M_{\rm ejecta,model}}{M_{\odot}} = \log \frac{M_{\rm ejecta,LC}}{M_{\odot}} + 0.15. \quad (5.26)$$

Here, $M_{\rm ejecta,model}$ and $M_{\rm ejecta,LC}$ are the ejecta mass of the progenitor model and the ejecta mass estimated from the early phase light curve respectively. While for the sample of Taddia et al. (2018), we directly apply their $M_{\rm ejecta}$ estimated based on the radiation hydrodynamic simulation. The ejecta mass is further transformed to the CO core mass using Equations 5.23, 5.24, 5.25 and 5.26. The $M_{\rm CO}$ are then compared with the kinetic energies derived from the early phase light curve. The results are shown in Figure 5.12. The early-phase analyses from Lyman et al. (2016) and Taddia et al. (2018) are plotted in the upper and lower panels of Figure 5.12 respectively. The helium-rich SNe (IIb + Ib) and the helium-deficient SNe (Ic + Ic-BL) are labeled by different colors and markers. The $M_{\rm CO}$-$E_{\rm K}$ relation derived from nebular spectra (lower panel of Figure 5.8) is also plotted for comparison.

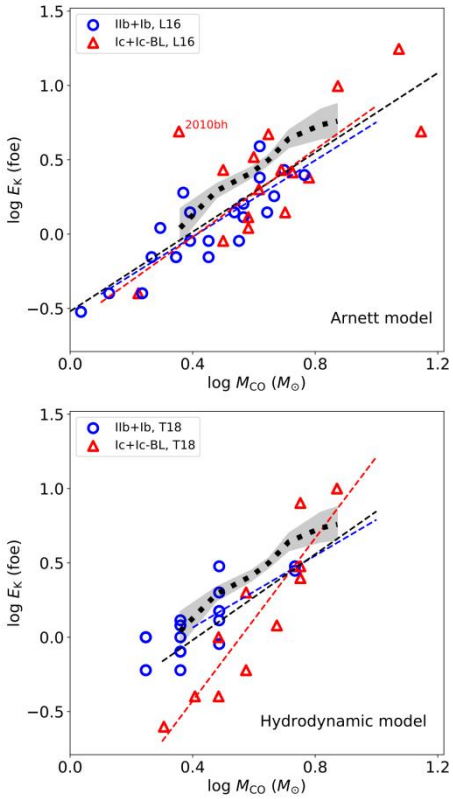

Figure 5.12.**The M_{CO}-E_K relation derived from the early phase observation.** The scatter points are individual objects, with SNe IIb + Ib labeled by blue circles and SNe Ic + IcBL labeled by red triangles. The blue and red dashed lines are the linear regressions to the helium-rich and deficient SNe respectively. The black dashed lines are the linear regressions to the full sample. The black dotted line is the result derived from nebular spectrum, with the shaded area showing the 95% confidence level (lower panel of Figure 5.8). Upper panel: early phase observation from Lyman et al. (2016) with M_{ej} and E_K estimated from Arnett model; Lower panel: early phase observation from Taddia et al. (2018) with M_{ej} and E_K estimated from hydrodynamic model.

Section 5.1. *Comparison with Lyman et al. (2016)*

The M_{ej} and E_K of the Lyman et al. (2016) sample is derived based on the Arnett model with several simplified assumptions, for which the readers may refer to Arnett (1982) and Lyman et al. (2016) for more details.

For the Lyman et al. (2016) sample, the linear regressions to SNe IIb+Ib and SNe Ic+Ic-BL give

$$E_K \propto M_{CO}^{1.31\pm0.18}, \quad (5.27)$$

and

$$E_K \propto M_{CO}^{1.18\pm0.33}, \quad (5.28)$$

respectively. If the linear regression is performed to the full sample, we have

$$E_K \propto M_{CO}^{1.36\pm0.16}. \quad (5.29)$$

The slope of the M_{CO}-E_K relation of SNe IIb+Ib is consistent with the one derived from the nebular phase observation. The consistency between the early phase and nebular phase observation further suggests the effects of E_K and the degree of microscopic mixing on [O I]/[Ca II] is probably not very strong. To be more specific, we now look into Equation 5.18. To match with the result from nebular phase observation, with δ=1.31 derived from the early phase observation, the values of α and β are constrained by

$$0.31\alpha + 0.24\beta = 0.03, \quad (5.30)$$

therefore α<0.10 and β<0.13 (α, β>0. See discussions in Section 4.1).

For the He-deficient SNe, the power index δ derived from the early phase observation is smaller than the one derived from nebular phase (Equation 5.22), but still the two relations are consistent within uncertainty. Further, if the possible outlier SN 2010bh is excluded (as labeled out in the upper panel of Figure 5.12), the linear regression gives

$$E_{\rm K} \propto M_{\rm CO}^{1.47\pm0.29}. \quad (5.31)$$

In conclusion, for SNe IIb/Ib and SNe Ic/Ic-BL, the $M_{\rm CO}$-$E_{\rm K}$ relations from both the early phase and nebular phase observations are consistent.

Section 5.2. *Comparison with Taddia et al. (2018)*

Instead of using Arnett model, $M_{\rm eje}$ and $E_{\rm K}$ of the Taddia et al. (2018) sample is derived based on the radiation hydrodynamic model. The light curve of the SNe in the sample is compared with the simulated light curves, which are generated by exploding a series of helium star models with different progenitor mass by a range of the kinetic energy. The ejecta mass $M_{\rm eje}$ of the Taddia et al. (2018) sample is transformed to the CO core mass $M_{\rm CO}$ via Equations 5.23, 5.24, 5.25.

The linear regressions to SNe IIb+Ib and SNe Ic+Ic-BL of the Taddia et al. (2018) sample give

$$E_{\rm K} \propto M_{\rm CO}^{1.23\pm0.22} \quad (5.32)$$

and

$$E_{\rm K} \propto M_{\rm CO}^{2.74\pm0.39} \quad (5.33)$$

respectively. The $M_{\rm CO}$-$E_{\rm K}$ relation of SNe IIb+Ib derived based on early phase observation is consistent with the one from the nebular phase observation within uncertainty. Similar to the analysis to the Lyman et al. (2016) sample, Equation 5.32 constrains the value of α and β through

$$0.31\alpha + 0.22\beta = 0.06, \quad (5.34)$$

and α<0.21 and β<0.29, i.e., the effects of $E_{\rm K}$ and microscopic mixing on [O I]/[Ca II] are negligible, which is similar with the case of Lyman et al. (2016) sample.

However, for the SNe Ic/Ic-BL sample, the slope of Equation 5.33 is much larger than the ones derived from the nebular analysis (Equation 5.13) and the sample of Lyman et al. (2016). This is possibly because Taddia et al. (2018) estimate $E_{\rm K}$ and $M_{\rm eje}$ of the helium-deficient SNe by comparing their observed light curves with the simulated light curves of the helium-rich star models. The inconsistency in the composition potentially introduces a systematic offset in $E_{\rm K}$ and $M_{\rm eje}$, which in turn affects the slope of Equation 5.33.

Section 6. Conclusion

Based on the large nebular spectra sample of stripped-envelope core-collapse supernovae, Fang et al. (2022) find a correlation between [O I]/[Ca II] (which measures the progenitor mass) and [O I] width (which measures the expansion velocity of the O-rich material). This work aims to explain this correlation from a theoretical aspect.

The one-dimensional simulations of massive-star evolution from 13 to 28$M_{\odot}$, with the hydrogen-rich envelope or the helium-rich envelope stripped, are carried out by MESA. When the massive stars evolve to the time of core-collapse, they are used as the input models for SNEC, and further exploded as CCSNe by injecting different amount of kinetic energy ($1 \sim 10 \times 10^{51}$ erg) into the central regions. The oxygen mass of the model is transformed to the [O I]/[Ca II] ratio by assuming the scaling relation derived from the nebular SN IIb models of Jerkstrand et al. (2015a). The velocity of the O-rich materials as weighted by the local γ-ray deposition rate is connected to the observed [O I] width. The analysis in this work suggests the following to produce the correlation between [O I]/[Ca II] and [O I] width; the kinetic energy of the explosion should correlate with the CO core mass of the ejecta, and scales as $E_{\rm K} \propto M_{\rm CO}^{1.41}$. Further, SNe Ic/Ic-BL follow almost the same $M_{\rm CO}$-$E_{\rm K}$ relation as SNe IIb/Ib, i.e., $E_{\rm K} \propto M_{\rm CO}^{1.34}$, which suggests the helium-rich and the helium-deficient SNe possibly share the same explosion mechanism.

However, the above inferences are made based on very simplified assumptions and empirical relations (for example, we adopt a specific model sequence for SNe IIb by Jerkstrand et al. 2015a for the conversion between [O I]/[Ca II] and $M_{\rm O}$). Lacking consistent nebular model spectra of SESNe exploded by a large range of kinetic energy, it is difficult to estimate the accuracy of the $M_{\rm CO}$-$E_{\rm K}$ relation derived from the method presented in this work. We have discussed several factors that would possibly affect the result. With the scaling analysis, we conclude that the power index of the $M_{\rm CO}$-$E_{\rm K}$ relation of the helium-rich SNe is affected by the dependence of the [O I]/[Ca II] ratio on $E_{\rm K}$ and the degree of microscopic mixing. However, the power index of the $M_{\rm CO}$-$E_{\rm K}$ relation of the helium-deficient SNe is insensitive to such dependence. Further, the macroscopic mixing induced by the instabilities develop during the explosion will bring the material in the CO core up to outer region, increasing the average velocity of the O-rich material and the [O I] width. Different degrees of macroscopic mixing can create the scatter of the observed line width.

The derivation of an accurate $M_{\rm CO}$-$E_{\rm K}$ relation is associated with these complicated physical issues, therefore would require a large grid of detailed radiative transfer modeling with the above factors taken into account. Sophisticated stellar evolution modeling is also needed to estimate the occurrence rate of the microscopic mixing of the calcium into the O-rich shell, which is caused by the shell merger developed during the advanced nuclear burning stage.

With the above caveats in mind, we compare the $M_{\rm CO}$-$E_{\rm K}$ relation derived from this work with the early phase observation of Lyman et al. (2016) and Taddia et al. (2018). During the early phase, the ejecta is optically thick, and the observation traces the nature of the outer region. When the ejecta enters nebular phase, it becomes transparent, and the observation probes the nature of the densest region, i.e., the innermost part. The observations at different phases are thus independently constraining the natures of different regions within the ejecta. Interestingly, for the helium-rich SNe, the $M_{\rm CO}$-$E_{\rm K}$ relation derived from these two methods are in good agreement. It is largely the case for the helium-deficient SNe as well, but the situation is less clear; While the scaling we have derived for the core region agrees with the one derived from the outer region by Lyman et al. (2016), the power-law index of the $M_{\rm CO}$-$E_{\rm K}$ derived from the sample of Taddia et al. (2018) is too steep compared with the observation of nebular phase. This is possibly because the analysis of the SNe Ic/Ic-BL in the sample of Taddia et al. (2018) is based on helium-rich models. We emphasize that the $M_{\rm CO}$-$E_{\rm K}$ relations derived for the outer region (by the early-phase analysis) and for the innermost region (by the late-phase analysis) do not have to agree, as different regions are probed.

In this work, we present a method to investigate the relation between the progenitor mass and the kinetic energy of the explosion through nebular observation. Although this method suffers from the lack of consistent nebular spectra models, it can serve as a cross-reference of the ejecta properties inferred from early phase observation, which is frequently adopted in the previous literature. The combined analysis of the early and late phase observation provides us the chance to scan through the full ejecta from the outermost region to the dense inner part. The consistency, and the inconsistency of the two methods are also important to investigate the completeness of the current assumptions on the explosion process, which is crucial to reveal the explosion mechanism of core-collapse supernovae.

Q.F. acknowledges support by Japan Society for the Promotion of Science (JSPS) KAKENHI Grant (20J23342). K.M. acknowledges support by JSPS KAKENHI Grant (18H05223, 20H00174, 20H04737).

Chapter 6. Asphericiy in the explosive burning ash of core-collapse supernova

Fang, Q., Maeda, K. and et al., submitted to Science

A core-collapse supernova (CCSN) is the explosion that announces the death of a massive star. Outstanding questions remain about the explosion mechanism, as reflected in the geometry of the innermost ejecta and its relation with the progenitor mass. Here we present late-phase spectra of a large sample of CCSNe from stripped-envelope stars, and use the profiles of the calcium and oxygen lines, which are emitted from the explosive burning ash and the unburnt material respectively, to explore the geometries of these two regions and their mutual relations. About half of the objects show clear signatures of substantial deviation from a spherically-symmetric explosion. Furthermore, in these 'aspherical' SNe, the calcium and oxygen profiles show a clear anti-correlation; either a double-peaked calcium with a single-peaked oxygen, or a single-peaked calcium with a double-peaked oxygen. This anti-correlation can be naturally explained by viewing angle effect, if the explosion creates a bi-modal distribution in the iron- and calcium-rich burning ash. The combined analysis of the line profiles and the progenitor mass further suggests the degree of the asphericity grows with the mass of the carbon-oxygen core, posing a strong constrain on the explosion mechanism of CCSNe.

Section 1. *Main text*

When the nuclear fuel deep inside a massive star (with the zero-age main-sequence mass > $8M_{\odot}$) is exhausted, the central part collapses to form a neutron star or a black hole. A large amount of the gravitational energy is released, part of which is transformed to the kinetic energy expelling the rest of the star, leading to a core-collapse supernova (CCSN).

The CCSN explosion mechanism is one of the major long-standing problems in astrophysics. The geometry of the explosion, and its relation with the mass of the progenitor, should shed light on this unresolved issue. If the released energy is concentrated to a specific direction, the explosion will form a so-called bipolar explosion (Khokhlov et al. 1999; Wang et al. 2001). During this process, the O-rich materials are compressed to the equatorial plane, and the explosive burning takes place along the axis perpendicular to the oxygen-rich plane (Maeda&Nomoto 2003; Maeda et al. 2006). The bipolar explosion is also interesting because of its potential connection with a gamma-ray burst (GRB), which requires a collimated relativistic beam and can be observed only when viewed on-axis (Galama et al. 1998; Iwamoto et al. 1998; Hjorth et al. 2003; Woosley & Bloom 2006).

The late-phase (nebular) spectroscopy of a subtype of CCSNe, i.e., stripped-envelope supernovae (SESNe), is a unique tool to study the geometry of the innermost ejecta. An SESN is produced by a massive star that has lost most of its hydrogen envelope before the explosion (Nomoto et al. 1995; Filippenko 1997; Gal-yam 2017). Several months after the explosion, without being blocked by the massive envelope, the ejecta of SESN become optically thin following its expansion, and the central region is exposed. During this phase, the spectrum of an SESN is dominated by forbidden lines, in particular [O I] $\lambda\lambda$6300,6363 and [Ca II]

λλ7291,7323. Research works in the past focus on the [O I], the profile of which strongly depends on the viewing angle (Maeda et al. 2002; Mazzali et al. 2005). The double-peaked [O I], which is a distinct feature of a bipolar explosion, is found to be common for SESNe (Maeda et al. 2008). This result is later justified by latter efforts based on larger samples (Modjaz et al. 2008; Taubenberger et al. 2009; Milisavljevic et al. 2010; Fang et al. 2022). However, inferring the geometry of the explosion using only the [O I] falls into a dilemma: (1) When viewed from the on-axis direction, the [O I] will appear to be sharp and single-peaked, making it indistinguishable from a spherical explosion; (2) the double-peaked [O I], which is a smoking gun of bipolar explosion, suggests the explosion is viewed off-axis, its possible connection with a GRB is therefore missing (Mazzali et al. 2005). Further, the interpretation of the 2-dimensional configuration based on 1-dimensional line profile is degenerated (Taubenberger et al. 2009; Milisavljevic et al. 2010; Fang et al. 2022). We thus need an improved method to infer the explosion geometry, especially the characteristic features when the bipolar explosion is viewed on-axis.

When the explosion occurs, oxygen is burnt into iron-peak elements in the direction to which a large amount of the energy is released; outside of this region, the material is still O-rich, and the fractions of the heavy elements are negligible. The burning ash and the unburnt material are therefore decoupled in geometry. The relation of the profiles of the emission lines originating in these two regions is thus a good probe to the geometry. [O I] has been routinely employed to infer the geometry of the O-rich material. For SESNe, the [Ca II] is mainly emitted from the burning ash, and it is strong in most SESNe, making it an ideal tool to trace the distribution of the explosion ash (Jerkstrand 2017; Dessart et al. 2021; Prentice et al. 2022).

In this work, we propose to combine the analyses of the [O I] and [Ca II] profiles to infer the geometry of the explosion. Horned-like and flat-topped profiles (hereafter unified as double-peaked (DP), to be distinguished from single-peaked (SP)) in either of the two lines are considered as the signature of an aspherical explosion. We look into our nebular spectroscopy sample of 80 SESNe. Among these objects, 42 objects show SP [O I] and SP [Ca II] (OSCaS). For objects considered as bipolar explosion (i.e., with either DP [O I] or [Ca II]), the [O I] and [Ca II] profiles appear to be anti-correlated: 26 objects have DP [O I] with SP [Ca II] (ODCaS) while 12 objects have SP [O I] with DP [Ca II] (OSCaD). Such anti-correlation can be understood by varying the viewing angle of an axisymmetric model characterized by a bi-modal burning ash distributed along the axis, surrounded by an O-rich torus; when viewed on-axis, the Doppler shifts of the bi-modal calcium elements give rise to the horned-like profile of [Ca II], while most of the oxygen elements on the torus move perpendicularly to the line of sight (LOS), producing SP [O I]; on the other hand, when viewed from the direction perpendicular to the axis, the [O I] profile is horned-like and the [Ca II] is SP for the similar reason.This simple picture is supported further by the data; (1) the line profiles are largely explained either by SP or DP, and (2) there is no object showing both DP [O I] and DP [Ca II].

Evidence of asphericty can also be inferred from the widths of the [O I] and [Ca II]. Since the velocity of the expanding material is proportional to its radial coordinate, the width of a line reflects the spatial extension of its emitting element along the LOS (Taubenberger et al. 2009; Maurer et al. 2010a; Jerkstrand 2018; Fang et al. 2022; Prentice et al. 2022). The full-width at half-maximum (FWHM) of the [O I] and that of the [Ca II] are compared in Figure 6.1 (A). For OSCaS and ODCaS objects, the [O I] is broader than [Ca II] in more than ~80% cases. While for OSCaD objects, the [Ca II] is broader than [O I] in most cases.The difference between the [Ca II] and [O I] widths is shown in Figure 6.1 (B), and the OSCaD objects have distinct population from the other types, with $p<0.001$ from the Anderson-Darling (AD) test. The large FWHM of the [Ca II]

contradicts with a spherical explosion, where heavier elements are explosively synthesized in inner region and expelled at lower velocities. However, it can be naturally explained by the bipolar explosion; heavy elements are synthesized along a specific axis and can be ejected at high velocities. If viewed closely from the axis, the average LOS velocity of the iron-rich ash can be faster than that of the O-rich material, producing broader [Ca II] (Maeda et al. 2006).

The peculiar double-peaked profile of the [Ca II], along with its broadness, strongly suggest a bi-modal distribution in its emitting region. We propose an idealized axisymmetric model (Figure 6.2) to explain the profiles of the OSCaD and ODCaS objects. The model is characterized by two separated zones: the calcium elements are distributed in a peanut-like region ($X_{\rm O}$ =0, $X_{\rm Ca}$=1. Here X is the mass fraction), while outside of this region, the material is O-rich ($X_{\rm O}$ =1, $X_{\rm Ca}$=0). We assume the physical properties (e.g., mass fractions, gamma-ray deposition rate) are uniform in each zone for simplicity. No radiation transfer process is included. These simplifications allow us to focus on the geometry effect. When viewed from θ=15◦ ,50◦ and 75◦ from the axis, the model produces SP [O I]/horned-like [Ca II], SP [O I]/flat-topped [Ca II] and horned-like [O I]/SP [Ca II] respectively, in good agreement with the observed profiles of SNe 2008im, 2005nb and 2004ao as examples. It is surprising that such a simple model involving only 2 parameters (the maximum velocity $V_{\rm max}$ and the viewing angle θ) can explain the wide range of the [O I] and [Ca II] profiles simultaneously, especially their anti-correlation. This result suggests that the geometry effect is responsible for the diversity seen in the line profiiles. Including other ingredients (e.g., the density distribution, radiation transfer) may improve the fit, although they probably play a secondary role.

Statistics is useful to constrain the nature of the explosion geometry. The occurrence rate of the bipolar explosion ($N_{\rm Bipolar}$=$N_{\rm DP\ [Ca\ II]}$+$N_{\rm DP\ [O\ I]}$) is 0.48 (=38/80), implying about half of the SESNe explode with non-negligible departure from a spherical configuration. Within this bipolar explosion category, the occurrence rate of DP [Ca II] is 0.32 (=12/38), which is consistent with the axisymmetric model: at $\theta \sim 45$◦ , the [Ca II] profile transforms from DP to SP. If no bias in orientation is involved, the expected occurrence rate of DP [Ca II] in this model is 0.29 ± 0.06 for this sample size.

The dependency of the explosion geometry on the progenitor mass is crucial to reveal the explosion mechanism of CCSNe. However, observational hints are still missing. In this work, we employ the intensity ratio of the [O I] to [Ca II] (hereafter denoted as [O I]/[Ca II]) as a proxy of the CO core mass under the assumption that the amount of the burning ash is not sensitively dependent on the CO core mass. This relation is routinely adopted by past theoretical and observational works, with a larger [O I]/[Ca II] ratio implying more massive CO core (Fransson & Chevalier 1989; Kuncarayakti et al. 2015; Jerkstrand et al. 2015a; Fang et al. 2019;Fang et al. 2022). To investigate the relation between [O I]/[Ca II] and the asphericity of the explosion, the sample is binned into 10 groups according to the [O I]/[Ca II] sequence, and the relation between the [O I]/[Ca II] ratio and the bipolar rate ($N_{\rm DP\ [Ca\ II]}$+$N_{\rm DP\ [O\ I]}$ divided by the total number of the objects) in each group is investigated; no correlation is discerned (Spearman correlation coefficient ρ=0.03), as shown in Figure 6.3 (A). The association of the [O I]/[Ca II] ratio to the CO core mass will require further quantification; for example, if the explosion energy tends to be larger for a more massive CO core (Maeda & Nomoto 2003; Nakamura et al. 2015; Fang et al. 2022) creating a larger amount of Ca (Woosley et al. 2002; Limongi&Chieffi 2003; Tominaga 2009), this relation may be diluted. In any case, the statistical investigation here indicates that a common explosion mechanism is behind CCSNe across a range of the CO core mass, at least in the sample of (canonical) SESNe studied in the present work; the asphericity in the energy release

must be a key to producing CCSNe, with about half of the sample showing the detectable level of the bimodal distribution as seen either in the [O I] or [Ca II].

A similar practice is applied to the bipolar sample. The cumulative distributions of the [O I]/[Ca II] of the OSCaD and ODCaS objects are compared with those of the full sample in Figure 6.3 (B). Surprisingly, the objects with DP [Ca II] have a larger [O I]/[Ca II] ratio than those with DP [O I] (p<0.05 from the Anderson–Darling test). At the low [O I]/[Ca II] range, the presence of DP [O I] suggests that the explosion is bipolar, while the distribution of the burning ash is not extremely bi-modal as inferred from the absence of DP [Ca II]. By binning the bipolar SNe into 5 groups according to the [O I]/[Ca II] sequence, we find a hint that the occurrence rate of the DP [Ca II] in each group increases with the average [O I]/[Ca II] (ρ=0.99, p <0.0001. See Figure 6.3 (C)), although the statistical significance is limited by the relatively small number in each bin. This tendency can be explained by the transition angle $\theta_{\rm trans}$, above which the [Ca II] profile transforms from DP to SP, is increasing with [O I]/[Ca II], i.e., larger $\theta_{\rm trans}$ for an explosion with a larger degree of asphericity.

This finding here is consistent with the scenario where the explosion tends to become more aspherical, and the burning ash becomes more bi-modal and concentrated along a specific direction as the CO core grows, as schematically shown in Figure 6.3 (C). Indeed, the probable non-correlation exhibited in Figure 6.3 (A) may suggest that there are at least two progenitor properties that play key roles in the explosion; one may be either rotation or magnetic field, or something else, that is responsible to the initiation of the explosion; the other is the CO core mass that is responsible to determine the nature of the explosion.

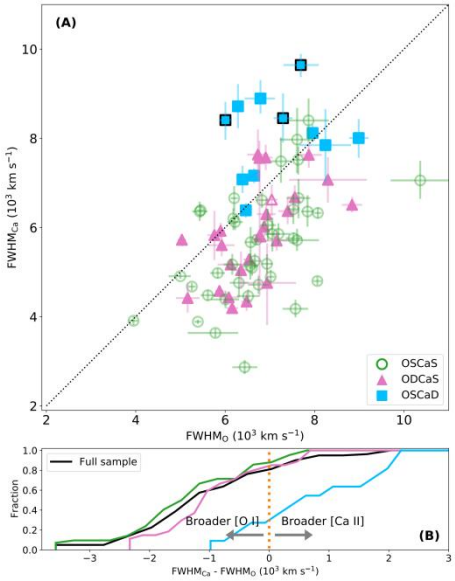

Figure 6.1. **The analysis of the line widths.** Upper panel: The relation between the FWHM of [O I] and [Ca II] sample. Objects of different line profile category (classified by the profiles of [O I] and [Ca II]) are labeled by different colors and markers. Objects with horned-like [Ca II] are highlighted by the thick edges. Lower panel: the cumulative fractions of the difference between [Ca II] width and [O I] width.

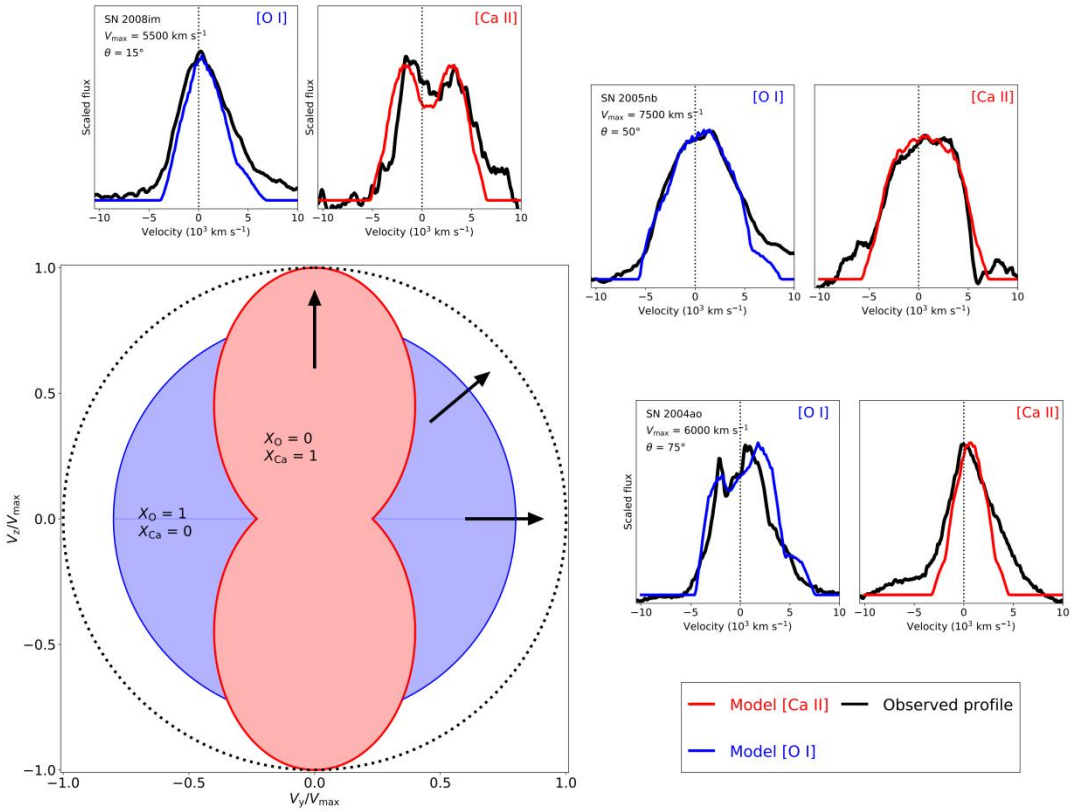

Figure 6.2.**The configuration of the axisymmetric model.** The O-rich region (labeled by blue) and the iron-rich ash (labeled by red) are complementary in geometry. The profiles of the synthesized [O I] (blue) and [Ca II] (red) strongly depend on the viewing angle, which are compared with the observed [O I] and [Ca II] (black lines) of SN 2008im (OSCaD), SN 2005nb (OSCaD) and SN 2004ao (ODCaS).

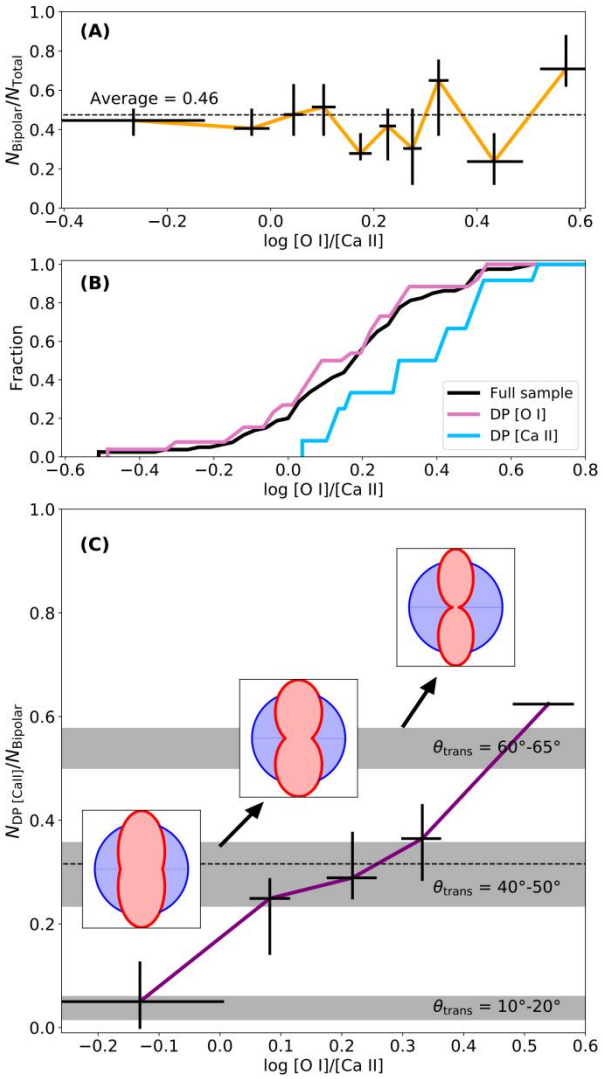

Figure 6.3. **The occurrence rates of bipolar SNe and double-peaked [Ca II] as functions of [O I]/[Ca II].** Upper panel: the occurrence rate of bipolar SN as function of [O I]/[Ca II] (orange); Middle panel: the cumulative distribution of the [O I]/[Ca II] ratio of the full sample (black), objects with DP [Ca II] (light blue) and DP [O I] (pink); Lower panel: the occurrence rate of DP [Ca II] as function of [O I]/[Ca II] (purple). The insert panels illustrate a schematic progenitor CO core mass dependent sequence of explosion geometry to explain the observed relation. The shaded regions mark the expected DP [Ca II] rates of these three models.

Section 2. *Supplementary Material*

Section 2.1. Data

The SESN sample in this work is the same with the one used in Fang et al. (2022). The sample includes the nebular spectra of 103 objects, most of which are compiled from the literature (Yaron&Gal-Yam 2012; Shivvers et al. 2019). In this sample, 80 objects have spectra with good signal-to-noise ratio to allow the investigation of both the [O I] λλ6300,6363 and [Ca II] λλ7291,7323 profiles, and are selected for further analysis. Note here that the SNe associated with a GRB or X-ray flash (XRF, a low energy analog of a GRB), SNe 1998bw/GRB 980425, and 2006aj/XRF 060218, are already excluded from analysis to avoid introducing any bias in orientation (Galama et al. 1998; Iwamoto et al. 1998; Pian et al. 2006; Mazzali et al. 2006). SN

2012ap, which is suggested as a GRB SN viewed off-axis, is also excluded for the same reason (Milisavljevic et al. 2015b; Chakraborti et al. 2015). The very peculiar SN 2005bf, whose explosion mechanism is probably different from normal SESNe, is also not included (Maeda et al. 2007b).

The SESN nebular spectra used in this work are as follow: 1985F; 1987K; 1987M; 1990U; 1990W; 1990aj; 1991A;1993J;1994I;1996aq;1996cb;1997X;1997dq; 2000ew; 2001ig; 2002ap; 2003bg; 2003gf, 2004ao; 2004aw; 2004dk; 2004fe; 2004gk; 2004gn; 2004gq; 2004gt; 2004gv; 2005N; 2005aj; 2005bj; 2006G; 2006ep; 2005kl; 2005kz; 2005nb; 2006F; 2006T; 2006ck; 2006gi; 2007C; 2007I; 2007Y; 2007gr; 2007uy; 2008D; 2008aq; 2008ax; 2008bo; 2008fo; 2008hh; 2008ie; 2008im; 2009C; 2009K; 2009ka; 2009jf; 2009jy; 2010as; 2010mb; 2011bm; 2011dh:; 2011ei; 2011fu; 2011hs; 2012P; 2012au; 2012dy; 2012fh; PTF12gzk; 2013ak; 2013df; 2013ge; iPTF13bvn; 2014C; 2014L;asassn14az; 2014eh; 2015Q; 2015ah; iPTF15dtg. See Table 4A-1 for references.

Section 2.2. Line width measurement

Before measuring the line width of the [O I] and [Ca I], the nebular spectrum is firstly corrected for redshift, which is derived from the central wavelengths of the narrow emission lines from the explosion site (Hα, [N II], etc.) or the redshift of the host galaxy. The next step is to remove the underlying continuum. We use the same method as the previous works (Fang & Maeda 2018; Fang et al. 2019; Fang et al. 2022), where the line connecting the minima at both sides of the emission is defined to be the local continuum and then excised, as illustrated in Figure 6S-1.

To derive the isolated [O I], we need to subtract the broad Hα-like structure located at the red wing of [O I]. This emission is assumed to be symmetric with respect to 6563Å, and is constructed by reflecting its red side (not contaminated by the relatively narrow [O I]) to the blue side. A similar practice is applied to derive the profile of [Ca II], which is complicated by many emissions at similar wavelength ranges emitted by the iron-peak elements. However, most of these lines are usually very weak compared with [Ca II], and is not taken into consideration to avoid further complication. We first subtract the He I λ7065 by assuming it is symmetric with respect to its central wavelength, and the profile is constructed by reflecting its blue side to the red side. After the He I is subtracted, the profile of [Fe I] λ7155 is constructed based on the same method. The separation of the central wavelengths of the [Fe I] and [Ca II] is ~5700 km s^{-1}, while the half-width at half maximum (HWHM) of [Ca II] is always smaller than ~5000 km s^{-1} (see Figure 1 in the main text), the blue side of [Fe I] is therefore hardly contaminated by [Ca II]. The [Ni II] λ7377 is difficult to be removed from the [Ca II] complex, because its separation from the central wavelength of the [Ca II] is small (~3500 km s^{-1}). We assume the [Ni II] and [Fe I] have the same profile, and the ratio of the intensities L_{7377}/L_{7155} is 0.6 (for the solar Ni/Fe ratio and temperature of the emission region ~4000K; see Jerkstrand et al. 2015b; 2015c). The profile of [Ca II] is derived by subtracting the He I, [Fe I] and [Ni II] profiles from the complex. The FWHM of the isolated [O I] and [Ca II] are then measured and corrected for the instrumental broadening. Some examples of FWHM measurement are shown in Figure 6S-1.

The uncertainty of the FWHM is estimated as follows: the original spectrum is slightly smoothed by convolving it with a boxcar filter. The smoothed spectrum is subtracted from the original one, and the standard deviation of the residual flux at the wavelength range 6000 to 8000 Å is estimated as the noise level

of the spectrum. A new spectrum is generated by adding the normal-distributed noise to the smoothed one. For the simulated spectrum, the end points of the local continuum, the central wavelengths of the Hα-like structure, He I, [Fe I] and [Ni II] are allowed to varied by ±500 km s^{-1}, following the flat distributions. The FWHM is then calculated. The above procedure is repeated for 10^4 times, and the 16 and 84 percentages of the 10^4 measurements are estimated as the lower and higher limits of FWHM.

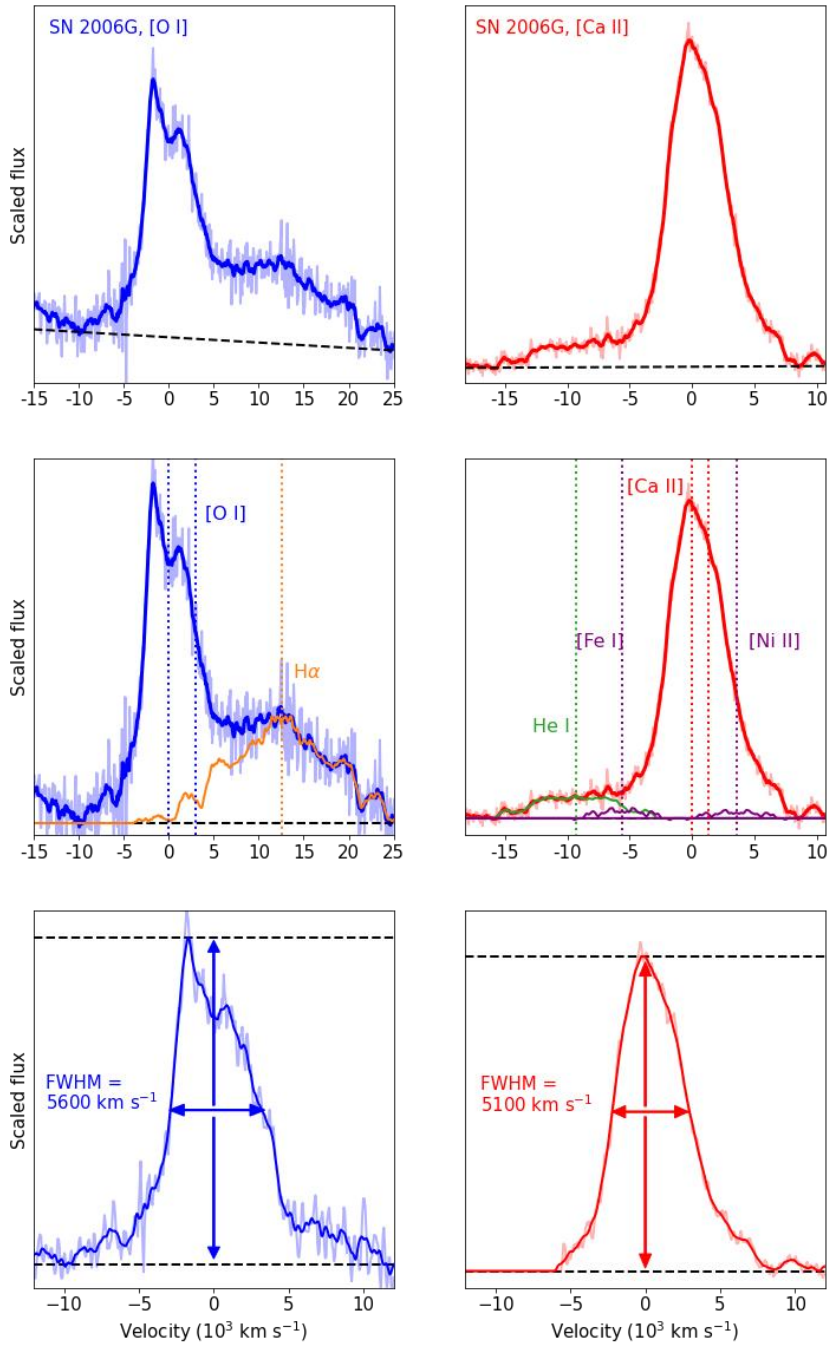

Figure 6S-1. **A demonstration of the line width measurement procedure of [O I] (left panels) and [Ca II] (right panels).** The continuum (black dashed line) is firstly excised (upper panels). Other species that contaminate the [O I] and [Ca II], including Hα, He I, [Fe I] and [Ni II], are labeled by different colors in the middle panels. The lower panels show the FWHM measurement after the continuum and the contamination are subtracted.

Section 2.3. Axisymmetric model

Rather than working on multi-dimensional radiative transfer based on the models with very detailed treatment on the hydrodynamic and nucleosynthesis, in this work, we attempt to develop a simplified axisymmetric model that can produce the unique double-peaked profiles of the [O I] and [Ca II], and their anti-correlation. The model is characterized by two separated zones: (1) the explosion burning ash described by two symmetric (with respect to the plane perpendicular to the axis of symmetry), off-center ellipsoids. The velocity of the edge of the ellipsoid is V_{max}, the maximum velocity of the model. In this zone, the oxygen elements synthesized during stellar evolution are burnt into heavier elements, with X_O=0 and X_{Ca}=1 (we are only interested in calcium, other iron-peak elements are thus not included); (2) the O-rich zone enclosed in the sphere with radius V_O (with V_O/V_{max} = 0.8 as default value). Its overlap with the iron-rich ellipsoids is excised. This zone is filled with the unburnt material where the fractions of the iron-peak elements are negligible, with X_O=1 and X_{Ca}=0. In the two regions, the mass fractions and the density are homogeneous.

The above model is mapped onto a 3-dimensional cube which is divided into 500×500×500 grids in the Cartesian coordinate, with each side bounded by $-V_{max}...+V_{max}$. The ejecta follows the homologous expansion, i.e, a grid point is moving along the radial direction with the velocity proportional to its radial coordinate. Further, no radiation transfer is introduced, and the flux from each grid point is assumed to be proportional to its volume. The specific flux of [O I] (or [Ca II]) $F_V dV$ at velocity V is calculated by summing up the fluxes from the O-rich (or iron-rich) grid points with the LOS velocities in the range of $V...V+dV$. The [O I] contains two components separated by ~3000 km s^{-1} with intensity ratio 3:1 (optically thin assumption). For [Ca II], the two components are separated by ~1300 km s^{-1}, and their intensity ratio is fixed to be 1:1 (optically thin assumption). The synthesized [O I] and [Ca II] profiles, with V_{max} =5000 km s^{-1} and viewing angle θ varies from 0º (on-axis) to 90º (on-dege), are shown in Figure 6S-2.

The axisymmetric model predicts the unique features of both [O I] and [Ca II] profiles, and their anti correlation. The [O I] and [Ca II] profiles are determined by θ with the opposite tendency: viewed from θ=0º (on-axis), the synthesized [Ca II] shows a horned-like structure and [O I] is single-peaked; while viewed from θ=90º (on-edge), [Ca II] becomes single-peaked and [O I] transforms to the horned-like profile.

The observed [O I] and [Ca II] profiles of the SNe with either double-peaked [Ca II] or double-peaked [O I] are fitted by the synthesized profiles, with V_{max} (which determines the line width) and the viewing angle θ (which determines the line profiles) taken as free parameters. In some cases, the third parameter, i.e., the maximum velocity of the O-rich region V_O, is involved, although in most cases fixing r_O(= V_O/V_{max})=0.8 already produces reasonable good fit. The results are shown in Figure 6S-3.

The [O I] and [Ca II] profiles synthesized from the simplified model indeed captures the main features of the [O I] and [Ca II], although failed to produce some substructures, which may require introducing the clumpy structures (for example, a moving O-rich blob as exemplified by SN 1996aq. See Taubenberger et al. 2009) or the centrally-concentrated density profile (SN 1990aj, SN 2002ap and SN 2006ck). For the [O I] profiles with horned-like structure, the model predicts that the intensity of the peak at redder wavelength is larger than the bluer one because of the contribution from the secondary component of the [O I] doublet (centered at 6363 Å). However, observation shows some objects have a flat-topped profile (SN 1990U and SN 2005aj, etc.) or a stronger blue-peak (SN 2000ew, SN 2004gt and iPTF13bvn). This could be explained by the effect of the

residual opacity: the photon escaped from the rear side of the ejecta experiences twice the scattering or absorption (see Jerkstrand et al. 2015a), which will effectively reduce the flux at redder wavelength. If the fluxes from the grid points located at the rear side (i.e.,with LOS velocity <0) are manually reduced by 10-40%, the model indeed produces [O I] with flat-topped profile or horned-like profile with the stronger blue-peak.

In conclusion, the axisymmetric model can produce the [O I] and [Ca II] profiles of the SESNe with signatures of a bipolar explosion in the sample of this work, as well as their anti-correlation. Including other ingredients (for example, clumpy structure, centrally concentrated density profile or non-axisymmetry) and radiative transfer effect will improve the fit, but the bulk properties (single peak versus double peak) will not be significantly affected.

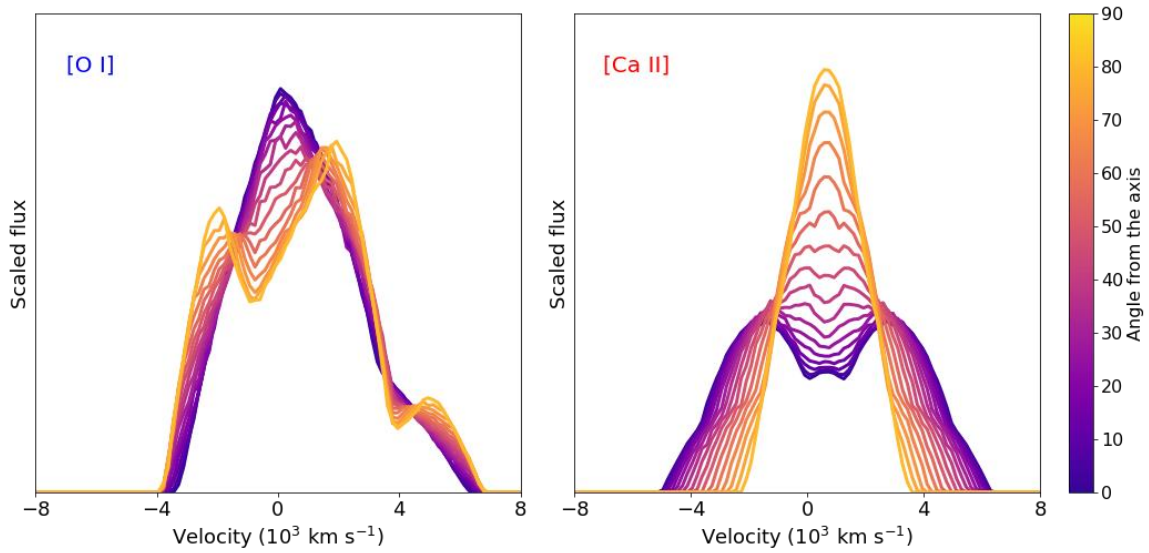

Figure 6S-2. **The synthesized [O I] (left) and [Ca II] (right) with V_{max}=5000 km s^{-1}.** The profiles when viewed from different angles from the axis are label by different colors, changing from θ=0º (blue end) to 90º (orange end).

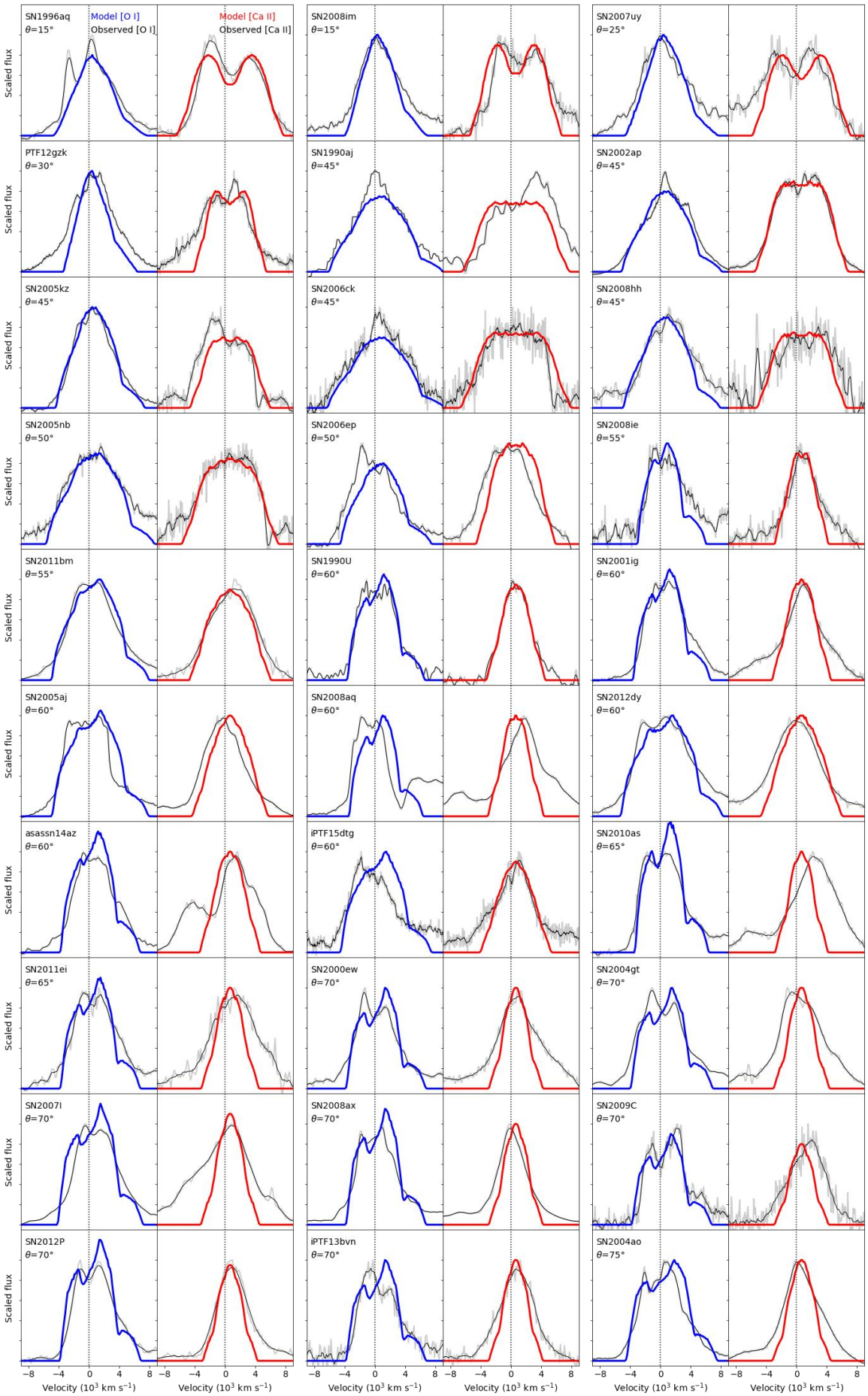
SN1996aq θ=15°
Model [O I]
Observed [O I]
Model [Ca II]
Observed [Ca II]
SN2008im θ=15°
SN2007uy θ=25°
PTF12gzk θ=30°
SN1990aj θ=45°
SN2002ap θ=45°
SN2005kz θ=45°
SN2006ck θ=45°
SN2008hh θ=45°
SN2005nb θ=50°
SN2006ep θ=50°
SN2008ie θ=55°
SN2011bm θ=55°
SN1990U θ=60°
SN2001ig θ=60°
SN2005aj θ=60°
SN2008aq θ=60°
SN2012dy θ=60°
asassn14az θ=60°
iPTF15dtg θ=60°
SN2010as θ=65°
SN2011ei θ=65°
SN2000ew θ=70°
SN2004gt θ=70°
SN2007I θ=70°
SN2008ax θ=70°
SN2009C θ=70°
SN2012P θ=70°
iPTF13bvn θ=70°
SN2004ao θ=75°
Scaled flux
Velocity (10³ km s⁻¹)

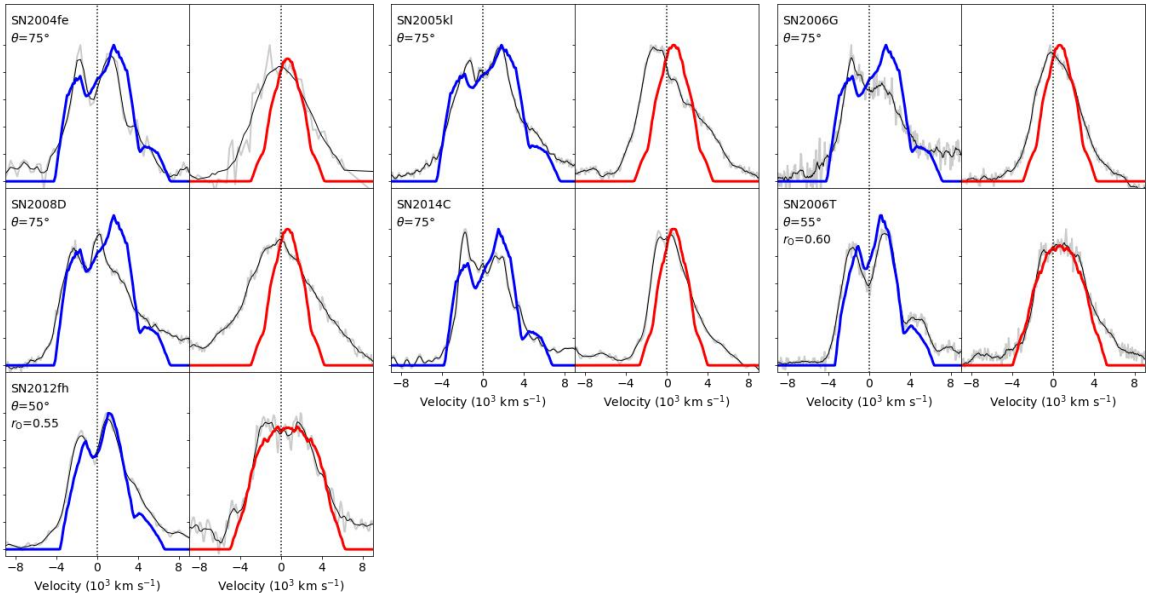

Figure 6S-3. **The fit of the synthesized [O I] (blue) and [Ca II] (red) to the observed line profiles (black) of the objects considered as bipolar explosion in this work.**

Section 2.4. Peculiar object: SN 2015ah

SN 2015ah is classified as OSCaD object, with the [Ca II] complex showing horned-like profile. However, the complex seems to be red-shifted, with the trough located at ~ 4000 km s^{-1}, similar to the central wavelength of [Ni II] (~3600 km s^{-1}). There is also a shallow trough located at the central wavelength of [Fe II] (~-5600 km s^{-1}). The above features suggest this complex is probably not dominated by [Ca II] as the rest of the sample. Instead, [Ni II] may be the main contributor. The [Fe I] and [Ni II] are also emitted from the burning ash. If we assume they have the same spatial distribution as the emitting region of [Ca II], by adjusting the intensity ratios of the lines (L_{7377}/L_{7291}~3.7 and L_{7155}/L_{7291}~1.1), the model indeed reproduces the profile of the [Ca II] complex, as shown in Figure S4.

The strong [Ni II] (L_{7377}/L_{7155}~3.4) suggests this object has strongly super-solar Ni/Fe production, which is about a factor of 5 times the solar value (Jerkstrand et al. 2015b; 2015c). To our knowledge, this is the third CCSNe with super-solar Ni/Fe ratio reported. The other two cases are SNe 2012ec (Jerkstrand et al. 2015c) and 2006aj (Maeda et al. 2007a). Although the sample is still very small, it seems that the excess in Ni/Fe ratio can occur for all types of CCSN, irrespective of the presence or absence of the outer envelope: SN 2012ec is hydrogen-rich; SN 2015ah is hydrogen-deficient but helium-rich; SN 2006aj lacks both hydrogen and helium layers. Further, two out of the three cases are associated with a non-sphercial explosion:SN 2006aj is indeed associated with XRF060218 (Pian et al. 2006; Mazzali et al. 2006) and the burning ash of SN 2015ah is suggested to be bi-modal in this section. Indeed, the asymmetry in explosion can effectively eject the deep-lying burning ash, leading to the change in the Ni/Fe ratio (Maeda et al. 2003). However, the excess in Ni/Fe ratio is not seen in other SESNe with either double-peaked [O I] or [Ca II], which suggests asymmetry is not the only condition. A systematic investigation of the relation between the Ni/Fe ratio and the properties of the explosion (progenitor mass, the amount of the kinetic energy, the geometry of the explosion, etc.) will be important to reveal the origin of the iron-peak elements, and provide constrain on the explosion mechanism of CCSNe.

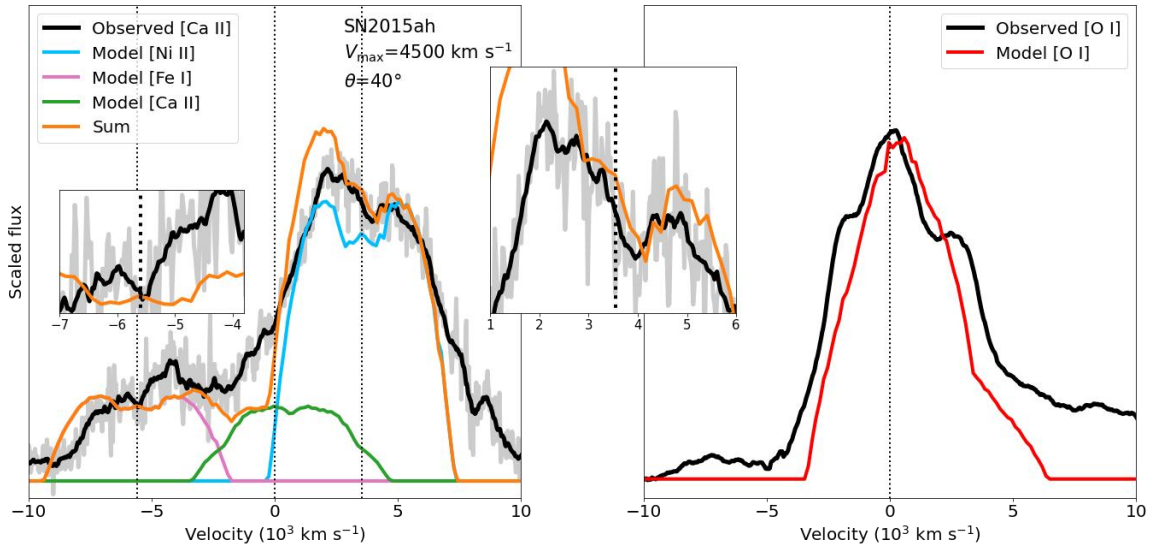

Figure 6S-4. **The fit to the [Ca II] complex (left) and [O I] (right) of SN 2015ah.** Assuming the Ni and Fe have the same spatial distribution as Ca, the sum of the synthesized emissions from the iron-peak elements (orange), i.e., [Fe I] (pink), [Ca II] (green) and [Ni II] (light blue) indeed produces the observed [Ca II] complex (black). The central wavelengths of [Fe I], [Ca II] and [Ni II] are labeled by the vertical dotted lines. At the sane time, the synthesized [O I] (red line in the right panel) also matches with the observed single-peak profile.

Chapter 7. Conclusion

This thesis aims to apply the SESNe nebular spectra, acquired during the phase when the ejecta become transparent in optical, to study the properties of the pre-SN progenitors, the post-SN ejecta dynamics, and their mutual relations. In **Chapter 1** we introduce the basic concepts of SNe, and the long-standing problems to which we plan to attack in this thesis, including the pre-SM mass-loss mechanism and the explosion mechanism hidden behind the expanding ejecta. In **Chapter 2,** we develope a novel method to measure the degree of He-rich layer stripping, which is then compared to the progenitor mass based on a large nebular spectra sample of SESNe in **Chapter 3.** In the following Chapters we investigate the ejecta dynamics. **Chapter 4** focuses on observation, where we find the widths of the oxygen lines are positively correlated with its relative strengths. This correlation is interpreted as the dependence of the explosion energy on the progenitor mass, the quantitative relation of which is later derived in **Chapter 5** based on hydrodynamic simulations and scaling analysis. In **Chapter 6**, we apply the [Ca II] line profiles to study the geometry of the explosive burning ash. A fraction of objects display double-peaked [Ca II], which is naturally expected if the explosion-made region is characterized by two separated iron-rich bubbles. Our analysis further suggests whether a massive star explode spherically is not determined by its mass; however, once the star explode in a bipolar configuration, its asphericity strongly depends on the progenitor CO core mass. We will briefly conclude how the results in this work are related to the large scientific problems raised in the **Introduction** part, and discuss the challenges left to future studies.

Section 7.1. Pre-SN mass-loss

Our analysis on the nebular spectra of SNe IIb leads to a novel method to measure the degree of He-rich layer stripping, i.e., the relative strength of [N II] $\lambda\lambda$ 6548, 6583 (**Chapter 2**). Because the emitting region of [N II] $\lambda\lambda$ 6548, 6583 is at the outermost region of the He-rich layer, even a small amount of mass-loss will lead to the rapid vanish of this line; further, the H-rich envelopes are still attached to the progenitors of SNe IIb , therefore the [N II] strengths can be considered as the cases when the He-rich layers are not stripped. By comparing with the progenitor mass (indicated by the intensities ratio of [O I] and [Ca II]), we find at low mass end, the He-rich layers are fully attached for both SNe IIb/Ib; meanwhile, SNe Ic have distinguishably more massive progenitors (**Chapter 3**). These evidences suggest the stripping process of helium sensitively depends on the mass of the progenitor, and the line-driven wind can be the strong candidate. However, SNe IIb with massive, extensive H-rich envelope (~1 $M_{\odot}$) share the same progenitor masses with those with compact, low-mass H-rich envelope (< 0.01 $M_{\odot}$) and SNe Ib (without H-rich envelope). The residual H-rich envelopes are diverse in properties (therefore very different hydrogen-stripping histories; see Ouchi & Maeda 2017 for example), such diversity seems to be not related to the progenitor mass. The mass-insensitive mechanism, i.e., binary interaction, is responsible to this process. The results in **Chapter 2** and **Chapter 3** suggest a hybrid mechanism is at work for the pre-SN mass-loss: binary interaction removes the H-rich envelope; the residual helium-rich layer is stripped by the line-driven stellar wind.

One of the main challenge in the future is producing the SNe IIb/Ib/Ic progenitors by detailed stellar evolution. Numerous numerical simulations of binary interactions have been carried out (see for example Ouchi &Maeda 2017; Gilkis et al. 2019; Gilkis & Arcavi 2022) to produce the progenitors of SNe IIb/Ib, and the amount of the leftover H-rich envelope is sensitively dependent on the orbit parameters. However, further stripping of the He-rich layer by the stellar wind is proved to be difficult. Observationally, the progenitor mass boundary

of the He-rich and He-deficient SNe is roughly 18 $M_{\odot}$ (Figure 3.3). With the H-rich layer totally removed, the massive star with $M_{ZAMS} = 25\ M_{\odot}$ and metallicity $Z = 0.05$ (2.5 times the solar metallicity) can not strip the He-rich layer via the Dutch wind scheme (Nugis & Lamer 2000; Vink et al. 2001). Several factors may contribute to such numerical difficulty: (1) our current knowledge on the stellar wind is not complete. Indeed the mass-loss rates through winds are empirically concluded from the selected sample of Wolf-Rayet stars in near fields, which involve large uncertainties. Yoon 2017 proposed to include a scaling factor to account for the uncertainty introduced by the empirical estimation. By adjusting this scaling factor, the stellar wind can be enhanced and hopefully the He-rich layer can be successfully stripped for the He star models with moderate M_{ZAMS} (say, ~18 $M_{\odot}$). With such practice, by comparing the outcomes of the stripped models with observations, we can inversely constrain the wind scaling factor, which will certainly improve our knowledge on the wind mass-loss mechanism; (2) rather than the stellar wind, the eruptive stellar activity at the late phase of stellar evolution, can be responsible for the stripping of the He-rich layer. However, in most cases, the candidate mechanisms of these catastrophic activities favor very massive progenitors (see review by Smith 2014), which seem not fall in the mass range of SNe Ic estimated from the nebular spectra; further, the occurrence rates of these dramatic events are probably to low to be compatible with the SNe Ic rate (Li et al. 2011). In should be noted that the observational constraint on the violent eruption is very limited, with many mysteries remain to be solved, and their (possible) connections with the "normal" SESNe will undoubtedly be the important pieces toward completing the puzzle.

Section 7.2. Explosion energy yield

How the massive stars explode is a long-lasting question in the field of astrophysics. A basic ingredient toward the answer of this question is how the total released gravitational energy is transformed to the observable kinetic energy of the expanding ejecta. In the past works, the investigation on this topic is usually done by using early phase observations, where the kinetic energy and the ejecta mass derived from the light curves are compared (Lyman et al. 2016; Taddia et al. 2018). However, the transformation from the ejecta mass to the progenitor mass is not straightforward, and can be significantly affected by the pre-SN mass-loss scheme which is still not well understood (see **Section 7.1**).

In this thesis, we attempt to tackle with this topic by looking into the deep-lying core region. Because the explosion takes place in the innermost region, one would expect the most dramatic change will occur in this region if different explosion mechanisms are involved. By comparing the progenitor mass (measured by the intensities ratio of [O I]/[Ca II]) and the expansion velocity of the O-rich core (measured by the width of [O I]), we find a positive correlation between these quantities, which indicates the inner region of the ejecta more massive progenitors expand faster (**Chapter 4**). Such correlation cannot be explain by the constant kinetic energy (say, 1 foe) frequently adopted in modeling the SNe spectra. To explain this correlation, we simulate He stars and CO core models, which are latter exploded by a range of kinetic energy. By connecting the oxygen content with the [O I]/[Ca II] (based on the empirical relations derived from the models of Jerkstrand et al. 2015a), and the properly-weighted velocities with the line widths, we find $E_K \propto M_{CO}^{1.40}$ can reproduce the observed [O I]/[Ca II]-[O I] width correlation (**Chapter 5**). We further compare the M_{CO}-E_K relation with those obtained from the early phase observation, and find they are largely consistent. The early phase and nebular phase observations are indeed looking at different regions of the ejecta. The early phase observation is not directly related to the CO core, while it is a good probe of E_K because a large fraction of E_K is stored in the outermost region; the nebular phase observation can reliably measure the CO core mass, while it bias toward

the inner core region, therefore the measurement of E_K is probably not accurate. The merits and demerits of these two methods are indeed complementary.The combination of the early and nebular phase observation therefore provides us the unique chance to scan through the ejecta from the outermost region to the innermost core and test our assumptions on the dynamics of the ejecta. The analysis in this thesis provides the first step toward such investigation.

The M_{CO}-E_K relation derived in this work is based on several simplified assumptions, which make use of the empirical relation (extrapolated to large progenitor mass range) and the weighted velocities. We have discussed several factors, including the effects of E_K and the microscopic mixing on [O I]/[Ca II], and the macroscopic mixing, which would possibly affect the M_{CO}-E_K relation. In the future study, sophisticated nebular spectra models (for both He star and CO core) with the above factors included, and with a wide range of E_K taken into account, should be run to test the validity of the method proposed in this work.

Section 7.3. Explosion geometry

It is widely believed that a large fraction of CCSNe explode aspherically (Wang et al. 2001; Leonard et al. 2006). Accumulating evidences show that the specific configuration, i.e., bipolar explosion where the explosion energy is released along a specific direction rather than distributed spherically (as would be expected for spherical explosion), is not the exception, but the rule for at least a large fraction of CCSNe (Maeda et al. 2008; Modjaz et al. 2008; Taubenberger et al. 2009; Fang et al. 2022). The strongest evidence for such peculiar geometry comes from the horn-like profile of the [O I] nebular line, which is expected if the oxygen elements are distributed in the torus (i.e., the disk with a hole in the center) and viewed from the on-edge direction. The straightforward way to create the torus from the originally spherical O-rich region (created by stellar nucleosynthesis) is bipolar explosion: the ram pressure of the collimated released energy will compress the O-rich material onto the equatorial plane. The bow shock spreads around the axis, which creates the so-called “cocoon” with high entropy. In the cocoon, the stellar material is burnt into the heavier iron-peak elements, leaving the center of the O-rich disk rich in iron but deficient in oxygen. However, the horn-like [O I] is only the indirect evidence:it traces the spatial distribution of the unburnt material, while the geometry of the burning region remains unknown.

In this work, we use the [Ca II] emitted from the explosive burning ash to study the properties of this region. We have noticed that a fraction of the objects show double-peaked or flat-topped [Ca II], which is not reported in previous works. The peculiar double-peaked profiles of [Ca II], along with their broad natures, suggest the iron-rich burning ash are bi-modal distributed, i.e., characterized by two detached bubbles. A simple bipolar model can explain the diversity seen in the profiles of [O I] and [Ca II] by varying the viewing angle. The combined analysis of the geometry (indicated by the line profiles) and the progenitor mass (measured by the relative strength of [O I]) further suggests whether the SNe explode spherically are not dependent, while the asphericity of the bipolar explosions strongly depend, on their CO core masses.

To investigate the geometry of the explosion, we have proposed a relatively simplified bipolar model which involves only two parameters but successfully produced the diversity seen in the [O I] and [Ca II] profiles. However, when it comes to the case-to-case fitting, we can see the current model fails to capture some details of the line profiles, which would require one to introduce the clumpy structures or radiative transfer processes into the ejecta. Further, in reality, the distributions of the physical quantities, including density, temperature,

mass fractions, etc., are not flat as assumed in the current model. Following the expansion of the ejecta, we are looking into deeper and deeper region, the thermal conditions are therefore changed and the line formation processes are accordingly affected. The analysis of the evolution of the line profiles will provide us with the valuable information of the spatial distributions of the physical quantities in the ejecta. These issues will be addressed in the future studies.

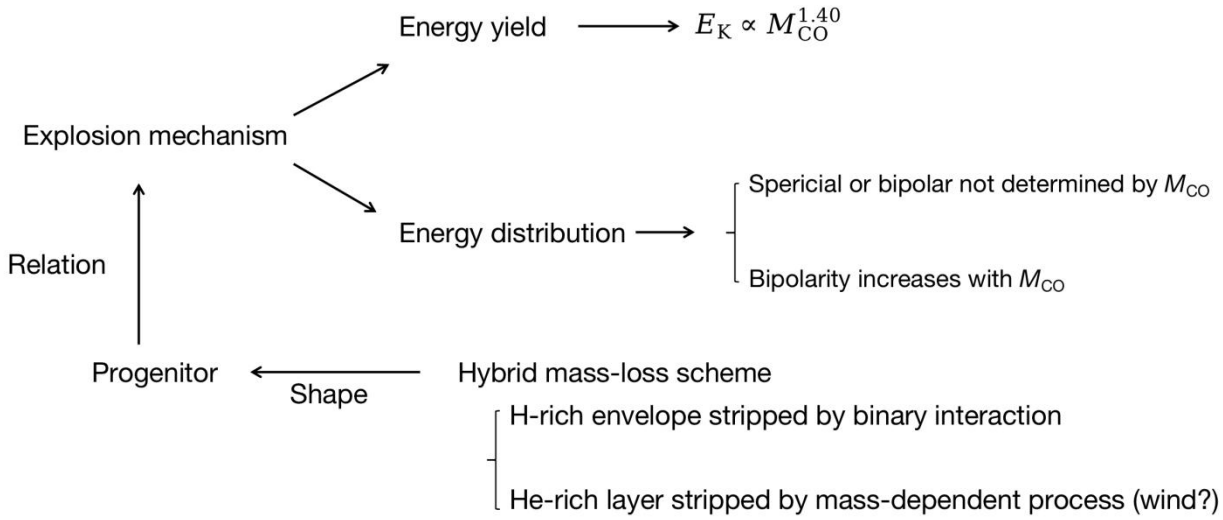

Figure 7.1. The schematic conclusion of the results derived in the thesis.

Bibliography

Anderson, J. P., Habergham, S. M., James, P. A., & Hamuy, M., 2012, MNRAS, 424, 1372
Anderson, J. P., Dessart, L., Gutiérrez, C. P., et al. 2018, NatAs, 2, 574

Arnett, W. D., 1980, ApJ, 237, 541

Arnett, W. D., 1982, ApJ, 253, 785

Astropy Collaboration, Robitaille, T. P., Tollerud, E. J., et al. 2013, A&A, 558, A33

Astropy Collaboration, Price-Whelan, A. M., Sipőcz, B. M., et al. 2018, AJ, 156, 123

Barbon, R., Ciatti, F., & Rosino, L. 1979, A&A, 72, 287

Barbon, R., Benetti, S., Cappellaro, E., et al. 1995, A&AS, 110, 513

Ben-Ami, S., Gal-Yam, A., Mazzali, P. A., et al. 2014, ApJ, 785, 37

Ben-Ami, S., Hachinger, S., Gal-Yam, A., et al. 2015, ApJ, 803, 40

Benetti, S., Turatto, M., Valenti, S., et al. 2011, MNRAS, 411, 2726

Bersten, M. C., Benvenuto, O. G., Nomoto, K., et al. 2012, ApJ, 757, 31

Bersten, M. C., Benvenuto, O. G., Folatelli, G., et al. 2014, AJ, 148, 68
Bersten, M. C., Folatelli, G., García, F., et al. 2018, Nature, 554, 497

Bessell, M., & Murphy, S. 2012, PASP, 124, 140

Bianco, F. B., Modjaz, M., Hicken, M., et al. 2014, ApJS, 213, 19

Blondin, S., Modjaz, M., Kirshner, R., et al. 2007, CBE Telegram, 808, 1

Brown, P. J., Breeveld, A. A., Holland, S., Kuin, P., & Pritchard, T., 2014, Astrophys. Space Sci. 354, 89

Bufano, F., Pignata, G., Bersten, M., et al. 2014, MNRAS, 439, 1807

Cano, Z. 2013, MNRAS, 434, 1098

Cao, Y., Kasliwal, M. M., Arcavi, I., et al. 2013, ApJL, 775, L7

Cappellaro, E., Mazzali, P. A., Benetti, S., et al. 1997, A&A, 328, 203

Cardelli, J. A., Clayton, G. C., & Mathis, J. S. 1989, ApJ, 345, 245

Chevalier, R. A., & Soderberg, A. M. 2010, ApJL, 711, L40

Chakraborti, S., Soderberg, A., Chomiuk, L., et al. 2015, ApJ, 805, 187

Chornock, R., Filippenko, A. V., Li, W., et al. 2011, ApJ, 739, 41

Clocchiatti, A., Wheeler, J. C., Brotherton, M. S., et al. 1996, ApJ, 462, 462

Clocchiatti, A., Suntzeff, N. B., Covarrubias, R., et al. 2011, AJ, 141, 163

Colesanti, C., Jacques, C., Pimentel, E., et al. 2006, IAU Circ., 8713, 1

Collins, C., Müller, B., & Heger, A. 2018, MNRAS, 473, 1695

Dessart, L., Hillier, D. J., Li, C., & Woosley, S., 2012, MNRAS, 424, 2139

Dessart, L., Hillier, D. J., Woosley, S., et al. 2016, MNRAS, 458, 1618

Dessart, L., & Hillier, D. J. 2020, A&A, 642, A33

Dessart, L., Yoon, S.-C., Aguilera-Dena, D. R., et al. 2020, A&A, 642, A106

Dessart, L., Hillier, D. J., Sukhbold, T., et al. 2021, A&A, 656, A61

Drissen, L., Robert, C., Dutil, Y., et al. 1996, IAU Circ., 6317, 2

Drout, M. R., Soderberg, A. M., Gal-Yam, A., et al. 2011, ApJ, 741, 97

Drout, M. R., Milisavljevic, D., Parrent, J., et al. 2016, ApJ, 821, 57

Eldridge, J. J., Fraser, M., Smartt, S. J., et al. 2013, MNRAS, 436, 774

Elmhamdi, A., Danziger, I. J., Cappellaro, E., et al. 2004, A&A, 426, 963

Elmhamdi, A., Tsvetkov, D., Danziger, I. J., et al. 2011, ApJ, 731, 129

Elmhamdi, A. 2011, Acta Astronomica, 61, 179

Ennis, J. A., Rudnick, L., Reach, W. T., et al. 2006, ApJ, 652, 376

Ergon, M., Sollerman, J., Fraser, M., et al. 2014, A&A, 562, A17

Ergon, M., Jerkstrand, A., Sollerman, J., et al. 2015, A&A, 580, A142

Evans, R., Sadler, E., & McNaught, R. H. 1990, IAU Circ., 5076, 1

Fang, Q., & Maeda, K. 2018, ApJ, 864, 47

Fang, Q., Maeda, K., Kuncarayakti, H., et al. 2019, NatAs, 3, 434

Fang, Q., Maeda, K., Kuncarayakti, H., et al. 2022, ApJ, 928, 151

Filippenko, A. V., & Sargent, W. L. W. 1986, AJ, 91, 691

Filippenko, A. V. 1988, AJ, 96, 1941

Filippenko, A. V., Porter, A. C., & Sargent, W. L. W. 1990, AJ, 100, 1575

Filippenko, A. V., & Korth, S. 1991, IAU Circ., 5234, 1

Filippenko, A. V., Matheson, T., & Ho, L. C. 1993, ApJL, 415, L103

Filippenko, A. V., Barth, A. J., Matheson, T., et al. 1995, ApJL, 450, L11

Filippenko, A. V. 1997, ARA&A, 35, 309

Filippenko, A. V., Foley, R. J., & Matheson, T. 2005, IAU Circ., 8639, 2

Folatelli, G., Contreras, C., Phillips, M. M., et al. 2006, ApJ, 641, 1039

Folatelli, G., Bersten, M. C., Kuncarayakti, H., et al. 2014, ApJ, 792, 7

Folatelli, G., Bersten, M. C., Kuncarayakti, H., et al. 2015, ApJ, 811, 147

Foley, R. J., Papenkova, M. S., Swift, B. J., et al. 2003, PASP, 115, 1220

Fransson, C., & Chevalier, R. A. 1989, ApJ, 343, 323

Fremling, C., Sollerman, J., Taddia, F., et al. 2016, A&A, 593, A68

Fremling, C., Sollerman, J., Kasliwal, M. M., et al. 2018, A&A, 618, A37

Galama, T. J., Vreeswijk, P. M., van Paradijs, J., et al. 1998, Nature, 395, 670

Gal-Yam, A., Fox, D. B., Kulkarni, S. R., et al. 2005, ApJL, 630, L29

Gal-Yam, A. 2017, Handbook of Supernovae, 195

Gilkis, A., Vink, J. S., Eldridge, J. J., et al. 2019, MNRAS, 486, 4451

Gilkis, A. & Arcavi, I. 2022, MNRAS, 511, 691

Gómez, G., & López, R. 1994, AJ, 108, 195

Gómez, G., & López, R. 2002, AJ, 123, 328

Gräfener, G., & Vink, J. S. 2016, MNRAS, 455, 112

Green, D. W. E. 2006, CBE Telegram, 368, 2

Groh, J. H., Georgy, C., & Ekström, S. 2013, A&A, 558, L1

Guillochon, J., Parrent, J., Kelley, L. Z., et al. 2017, ApJ, 835, 64

Hamuy, M., Deng, J., Mazzali, P. A., et al. 2009, ApJ, 703, 1612

Harris, C. R., Millman, K. J., van der Walt, S. J., et al. 2020, Natur, 585, 357

Harutyunyan, A. H., Pfahler, P., Pastorello, A., et al. 2008, A&A, 488, 383

Heger, A., Fryer, C. L., Woosley, S. E., et al. 2003, ApJ, 591, 288

Hjorth, J., Sollerman, J., Møller, P., et al. 2003, Nature, 423, 847

Holland-Ashford, T., Lopez, L. A., Auchettl, K., et al. 2017, ApJ, 844, 84

Houck, J. C., & Fransson, C. 1996, ApJ, 456, 811

Hunter, J. D. 2007, CSE, 9, 90

Hunter, D. J., Valenti, S., Kotak, R., et al. 2009, A&A. 508, 371

Iwamoto, K., Mazzali, P. A., Nomoto, K., et al. 1998, Nature. 395, 672

Iwamoto, K., Nakamura, T., Nomoto, K., et al. 2000, ApJ, 534, 660

Jeffery, D. J., Branch, D., Filippenko, A. V., et al. 1991, ApJL, 377, L89

Jerkstrand, A., Fransson, C., Maguire, K., et al. 2012, A&A, 546, A28

Jerkstrand, A., Smartt, S. J., Fraser, M., et al. 2014, MNRAS, 439, 3694

Jerkstrand, A., Ergon, M., Smartt, S. J., et al. 2015a, A&A, 573, A12

Jerkstrand, A., Timmes, F. X., Magkotsios, G., et al. 2015b, ApJ, 807, 110

Jerkstrand, A., Smartt, S. J., Sollerman, J., et al. 2015c, MNRAS, 448, 2482

Jerkstrand, A. 2017, Handbook of Supernovae (Cham: Springer), 795

Jerkstrand, A., Smartt, S. J., Inserra, C., et al. 2017, ApJ, 835, 13

Kashikawa, N., Aoki, K., Asai, R., et al. 2002, PASJ, 54, 819

Katsuda, S., Morii, M., Janka, H.-T., et al. 2018, ApJ, 856, 18

Khokhlov, A.M., Höflich, P.A., Oran, E.S., et al. 1999, ApJ, 524, L107
Kifonidis, K., Plewa, T., Janka, H. T., et al. 2003, A&A, 408, 621
Kifonidis, K., Plewa, T., Scheck, L., et al. 2006, A&A, 453, 661

Kilpatrick, C. D., Foley, R. J., Abramson, L. E., et al. 2017, MNRAS, 465, 4650

Kilpatrick, C. D., Drout, M. R., Auchettl, K., et al. 2021, MNRAS, 504, 2073

Kozma, C., & Fransson, C. 1992, ApJ, 390, 602

Kozma, C., & Fransson, C. 1998, ApJ, 497, 431

Kuncarayakti, H., Maeda, K., Bersten, M. C., et al. 2015, A&A, 579, A95

Kuncarayakti, H., Anderson, J. P., Galbany, L., et al. 2018, A&A, 613, A35

Li, H., & McCray, R. 1996, ApJ, 456, 370

Li, W., Leaman, J., Chornock, R., et al. 2011, MNRAS, 412, 1441

Limongi, M., & Chieffi, A. 2003, ApJ, 592, 404

Liu, Y.-Q., Modjaz, M., Bianco, F. B., & Graur, O. 2016, ApJ, 827, 90

Leonard, D. C., Filippenko, A. V., Gates, E. L., et al. 2002, PASP, 114, 35

Leonard, D. C., Filippenko, A. V., Ganeshalingam, M., et al. 2006, Nature, 440, 505

Loader, C. 1999, Local Regression and Likelihood (New York: Springer)

Loader, C. 2018, locfit: Local Regression, Likelihood and Density Estimation

Lyman, J. D., Bersier, D., James, P. A., et al. 2016, MNRAS, 457, 328

Maeda, K., Nakamura, T., Nomoto, K., et al. 2002, ApJ, 565, 405

Maeda, K., & Nomoto, K. 2003, ApJ, 598, 1163

Maeda, K., Mazzali, P. A., Deng, J., et al. 2003, ApJ, 593, 931

Maeda, K., Nomoto, K., Mazzali, P. A., et al. 2006a, ApJ, 640, 854

Maeda, K., Mazzali, P. A., & Nomoto, K. 2006b, ApJ, 645, 1331

Maeda, K., Kawabata, K., Tanaka, M., et al. 2007a, ApJL, 658, L5

Maeda, K., Tanaka, M., Nomoto, K., et al. 2007b, ApJ, 666, 1069

Maeda, K., Kawabata, K., Mazzali, P. A., et al. 2008, Sci, 319, 1220

Maeda, K., Hattori, T., Milisavljevic, D., et al. 2015, ApJ, 807, 35

Makarov, D., Prugniel, P., Terekhova, N., et al. 2014, A&A, 570, A13

Malesani, D., Fynbo, J. P. U., Hjorth, J., et al.2009, Probing Stellar Populations Out to the Distant Universe:

Cefalu 2008, Proceedings of the International Conference, 1111, 627

Matheson, T., Filippenko, A. V., Barth, A. J., et al. 2000a, AJ, 120, 1487

Matheson, T., Filippenko, A. V., Ho, L. C., et al. 2000b, AJ, 120, 1499

Matheson, T., Filippenko, A. V., Li, W., et al. 2001, AJ, 121, 1648

Maund, J. R., Smartt, S. J., Kudritzki, R. P., et al. 2004, Nature, 427, 129

Maund, J. R., Wheeler, J. C., Patat, F., et al. 2007, ApJ, 671, 1944

Maund, J. R., Fraser, M., Ergon, M., et al. 2011, ApJL, 739, L37

Maurer, J. I., Mazzali, P. A., Deng, J., et al. 2010a, MNRAS, 402, 161

Maurer, I., Mazzali, P. A., Taubenberger, S., & Hachinger, S. 2010b, MNRAS, 409, 1441

Mazzali, P. A., Iwamoto, K., & Nomoto, K. 2000, ApJ, 545, 407

Mazzali, P. A., Deng, J., Maeda, K., et al. 2002, ApJL, 572, L61

Mazzali, P. A., Kawabata, K. S., Maeda, K., et al. 2005, Science, 308, 1284

Mazzali, P. A., Deng, J., Nomoto, K., et al. 2006, Nature, 442, 1018

Milisavljevic, D., Fesen, R. A., Gerardy, C. L., et al. 2010, ApJ, 709, 1343

Milisavljevic, D., Margutti, R., Soderberg, A. M., et al. 2013a, ApJ, 767, 71

Milisavljevic, D., Soderberg, A. M., Margutti, R., et al. 2013b, ApJL, 770, L38

Milisavljevic, D., Margutti, R., Kamble, A., et al. 2015a, ApJ, 815, 120

Milisavljevic, D., Margutti, R., Parrent, J. T., et al. 2015b, ApJ, 799, 51

Minkowski, R. 1941, PASP, 53, 224

Modjaz, M., Stanek, K. Z., Garnavich, P. M., et al. 2006, ApJL, 645, L21

Modjaz, M. 2007, PhD thesis, Harvard Univ.

Modjaz, M., Kirshner, R. P., Blondin, S., et al. 2008, ApJL, 687, L9

Modjaz, M., Li, W., Butler, N., et al. 2009, ApJ, 702, 226

Modjaz, M., Blondin, S., Kirshner, R. P., et al. 2014, AJ, 147, 99

Modjaz, M., Liu, Y. Q., Bianco, F. B., et al. 2016, ApJ, 832, 108

Morales-Garoffolo, A., Elias-Rosa, N., Benetti, S., et al. 2014, MNRAS, 445, 1647

Morales-Garoffolo, A., Elias-Rosa, N., Bersten, M., et al. 2015, MNRAS, 454, 95

Morales-Garoffolo, A. 2016, Ph.D. Thesis

Moriya, T. J., Suzuki, A., Takiwaki, T., et al. 2020, MNRAS, 497, 1619

Morozova, V., Piro, A. L., Renzo, M., et al. 2015, ApJ, 814, 63

Müller, B., Heger, A., Liptai, D., et al. 2016, MNRAS, 460, 742

Nagao, T., Patat, F., Taubenberger, S., et al. 2021, MNRAS, 505, 3664

Nakamura, T., Mazzali, P. A., Nomoto, K., et al. 2001, ApJ, 550, 991

Nakamura, K., Takiwaki, T., Kuroda, T., et al. 2015, PASJ, 67, 107

Nakano, S., Aoki, M., Kushida, R., et al. 1996, IAU Circ., 6454, 1

Nakano, S., Aoki, M., Jha, S., et al. 1997, IAU Circ., 6770, 2

Nomoto, K. I., Iwamoto, K., & Suzuki, T. 1995, Phys. Rep. 256, 173
O'Connor, E., & Ott, C. D., 2011, ApJ, 730, 70

Ouchi, R., & Maeda, K. 2017, ApJ, 840, 90

Park, T., Kashyap, V. L., Siemiginowska, A., et al. 2006, ApJ, 652, 610

Pastorello, A., Smartt, S. J., Mattila, S., et al. 2007, Nature, 447, 829
Patat, F., Chugai, N., & Mazzali, P. A. 1995, A&A, 299, 715

Patat, F., Cappellaro, E., Danziger, J., et al. 2001, ApJ, 555, 900

Paxton, B., Bildsten, L., Dotter, A., et al. 2011, ApJS, 192, 3
Paxton, B., Cantiello, M., Arras, P., et al. 2013, ApJS, 208, 4
Paxton, B., Marchant, P., Schwab, J., et al. 2015, ApJS, 220, 15
Paxton, B., Schwab, J., Bauer, E. B., et al. 2018, ApJS, 234, 34
Paxton, B., Smolec, R., Schwab, J., et al. 2019, ApJS, 243, 10
Pian, E., Mazzali, P. A., Masetti, N., et al. 2006, Nature, 442, 1011

Prentice, S. J., Mazzali, P. A., Pian, E., et al. 2016, MNRAS, 458, 2973

Prentice, S. J., & Mazzali, P. A. 2017, ApJ, 469, 2672

Prentice, S. J., Maguire, K., Siebenaler, L., et al. 2022, MNRAS, 514, 5686

Qiu, Y., Li, W., Qiao, Q., et al. 1999, AJ, 117, 736

Quimby, R., Mondol, P., Castro, F., et al. 2006, IAU Circ., 8657, 1

R Core Team 2021, R: A Language and Environment for Statistical Computing (Vienna)

Richmond, M. W., Treffers, R. R., Filippenko, A. V., & Paik, Y. 1996a, AJ, 112, 732

Richmond, M. W., van Dyk, S. D., Ho, W., et al. 1996b, AJ, 111, 327

Roy, R., Kumar, B., Maund, J. R., et al. 2013, MNRAS, 434, 2032

Sahu, D. K., Gurugubelli, U. K., Anupama, G. C., et al. 2011, MNRAS, 413, 2583

Shigeyama, T., Suzuki, T., Kumagai, S., et al. 1994, ApJ, 420, 341

Shivvers, I., Mazzali, P., Silverman, J. M., et al. 2013, MNRAS, 436, 3614

Shivvers, I., Modjaz, M., Zheng, W., et al. 2017, PASP, 129, 054201

Shivvers, I., Filippenko, A. V., Silverman, J. M., et al. 2019, MNRAS, 482, 1545

Silverman, J. M., Mazzali, P., Chornock, R., et al. 2009, PASP, 121, 689

Smartt, S. J. 2009, ARA&A, 47, 63

Smartt, S. J. 2015, PASA, 32, e016

Smith, N., Li, W., Filippenko, A. V., & Chornock, R. 2011, MNRAS, 412, 1522

Smith, N. 2014, ARA&A, 52, 487

Smith, N., Mauerhan, J. C., & Prieto, J. L., 2014, MNRAS, 438, 1191

Stancliffe, R. J., & Eldridge, J. J., 2009, MNRAS, 396, 1699

Stritzinger, M., Mazzali, P., Phillips, M. M., et al. 2009, ApJ, 696, 713

Stritzinger, M. D., Anderson, J. P., Contreras, C., et al. 2018, A&A, 609, A134

Sukhbold, T., Ertl, T., Woosley, S. E., et al. 2016, ApJ, 821, 38

Suwa, Y., Tominaga, N., & Maeda, K., 2019, MNRAS, 483, 3607

Szalai, T., Vinkó, J., Nagy, A. P., et al. 2016, MNRAS, 460, 1500

Taddia, F., Fremling, C., Sollerman, J., et al. 2016, A&A, 592, A89

Taddia, F., Stritzinger, M. D., Bersten, M., et al. 2018, A&A, 609, A136

Taddia, F., Sollerman, J., Fremling, C., et al. 2019, A&A, 621, A64

Tartaglia, L., Fraser, M., Sand, D. J., et al. 2017, ApJL, 836, L12

Taubenberger, S., Pastorello, A., Mazzali, P. A., et al. 2006, MNRAS, 371, 1459

Taubenberger, S., Valenti, S., Benetti, S., et al. 2009, MNRAS, 397, 677

Taubenberger, S., Navasardyan, H., Maurer, J. I., et al. 2011, MNRAS, 413, 2140

Tauris, T. M., Langer, N., & Podsiadlowski, P., 2015, MNRAS., 451, 2123

Terreran, G., Jerkstrand, A., Benetti, S., et al. 2016, MNRAS, 462, 137

Tody, D. 1986, Proc. SPIE, 627, 733

Tody, D. 1993, in ASP Conf. Ser. 52, Astronomical Data Analysis Software and Systems II, ed. R. J. Hanisch (San Francisco, CA: ASP), 173

Tominaga, N. 2009, ApJ, 343 690, 526

Tsvetkov, D. Y., Volkov, I. M., Baklanov, P., Blinnikov, S., & Tuchin, O. 2009, Perem. Zvezdy, 29, 2

Tully, R. B., Courtois, H. M., Dolphin, A. E., et al. 2013, AJ, 146, 86

Turatto, M., Benetti, S., & Cappellaro, E. 2003, in From Twilight to Highlight: The Physics of Supernovae, ed. W. Hillebrandt & B. Leibundgut (Berlin: Springer), 200

Ugliano, M., Janka, H.-T., Marek, A., et al. 2012, ApJ, 757, 69

Valenti, S., Benetti, S., Cappellaro, E., et al. 2008, MNRAS, 383, 1485

Valenti, S., Fraser, M., Benetti, S., et al. 2011, MNRAS, 416, 3138

Valenti, S., Taubenberger, S., Pastorello, A., et al. 2012, ApJL, 749, L28

Vanbeveren, D., De Loore, C., & Van Rensbergen, W., 1998, Astron. Astrophys. Rev. 9, 63

van Dokkum, P. G. 2001, PASP, 113, 1420

Van Dyk, S. D., Zheng, W., Fox, O. D., et al. 2014, AJ, 147, 37

Virtanen, P., Gommers, R., Oliphant, T. E., et al. 2020, NatMe, 17, 261

Walker, E. S., Mazzali, P. A., Pian, E., et al. 2014, MNRAS, 442, 2768

Wang, L., Howell, D. A., Höflflich, P., et al. 2001, ApJ, 550, 1030

Wang, L., & Wheeler, J. C. 2008, ARA&A, 46, 433

Weiler, K. W., Williams, C. L., Panagia, N., et al. 2007, ApJ, 671, 1959

Wheeler, J. C., Harkness, R. P., Clocchiatti, A., et al. 1994, ApJL, 436, L135

Wongwathanarat, A., Muller, E., & Janka, H. T. 2015, A&A, 577, A48

Woosley, S. E., Heger, A., & Weaver, T. A. 2002, Rev. Mod. Phys. 74, 1015

Woosley, S. E., & Bloom, J. S. 2006, ARA&A, 44, 507

Yaron, O., & Gal-Yam, A. 2012, PASP, 124, 668

Yoon, S.-C. 2015, PASA, 32, e015

Yoon, S.-C. 2017, MNRAS, 470, 3970

Yoon, S.-C., Dessart, L., & Clocchiatti, A., 2017, ApJ., 840, 10

Yoon, S.-C., Chun, W., Tolstov, A., et al. 2019, ApJ, 872, 174

Yoshida, M., Shimizu, Y., Sasaki, T., et al. 2000, Proc. SPIE, 4009, 240

Yoshii, Y., Tomita, H., Kobayashi, Y., et al. 2003, ApJ, 592, 467

Zhang, J., Wang, X., Vinkó, J., et al. 2018, ApJ, 863, 109

List of Figures

List of Tables